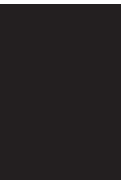


Advances in Optical Technologies

# **Advanced Infrared Technology and Applications**

Guest Editors: Ovidio Salvetti, Laura Abbozzo Ronchi, Carlo Corsi,  
Ermanno Grinzato, Antoni Rogalski, and Marija Strojnik





---

# **Advanced Infrared Technology and Applications**

Advances in Optical Technologies

---

## **Advanced Infrared Technology and Applications**

Guest Editors: Ovidio Salvetti, Laura Abbozzo Ronchi,  
Carlo Corsi, Ermanno Grinzato, Antoni Rogalski,  
and Marija Strojnik



---

Copyright © 2013 Hindawi Publishing Corporation. All rights reserved.

This is a special issue published in "Advances in Optical Technologies." All articles are open access articles distributed under the Creative Commons Attribution License, which permits unrestricted use, distribution, and reproduction in any medium, provided the original work is properly cited.

## Editorial Board

Mustafa A. G. Abushagur, USA  
Partha P. Banerjee, USA  
Ralph Barry Johnson, USA  
Augusto Belendez, Spain  
Steve Blair, USA  
Maria Luisa Calvo, Spain  
Pierre Chavel, France  
Zhongping Chen, USA  
Fu-Pen Chiang, USA  
Petr Eliseev, USA  
Michael A. Fiddy, USA  
Patti Gillespie, USA

Richard B. Hoover, USA  
Zoran Ikonc, UK  
Saulius Juodkazis, Australia  
Mark A. Kahan, USA  
Alexander A. Kaminskii, Russia  
Qiang Lin, China  
Liren Liu, China  
Qingming Luo, China  
Daniel Malacara, Mexico  
Mikhail Noginov, USA  
Ci-Ling Pan, Taiwan  
Markus Pessa, Finland

Giancarlo C. Righini, Italy  
Joseph Rosen, Israel  
José Luís Santos, Portugal  
Colin J. R. Sheppard, Singapore  
Kiyoshi Shimamura, Japan  
Jagdish P. Singh, USA  
Yinglin Song, China  
Theo Tschudi, Germany  
Leonid P. Yaroslavsky, Israel  
Jianping Yin, China  
Yong Zhao, China

# Contents

**Advanced Infrared Technology and Applications**, Ovidio Salvetti, Laura Abbozzo Ronchi, Carlo Corsi, Antoni Rogalski, and Marija Strojnik  
Volume 2013, Article ID 459074, 2 pages

**Optical System for Bispectral Imaging in Mid-IR at 1000 Frames per Second**, Marija Strojnik and Gonzalo Paez  
Volume 2013, Article ID 905870, 7 pages

**In Search of Early Time: An Original Approach in the Thermographic Identification of Thermophysical Properties and Defects**, Daniel L. Balageas  
Volume 2013, Article ID 314906, 13 pages

**End-to-End Image Simulator for Optical Imaging Systems: Equations and Simulation Examples**, Peter Coppo, Leandro Chiarantini, and Luciano Alparone  
Volume 2013, Article ID 295950, 23 pages

**Heat Diffusion in Klinker Facade: The Study Case of a Gio Ponti Building**, N. Ludwig, E. Rosina, S. Caglio, M. Gargano, and V. Redaelli  
Volume 2012, Article ID 738943, 6 pages

**Micro-Scale Thermal Imaging of Organic and Polymeric Materials with Cooled and Uncooled Infrared Cameras**, J. Morikawa, E. Hayakawa, and T. Hashimoto  
Volume 2012, Article ID 484650, 7 pages

**Emissivity Measurement of Semitransparent Textiles**, P. Bison, A. Bortolin, G. Cadelano, G. Ferrarini, and E. Grinzato  
Volume 2012, Article ID 373926, 5 pages

**Infrared Camera Analysis of Laser Hardening**, J. Tesar, P. Vacikova, O. Soukup, and S. Houdkova  
Volume 2012, Article ID 593893, 6 pages

**Infrared: A Key Technology for Security Systems**, Carlo Corsi  
Volume 2012, Article ID 838752, 15 pages

**Nanoscale Biomolecular Detection Limit for Gold Nanoparticles Based on Near-Infrared Response**, Mario D'Acunto, Davide Moroni, and Ovidio Salvetti  
Volume 2012, Article ID 278194, 8 pages

**Porosity and Inclusion Detection in CFRP by Infrared Thermography**, C. Toscano, C. Meola, M. C. Iorio, and G. M. Carlomagno  
Volume 2012, Article ID 765953, 6 pages

**Contribution of Series Resistance in Modelling of High-Temperature Type II Superlattice p-i-n Photodiodes**, Jaroslaw Wróbel, Piotr Martyniuk, and Antoni Rogalski  
Volume 2012, Article ID 926365, 5 pages

**High-Quality Growth of GaInNAs for Application to Near-Infrared Laser Diodes**, Masahiko Kondow and Fumitaro Ishikawa

Volume 2012, Article ID 754546, 11 pages

**Monitoring Composites under Bending Tests with Infrared Thermography**, Carosena Meola, Giovanni Maria Carlomagno, Carmela Bonavolontà, and Massimo Valentino

Volume 2012, Article ID 720813, 7 pages

**Chemical Warfare Agents Analyzer Based on Low Cost, Room Temperature, and Infrared Microbolometer Smart Sensors**, Carlo Corsi, Andrea Dundee, Paolo Laurenzi, Nicola Liberatore, Domenico Luciani, Sandro Mengali, Angelo Mercuri, Andrea Pifferi, Mirko Simeoni, Gaetano Tosone, Roberto Viola, and Donatella Zintu

Volume 2012, Article ID 808541, 5 pages

## Editorial

# Advanced Infrared Technology and Applications

**Ovidio Salvetti,<sup>1</sup> Laura Abbozzo Ronchi,<sup>2</sup> Carlo Corsi,<sup>3</sup>  
Antoni Rogalski,<sup>4</sup> and Marija Strojnik<sup>5</sup>**

<sup>1</sup> *Institute of Information Science and Technologies, National Research Council of Italy, Pisa, Italy*

<sup>2</sup> *Giorgio Ronchi Foundation, Florence, Italy*

<sup>3</sup> *Electro-Optics Research Center, C.R.E.O., L'Aquila, Italy*

<sup>4</sup> *Institute of Applied Physics, Military University of Technology, Warsaw, Poland*

<sup>5</sup> *Center for Research in Optics, Leon, GTO, Mexico*

Correspondence should be addressed to Ovidio Salvetti; [ovidio.salvetti@isti.cnr.it](mailto:ovidio.salvetti@isti.cnr.it)

Received 13 January 2013; Accepted 13 January 2013

Copyright © 2013 Ovidio Salvetti et al. This is an open access article distributed under the Creative Commons Attribution License, which permits unrestricted use, distribution, and reproduction in any medium, provided the original work is properly cited.

Nowadays, advanced infrared techniques are a key ingredient in disparate applications, ranging from medical diagnostics and treatment to industrial inspection and environmental monitoring. We believe that the success of such infrared applications highly depends on a continuous exchange between scientific advances and technological progresses.

After the success of the 11th International Workshop Advanced Infrared Technology and Applications (AITA) held in L'Aquila (Italy), September 2011, it was then decided to organize this special issue in order to further foster such synergy by assessing the state of the art of the technology in the near, mid, and far Infrared and by presenting its most interesting and innovative applications.

AITA workshop, an event of a biennial series started in 1991 and organized by the "Giorgio Ronchi" Foundation (Florence), the Institutes of Information Science and Technologies "Alessandro Faedo" (Pisa), Construction Technologies (Padova), Applied Physics "Nello Carrara" (Florence) of the National Research Council of Italy and C.R.E.O. Consortium L'Aquila, constitutes an international forum bringing together academic and industrial researchers to exchange knowledge, ideas, and experiences in the field of infrared science and technology.

Main topics of the workshop included in particular advanced technology and materials, smart and fiber-optic sensors, aerospace and industrial applications, astronomy and earth monitoring, nondestructive tests and evaluation, systems for cultural heritage, near-, mid-, and long wave-length systems, and image processing and data analysis.

The special issue was not only intended to collect extended version of selected papers presented at the workshop, but submission was open to every investigator in the field, with the aim to have an even wider coverage of all advances in this area.

This special issue includes fourteen papers which discuss scientific and technological aspects related to these areas.

In the area of advanced sensors, C. Corsi illustrates the highlights of the main historical IR developments and their impact in security applications and, correlated with the leading technology of Silicon Microelectronics, scientific and economic comparisons are discussed.

M. Kondow and F. Ishikawa study reproducible growth of high-quality GaInNAs by molecular beam epitaxy, while a chemical warfare agents analyzer is introduced by C. Corsi et al. where the authors propose low cost, room temperature, micro-bolometer sensors.

Finally, J. Wrobel et al. analyze some of the consequences of omitting series resistance in InAs/GaSb p-i-n T2SL photodiode dark current modeling, using simplified p-n junction model. As is shown, incorrect series resistance value might cause discrepancies between generation/recombination and diffusion effective carrier lifetimes over one order of magnitude.

In the area of advanced technology and materials, M. D'Acunto et al. propose a single molecule detection based on near-infrared sensors and discuss biomedical applications. In particular, they study how the optical properties of gold nanoparticles and core-gold nanoshells are changed

as a function of different sizes, shapes, composition, and biomolecular coating with characteristic shifts towards near-infrared region. J. Tesar et al. instead consider improvement procedures of surface properties such as laser hardening which are becoming more and more important in present manufacturing and discuss methods for their analysis through infrared imaging.

In the area of image processing and data analysis, Strojnik and G. Paez propose and demonstrate the performance of an optical/IR double-image setup capable to observe rapidly varying phenomena up to 1000 frames per second. Applications to flame analysis for combustion efficiency are given.

In Morikawa et al., the applicability of the uncooled microbolometer to the microscale thermal analysis on phase transitions of organic and polymeric materials is discussed in comparison with the photon detector. Their study is motivated by the fact that noncontact thermal imaging methods are preferred in characterization of materials in increasing number of applications. In particular, creating and monitoring thermal distributions with a spatial resolution of  $\sim 10 \mu\text{m}$  is required for the materials developed in the energy saving and renewable technology.

The paper by D. Balageas starts with the observation that active thermography can give the possibility to characterize thermophysical properties and defects in complex structures, but that pixel-wise data processing based on 1-D model is the only reasonable approach for rapid image processing, due to the size of modern thermographic images. It is then argued that the only way to conciliate these two constraints when dealing with time-resolved experiments lies in the earlier possible detection/characterization. This approach is illustrated by several different applications and compared to more classical methods, demonstrating that simplicity of models and calculations is compatible with efficient and accurate identifications.

The area of Infrared-based nondestructive evaluation and industrial applications collects three contributions. C. Meola et al. present a method for monitoring composites under cyclic bending tests by means of infrared thermography. They focus on three types of composites including an epoxy matrix reinforced with either carbon fibers or glass fibers and hybrid composite involving glass fibers and aluminum layers. C. Toscano et al. introduce thermography methods for detecting porosity and inclusions in carbon fiber reinforced polymers, widely used in the aeronautical industry. More precisely, they consider both lock-in and pulse thermography in the transmission mode and conclude that both the techniques are definitely able to reveal the presence of the defects above mentioned; nevertheless, the techniques could be considered complementary in order to better assess the nature of defects.

Emissivity measurement of semitransparent textile is addressed by P. Bison et al., where the authors compare three textiles, namely one normal and two "special" with  $\text{Ag}^+$  ions and carbon powder added, with different colors. It is argued that colors used in the textiles actually affect emissivity more than the charging elements. Notice that the test used to achieve this result required some nonstandard procedure due to the semitransparent nature of textiles as opposed to conventional techniques for opaque surfaces.

In the area of buildings and infrastructures infrared applications, S. Caglio et al. focus on an infrared thermography procedure for heat diffusion in ceramics finishing materials of contemporary architecture. The aim of the research is the development of a method for the thermal characterization of clinkers, a very common ceramic finishing material of buildings. To this end, they analyze correlation between parameters found by thermography and the damage level in the specimens; a Gio Ponti building is discussed as case study.

Finally, in the area of remote sensing, P. Coppo et al. describe a simplified end-to-end software tool for simulation of data produced by optical instruments, starting from either synthetic or airborne hyperspectral data. Some simulation examples of hyper spectral and panchromatic images for existing and future design instruments are also reported. Both high spatial/spectral resolution images with low intrinsic noise and the sensor/mission specifications are used as inputs for simulations, thus showing the tool capabilities in simulating target detection scenario, including data quality assessment and class discrimination, as well as in understanding the impact of optical design on image quality.

## Acknowledgments

AITA Conference in L'Aquila as well as all the previous AITA Conferences were enjoying the support and participation of a great scientist and overall a great man, Ermanno Grinzato. Ermanno, one of the best examples of the Veneto's culture, was teaching us as real man should be: honest, sincere, and lovers of life and any good aspects of it. Probably life, due to the exchange of this love, was calling him too early, leaving us and to all the world his great lesson of sincerity, honesty, and love for the good things. For this all of us are missing him and his love for the important aspects of life. Arrivederci Ermanno and thanks for your great lesson.

*Ovidio Salvetti  
Laura Abbozzo Ronchi  
Carlo Corsi  
Antoni Rogalski  
Marija Strojnik*

## Research Article

# Optical System for Bispectral Imaging in Mid-IR at 1000 Frames per Second

**Marija Strojnik and Gonzalo Paez**

*Infrared Group, Research Directorate, Optics Research Center, P.O. Box 1-948, 37000 Leon, GTO, Mexico*

Correspondence should be addressed to Marija Strojnik; [mstrojnik@aol.com](mailto:mstrojnik@aol.com)

Received 9 August 2012; Accepted 27 November 2012

Academic Editor: Carlo Corsi

Copyright © 2013 M. Strojnik and G. Paez. This is an open access article distributed under the Creative Commons Attribution License, which permits unrestricted use, distribution, and reproduction in any medium, provided the original work is properly cited.

We propose, evaluate, and demonstrate the performance of an IR/optical double-image experimental setup where we capture two simultaneous images of a single object, in two different spectral bands, using a single detector array. With this arrangement, we may observe rapidly changing phenomena, at a rate of more than 1000 frames per second, without the loss of the spatial information about the test subject. We describe the optical system to perform simultaneous imaging in IR for slightly inclined optical axes. We verify the actual performance by applying the experimental method to flame analysis in the mid-IR to determine the combustion efficiency.

## 1. Introduction

Several methods to measure the combustion efficiency have been presented recently to decrease the amount of undesirable by-products and utilize prudently a nonrenewable resource. Among them, we may mention the infrared (IR) cameras to detect the detailed temporal evolution [1] and interferometric techniques to assess the airflow and heat travel throughout the flame volume [2]. The applications with IR cameras allow studying the flame evolution; however, they only record the nontransparent imaginary surface within the flame volume that emits the radiation. Another shortcoming of this technique is that the combustion is a volume effect [3]. The radiation has to travel through the volume where some of its components are attenuated. Furthermore, combustion is time- and position-dependent phenomenon, even after the apparent steady state has been achieved. Another technique that has been successfully implemented to measure the temporal dependence of an established flame is the lateral shearing interferometry. The fringe distribution at the time of its capture indicates the flow of the heated gases.

For many applications, the spatiotemporal information is even more important than the spectral one. Some multispectral imaging techniques already exist [4]. However, they require expensive and sophisticated equipment for the

acquisition, storage, and processing of data. They include, for example, hyperspectral imaging, available for the Earth, the ocean, and the atmospheric monitoring from mobile platforms [5]. Their usage restricts or even limits the frame rates and introduces novel focal plane layouts [6]. They often incorporate motion as a design parameter, with carefully controlled velocity vector [7]. An alternate approach has been to redistribute the spatial information into the optical fibers, and then to analyze each fiber individually [8]. This is a flexible light conduct to move image to the desired location. However, it imposes performance limitations on the achievable image resolution, while requiring a relatively elaborate experimental arrangement.

Most imaging systems capture a narrow wavelength-band image. Its width is determined by the characteristics of the optical system transmission, the detector sensitivity, and, of course, the spectral features of the object under investigation. Valuable information about a process of interest may often be obtained in just two wavelength bands. The design simplicity compensates for the loss of multispectral imaging capability. This tradeoff allows for the incorporation of additional features, as, for example, the possibility of recording detailed temporal information for the analysis of image evolution. Also, the elegance of the bispectral analysis may be of great value in routine applications of optics in medicine, including

remote thermometry [9], and blood oximetry [10]. Bispectral techniques have been successfully applied in the areas that do not require imaging. Recently, interest in developing dual-band IR detector arrays has been making excellent progress [11, 12].

A traditional method of recording bispectral images involves taking images of an object in succession, upon changing a filter each time [13, 14]. This technique limits the procedure to capturing relatively slow phenomena where temporal changes take place at a rate slower than the time to change the filter. Likewise, a relatively slow bispectral technique has been reported in the evaluation of aircraft models. Similarly, in microscopy a beam splitter may be inserted inside the instrument to generate two images in two planes [15].

In this experiment we are interested in determining the combustion efficiency throughout the volume. We propose to measure the relative quantities of two combustion by-products, within their characteristic spectral windows. This requires simultaneous measurement of transmitted radiation in two spectral channels. In this paper, we describe the optical system to achieve concurrent imaging in two IR spectral bands with precise point-to-point registration in the focal plane to allow taking ratio of detected radiation integrated over the corresponding pixel locations.

First, we lay out the preliminary experimental setup that conceptually accomplishes the bi

spectral imagery. This also serves to identify the performance requirements outlined in Section 3. On their basis the optical system is designed, accomplishing the goals. Preliminary results are presented in Section 4.

## 2. Bispectral Experiment

One of the advantages of the bispectral instrument, employed in this study, lies in measuring the relative strengths of two appropriately chosen spectral lines. Thus, only two relative measurements are needed to supply the requisite information for each pixel projected on the image plane. This makes the technique an ideal candidate for the high-speed imaging applications. We achieve bispectral imaging by capturing simultaneously two spectral images of the sample, followed by near real-time image processing, as illustrated schematically in Figure 1. We apply several algorithms to individual images. Then, we rebuild the final combined image.

With this IR/optical experimental setup we capture two images of a sample on a single detector array. They may be recorded at a rate higher than one frame per millisecond. We insert two external filters in two identical paths to overcome the limitations and possible jamming of relatively slow mechanisms. We image both onto the same detector array, but their images are spatially displaced for identification.

## 3. Optical System

In lateral or vectorial shearing interferometers, two identical beams follow “parallel paths”; while one is displaced with respect to the other, all the while remaining parallel. We

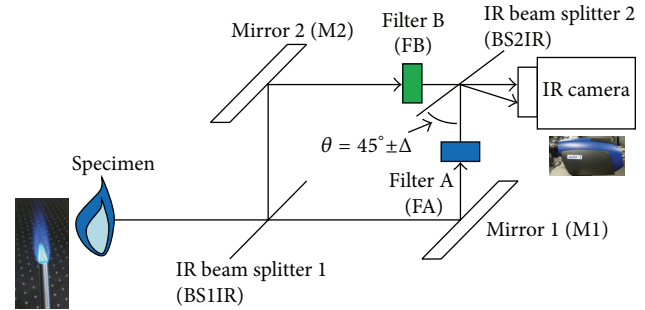
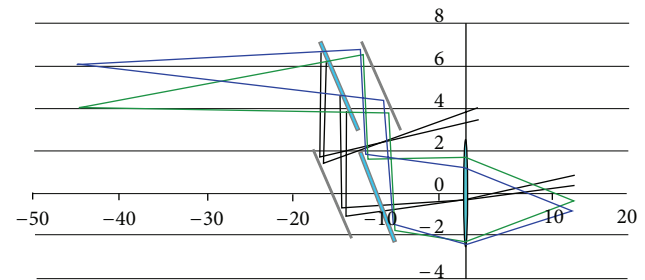
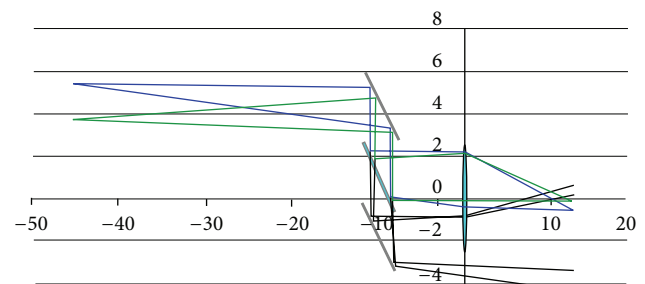


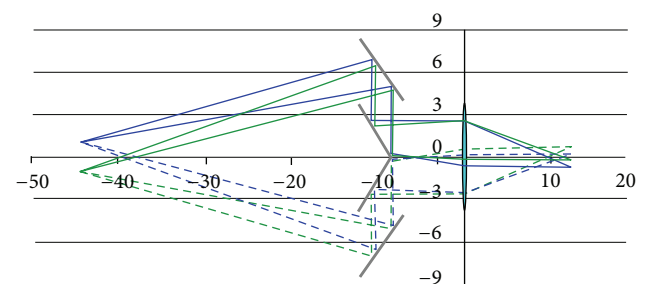
FIGURE 1: Experimental setup.



(a) 2 mirrors, 2 beam splitters



(b) 2 mirrors, 1 beam splitter



(c) 4 mirrors

FIGURE 2: Potential optical layouts to perform IR imaging in two spectral channels. The size of the instrument increases with increasing the number of mirrors.

employ a setup, somewhat similar to that known as a Mach-Zehnder interferometer, with some critical modifications. The most important of these is the image angular displacement, similar to that in the vectorial shearing interferometer [16].

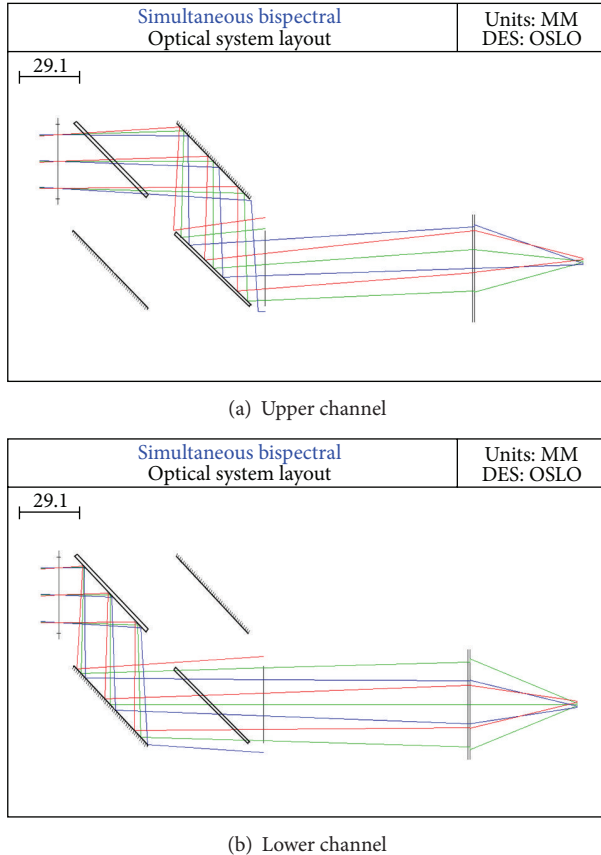


FIGURE 3: Separate imaging is accomplished through upper (a) and lower (b) channels. Each beam goes through the same path: one reflection at a beam splitter, one transmission at a beam splitter, and one reflection at a 45-degree mirror.

Next we examine the requirements for the optical system design and we look at several possible layouts. Then, we elaborate on the most promising choice for its implementation for our applications.

**3.1. Optical System Requirements.** The requirements on the optical system are derived from the layout and performance proposed to measure the efficiency of the combustion process. This is achieved by taking the ratio of the radiation emitted by the object/flame. The radiation is split into two beams, each with its own optical system. Each beam is transmitted through the selective filter. A rapid IR camera with a large number of pixels is suitable as a focal plane to incorporate as one of the principal components into the radiometric chain. There are great advantages of using one detecting surface for two paths, because it is only necessary to characterize and calibrate one detector. Furthermore, the camera signal post-processing is same for all pixels. Methods have been established long time ago to pick up the signal from the corresponding pixels [17] and to perform image processing.

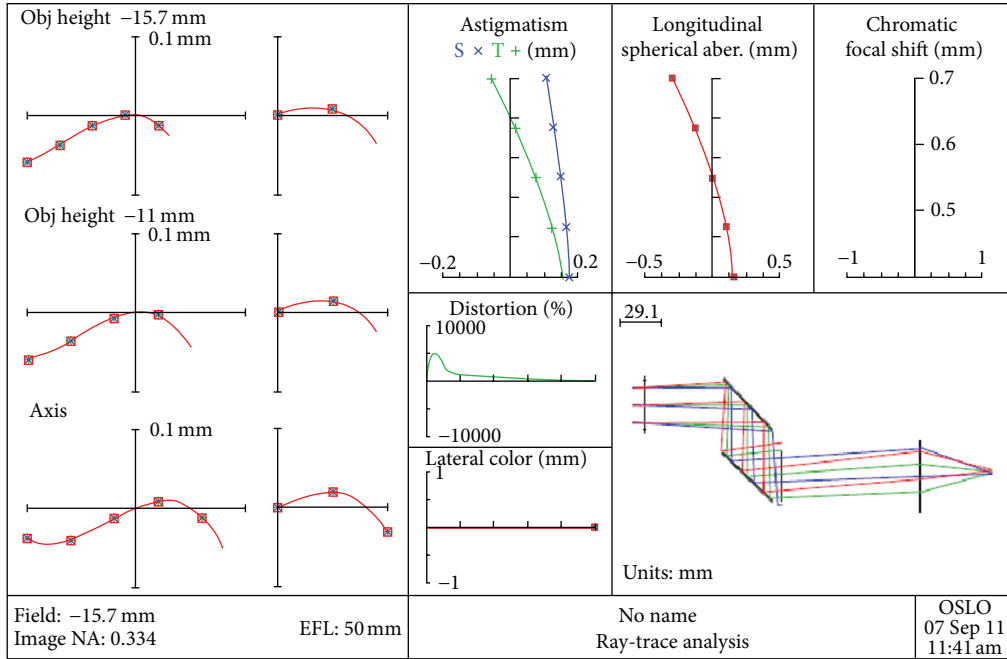
Two imaging channels for each spectral band need to be laid out, such that the flame is imaged on the adjacent area

on the camera focal plane with minimal and equal amount of aberrations. Due to imaging with two different wavelengths, the effects of the chromatic aberrations must be minimized. Then the radiation that is emitted from the same pixel on the flame projected on the object plane is imaged on the same area on two adjacent images. This requires two optical systems with the axis of one slightly inclined with respect to that of the other.

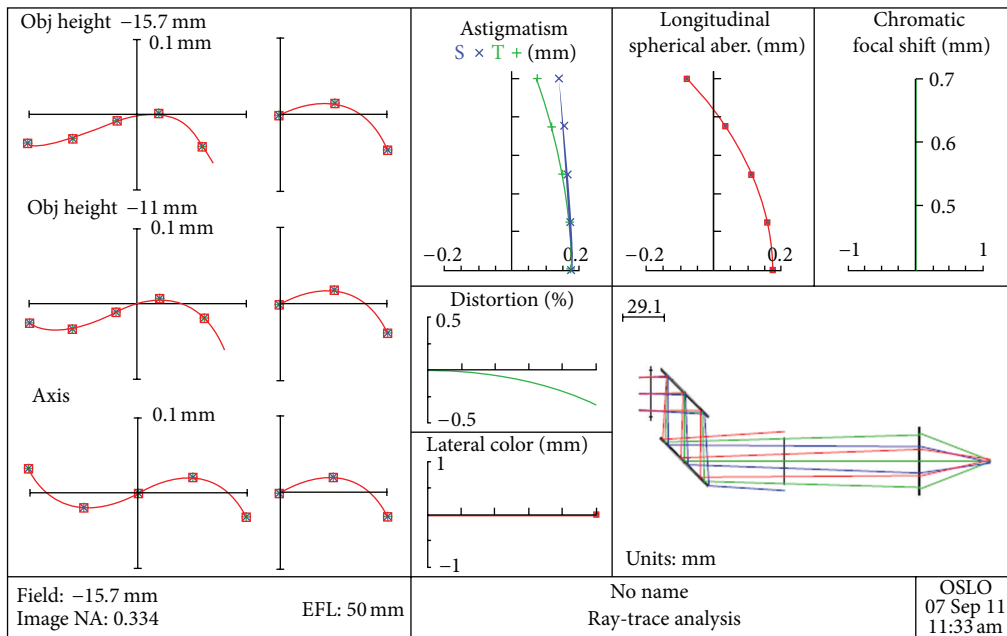
**3.2. Candidate Optical Layouts.** We examined three candidate optical systems as possible layouts for two-path IR imaging on adjacent locations on the focal plane. The optical systems incorporating two identical paths in the visible light have been well understood and described for their widespread incorporation into interferometric systems [18]. The situation is made somewhat more difficult in the IR because the coating materials do not have the same performance as in the visible. The alignment challenges are somewhat exacerbated due to the absence of visual information. A high throughput is not a requirement due to large amount of photon generation in the combustion. However, the amount of IR light that is not the signal contributes to the invisible noise that may interfere with the alignment and detected signal in the focal plane, as a stray light. All the design work was performed on OSLO. Figure 2 presents three layouts that were studied as to their overall feasibility [19]. Part (a) shows the two mirror, two beam splitter configuration; part (b) presents two-mirror, one-beam-splitter layout; and part (c) features a four-mirror proposal.

The first configuration (Figure 2(a)) is a symmetrical arrangement of two mirrors and two beam splitters. Symmetry is an advantage of this layout, including that the optical path is the same for both trajectories. The filters can be easily inserted. The same scene is split in two images. This layout transmits twenty five percent of the incoming light from the scene for each image. The second configuration (Figure 2(b)) consists of two mirrors and one beam splitter. This is the simplest of the three configurations but it has very limited physical space to accommodate the filters. This configuration transmits fifty percent of the incoming light. It has also different path length for each trajectory, so even in the best-focus plane it presents the worse performance. The third configuration (Figure 2(c)) is a symmetrical layout that uses no beam splitters, only mirrors, but each image is seen from a different perspective. We selected the first configuration because it is symmetrical, it has space to accommodate the filters, it is a layout with superior optical performance, and it is the only one that assures the same amplification and perspective of the inspected object for both images.

**3.3. Optimal Layout of the Optical System.** We selected a two-mirror, two-beam-splitter optical layout, indicated in Figure 3, similar to the traditional Mach-Zehnder interferometric configuration, but used in imaging mode [20]. The well-accepted beauty of this layout is its compactness, allowing the portability of this instrument for in-the-field, in situ measurements. The optical system layout for the upper channel is indicated in part (a), with the lower channel shown



(a) Upper arm



(b) Lower arm

FIGURE 4: Results of the exact ray-trace analysis, obtained with OSLO: (a) upper arm, (b) lower arm.

in part (b). The figure includes the ray tracing on axis and off axis. It shows the advantages that the symmetry of the optical system represents for the formation of both images from the same object. The optical axes of two channels are at a small angle with respect to each other to allow side-to-side positioning of two images in the focal plane. The image distortion is less than 0.5% (cannot be noticed with the bare

eye) and can be easily determined and corrected. The results of the ray-trace analysis performed with OSLO are presented in Figure 4, the upper arm in part (a), and the lower arm in part (b). It can be seen in the ray trace analysis that the aberrations are of the same order of magnitude for each arm; this is because of the symmetry of the system. Additionally, given that symmetry, in both cases the aberrations are quite

similar. The transversal aberration shows mainly a minor amount of astigmatism at the best focus, very similar on axis and off axis. Chromatic aberration is insignificant, because of the reflective surfaces, and there is only a minor contribution in the refraction of the beam splitter. Once more, the chromatic aberration is very similar for both arms, given the symmetry.

The image quality in general does not represent a significant concern for IR imaging due to its long wavelengths: the diffraction limit spot diameter is usually larger than the spot spread due to the aberrations. In this particular case, it is imperative that the performances of two parallel channels be identical because imaging in different IR wavelength (bands) may actually result in longitudinally displaced focal planes. This would be detrimental to the accuracy of the technique given that we actually count the number of photons incident from one pixel projected on the object onto two detector pixels. If the imaging is not faithful, different image pixels do not correspond to each other and the object pixel may be compressed along the optical axis. We simulate the imaging of the object screen to two images at the same focal plane location, along different arms. Upon examining Figure 5 we can deduce that images of a square mesh from both channels are equally well preserved. This results in excellent pixel-to-pixel correspondence between the upper and lower arms. Simultaneous, two-channel imaging through both arms is indicated in Figure 6, in a compact, two-mirror, two-beam splitter IR optical system.

**3.4. Spatially Displaced Bispectral Images.** We incorporate this optical system into an instrument, similar to the Mach-Zehnder shearing interferometer, with the modifications indicated in Figure 1. We chose this particular arrangement, because both optical paths are sufficiently similar to allow pixel-by-pixel comparison of two images. Otherwise, the bispectral images may appear in focus in displaced focal planes and exhibit different magnification. The differences between the bispectral and the interferometric imaging are that in the former the two beams and images are placed on different pixels of the detector array, and that there is no need for coherence. The symmetry of the optical system in two arms is also helpful in decreasing the vignetting after the data has been processed. Likewise, the pixel-by-pixel comparison is facilitated when both images travel through nearly identical optical systems.

The object of interest, referred in Figure 1 as a specimen, is placed on the left side of the optical system. The IR amplitude-dividing beam splitter transmits 50% of the collected radiation and reflects the other 50% of light. This beam splitter is placed at 45 degrees with respect to the optical axis, defined as the line connecting the center of the object with the center of the detector array, excluding the effects of beam direction-turning mirrors.

Mirrors M1 and M2 are placed at an angle of 45 degrees in each beam path to change the beam direction of each beam by 90 degrees. Mirrors MA and MB are standard silver-coated mirrors. BSA and BSB are MWIR 50/50 beam splitters. Inside each optical path we insert an IR band-pass filter

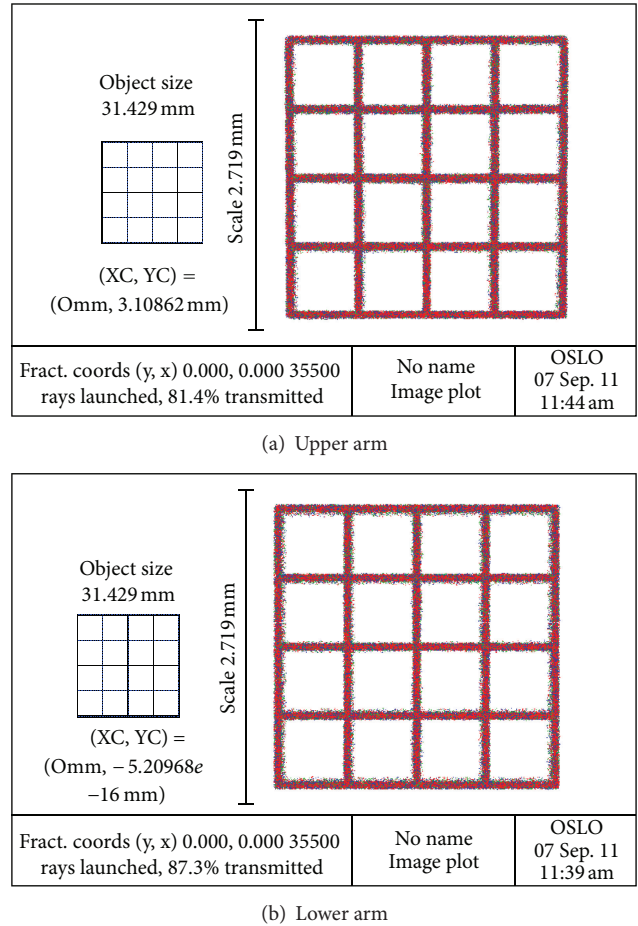


FIGURE 5: Simulation results of chromatic image formation: (a) upper arm, (b) lower arm.

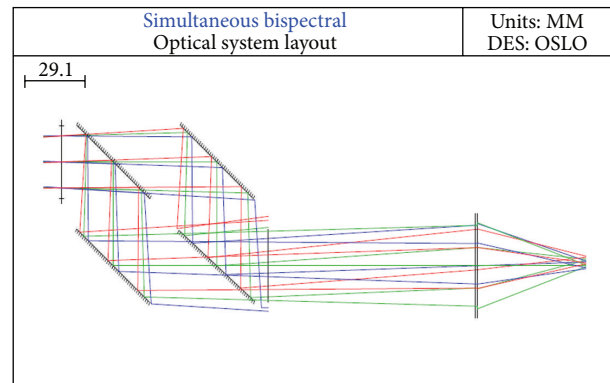


FIGURE 6: Exact ray tracing through the optical system that performs simultaneous bispectral imaging.

(FA and FB) that may be custom-selected for the specific application. The beams are identical just before they are incident on their respective filters. After they pass through the filters, the two beams are spectrally modified to transmit two spectral images, corresponding to the filter transmission

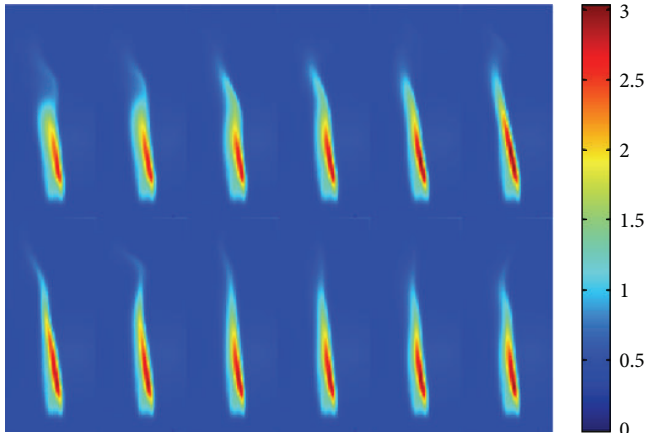


FIGURE 7: Twelve representative images illustrating the relative spatial combustion efficiency for a low-oxygenation flame during the initial one second after ignition, after the beginning of the combustion, from  $t = 0$  sec (top left image) to  $t = 1$  sec (bottom right image). In the black-and-white rendition, the dark lines inside the flames indicate ratio of about three between the amounts of carbon monoxide to that of dioxide. The inside region does not participate in an effective combustion, generating mostly carbon monoxide.

function. Each image is incident on the second amplitude-dividing beam splitter that is positioned at a small angle  $\Delta$  with respect to 45 degree line; say at 40 degrees with respect to the horizontal. The beam that is incident on the beam splitter from below reflects onto the detector to the right of the beam that is transmitted arriving from the left. We spatially separate the positions of the images on the focal plane of the IR camera, tagging each image by its location. It is also possible to modify the angles of the other optical components (MA, MB, and BSA) to achieve a wider image separation. Each beam, upon its incidence on the focal plane of the camera, forms a filtered in-focus image. All the distances are kept small to facilitate the component alignment, to maximize the optical throughput and to keep the instrument compact.

In our experimental setup, we integrate the IR camera *Silver*, manufactured by *Cedip*. It operates in the  $[3.6 \mu\text{m} - 5.1 \mu\text{m}]$  spectral interval. We incorporate advanced electronic features of this camera, allowing them to drive some of the other system parameters. The *Silver* model includes a motorized focus and an internal filter wheel. The former restricts the space inside the camera enclosure, so we implement the external filter arrangement with a separate path for each filter. The simultaneous image taking guarantees identical exposures even for a rapidly changing object.

In the field of spectroscopy, the flame is characterized with chemical by-products, with specific spectral lines. Their relative magnitude indicates the degree of efficiency of fuel utilization. Thus, our “parallel-path” optical systems allow us to identify and quantify the by-products to measure the efficiency of the fuel consumption at a very rapid rate. A single camera assures simultaneous detection of two images during the time interval equal to about one millisecond of the detector-integration time.

#### 4. Bispectral Imaging Applied to Combustion

The development of this technique has been motivated by the need to study the combustion efficiency of the ignition process and evolution. The ideal combustion of fossil fuels produces only water vapor and carbon dioxide. As the combustion efficiency deteriorates, amounts of intermediate species increase, in particular, that of the carbon monoxide. Carbon dioxide has a strong emission band centered on  $4.3 \mu\text{m}$ , while carbon monoxide has one centered on  $4.8 \mu\text{m}$  and several lines near  $4.66 \mu\text{m}$  [21]. On each image detected on the camera focal plane, the left flame, from the viewer’s point of view, is filtered using a  $4.66 \mu\text{m}$  centered filter B ( $0.164 \mu\text{m}$  full width at half maximum, FWHM, transmission band) to monitor the carbon monoxide emission band. The right flame is filtered with a  $4.3 \mu\text{m}$  centered filter A ( $0.181 \mu\text{m}$ , FWHM, transmission band), corresponding to the carbon dioxide emission band.

We study a butane flame, generated by a Bunsen burner, controlling the amounts of oxygen. We display the representative results in Figure 7, demonstrating the feasibility of this technique. It illustrates twelve bispectral images of a small flame, generated by a low-oxygenation butane burner, during the first second. We obtain them at the rate of 1200 per second, by dividing incidence through one filtered image by the other, pixel by pixel. Appreciable signal at  $4.66 \mu\text{m}$  filter B indicates carbon monoxide.

The radiation carrying useful flame information is incident on and detected by the central part of the detector array. This permits us to employ image subframing features of the *Silver* camera model. With the limitation of the pixel integration time, the experimentalist may capture up to 1,200 frames per second. We operate the camera in subframing mode in order to obtain 1200 frames per second, with a resolution of  $160 \times 128$  pixels. Depending on the specific application, it would be necessary to have a higher spatial resolution, possible by reducing the frame rate.

#### 5. Summary

In this work we presented the design of an optical system for bispectral imaging with inclined axes, using a single camera. It has been incorporated into a versatile experimental setup to measure the beam transmission through two channels, allowing the incorporation of spectral filters to verify the presence of specific spectral components and to quantify them. Its excellent performance allowed precise imaging of one projected pixel on the object plane to two pixels on the image plane with the same and very small image deterioration.

The main advantage of bispectral imaging over other techniques is that it allows capturing two simultaneous images of a sample, at a high rate. Both (flame) images are captured on the same focal plane and on the same frame. Over 1000 frames per second may be recorded when the object is of adequate size to permit subframing. After performing pixel-by-pixel ratio of both channels for the same projected pixel, a determination about the efficiency of the combustion process may be made.

Experimental work is in progress to determine the efficiency through the volume corresponding to each pixel as a function of time for different combustion conditions. We are particularly interested in understanding the nature of the small instabilities that are colloquially described as scintillations on the top of the flame.

## References

- [1] M. Strojnik, G. Paez, and C. Vasquez-Jaccaud, "Flame evaluation during first second after ignition in a gas stove," in *Infrared Spaceborne Remote Sensing and Instrumentation XVI*, vol. 7082 of *Proceedings of SPIE*, pp. 70820N-1–70820N-7, SPIE, Bellingham, Wash, USA, 2008.
- [2] G. Paez and M. Strojnik, "Interferometric characterization of flames," in *Unconventional Imaging II*, Proceedings of SPIE, pp. 6307–635, SPIE, Bellingham, Wash, USA, 2006.
- [3] M. Strojnik, G. Paez, and J. C. Granados, "Flame thermometry," in *Unconventional Imaging II*, vol. 6307 of *Proceedings of SPIE*, pp. 63070L1–63070L8, SPIE, Bellingham, Wash, USA, 2006.
- [4] B. García-Lorenzo, J. J. Fuensalida, M. A. C. Rodríguez-Hernández et al., "EDiFiSE: equalized and diffraction-limited field spectrograph experiment," in *Ground-based and Airborne Instrumentation for Astronomy II*, 70144B, vol. 7014 of *Proceedings of SPIE*, SPIE, Bellingham, Wash, USA, 2008.
- [5] T. Wilson and C. Davis, "Hyperspectral Remote Sensing Technology (HRST) program and the Naval EarthMap Observer (NEMO) satellite," in *Conference on Infrared Spaceborne Remote Sensing VI*, vol. 3437 of *Proceedings of SPIE*, pp. 2–10, SPIE, Bellingham, Wash, USA, July 1998.
- [6] G. S. Libonate, B. Denley, E. E. Krueger, J. H. Rutter, J. A. Stobie, and C. L. Terzis, "Development status of the AIRS IR focal plane assembly," in *Infrared Spaceborne Remote Sensing V*, vol. 3122 of *Proceedings of SPIE*, pp. 174–184, Bellingham, Wash, USA.
- [7] M. S. Scholl, Y. Wang, J. E. Randolph, and J. A. Ayon, "Site certification imaging sensor for mars exploration," *Optical Engineering*, vol. 30, no. 5, pp. 590–597, 1991.
- [8] J. Castellon, G. Paez, and M. Strojnik, "Remote temperature sensor employing erbium-doped silica fiber," *Infrared Physics and Technology*, vol. 43, no. 3-5, pp. 219–222, 2002.
- [9] A. Aranda, M. Strojnik, G. Paez, and G. Moreno, "Two-wavelength differential thermometry for microscopic extended source," *Infrared Physics and Technology*, vol. 49, no. 3, pp. 205–209, 2007.
- [10] C. Vazquez-Jaccaud, G. Paez, and M. Strojnik, "Wavelength selection method with standard deviation: application to pulse oximetry," *Annals of Biomedical Engineering*, vol. 39, no. 7, pp. 1994–2009, 2011.
- [11] P. Mitra, S. L. Barnes, F. C. Case et al., "MOCVD of bandgap-engineered HgCdTe p-n-N-P dual-band infrared detector arrays," *Journal of Electronic Materials*, vol. 26, no. 6, pp. 482–487, 1997.
- [12] S. D. Gunapala, S. V. Bandara, J. K. Liu et al., "1024 × 1024 Format pixel co-located simultaneously readable dual-band QWIP focal plane," *Infrared Physics and Technology*, vol. 52, no. 6, pp. 395–398, 2009.
- [13] L. N. Phong and I. Shih, "Optically coated dual sensors for wavelength detection," in *Infrared Technology and Applications XXIII*, vol. 3061 of *Proceedings of SPIE*, pp. 172–184, SPIE, Bellingham, Wash, USA, 1997.
- [14] R. P. Jones, D. P. Jones, and M. Lidwell, "Dual waveband optics for the visible and mid-infrared waveband infrared," in *Infrared Technology and Applications XXIII*, vol. 3061 of *Proceedings of SPIE*, pp. 388–395, SPIE, Bellingham, Wash, USA, 1997.
- [15] K. Kinoshita, H. Itoh, S. Ishiwata, K. Hirano, T. Nishizaka, and T. Hayakawa, "Dual-view microscopy with a single camera: real-time imaging of molecular orientations and calcium," *Journal of Cell Biology*, vol. 115, no. 1, pp. 67–73, 1991.
- [16] G. Garcia-Torales, M. Strojnik, and G. Paez, "Risley prisms to control wave-front tilt and displacement in a vectorial shearing interferometer," *Applied Optics*, vol. 41, no. 7, pp. 1380–1384, 2002.
- [17] M. Strojnik, "From radiometric and thermographic techniques to characterize an IR target to temperature monitoring of a diabetic foot," in *Tribute to William Wolfe*, Proceedings of SPIE, pp. 8483–8487, SPIE, Bellingham, Wash, USA, 2012.
- [18] I. Moreno, G. Paez, and M. Strojnik, "Dove prism with increased throughput for implementation in a rotational-shearing interferometer," *Applied Optics*, vol. 42, no. 22, pp. 4514–4521, 2003.
- [19] H. Gross, F. Blechinger, and B. Aichtner, *Handbook of Optical Systems, Survey of Optical Instruments*, vol. 402, Wiley-VCH, 2008.
- [20] C. Ramirez and M. Strojnik, "Performance evaluation of a wave-front displacement system for vectorial shearing interferometer," *Optics Communications*, vol. 281, no. 3, pp. 347–355, 2008.
- [21] S. Wedemeyer-Böhm, I. Kamp, J. Bruls, and B. Freytag, "Carbon monoxide in the solar atmosphere," *Astronomy & Astrophysics*, vol. 438, pp. 1043–1057, 2005.

## Research Article

# In Search of Early Time: An Original Approach in the Thermographic Identification of Thermophysical Properties and Defects

Daniel L. Balageas<sup>1,2</sup>

<sup>1</sup> Composite Materials and Systems Department, ONERA, BP 72, 92322 Châtillon Cedex, France

<sup>2</sup> TREFLE Department, ENSAM, Institute of Mechanics and Engineering of Bordeaux (I2M), Esplanade des Arts et Métiers, 33405 Talence Cedex, France

Correspondence should be addressed to Daniel L. Balageas; [daniel.balageas@u-bordeaux1.fr](mailto:daniel.balageas@u-bordeaux1.fr)

Received 11 August 2012; Accepted 25 November 2012

Academic Editor: Carlo Corsi

Copyright © 2013 Daniel L. Balageas. This is an open access article distributed under the Creative Commons Attribution License, which permits unrestricted use, distribution, and reproduction in any medium, provided the original work is properly cited.

Active thermography gives the possibility to characterize thermophysical properties and defects in complex structures presenting heterogeneities. The produced thermal fields can be rapidly 3D. On the other hand, due to the size of modern thermographic images, pixel-wise data processing based on 1D models is the only reasonable approach for a rapid image processing. The only way to conciliate these two constraints when dealing with time-resolved experiments lies in the earlier possible detection/characterization. This approach is illustrated by several different applications and compared to more classical methods, demonstrating that simplicity of models and calculations is compatible with efficient and accurate identifications.

## 1. Introduction

The evolution of thermophysical properties metrology and nondestructive evaluation (NDE) is characterized by the increased use of refined inverse techniques [1] requiring the establishment of models taking into account many parameters, although among these parameters often only one parameter is of interest for the experimenter. This complexity is particularly important when the analyzed thermal fields are 3D, a situation characteristic of the experiments realized with thermographic systems producing sequences of large thermal images of complex structures presenting important heterogeneities in their thermal properties, internal geometries, and boundary conditions. This approach leads to time-consuming calculations that may be prohibitive for thermographic data processing. Furthermore, it happens that in many situations the reality remains more complex than the sophisticated model used.

How to conciliate the existence 3D thermal situations involving numerous parameters and the necessity to have rapid calculations compatible with the very high number of information to process in a thermographic image sequence?

A solution lies in the use of 1D thermal models for pixel-wise data processing and the choice of a limited early time domain (for time-resolved techniques) or high frequency domain (for modulated techniques) for which the measured temperatures are essentially depending on the sole parameter to be identified and weakly affected by the 3D heat transfer. To achieve that, the proposed approach consists in performing the identification at the earlier possible time (or at the higher possible frequency) after the thermal stimulation. Here, we will mainly consider time-resolved techniques and early time detection (emerging signal).

The present work wants to show the following.

- (i) A detailed procedure can be defined for early detection and characterization (see Section 2).
- (ii) That this approach is not new. In a first step, it has been applied in the field of thermophysical properties measurements (period 1970–1990). This review is the subject of Section 3.
- (iii) The application to NDE, started at the beginning of the 90's, continues to give rise to new developments (Section 4).

The goal of the present work is to put into perspective results spread over three decades, showing the unity of the approaches up to now hidden by the diversity of the applications and to emphasize that in thermal methods precociousness is as important as signal-to-noise ratio.

## 2. Presentation of the Early Detection Approach

The early detection approach can be considered as the sequence of the following six operations:

- (i) choice of a model simpler than the actual configuration, generally 1D,
- (ii) choice of an early time window for the analysis of the thermograms, in such a way that very few parameters (one if possible) be influent,
- (iii) inverse problem solving in these conditions,
- (iv) Analysis of the time evolution of the so-identified parameter for the assessment of its accuracy,
- (v) choice of a fitting function,
- (vi) extrapolation to zero time (thermophysics application) or zero contrast (NDE) for obtaining the most precise parameter estimate.

Most of the examples that will be given consider models with only one parameter to be identified. Nevertheless, more complex situations are possible. The second example of Section 3 presents a model in which three parameters are to be identified. Consequently the procedure is more complex, involving two time window analysis and time extrapolations followed by two space extrapolations thanks to the use of several samples of different thicknesses.

## 3. Application in the Field of Thermophysical Properties Measurements

The early detection approach defined in Section 2 is illustrated in Section 3.1 in the case of a simple configuration (rear face flash diffusivity experiment), universally known under the name of Parker's method [2], applied to the diffusivity measurement of an homogeneous slab.

In Section 3.2, a more complex procedure is presented dealing with the same type of experiment (rear face flash diffusivity), identifying the *in situ* diffusivities of the components (matrix and reinforcement) of a 3D C/C composite and the thermal contact resistance characterizing the interface between them.

**3.1. Rear Face Flash Diffusivity Measurement.** In flash thermal diffusivity measurements on the face opposite to the pulsed heat deposition the sample heat losses distort the rear face temperature time history. These thermal losses occurring necessarily after the flash, the temperature is all the less disturbed as time is nearer the origin. Consequently, the diffusivity identification by extrapolating towards the initial time the apparent diffusivity-versus-time history resulting from the use of an adiabatic solution was proposed in 1982

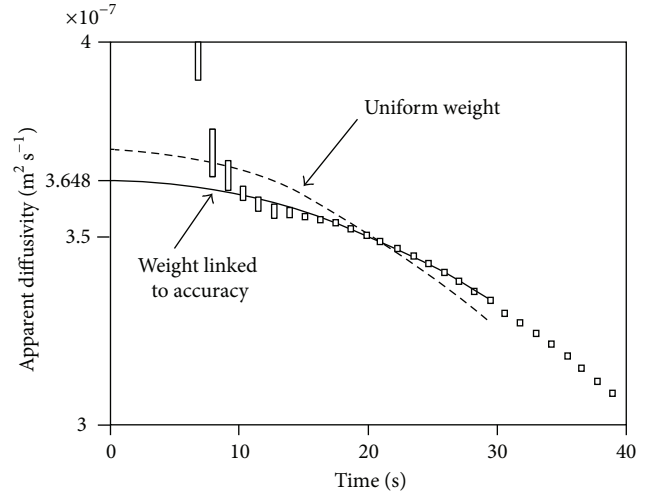


FIGURE 1: Test no. 2 on plaster identified apparent diffusivity law and regression parabola with a uniform weight and with a nonuniform weight linked to the accuracy of the measurement, taken from [4].

[3, 4]. It was demonstrated that the early phase of the thermogram (for instance for a defect Fourier number  $Fo_d = \kappa t/z_d^2 < 0.1$ , where  $\kappa$  is the diffusivity of the material and  $z_d$  the defect depth) may be used for this early detection if an estimate of the final adiabatic temperature increase,  $\Delta T_{lim}$ , is deduced without any assumption concerning the heat losses from the maximum temperature reached with losses,  $\Delta T_{max}$ . A relation between these two parameters was proposed

$$\text{Log}_{10} \left[ \text{Log}_{10} \left( \frac{\Delta T_{lim}}{\Delta T_{max}} \right) \right] = -\frac{0.667t_{max}}{t_{1/2}} + 1.113, \quad (1)$$

where  $t_{max}$  and  $t_{1/2}$  are, respectively, the measured occurrence times of the maximum and half maximum temperature increase at the center of the sample. This relation allows to normalize the thermogram:  $\Delta T(t)/\Delta T_{lim} = (\Delta T(t)/\Delta T_{max}) \times (\Delta T_{max}/\Delta T_{lim})$ , and using a look-up table to build an apparent diffusivity curve,  $\kappa(t)$ , from the analytical solution for the 1D rear face adiabatic sample submitted to a pulsed stimulation. Whatever is the accuracy of the estimated  $\Delta T_{lim}$ , it was verified that the law  $\kappa(t)$  starts at  $t = 0$  from the actual diffusivity value, and that if the estimation is sufficiently accurate, the apparent diffusivity evolution in the early times ( $Fo_d < 0.1$ ) can be approximated by a parabolic law whose peak is obtained for  $t = 0$ . To improve the accuracy of the parabolic fitting using least mean squares, the experimental points were weighted by the accuracy of the diffusivity measurement deduced from the a sensitivity analysis. It was imposed to the parabola to have a zero slope at  $t = 0$ .

Figure 1 presents, taken from [4], the extrapolation in the case of a measurement on a 10 mm thick disk-shaped plaster sample, with a radius over thickness ratio  $R/L = 1.206$ . An extrapolated value of diffusivity is found  $3.65 \cdot 10^{-7} \text{ m}^2 \text{ s}^{-1}$ .

Table 1 summarizes the diffusivity results obtained by this method and compares them to results obtained with exactly the same samples by three methods (round robin tests) as follows.

TABLE 1: Present method result and comparison to Parker's and Degiovanni's methods.

Material	Test number	Sample		Parker's method	Identified diffusivity ( $\text{m}^2 \text{s}^{-1}$ ) $\times 10^7$				
		Thickness (mm)	$R/L$		Degiovanni [5]			Degiovanni [6]	Balageas [4]
					$\kappa_{2/3}$	$\kappa_{1/2}$	$\kappa_{1/3}$		
Plaster	#1	9.96	1.206	4.759	3.675	3.703	3.689	3.69	<b>3.703</b>
Plaster	#2	9.96	1.206	4.734	3.618	3.644	3.645	3.64	<b>3.648</b>
Chalk	#3	6.16	1.950	3.548	2.861	2.881	2.886	2.89	<b>2.905</b>

- (i) The Parker's formula,  $\kappa = 0.139 L^2/t_{1/2}$ , with  $t_{1/2}$  the half rise time, which considers the sample adiabatic and leads to considerable errors due to the low conductivities of the three materials chosen for the tests.
- (ii) The more precise method at the time of the publication of the present method: the partial times method of Degiovanni [5]. The method of partial times considers for the identification several pairs of points of the thermogram corresponding to the following normalized temperature increases  $\Delta T(t)/\Delta T_{\max}$ : 1/3 and 5/6, 1/2 and 5/6, 2/3 and 5/6. It is interesting to compare the Degiovanni's method with the present early detection approach because, as shown in Figure 2, the extrapolation method results are coherent with the evolution with time of the identified diffusivities of the points considered in the data processing of the Degiovanni's partial times method. We see that the present method corrects the bias of this method, which increases with identification times.
- (iii) The method of partial moments, proposed by Degiovanni [6] that is still considered as a reference. There is a perfect agreement with this method. The results of the partial moments are not plotted in Figure 2 because they would not be distinguishable from those of the present method.

### 3.2. Rear Face Flash Measurement of the In Situ Diffusivities of the Components of Periodic Directional-Reinforced Composites

**3.2.1. Periodic Directional Reinforced Composites (PDRCs).** The types of materials here considered are PDRCs (periodic directional reinforced composites) in which the reinforcement is arranged following preferential directions. For instance, unidirectional carbon/epoxy composites and 3D carbon/carbon composites belong to this family of materials and the identification method here presented can be applied to them. These materials are difficult to homogenize when there is a large difference between the thermal conductivities of the composite components (matrix and reinforcement) and when the main heat transfer is parallel to a reinforcement direction [7].

Considering the same type of measurements as in the previous section (rear face flash diffusivity), a more complex procedure is presented, which identifies the *in situ* diffusivities of the matrix and reinforcement and the thermal contact

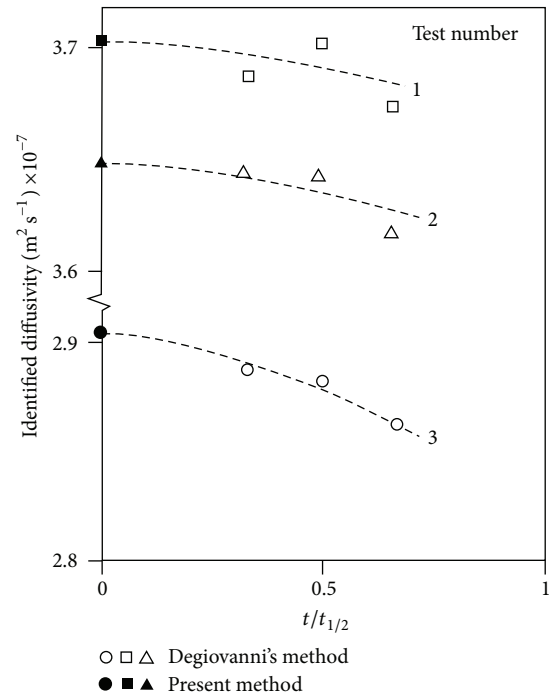


FIGURE 2: Compared results of Degiovanni's partial times method and present method, taken from [4].

resistance characterizing the interface between them in the case of a 3D C/C composite [8–10]. The method supposes that the composite sample is quasi adiabatic (no heat losses).

The simplest PDRCs that can be imagined are presented in Figure 3. They are unidirectional PDRCs. The two components are arranged in alternated slabs parallel to the imposed heat flux (Figure 3(a)) or following a chessboard pattern (Figure 3(b)). The dimensional geometric parameters are the space period of the pattern,  $\omega$ , the thickness of the medium,  $L$ , and the volume ratio of the components ( $\tau_i$ ). For these first two composites  $\tau_1 = \tau_2 = 0.5$ . The more thermally conductive component is supposed to be the reinforcement, since it is usually the case (i.e., in C/epoxy or C/C composites).

A slightly more general arrangement for 1D PRDC is given in Figure 4(a). Figure 4(b) corresponds to a more realistic arrangement representative of carbon/epoxy composite and Figure 4(c) to a 3D C/C material with orthogonal  $x$ ,  $y$ ,  $z$  reinforcements.

Based on numerous numerical simulations [9], it has been demonstrated that the transient thermal behavior of 1D

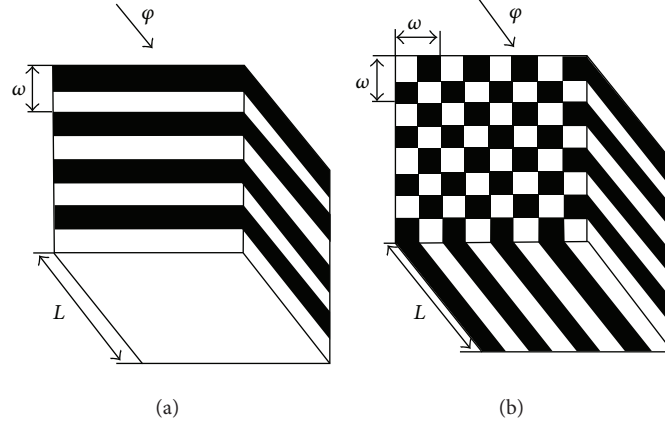


FIGURE 3: Simple configurations of unidirectional PDRCs: (a) stack of parallel layers, (b) chessboard pattern (from [9]).

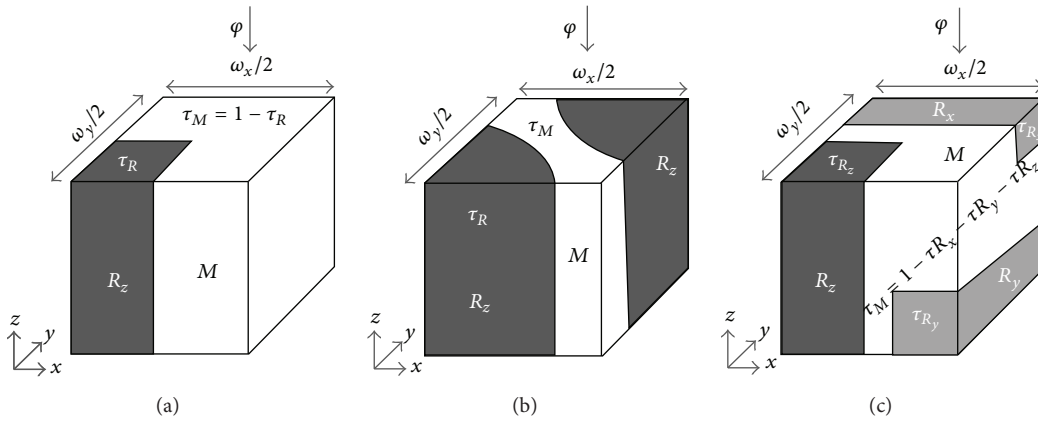


FIGURE 4: (a) Model of the elementary volume (1/4 of the repetitive cell) of a 1D PDRC, (b) idem for a 1D C/epoxy composite, (c) idem for a 3D C/C with  $x$ ,  $y$ ,  $z$  orthogonal reinforcements, from [10, 11].

PDRCs, when considering the mean temperature evolution,  $\bar{T}(t)$  depends only on five nondimensional parameters:

- (i) volume content of the reinforcement,  $\tau_R$ ;
- (ii) the reinforcement-to-matrix ratio of thermal conductivities,  $k_{R/M} = k_R/k_M$ ;
- (iii) the reinforcement-to-matrix ratio of volume specific heats,  $C_{R/M} = C_R/C_M$ ;
- (iv) the specific contact surface between reinforcement and matrix per unit surface of composite:  $\sigma = L\Sigma$ , where  $L$  is the sample thickness, and  $\Sigma$  the specific contact surface between reinforcement and matrix per unit volume, parameter which depends on the shape of the section of the reinforcement;
- (v) the specific contact thermal resistance between reinforcement and matrix:  $\rho = Rk_M\Sigma$ ,  $R$  being the contact thermal resistance of the interface.

This mean temperature  $\bar{T}(t)$  is easily measured by using IR radiometer or thermography if the emissivity of the surfaces are homogenized by a black coating insuring uniform emissivity.

**3.2.2. Principle of the Identification of the Reinforcement Diffusivity and Homogenized Diffusivity from the Time Evolution of the Rear Face Mean Temperature  $\bar{T}(t)$  in the Case of 1D DRC.** Let us consider a 1D PDRC with a periodic pattern such as those of Figures 4(a) and 4(b). A typical mean temperature evolution of the rear face of the sample in flash diffusivity measurement is given in Figure 5(a) and compared to the theoretical response of a homogenized material.

At the beginning, the energy that arrives at the rear face of a sample of thickness  $L$  has travelled through the more conductive component of the PDRC, here the reinforcement. If the identification is performed for each and every points of the curve, the identified diffusivity varies with time and the earlier the considered point, the nearer of the reinforcement diffusivity it is. Thus, following the early detection approach,

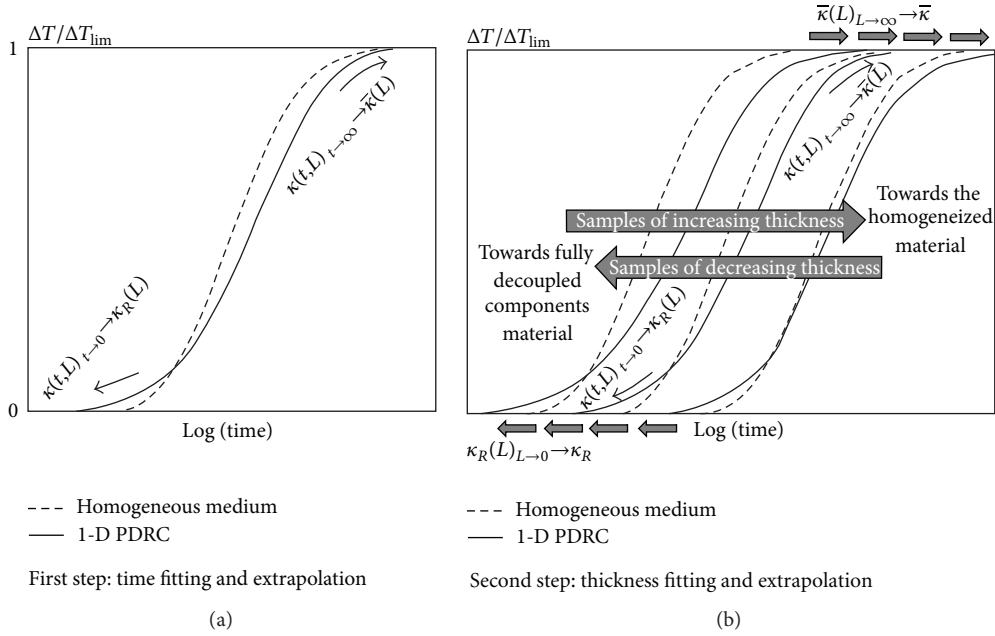


FIGURE 5: *In situ* characterization of a 1D PDRC. Principle of the early time and later time identifications (a), followed by spatial extrapolations to zero and infinite sample thicknesses (b).

by fitting the early part of the apparent diffusivity law and extrapolating it to zero time, an estimate of the reinforcement diffusivity is reached. This diffusivity is depending on  $L$

$$\kappa(t, L)_{t \rightarrow 0} \longrightarrow \kappa_R(L). \quad (2)$$

Using several samples of different thicknesses the law  $\kappa_R(L)$  can be extrapolated to zero thickness and the so-extrapolated diffusivity can be considered as the best possible estimate of the reinforcement diffusivity

$$\kappa_R(L)_{L \rightarrow 0} \longrightarrow \kappa_R. \quad (3)$$

On the contrary, the energy arriving at the end of the experiment can be considered as representative of a partially homogenized material. In effect, for long times, 3D heat transfers have enough time to become important and homogenize the temperature of the two components (reinforcement and matrix). These 3D effects, which are generally considered as a disturbing phenomenon, have in the present case a beneficial role, becoming a source of information about the material. The identified diffusivity law presents a final asymptote that can be considered as an approximate estimate of the fully homogenized material

$$\kappa(t, L)_{t \rightarrow \infty} \longrightarrow \bar{\kappa}(L). \quad (4)$$

Thanks to the series of measurements performed with the different samples of various thicknesses, the law of partially homogenized diffusivity versus thickness can be extrapolated to an infinite thickness and the so-extrapolated value can be considered as the best estimate of the diffusivity of the fully homogenized material equivalent to the composite

$$\bar{\kappa}(L)_{L \rightarrow \infty} \longrightarrow \bar{\kappa}. \quad (5)$$

In a third step, with a few assumptions which depends on the considered composite, from  $\kappa_R$  and  $\bar{\kappa}$ , it is possible to deduce the value of the diffusivity of the less conductive component (generally the matrix),  $\kappa_M$ , and the thermal resistance,  $R$ , characterizing the interface between the two components (see in particular [10, 12, 13]).

**3.2.3. Application to 3D C/C Composites.** The method has been applied to two 3D C/C composites in which the reinforcement is constituted of bundles of carbon fibers highly anisotropic and highly axially conductive, oriented in the three Cartesian directions  $x$ ,  $y$ ,  $z$ .

The first step consists to consider the 1D PDRC model of Figure 4(a) as an approximation equivalent to the 3D PDRC of Figure 4(c) in the case of the 3D C/C composite, considering that, due to the anisotropy of the reinforcement and the same chemical nature of the matrix and the reinforcement, it is possible to replace the actual matrix and the transverse reinforcement (following  $x$  and  $y$  directions) by an equivalent matrix. The identification procedure of Section 3.2.2 is then applied to this 1D PDRC. The operation can be repeated with the two other orientations of the samples to obtain the diffusivity of the three reinforcements if the composite is not equilibrated.

Figure 6 presents the experimental thermograms obtained for the 3D C/C no. 3 the flux being parallel to the  $z$ -reinforcement. They are compared to the thermograms of the equivalent homogenized material with the identified homogenized diffusivity,  $\bar{\kappa}$ , and the thermograms calculated using the equivalent 1D PDRC model with the identified parameters. The identified parameters are presented in Table 2 for two materials (3D C/C no. 1 and 3D C/C no. 3 for two orientations). These results show that even for a coupon

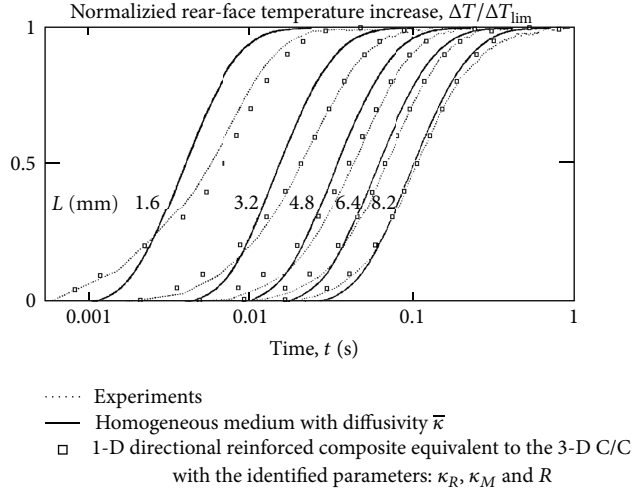


FIGURE 6: Normalized experimental pulse diffusivity rear face thermograms (mean temperature) obtained with a series of 3D C/C coupons of different thicknesses. Comparison to the homogeneous medium solution with the identified homogenized diffusivity,  $\bar{\kappa}$ , and to the 1D directional reinforcement composite equivalent to the 3D C/C using the identified parameters: axial thermal diffusivity of the reinforcement,  $\kappa_R$ , diffusivity of the matrix,  $\kappa_M$ , and thermal contact resistance of the reinforcement/matrix interface,  $R$ . Taken from [10, 13].

thickness of 8.2 mm, the material transient behavior is not exactly that of a homogeneous material. This thickness, knowing that the  $z$ -space period is 0.8 mm, represents ten times the space period.

These results were obtained with an IR radiometer viewing an area of the rear face much larger than a mesh of material to obtain a mean temperature measurement. It could be easily performed with an IR camera.

The main merit of the method is the fact that the measured properties are relative to *in situ* materials, which is of prime importance since the material process has a strong influence on the resulting final thermal properties of the product, in particular the axial diffusivity of the reinforcement.

**3.2.4. Complementarity of Front-Face and Rear Face Pulse Measurements.** The front-face and rear face pulse experiments are complementary [14]. In effect, let us apply the zero-time extrapolation to the apparent diffusivity identified from the rear face mean-temperature time evolution (see Figure 7(a)) and to the apparent effusivity identified from the front-face mean-temperature time evolution (see Figure 7(b)). These operations permit, respectively, the identification of characteristic thermal properties of the reinforcement parallel to the flux (longitudinal diffusivity) and of the equivalent matrix resulting from the homogenization of the matrix (isotropic effusivity) and of the two reinforcements perpendicular to the heat flux (radial effusivity). In other words, at the beginning of the pulse experiments, on the front-face the heating is driven by the less conductive component of

the composite and on the rear face by the more conductive component.

## 4. Application to Nondestructive Evaluation (NDE)

**4.1. Notion and Interest of the Emerging Contrast.** For NDE, the experimental data from which defect parameters can be identified are not thermograms (temperature increase, a function of time:  $\Delta T(x, y, t) = T(x, y, t) - T(x, y, t = 0)$ ) but the time evolution of the contrasts between the temperature rise of a defective zone and the one of a sound zone taken as a reference,  $Cr(x, y, t) = (\Delta T(x, y, t)_d - \Delta T(x, y, t)_s) / \Delta T(x, y, t)_s$ . Consequently, the early detection approach in NDE consists in exploiting the contrast when it is just emerging from the noise, reason why we proposed to call it “the emerging contrast.” Figure 8 presents the principle of the detection of the emerging contrast.

This attitude is contrary to common practice. In effect, traditionally, pulse thermography users favored the maximum contrast to identify the depth and thermal resistance of defects, starting from the *a priori* justified reason that it corresponds to the best SNR. This choice, which could be understood when the performances of cameras were limited ( $\text{NETD} \geq 100 \text{ mK}$ ), is unfortunate and inappropriate. Nevertheless, it is still used by most of the users of the pulse technique. The early detection approach by the use of the emerging contrast is an efficient alternative that deserves to be promoted, as it will be demonstrated here.

**4.1.1. “Universality” of the Emerging Contrast (Pulse Thermography).** Let us consider the simple 1D configuration of a thermally imperfect interface (thermal resistance) inside two layers of solid materials. The interface is characterized by an extrinsic parameter, its location depth,  $z_d$ , and by an intrinsic thermal property, its thermal resistance,  $R_d$ . If  $R_d = 0$ , the structure is considered as sound and if  $R_d > 0$ , it is considered as being defective, with a resistive defect which has to be detected and characterized.

The problem is that the time-evolution of  $Cr$  depends on a large number of factors: the depth  $z_d$ , the thermal resistance,  $R_d$ , but also the total thickness of the structure,  $L$ , the thermal properties of the two layers effusivities and diffusivities, and the boundary conditions characterized by heat transfer coefficients  $h$ .

Figure 9 presents the wide variety of contrast evolutions that can be encountered. These data are the synthesis of simulation results taken from [15]. All parameters are non-dimensional and the graph is in log-log scales to conveniently show the various time scales. The possible domain in which the contrast may evolve, here lightly coloured in grey, is enormous, and it is obvious that to solve the inverse problem it is necessary to rely on a model taking into consideration all the aforementioned parameters.

A simple explicit expression relating the time of occurrence and the amplitude of the maximum relative contrast, a universally known and used approach, cannot be *a priori*

TABLE 2: *In situ* identified thermal properties of two 3D C/C composites, taken from [10].

Identified thermal parameters	Materials		
	3-D C/C no. 1	3-D C/C no. 3 //	3-D C/C no. 3 ⊥
Mean volume heat capacity <sup>a</sup>			
$\bar{c}$ (MJ m <sup>-3</sup> K <sup>-1</sup> )	1.4	1.4	1.4
Homogenized properties			
$\bar{\kappa}$ (cm <sup>2</sup> s <sup>-1</sup> )	1.09	0.90	1.06
$\bar{k}$ (W m <sup>-1</sup> K <sup>-1</sup> )	154	127	149
Reinforcement//heat flux			
$\kappa_R$ (cm <sup>2</sup> s <sup>-1</sup> )	3.0	2.6	3.1
$k_R$ (W m <sup>-1</sup> K <sup>-1</sup> )	423	366	437
Equivalent matrix			
$\kappa_M$ (cm <sup>2</sup> s <sup>-1</sup> )	0.27	0.33	0.48
$k_M$ (W m <sup>-1</sup> K <sup>-1</sup> )	38	46	68
Reinforcement/matrix interface			
$\rho$	0.01	1.6	6.6
$R$ (m <sup>2</sup> K W <sup>-1</sup> )	2.0·10 <sup>-7</sup>	2.8·10 <sup>-5</sup>	5.7·10 <sup>-5</sup>

<sup>a</sup> Estimated value.

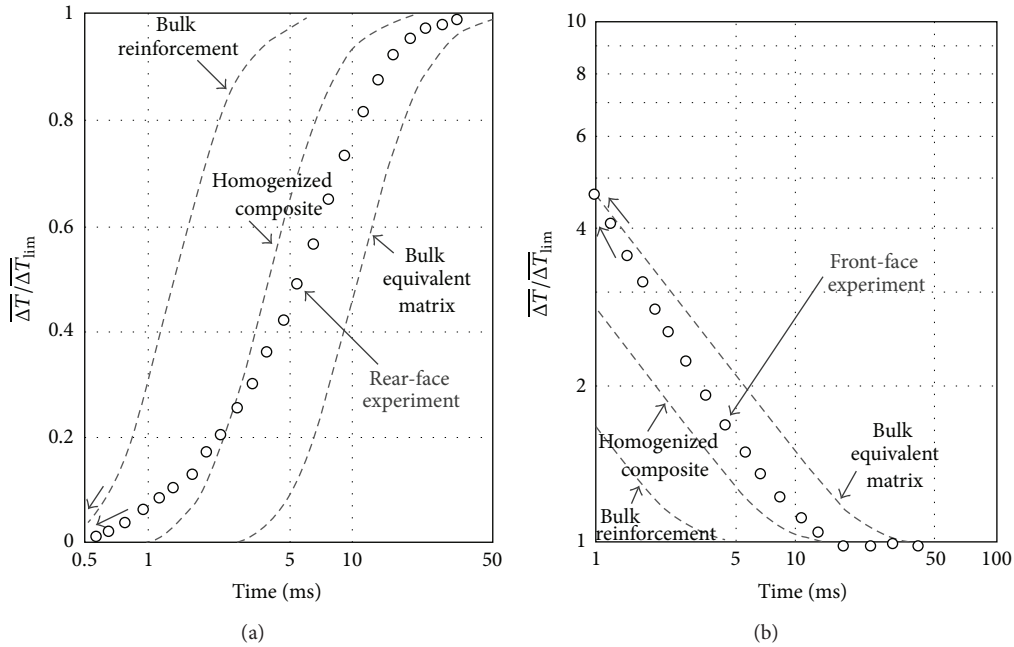


FIGURE 7: Compared mean temperature time histories of the front- and rear faces in the case of the 3D C/C #3// and comparison to the calculated thermograms corresponding to the thermal properties of the bulk reinforcement (longitudinal properties), bulk equivalent matrix, and fully homogenised composite, taken from [14].

satisfying when one considers the wide scatter existing on these two parameters.

Nevertheless, the main lesson which can be drawn from this graph is the existence, at the origin, of a narrow tail-shaped domain in which all curves merge, thus where a unique correlation between the relative contrast  $Cr$  and the defect Fourier number  $Fo_d$  can be used for the identification of the defect depth whatever is the thermal resistance and the other already mentioned parameters.

If we suppose that one can evaluate the occurrence time of a contrast of 1%, the maximum error on the identified depth is  $\pm 7\%$ . Of course an earlier identification, based on a still lower contrast, leads to a more precise identified depth. The aim to be reached is clear; the problem is in the way to practically achieve the required experimental accuracy.

This simple example illustrates the main virtue of the emerging contrast: the “universality” of its applicability.

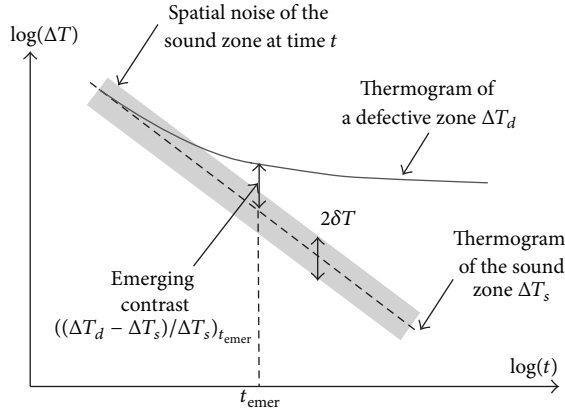


FIGURE 8: Principle of the detection of the emerging contrast.

Another illustration of this universality is given by the following study of the characterization of a defect embedded at different depths in a slab of a homogeneous sample. Let us consider a slab of thickness  $L$ , with a 1D defect located at the depth  $z_d$  and characterized by a thermal resistance  $R_d$ . For such a defect embedded in a semi-infinite medium, the thermal contrast associated with the 1D defect is depending on two non dimensional parameters: the Fourier number related to the defect depth,  $Fo_d = \kappa t/z_d^2$ , and the non dimensional thermal resistance  $R^* = R_d/(z_d/k)$ , the ratio of the defect thermal resistance to the one of the material layer in between the defect and the front-surface (see for instance [16, 17]). In these expressions,  $\kappa$  and  $k$  are, respectively, the diffusivity and the thermal conductivity of the material in between the monitored surface and the defect. In the case of a slab, the situation is more complex as seen in Figure 10(a). This Figure presents the Fourier-evolution of the relative contrast for various values of the normalized defect depth,  $z_d/L$ , and for  $R^* = 1$ . Similar (but different) nets would be obtained for other values of this last parameter. The shape of the contrast curves presents a maximum highly dependent on  $R^*$  and  $z_d/L$  parameters. The influence of the rear face “echo” gains in importance with increasing  $z_d/L$  and drastically decreases the amplitude of the relative contrast when the defect is approaching from this rear face, making the detection more and more problematic. Like in Figure 9, the large spreading of the net is converging to a narrow “tail” in which all curves merge for early times when the contrast is emerging from the noise. Thus, considering the emerging contrast domain ( $Fo_d < 0.5$  and  $Cr$  of a few percents), for identification purpose, we can use the unique curve  $Cr(Fo_d, R^* = 1)$  corresponding to the case of the defect embedded in a semi-infinite medium, for which there is no rear face reflection (see Figure 10(b)).

**4.1.2. Identification Based on Emerging Contrast Needs Simpler Model than That Based on Maximum Contrast.** Figure 10(b) presents the emerging contrast domain taken from Figure 10(a) and compares the contrast curves net to the two grey dotted curves of relative contrast related to the defects

of infinite thermal resistance and  $R^* = 1$  in a semi-infinite medium, curves taken from [19, 20]. We see that this second curve remains near of the curves of the net for contrast of a few percents when  $z_d/L$  is smaller than 0.8. This means that we can use the semi-infinite medium solution  $Cr(Fo_d, R^*)$  for identifying the depth and thermal resistance of a defect in this early time domain, instead of using a  $Cr(Fo_d, R^*, z_d/L)$  function.

**4.1.3. Early Detection and Characterization Lead to Less Blurred Images and More Accurate Identified Defect Parameters.** Both Figures 9 and 10 show that the gain in precociousness of the identification when going from maximum contrasts to emerging contrasts can be very important (up to one order of magnitude). This gain is important since less time is given to 3D internal heat diffusion effects. This means from a qualitative point of view that the defect images will be less blurred, an important quality that increases the detectivity of the method, and quantitatively this produces a gain in accuracy for the identified parameters. This has been demonstrated in [19, 20].

**4.2. Rapid Survey of the Early Detection and Characterization Approach in the NDE Literature.** At the beginning of the 90’s, the attention of several authors was drawn to the fact that it would be better to consider the contrast at its beginning to achieve an early detection.

The idea of an early identification of the defect depth,  $z_d$ , from the emerging contrast time was first formulated by Bontaz [21, 22] who proposed the following empirical relation:

$$t_0 = \frac{z_d^2}{2\pi\kappa}, \quad (6)$$

where  $t_0$  is the origin time of the contrast, called by the authors the “divergence” time. This relation can be formulated using the defect Fourier number

$$Fo_d = \frac{\kappa t_0}{z_d^2} = \frac{1}{2\pi} = 0.159. \quad (7)$$

The weakness of this approach was double: (i) the relation between defect depth and divergence time was totally empirical and no precise procedure was proposed since the emergence had to be localized by the simple examination of the contrast curve without any indication given concerning the relative contrast value to consider for this determination of  $t_0$ ; (ii) for the thermal resistance,  $R_d$ , the identification was similar to the temporal moment approach already proposed for diffusivity identification by Degiovanni [6], and for defect characterization by Balageas et al. [23], and was based on the use of the time integral of the full contrast from its origin to its extinction, then comprising data related to high Fourier numbers and consequently corrupted by 3D conduction effects.

Finally, Krapez et al. [18, 24, 25] kept the idea of performing the identification as early as possible with the emerging contrast, but developed a precise methodology

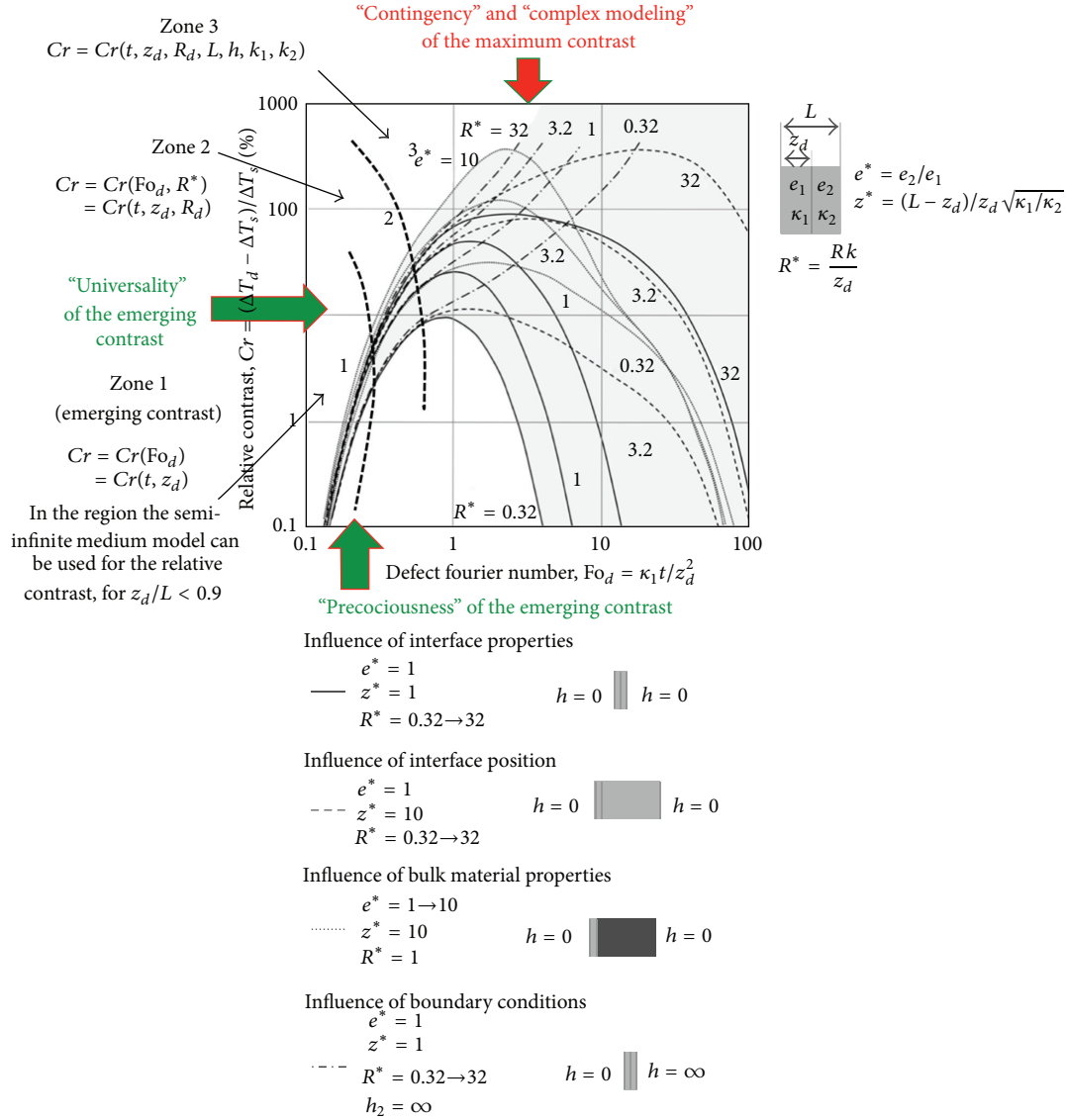


FIGURE 9: The virtues of the emerging contrast: universality, precociousness, and simple modeling. Comparison to the maximum contrast.

for the identification leading to propose explicit analytical formulas for identifying both depth and thermal resistance of a defect

$$z_d = \sqrt{\kappa_z t \text{Ln} \left[ \frac{2}{Cr(t)} \right]}, \tag{8}$$

$$R_d = \frac{Cr(t) \kappa_z t / k_z z_d}{\exp(-z_d^2 / \kappa_z t) - Cr(t) / 2},$$

expressions in which  $Cr(t)$  is the relative contrast measured at time  $t$ , and  $k_z$  and  $\kappa_z$  are, respectively, the thermal conductivity and thermal diffusivity of the material between the monitored surface and the defect. The identification was achieved in two steps. The first relation was used for relative

contrasts near of 1 to 3% and once the defect depth identified, the second formula was used for identifying the thermal resistance for slightly larger contrast (3 to 6%).

In parallel to this research, another way to perform early detection was explored. Almond et al. [26, 27] found from numerical simulations and from experiments on a sample with artificial defects of same thermal resistance, located at the same depth, but with different sizes, that the “thermal contrast slope at the beginning” was independent of the size of the defect and just related to the defect depth. He suggested that the “short-time slope” of the contrast-time curve can be used to assess the defect depth rather than the peak time (time of the maximum contrast). Thomas, Favro and coll [28–30], and Ringermacher et al. [31] proposed to use the time of occurrence of the “peak slope” of the contrast to identify the

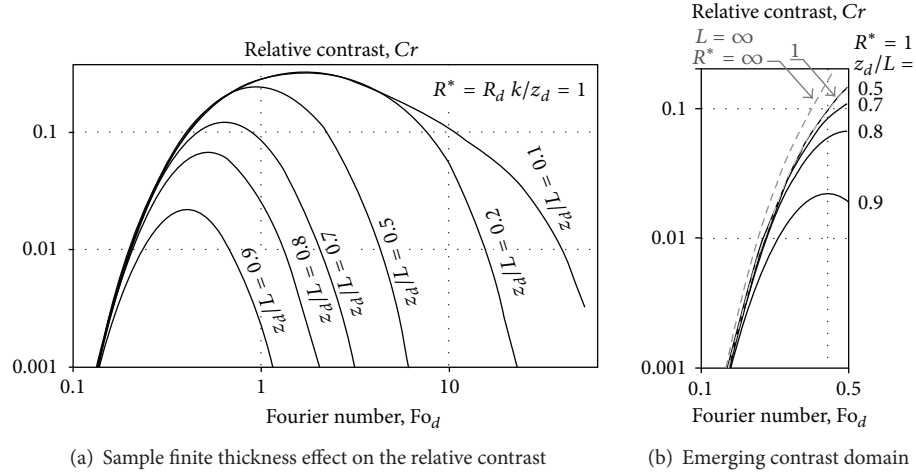


FIGURE 10: On the left: Influence of the normalized defect depth,  $z_d/L$ , on the relative contrast generated by a defect of normalized thermal resistance  $R^* = 1$  in a slab of thickness  $L$ . On the right: Comparison in the emerging contrast domain between the contrasts generated by the same defect in a semi-infinite medium (solution used for the depth and thermal resistance identification by the early detection technique) and in a slab of thickness  $L$ .

defect depth. This proposal remained qualitative, no explicit relation relating the defect depth to this time being proposed by these authors.

Recently, Sun [32] studied quantitatively the relation between the contrast slope peak time,  $t_{ps}$ , and the defect depth using a normalized time  $\omega_{def} = \pi^2 Fo_{def} = \pi^2 \kappa t_{ps} / z^2_{def}$ . His study, limited to the case of an infinite defect thermal resistance (case of a hole machined in a slab), shows that the maximum slope is reached for a  $Fo_{def} = 0.368$ , which allows to identify the defect depth

$$z_d = 1.65 \sqrt{\kappa t_{ps}}. \quad (9)$$

Nevertheless, this relation is only valid when the relative depth (ratio of the defect depth to the total sample thickness) is lower than 0.5. For higher values, the characteristic Fourier number is a strong function of the normalized defect depth, decreasing continuously down to 0.25 for a defect approaching the sample rear face.

This approach, although constituting a progress compared to the use of the occurrence time of the maximum contrast, is not as interesting as the early detection from the emerging contrast because the contrast slope peak occurs later than the emergence of the contrast ( $Fo_{def} = 0.368$  instead of  $Fo_{def} = 0.159$  for the Bontaz method, see (7)).

#### 4.3. Recent Developments in Early Detection and Characterization of Defects

**4.3.1. Improvement of the Emerging Contrast Technique by Linear Extrapolation to Nill Contrast.** Balageas [19, 20] recently reworked the method developed in the 90's [18, 24, 25], following rigorously the early detection procedure described in Section 2 and using the identification formulas (8). In particular, he proposed and experimentally validated the extrapolation to zero contrast of the law of the identified

defect depth as a function of the contrast. By this way, the most accurate estimate of the defect depth is obtained. A relation between the error on the so-identified defect depth and the value of the defect thermal resistance is found, allowing to correct the first estimate of the defect depth once estimated the thermal resistance, which improves the accuracy of the method.

The early detection approach using the described procedure allows to reach the optimum accuracy on both the depth and the thermal resistance of defects: between 0.1% and 10% for the depth, and less than 30% for the thermal resistance (see Figure 11). The values of accuracy here given are intrinsic to the method and do not include the influence of the experimental noise and the 3D heat transfer effect linked to the limited extent of defects. The experimental noise can be reduced with the modern thermographic cameras characterized by an NETD of 20 mK or less, and by the use of a preprocessing technique of the thermograms such as the TSR method (see following Section).

**4.3.2. Improvement of the Emerging Contrast Technique by the Combined Use of the Thermographic Signal Reconstruction Technique (TSR).** The TSR method [33–37], well known and largely used in pulse thermographic NDE, consists in the fitting of the experimental log-log plot thermogram by a logarithmic polynomial

$$\ln(\Delta T) = a_0 + a_1 \ln(t) + a_2 [\ln(t)]^2 \dots + a_n [\ln(t)]^n, \quad (10)$$

and the use for NDE purpose of the 1st and 2nd logarithmic derivatives of the thermogram, the derivation being achieved directly on the polynomial, then with a limited increase of the temporal noise.

The advantages of the fitting are as follows: (i) a noticeable noise reduction; (ii) the replacement of the sequence of temperature rise images,  $\Delta T(i, j, t)$ , by the series of  $(n + 1)$  images of the polynomial coefficients,

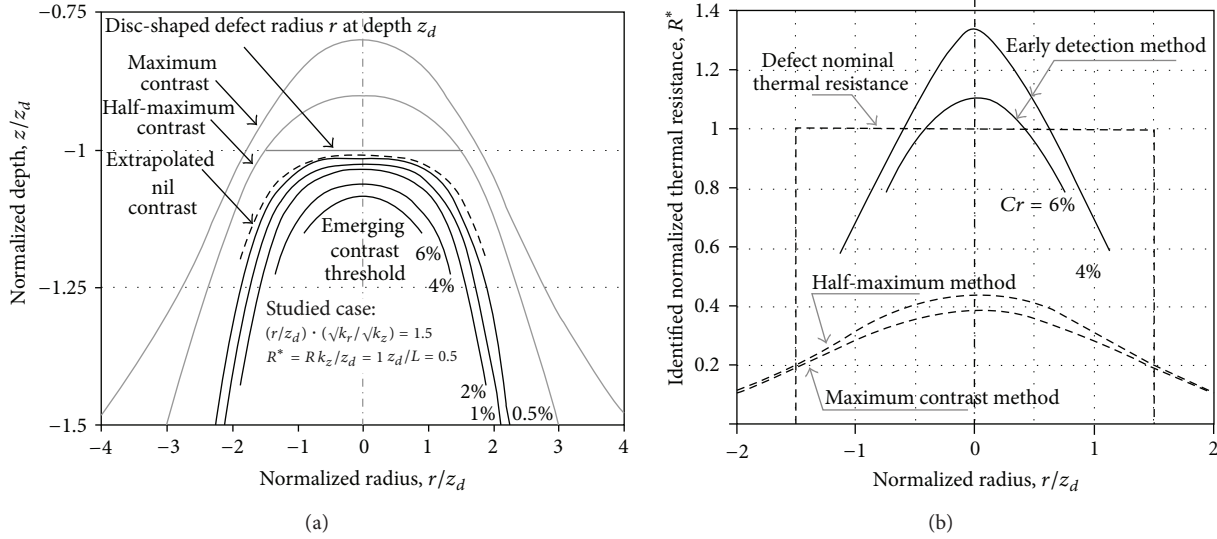


FIGURE 11: Simulation results: (a) identification of the depth profile of a circular defect ( $r_d/z_d = 1.5$  and  $R_d^* = R_d k_z / z_d = 1$ ) using the early detection/characterization with extrapolation to zero contrast and comparison to the results obtained with the maximum and half maximum contrast techniques (simulation results taken from Krapez and Balageas [18], revisited using a linear extrapolation [19, 20]; (b) identification of the thermal resistance profile, taken from [20].

$a_0(i, j), \dots, a_n(i, j)$ , which allows a drastic reduction of the data amount; (iii) the possibility of reconstructing a full thermographic sequence (from which the name of the method follows).

The logarithmic derivations are interesting too, because they produce a remarkable increase of detectivity and a “precession” of the detection [19, 20], which improve the precociousness of the defect detection.

So, it is easy to understand that both methods (early detection by emerging contrast and TSR) pursue identical purposes, and that consequently coupling them is beneficial. The increase of signal-to-noise ratio (SNR) given by the logarithmic fitting is particularly welcome since experimental crude thermal contrasts may have weak SNR, especially when deep defects are considered. In this case, the TSR technique is used as a preprocessing tool before application of the early detection process. An example of such a coupling is shown in [20].

A deeper coupling could be used, consisting in considering the emerging contrast of the 1st or 2nd logarithmic derivatives instead of the emerging contrast of the thermogram itself for the characterisation of the defect. Such an early detection method, which remains until now to be established regarding the quantitative identification of the defect parameters, is better than the one based on the half-rise time of the first derivative or the time of the maximum of the second derivative. Nevertheless, if the sole qualitative aspect is considered (detection of defects from thermographic images), the use of early images of the first and second logarithmic derivatives produces sharper defect images, a noticeable improvement compared to traditional maximum contrast images. Figure 12, taken from [19], demonstrates the ability of this approach to produce images with good SNR

and high sharpness, making the pulse thermographic NDE technique comparable to the better-established techniques, in particular ultrasonics.

4.3.3. *Application of the Early Detection and Characterization of Defects to Step-Heating Thermography.* The early detection and characterization approach based on the emerging contrast has been extended to step-heating thermography, leading to comparable improvements. The theory is given in [38], leading to identification formulas for defect depth and thermal resistance analogous to the ones found for pulse heating experiments (8).

## 5. Conclusion and Perspectives

A review of the literature of the early time detection approach in the field of thermophysical properties measurements and NDE has been made.

This approach has been built progressively and never presented as a well-defined general procedure. This is due to the fact that the applications of the method were spread in time (3 decades) and pertaining to different fields. Putting these works in perspective, it has been possible to describe and formalize the general procedure here called “the early detection and characterization.”

In the field of thermophysical properties measurements, two examples of flash diffusivity identification using rear face thermograms have been presented. They illustrate the philosophy of the approach and are well suited to thermography.

This paper demonstrates that in NDE by pulse-stimulated thermography, the generally followed attitude that consists in taking into account the sole signal-to-noise ratio when optimizing an identification process is an error. The optimization

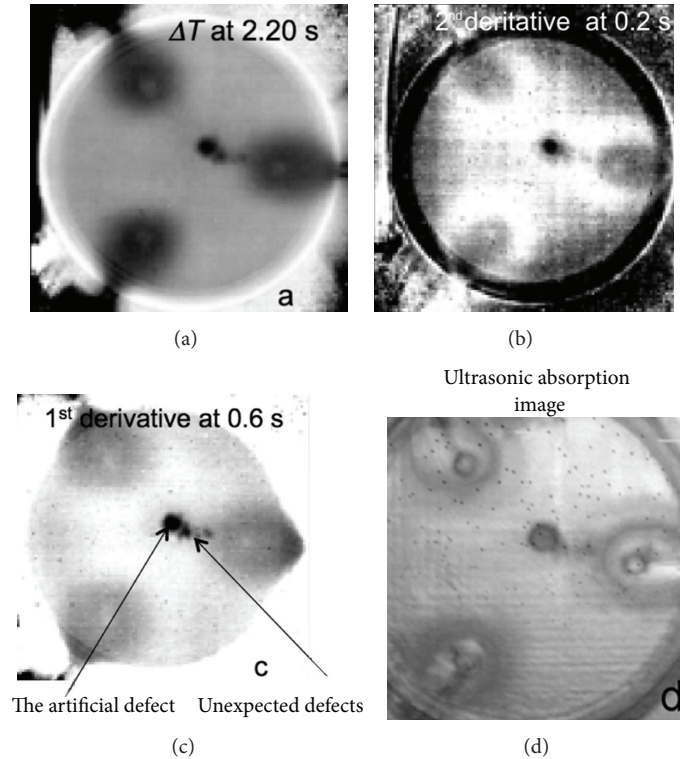


FIGURE 12: Comparison between the best images obtained by the TSR method coupled with an early detection approach and an ultrasonic D-scan: (a) Thermograms,  $\Delta T$  at 2.20 s; (b) 2nd derivative at 0.20 s; (c) 1st derivative at 0.6 s; (d) ultrasonic absorption image. The artificial defect to detect is located at the center of the sample. Unexpected defects were discovered in the near vicinity of the artificial defect. The chosen times of observation have not been optimized for imaging the 3 peripheral inner inserts that are sound regions.

must consider with the same weight the signal-to-noise ratio and the precociousness for both qualitative and quantitative purposes.

A way to conciliate both signal-to-noise ratio and precociousness is now more easily feasible by combining the early detection/characterization and the thermographic signal reconstruction (TSR) technique. Presently, this combination has given rise to recent developments in the field of NDE, increasing the attractiveness of time-resolved thermography.

## References

- [1] R. B. Orlande, O. Fudym, D. Mailet, and R. M. Cotta, Eds., *Thermal Measurements and Inverse Techniques*, CRC Press, 2011.
- [2] W. J. Parker, R. J. Jenkins, C. P. Butler, and G. L. et Abbot, "Flash method of determining thermal diffusivity, heat capacity and thermal conductivity," *Journal of Applied Physics*, vol. 32, no. 9, pp. 1679–1684, 1961.
- [3] D. Balageas, "Flash Thermal diffusivity measurements using a novel temperature-time history analysis," in *Proceedings of the 1st International Joint Conferences on Thermophysical Properties*, no. TP 1981-62, ONERA, Gaithersburg, Md, USA, June 1981.
- [4] D. L. Balageas, "Nouvelle méthode d'interprétation des thermogrammes pour la détermination de la diffusivité thermique par la méthode impulsionnelle (méthode flash)," *Revue de Physique Appliquée*, vol. 17, pp. 227–237, 1982 (French).
- [5] A. Degiovanni, "Diffusivité et méthode flash," *Revue Générale de Thermique*, vol. 16, no. 185, pp. 420–442, 1977 (French).
- [6] A. Degiovanni, "Identification de la diffusivité thermique par l'utilisation des moments temporels partiels," *High Temperatures-High Pressures*, vol. 17, pp. 683–689, 1985 (French).
- [7] D. L. Balageas and A. M. Luc, "Transient thermal behavior of directional reinforced composites: applicability limits of homogeneous property model," *AIAA Journal*, vol. 24, no. 1, pp. 109–114, 1986.
- [8] A. M. Luc and D. L. Balageas, "Non-stationary thermal behavior of reinforced composites—a better evaluation of wall energy balance for convective conditions," in *Proceedings of the 1st International Joint Conferences on Thermophysical Properties*, no. TP 1981-61, ONERA, Gaithersburg, Md, USA, June 1981.
- [9] A. M. Luc-Bouhali, R. M. Pujolà, and D. L. Balageas, "Thermal diffusivity in situ measurements of carbon/carbon composite reinforcements," in *Thermal Conductivity*, T. Ashworth and D. R. Smith, Eds., vol. 18, pp. 613–624, Plenum, London, UK, 1984.
- [10] R. M. Pujolà and D. L. Balageas, "Derniers développements de la méthode flash adaptée aux matériaux composites à renforcement orienté," *High Temperature-High Pressure*, vol. 17, pp. 623–632, 1985 (French).
- [11] D. L. Balageas, "Détermination par méthode flash des propriétés thermiques des constituants d'un composite à renforcement orienté," *High Temperatures-High Pressures*, vol. 16, pp. 199–208, 1984 (French).

- [12] D. L. Balageas, "Détermination de la diffusivité thermique du milieu homogène équivalent à un matériau composite à renforcement orienté," *Comptes-Rendus des Séances de l'Académie des Sciences*, vol. 299, no. 4, pp. 143–148, 1984 (French).
- [13] J.-P. Bardon, D. Balageas, A. Degiovanni, and J. Vuilliermes, "Thermics of composites and interfaces: current status and perspectives," *La Recherche Aérospatiale*, no. 1989-6, pp. 37–45, 1989.
- [14] D. Balageas, A. Déom, and D. Boscher, "Composite thermal properties measurements by pulse photothermal radiometry," in *Proceedings of the Eurotherm IV Conference Thermal Transfer in Composite Materials and Solid-Solid Interface*, pp. 92–95, Nancy, France, June–July 1988.
- [15] J. C. Krapez, *Contribution à la caractérisation des défauts de type délaminage ou cavité par thermographie stimulée [Ph.D. thesis]*, Ecole Centrale de Paris, Châtenay-Malabry, France, 1991.
- [16] D. L. Balageas, J. C. Krapez, and P. Cielo, "Pulsed photothermal modeling of layered materials," *Journal of Applied Physics*, vol. 59, no. 2, pp. 348–357, 1986.
- [17] D. L. Balageas, A. A. Deom, and D. M. Boscher, "Characterization and nondestructive testing of carbon-epoxy composites by a pulsed photothermal method," *Materials Evaluation*, vol. 45, no. 4, pp. 461–465, 1987.
- [18] J. C. Krapez and D. Balageas, "Early detection of thermal contrast in pulsed stimulated infrared thermography," in *Proceedings of the Quantitative Infrared Thermography, Editions Europ Thermosonde et Induction (QIRT '94)*, pp. 260–266, 1994, <http://qirt.gel.ulaval.ca/dynamique/index.php?idD=56>, paper # QIRT 1994-039.
- [19] D. L. Balageas, "Defense and illustration of time-resolved thermography for NDE," in *Proceedings of the SPIE Thermosense III*, vol. 8013, pp. 8013V-1–88013V-20, 2011, <http://publications.onera.fr/exl-php/cadcgp.php>.
- [20] D. Balageas, "Defense and illustration of time-resolved thermography for NDE," *Quantitative InfraRed Thermography Journal*, vol. 9, no. 1, pp. 5–38, 2012.
- [21] J. Bontaz, Ch. Fort, and B. Horbette, "Identification de la profondeur et de la valeur de la résistance thermique de contact dans des matériaux stratifiés par la méthode photothermique impulsionnelle," in *Proceedings of the Annual Conference of the Société Française des Thermiciens (SFT '90)*, pp. 221–224, Nantes, France, May 1990.
- [22] J. Bontaz, *Une méthode photothermique impulsionnelle appliquée au contrôle de matériaux composites [Ph.D. thesis]*, University of Bordeaux, 1991.
- [23] D. L. Balageas, D. M. Boscher, and A. A. Déom, *Temporal Moment Method in Pulsed Photothermal Radiometry. Application to Carbon Epoxy N.D.T.*, vol. 58 of *Springer Series in Optical Sciences*, Springer, 1987.
- [24] J. C. Krapez, D. Balageas, A. Deom, and F. Lepoutre, "Early detection by stimulated infrared thermography. Comparison with ultrasonics and holo/shearography," in *Advances in Signal Processing for Non Destructive Evaluation of Materials*, X. P. V. Maldague, Ed., vol. 262 of *NATO ASI Series E*, pp. 303–321, Kluwer Academic, 1994.
- [25] J.-C. Krapez, F. Lepoutre, and D. Balageas, "Early detection of thermal contrast in pulsed stimulated thermography," *Journal de Physique IV*, vol. 4, no. C7, pp. 47–50, 1994.
- [26] S. K. Lau, D. P. Almond, and J. M. Milne, "A quantitative analysis of pulsed video thermography," *NDT and E International*, vol. 24, no. 4, pp. 195–202, 1991.
- [27] D. P. Almond and S. K. Lau, "A quantitative analysis of pulsed video thermography," in *Proceedings of the Quantitative Infrared Thermography, Editions Europ Thermosonde et Induction (QIRT '92)*, pp. 207–211, QIRT, Paris, France, 1992, <http://qirt.gel.ulaval.ca/dynamique/index.php?idD=55>, paper # QIRT, 1992-031.
- [28] L. D. Favro, X. Han, P. K. Kuo, and R. L. Thomas, "Imaging the early time behavior of reflected thermal wave pulses," in *Proceedings of the Thermosense XVII: An International Conference on Thermal Sensing and Imaging Diagnostic Applications*, pp. 162–166, April 1995.
- [29] X. Han, L. D. Favro, P. K. Kuo, and R. L. Thomas, "Early-time pulse-echo thermal wave imaging," *Review of Progress in Quantitative Nondestructive Evaluation*, vol. 15, pp. 519–524, 1996.
- [30] R. L. Thomas, L. D. Favro, and P. K. Kuo, "Thermal wave imaging of hidden corrosion in aircraft components," Report AFOSR-TR-96, 1996.
- [31] H. I. Ringermacher et al., "Towards a flat-bottom hole standard for thermal imaging," in *Review of Progress in Quantitative Non-destructive Evaluation*, D. O. Thompson and D. E. Chimenti, Eds., vol. 17, pp. 425–429, Plenum Press, New York, NY, USA, 1998.
- [32] J. G. Sun, "Analysis of pulsed thermography methods for defect depth prediction," *Journal of Heat Transfer*, vol. 128, no. 4, pp. 329–338, 2006.
- [33] S. M. Shepard, T. Ahmed, B. A. Rubadeux, D. Wang, and J. R. Lhota, "Synthetic processing of pulsed thermographic data for inspection of turbine components," *Insight*, vol. 43, no. 9, pp. 587–589, 2001.
- [34] S. M. Shepard, J. R. Lhota, B. A. Rubadeux, D. Wang, and T. Ahmed, "Reconstruction and enhancement of active thermographic image sequences," *Optical Engineering*, vol. 42, no. 5, pp. 1337–1342, 2003.
- [35] S. M. Shepard, Y. L. Hou, T. Ahmed, and J. R. Lhota, "Reference-free interpretation of flash thermography data," *Insight*, vol. 48, no. 5, pp. 298–307, 2006.
- [36] S. M. Shepard, J. Hou, J. R. Lhota, and J. M. Golden, "Automated processing of thermographic derivatives for quality assurance," *Optical Engineering*, vol. 46, no. 5, Article ID 051008, 2007.
- [37] S. M. Shepard, "Flash thermography of aerospace composites," in *Proceedings of the 4th Pan American Conference for NDT*, Buenos Aires, Argentina, October 2007, <http://www.ndt.net/article/panndt2007/papers/132.pdf>.
- [38] D. Balageas and J. M. Roche, "Détection précoce et caractérisation de défauts par thermographie stimulée par échelon de flux et comparaison à la méthode impulsionnelle," in *Congrès Annuel de la Société Française de Thermique*, Bordeaux, France, May–June 2012, [http://publications.onera.fr/exl-doc/DOC401721\\_s1.pdf](http://publications.onera.fr/exl-doc/DOC401721_s1.pdf).

## Research Article

# End-to-End Image Simulator for Optical Imaging Systems: Equations and Simulation Examples

Peter Coppo,<sup>1</sup> Leandro Chiarantini,<sup>1</sup> and Luciano Alparone<sup>2</sup>

<sup>1</sup> *Selex Galileo, Via A. Einstein, 35, Florence, 50013 Campi Bisenzio, Italy*

<sup>2</sup> *Department of Electronics & Telecommunications, University of Florence, Via S. Marta 3, 50139 Florence, Italy*

Correspondence should be addressed to Peter Coppo; [peter.coppo@selexgalileo.com](mailto:peter.coppo@selexgalileo.com)

Received 7 August 2012; Accepted 27 September 2012

Academic Editor: Marija Strojnik

Copyright © 2013 Peter Coppo et al. This is an open access article distributed under the Creative Commons Attribution License, which permits unrestricted use, distribution, and reproduction in any medium, provided the original work is properly cited.

The theoretical description of a simplified end-to-end software tool for simulation of data produced by optical instruments, starting from either synthetic or airborne hyperspectral data, is described and some simulation examples of hyperspectral and panchromatic images for existing and future design instruments are also reported. High spatial/spectral resolution images with low intrinsic noise and the sensor/mission specifications are used as inputs for the simulations. The examples reported in this paper show the capabilities of the tool for simulating target detection scenarios, data quality assessment with respect to classification performance and class discrimination, impact of optical design on image quality, and 3D modelling of optical performances. The simulator is conceived as a tool (during phase O/A) for the specification and early development of new Earth observation optical instruments, whose compliance to user's requirements is achieved through a process of cost/performance trade-off. The Selex Galileo simulator, as compared with other existing image simulators for phase C/D projects of space-borne instruments, implements all modules necessary for a complete panchromatic and hyper spectral image simulation, and it allows excellent flexibility and expandability for new integrated functions because of the adopted IDL-ENVI software environment.

## 1. Introduction

Hyper-spectral imaging has dramatically changed the rationale of remote sensing of the Earth relying on spectral diversity.

Since the pioneering Hyperion mission launched in 2001 [1], hyper spectral imaging airborne and satellite sensors have shown their utility by obtaining calibrated data for determining a wide variety of bio- and geophysical products from the collected imagery.

However, all sensors have their own set of performance characteristics, response functions, noise statistics, and so on, which determine and can challenge the validity of the generated data products. Through simulation of the sensor response, the utility of a new sensor design can be ascertained prior to construction, by running algorithms on simulated remote sensing data sets. In the case of existing well-characterised sensors the generation of simulated data assists in debugging sensor problems and provides a better

understanding of a particular sensor's performance in new operational environments.

In this paper, an end-to-end Selex Galileo (SG) simulation tool developed in the ENVI-IDL [2] environment for the generation of simulated data from airborne/space-borne optical and infrared instruments, starting from high resolution imagery is presented.

High resolution hyper-spectral data from airborne campaigns can be typically used as input for space-borne sensors simulations. As an alternative, the input images can be completely synthesized by modelling the geometrical and spectral characteristics of the observed targets. The simulator is based on six different modules describing the reflectance scenario, the atmospheric conditions, the instrument models and the atmospheric inversion model.

The core modules aim to simulate instrument performances (spectral, spatial, and radiometric) from a variety of sensor parameters including optics, detector, scanning, and electronics characteristics. The Atmospheric module is based

on the standard Modtran [3] model, whereas the scenario simulation module aims at associating a spectral signature to each pixel of a synthetic thematic map, whenever a high resolution image taken by an airborne instrument is not available.

Compared to a detailed instrument simulator, typically developed for the realization and commissioning phases (B/C phases) of a spaceborne/airborne payload, the proposed simplified end-to-end simulator is conceived as a tool (phase 0/A) to enable the rapid dimensioning of a new optical instrument and to trace the link between user and instrument requirements. SG simulator (SG\_SIM) pursues a similar philosophy as other approaches useful for 0/A phases (e.g., SENSOR, MODO, CAMEO, and PICASSO), and it includes all main functions (implemented in the IDL-ENVI SW environment) necessary for a complete hyper spectral image simulation, which are not often simultaneously present in the others.

For instance, in comparison to SENSOR [4] the control of spectral mixing and the generation of synthetic scenes are also considered, whereas in comparison to US simulators, for example CAMEO [5] and PICASSO [6–8]), the extension to the MWIR/LWIR spectral bands, and a 3D reflectance rendering are missing.

After a detailed theoretical description of SG\_SIM model equations and its key concepts (Section 2), some simulation examples for satellite and airborne hyper spectral and panchromatic data study cases are reported (Section 3).

## 2. Simulator Equations Description

The flow diagram of the software tool is shown in Figure 1. The input data can be either airborne reflectance images at high spatial, spectral, and radiometric resolution or synthetic reflectance maps, coming from a thematic map and a reflectance data base, and specifications for the instrument to be simulated (e.g., spatial and spectral response, sampling, transfer function, noise model, viewing geometry, and quantisation).

The simulation procedure consists of four different processing steps. First the at-sensor radiance images are obtained by using the Atmospheric Modtran code, then the signal is spatially, spectrally, and radiometric degraded by applying the specific instrument response models to generate the instrument simulated radiance image.

**2.1. Atmospheric Simulation.** The Atmospheric Module ingests as input a reflectance image taken at high spatial and spectral resolution which is then transformed into sensor radiance images by using the atmospheric radiances and transmittances generated by the Modtran code.

A preliminary simplified atmospheric model has been used. It considers Lambertian surface scattering, near-nadir observation, no adjacency effects, and a flat Earth. The input spectral radiance  $L(\lambda, h)$  for an observation sensor at altitude  $h$  is obtained on the basis of the following relationship, derived from the radiative transfer model depicted in

Figure 2. The radiance is described from the following:

$$L(\lambda, h) = I_{\text{TOA-SUN}}(\lambda) \cdot \frac{\cos(\theta_{\text{sun}})}{d^2} \cdot \tau_{\downarrow}(\lambda) \cdot \frac{\rho(\lambda)}{\pi} \cdot \tau_{\uparrow}(\lambda, h) + L_{\uparrow\text{ATM}}(\lambda, h), \quad (1)$$

with

- (i)  $I_{\text{TOA-SUN}}(\lambda)$  = Top of atmosphere sun irradiance ( $\text{W}/\text{m}^2/\mu\text{m}$ );
- (ii)  $\rho(\lambda)$  = Earth surface reflectance;
- (iii)  $\theta_{\text{sun}}$  = Sun observation angle (function of latitude, longitude, day of the year, and time);
- (iv)  $d^2$  = Earth-Sun distance normalised to mean (depending from day of the year);
- (v)  $\tau_{\downarrow}(\lambda)$  = Total downwards atmosphere transmission;
- (vi)  $\tau_{\uparrow}(\lambda, h)$  = Total upwards atmosphere transmission from ground to the observation altitude  $h$ ;
- (vii)  $L_{\uparrow\text{ATM}}(\lambda, h)$  = Scattered atmosphere radiance ( $\text{W}/\text{m}^2/\text{sr}/\mu\text{m}$ ) from ground to the observation altitude  $h$ ;
- (viii)  $L(\lambda, h)$  = Total Atmosphere radiance ( $\text{W}/\text{m}^2/\text{sr}/\mu\text{m}$ ) which represents the input to the instrument at altitude  $h$ .

The downwards/upwards atmospheric transmittances  $\tau_{\downarrow}(\lambda)$ ,  $\tau_{\uparrow}(\lambda, h)$  and the atmospheric radiance  $L_{\uparrow\text{ATM}}(\lambda, h)$  depend on the concentration of all atmospheric gases and the aerosols distribution. The simulator allows the control of the major variable atmospheric gases (i.e., the columnar water vapour and  $\text{CO}_2$  contents), the aerosols visibility at a certain observation altitude  $h$ , and the aerosols profile. These parameters can be controlled by means of Modtran code inputs, while the other parameters are considered constant. A dedicated graphical interface is used to create the Modtran input charts.

Generally the surface reflectance's images  $\rho(\lambda)$ , used as input to the simulator, come from a data base of experimental airborne or ground truth data acquired with other spectrometers, and they are affected by the spectral response of those instruments used for the database acquisition.

The radiances  $L(\lambda, h)$  are generated from the Modtran code at the maximum spectral resolution ( $1 \text{ cm}^{-1}$ ) and are convolved with the spectral response (SR) of the instrument used to generate the data base. This spectral response (SR) is approximated with a Gaussian function with the centre wavelength  $\lambda_c$  and the Full Width at Half Maximum (FWHM) equal to  $\Delta\lambda/4$ , where the integral is performed in a  $\Delta\lambda$  spectral

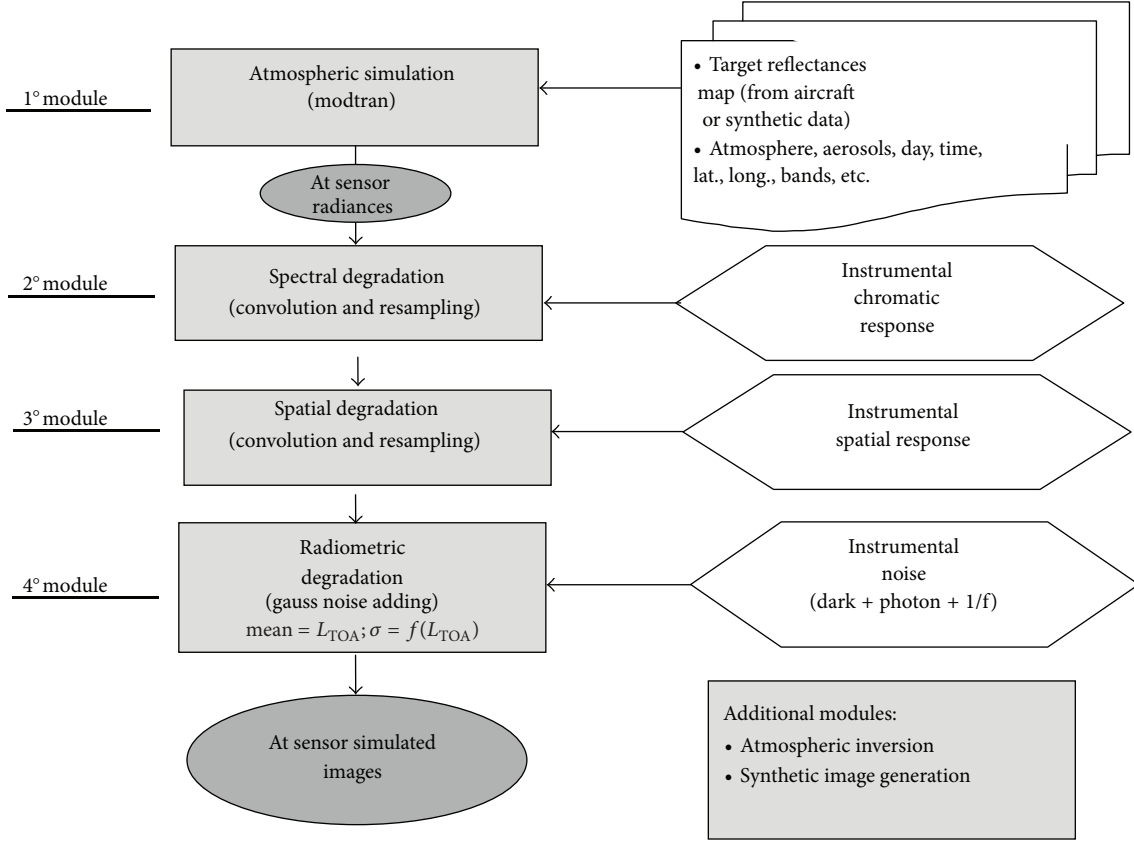


FIGURE 1: Airborne/space-borne optical sensor data simulator (flow diagram).

range centred in  $\lambda_c$ , and can be written as in the following:

$$\begin{aligned}
 L_{1i}(\lambda, h) &= \int_{\lambda_c - \Delta\lambda/2}^{\lambda_c + \Delta\lambda/2} \frac{L_i(\lambda, h) \cdot \text{SR}_i[\lambda_c(i) - \lambda] \cdot d\lambda}{\Delta\lambda} \\
 &= \int_{\lambda_c - \Delta\lambda/2}^{\lambda_c + \Delta\lambda/2} \left[ \frac{I_{\text{TOA-SUN}}(\lambda) \cdot \frac{\cos(\theta_{\text{sun}})}{d^2} \cdot \tau_{\downarrow}(\lambda)}{\pi} \cdot \frac{\rho_i(\lambda_c(i))}{\pi} \cdot \tau_{\uparrow}(\lambda, h) + L_{\uparrow\text{ATM}}(\lambda, h) \right] \\
 &\quad \cdot \frac{\text{SR}_i[\lambda_c(i) - \lambda] \cdot d\lambda}{\Delta\lambda} \\
 &\cong \int_{\lambda_c - \Delta\lambda/2}^{\lambda_c + \Delta\lambda/2} \left[ \frac{I_{\text{TOA-SUN}}(\lambda) \cdot \frac{\cos(\theta_{\text{sun}})}{d^2} \cdot \tau_{\downarrow}(\lambda)}{\pi} \cdot \frac{\bar{\rho}_i(\lambda_c, \Delta\lambda)}{\pi} \cdot \tau_{\uparrow}(\lambda, h) + L_{\uparrow\text{ATM}}(\lambda, h) \right] \\
 &\quad \cdot \frac{\text{SR}_i[\lambda_c(i) - \lambda] \cdot d\lambda}{\Delta\lambda} \\
 &= \int_{\lambda_c - \Delta\lambda/2}^{\lambda_c + \Delta\lambda/2} \frac{\bar{L}_i(\lambda, h) \cdot \text{SR}_i[\lambda_c(i) - \lambda] \cdot d\lambda}{\Delta\lambda}
 \end{aligned}$$

(2)

With

- (i)  $L_i(\lambda, h) = [I_{\text{TOA-SUN}}(\lambda) \cdot \cos(\theta_{\text{sun}})/d^2 \cdot \tau_{\downarrow}(\lambda) \cdot \rho_i(\lambda_c(i)) / \pi \cdot \tau_{\uparrow}(\lambda, h) + L_{\uparrow\text{ATM}}(\lambda, h)]$  the output spectral radiance obtained from Modtran by using the real surface reflectivity  $\rho_i(\lambda)$  for each spectral pixel  $i$ ;
- (ii)  $\text{SR}_i[\lambda, \lambda_c(i)]$  the normalised spectral response of instrument used to generate the data base for the  $i$ th spectral channel (with  $\lambda_c(i)$  the central wavelength) as a function of wavelength  $\lambda$ . Each  $\text{SR}_i[\lambda, \lambda_c(i)]$  has been simulated with a Gaussian response centred at  $\lambda_c$  and FWHM equal to  $\Delta\lambda/4$ .
- (iii)  $\bar{L}_i(\lambda, h) = [I_{\text{TOA-SUN}}(\lambda) \cdot \cos(\theta_{\text{sun}})/d^2 \cdot \tau_{\downarrow}(\lambda) \cdot \bar{\rho}(\lambda_c(i), \Delta\lambda) / \pi \cdot \tau_{\uparrow}(\lambda, h) + L_{\uparrow\text{ATM}}(\lambda, h)]$  the output spectral radiance from Modtran by using the data base reflectivity value.
- (iv)  $\bar{\rho}_i(\lambda_c(i), \Delta\lambda) = (\int_{\lambda_c - \Delta\lambda/2}^{\lambda_c + \Delta\lambda/2} \rho_i(\lambda_c(i)) \cdot \text{SR}_i[\lambda_c(i) - \lambda] \cdot d\lambda) / \Delta\lambda$  the weighting mean of the Earth surface reflectivity within the  $\text{SR}(\lambda)$  spectral response, which represents the data-base reflectivity value.
- (v)  $L_{1i}(\lambda, h) (\text{W/m}^2/\text{sr}/\mu\text{m})$  the mean spectral radiance within the  $\text{SR}(\lambda)$  spectral response.

The high resolution at sensor radiance  $L_1(\lambda, h)$  is simulated with Modtran code for different values of the surface reflectivity and a 3D Look-Up-Table (reflectivity, radiance,

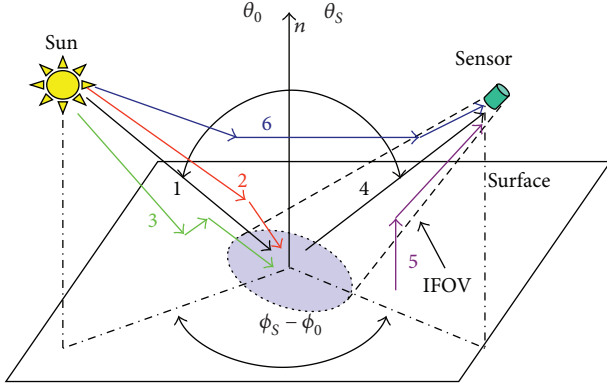


FIGURE 2: General atmospheric model scheme: the simplified atmospheric simulator takes into account in first approximation the 1, 2, 4, and 6 paths. The adjacent effects described from 3 and 5 paths will be updated in the next version of simulator.

and wavelength) is generated. Finally, for each wavelength, the simulation module determines the best linear fit between radiance and surface reflectivity, which is applied to all input reflectivity image pixels  $\rho_i(\Delta\lambda)$  to generate the at sensor radiances  $L_{1i}(\lambda, h)$ .

**2.2. Spectral Degradation.** The second processing block applies a spectral degradation where the at-sensor radiance image is further spectrally degraded to the spectral channels and response of the airborne/satellite instrument to be simulated by means of a spectral interpolation and a convolution with the Instrument Chromatic Response (ICR). The  $ICR_i[\lambda, \lambda_c(i)]$  represents the normalized to maximum instrument response for the  $i$ th spectral channel (with  $\lambda_c(i)$  defined as the central wavelength) to a spatially uniform monochromatic source as a function of wavelength  $\lambda$ . The at-sensor radiance  $L_2(\text{W}/\text{m}^2/\text{sr})$  is obtained from the following:

$$L_2(\lambda_c(i), h) = \int L_1(\lambda, h) \cdot ICR_i[\lambda_c(i) - \lambda] \cdot d\lambda. \quad (3)$$

**2.3. Spatial Degradation.** The spatial degradation module ingests the at-sensor radiance image and degrades it to the required spatial sampling. This process is applied by means of a convolution between the input image and the Instrument Spatial Response (ISR) of the optical sensor to be simulated followed by a resampling process (decimation) (Figure 3). The ISR is defined as the response of the overall instrument in a given spatial pixel to a spectrally uniform point source as a function of its position in space. The spatially degraded radiance image ( $L_3$ ) is described by the following:

$$L_3(\lambda_c(i), h, x, y) = \iint_{\text{image}} L_2(\lambda_c(i), h, x', y') \cdot \text{ISR}(x - x', y - y') \cdot dx' \cdot dy'. \quad (4)$$

The ISR is calculated as the Inverse Fourier Transform of the Modulation Transfer Function (MTF), which assumes

the overall system is a linear shift invariant system. Then a “cascade model” for the system MTF is applied on the hypothesis of independent subsystems.

The hypothesis of independent subsystems is exact for many instruments, while the use of MTF, without taking into account the phase effects is valid only as a first approximation in incoherent imaging systems using well-corrected optics [10].

The “cascade model” (Figure 4) takes into account the hypothesis of separability of spatial frequency variables. Due to the properties of the Fourier Transform, the separability in the frequency domain corresponds to separability in the space domain. The along-track and across-track MTFs are calculated starting from a theoretical formulation and the Inverse Fourier Transform is calculated and normalized to a unit integral for both. In this way two unidimensional digital filters have been obtained and convolved with the high resolution image by means of the following:

$$L_3(\lambda_c(i), h, x, y) = \int \left( \int L_2(\lambda_c(i), h, x', y') \cdot \text{ISR}_x(x - x') \cdot dx' \right) \cdot \text{ISR}_y(y - y') \cdot dy', \quad (5)$$

where:

- (i)  $\text{ISR}_x(x) = \text{IFFT}(\text{MTF}_x)$  the Instrument Spatial Response along  $x$  (e.g., along-track),
- (ii)  $\text{ISR}_y(y) = \text{IFFT}(\text{MTF}_y)$  the Instrument Spatial Response along  $y$  (e.g., across-track).

The along- and across-track  $\text{MTF}_{x,y}$  are calculated taking into account the image degradation contributions reported in Table 1.

The image quality can be affected from many factors such as the size of detector (spatial aperture), the detector degradations (e.g., pixel cross talk or charge transfer & reading smearing in CCD), the integration time during image motion (temporal aperture) caused from satellite motion or the scanning system (resp. for a push broom or a whisk-broom system), the electronic filtering, the focal plane jitter (instrument micro-vibrations), the optics diffraction and aberrations [11].

These components can influence both the across-track and/or the along-track MTF depending on the direction of scanning and the disposition of detector. Some of these components are described in annex.

Examples of simulated MTF and SRF functions for airborne and spaceborne instruments that were generated with the simulator are reported in Section 3.1.

**2.4. Radiometric Degradation.** The fourth processing module accounts for radiometric degradation. A random noise term is added to the images to simulate the  $Ne\Delta L$  (Noise Equivalent Difference Radiance in  $\text{W}/\text{m}^2/\text{sr}$ ) of the optical instrument. The radiance  $L_3(\lambda_c(i), x, y)$  of each pixel  $(x, y)$  and of the  $i$ th spectral band (with central wavelength  $\lambda_c(i)$ ) is

TABLE 1: MTF subsystems contributions for a push broom system.

Components	Terms	Parameters
MTF Across-Track	Satellite vibration, optics diffraction, optics aberration; detector size, CCD charge transfer, and electronic filter	Jitter, detector pitch, central obscuration, focal length, pupil diameter, aberration coefficient, detector pitch, number of charge transfer, charge transfer efficiency, and filter order
MTF Along-Track	Satellite vibration, satellite motion, optics diffraction, optics aberration, and detector size	Jitter, detector pitch, Integration time, central obscuration, focal length, pupil diameter, aberration coefficient, and detector pitch

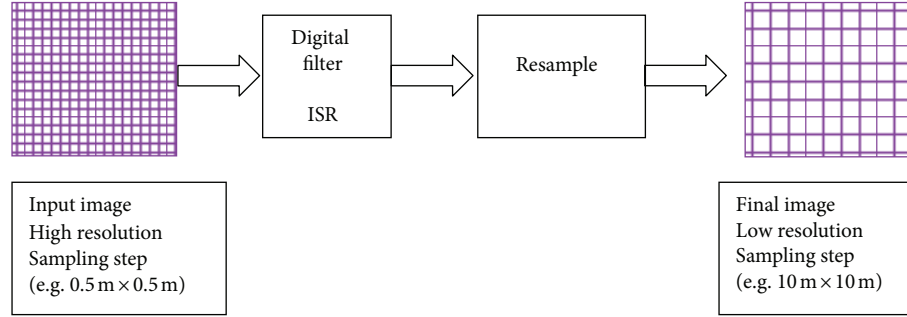


FIGURE 3: Spatial degradation module of the instrument simulator: convolution between the high spatial resolution image and the instrument spatial response (ISR) of the optical sensor that is to be simulated, followed by a resampling process (decimation).

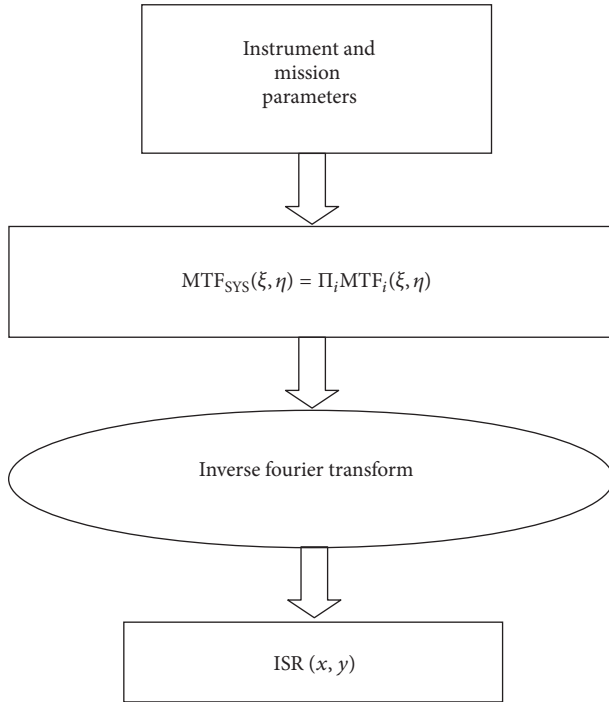


FIGURE 4: Flux diagram to calculate the instrument spatial response of the cascade model.

substituted with a random value taken from a Gaussian distribution, where  $L_3(\lambda_c(i), x, y)$  represents the mean radiance value ( $W/m^2/sr$ ) and  $Ne\Delta L$  ( $W/m^2/sr$ ) the noise equivalent radiance, which is the standard deviation of the instrument

temporal noise. The relationship between  $Ne\Delta L$  and the pixel radiance value  $L_3$  is described in the following:

$$Ne\Delta L(\lambda_c(i), x, y) = \sqrt{A(\lambda_c(i)) + B(\lambda_c(i)) \cdot L_3(\lambda_c(i), x, y)}, \quad (6)$$

where  $A(\lambda_c(i))$  is the noise variance of the detector (dark current, read-out and Johnson noises) plus FEE/ADC (Front End Electronics/Analog to Digital Converter) for the  $i$ th spectral band and the product  $[B(\lambda_c(i)) \cdot L_3(\lambda_c(i), x, y)]$  is the photon noise variance, which is proportional to the input signal  $[L_3(\lambda_c(i), x, y)]$ . A Gaussian distribution function for the noise is a good approximation also for the photon noise, because the Poisson distribution approximates a Gaussian function for a high number of generated photocarries.

$Ne\Delta L$  is the minimum variation of the input radiance which can be measured and represents the radiometric resolution of the instrument. Another representation of the sensor noise can be derived from the signal-to-noise ratio (SNR) for each pixel and for each wavelength. The SNR can be obtained from the following:

$$\begin{aligned} SNR_i(\lambda) &= \frac{L_3(\lambda_c(i), x, y)}{Ne\Delta L(\lambda_c(i), x, y)} \\ &= \frac{L_3(\lambda_c(i), x, y)}{\sqrt{A(\lambda_c(i)) + B(\lambda_c(i)) \cdot L_3(\lambda_c(i), x, y)}}. \end{aligned} \quad (7)$$

The photon noise formulation reported in (6) ( $[B(\lambda_c(i)) \cdot L_3(\lambda_c(i), x, y)]$ ) is based on the relationship between the number of acquired electrons  $Ne$  and the integrated input

radiance  $L_{IN}$  ( $W/m^2/sr$ ) for each spectral channel as described in the following:

$$\begin{aligned} N_e(e^-) &= \bar{L}_{IN} \left( \frac{W}{m^2 sr} \right) \cdot A_{pupil} (m^2) \cdot \Omega (sr) \cdot \bar{\tau} \\ &\cdot \left( \frac{\bar{\lambda}}{h \cdot c} \right) (J^{-1}) \cdot t_{int} (sec) \cdot \eta (e^-/phot) \\ &= K \cdot \bar{L}_{IN} (W/m^2 sr), \end{aligned} \quad (8)$$

with

- (i)  $\bar{\tau}$  = Total mean in band (with ICR) instrument transmittance;
- (ii)  $A_{pupil}$  = Input pupil area ( $m^2$ );
- (iii)  $\Omega$  = Scene pixel IFOV (sr);
- (iv)  $t_{int}$  = Integration time (sec);
- (v)  $\eta$  = Mean in band (with ICR) detector quantum efficiency (electrons/photon);
- (vi)  $hc/\lambda = (1,98E-19 \text{ Joule} \cdot \mu m)/\lambda =$  Energy of a photon of wavelength  $\lambda$  ( $\mu m$ );
- (vii)  $L_{IN}$  ( $W/m^2/sr$ ) = Spectrally integrated mean radiance in the ICR;
- (viii)  $K(e^-/(W/m^2 sr)) = A_{pupil}(m^2) \cdot \Omega(sr) \cdot \bar{\tau} \cdot (\bar{\lambda}/(h \cdot c)) \cdot t_{int}(sec) \cdot \bar{\eta}(e^-/phot)$  the coefficient of proportionality between the number of acquired electrons  $N_e$  and the input radiance  $L_{IN}$ .

The photon noise equivalent difference radiance  $Ne\Delta L$  is related to the photon noise equivalent difference electron  $Ne\Delta N_e$ , which can be obtained from the standard deviation of the Poisson noise distribution. This standard deviation is equal to the square root of the number of electrons itself and is described from the following:

$$\begin{aligned} Ne\Delta N_e &= \sqrt{N_e}, \\ Ne\Delta L &= \frac{\sqrt{N_e}}{K} = \frac{\sqrt{K \cdot \bar{L}_{IN}}}{K} = \sqrt{\frac{\bar{L}_{IN}}{K}} \equiv \sqrt{B \cdot \bar{L}_{IN}}, \\ B \left( \frac{W/m^2 sr}{e^-} \right) &= \frac{1}{K} = \frac{1}{A_{pupil} \cdot \Omega \cdot \bar{\tau} \cdot (\bar{\lambda}/(h \cdot c)) \cdot t_{int} \cdot \bar{\eta}}. \end{aligned} \quad (9)$$

The  $A$  and  $B$  coefficients, which depend from the selected spectral channel and are fed as input to the simulator, can be derived from the radiometric model of the simulated optical sensor or they can be evaluated on the basis of acquired images of homogeneous targets acquired by the sensor [13–16].

Two additional procedures have been implemented to permit the analysis of the simulated images (Sections 2.5 and 2.6).

**2.5. Atmospheric Correction.** The first permits the retrieval of surface reflectance from airborne and spaceborne sensor radiances. Two standard methods can be used: one is based on Modtran code, by inverting (1), to obtain the surface reflectance from the instrument radiance and the second based on the standard ENVI-FLAASH [17] software, which allows aerosols to be estimated by means of the dark pixel method (water bodies, shadowed area, and dense vegetation) and the water vapour map to be estimated by means of the 820, 940, and 1135 nm absorption bands ratio method [18].

**2.6. Synthetic Image Generation Module.** The second procedure permits to quantitatively evaluate the impact of instrumental parameters on simulated image quality when a low noise airborne input image is not available.

In particular it allows the creation of black and white bar test images with different modulations (square or sinusoidal), periods and shading, to the scope to evaluate the impact on the image quality of instrument parameters such as MTF and noise as a function of the spatial sampling interval and the target reflectivity, and to analyse the minimum detectable albedo contrast as a function of spatial frequency and illumination conditions (Figure 5).

It is also possible to generate synthetic hyper-spectral surface reflectance images at the desired spatial and spectral resolution by using as input a thematic map of the zone under investigation (derived synthetically or from a classification) and a spectral library of the surface materials of interest. A statistical mixing of spectral signatures for each zone with the Dirichlet method permits to control the percentage of the statistical variability [19].

The following further statistical variability, devoted to a better representation of a real scenario, can be introduced [20]:

- (i) a uniform or Gaussian variability for each spectral signature due to a possible spatial variation of the substance composition, such as contaminants, oxidation, and ageing, and so forth,
- (ii) a beta function distributed statistical variation of illumination, which takes into account possible image errors due uncompensated observation and surface slope angles,
- (iii) a Gaussian variability due to scenario noise, coming from uncompensated atmospheric and environment effects or uncompensated errors of sensors used to obtain the spectral library data.

Then the surface reflectance  $\bar{R}$ , represented from a column vector for each wavelength, is obtained by means of the following matrix mixing relationship:

$$\bar{R} = \bar{P} \cdot \gamma \cdot \bar{\Psi} \cdot [\bar{A} \cdot t + \bar{M} \cdot (1 - t)] + \bar{N}, \quad (10)$$

with

- (i)  $\bar{P}$  a matrix representing the end-members (pure elements) reflectance for each wavelength;

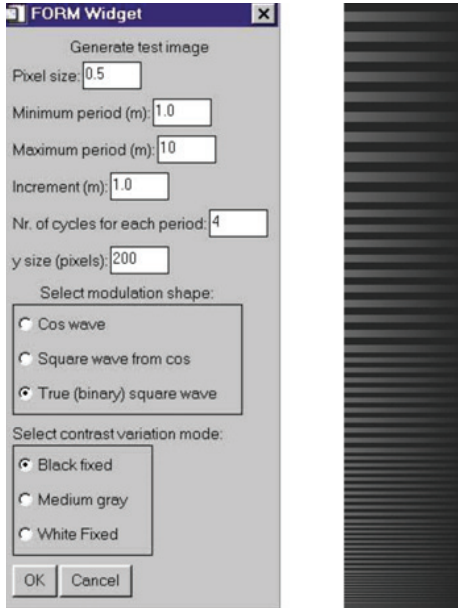


FIGURE 5: Input mask to generate the synthetic black and white images.

- (ii)  $\bar{A}$  a column vector representing the statistical variability of abundances, according to a Dirichlet distribution;
- (iii)  $\bar{M}$  a column vector representing the mean value of abundances for each wavelength;
- (iv)  $t$  a scalar parameter which describes the degree of statistical mixing ( $t = 0$  no mixing,  $t = 1$  all random mixing);
- (v)  $\gamma$  a statistical parameter obtained from a beta distribution, describing the illumination variation for each pixel;
- (vi)  $\bar{\Psi}$  a diagonal matrix derived from a uniform or a Gaussian density, representing the spatial variation of end members;
- (vii)  $\bar{N}$  a column vector representing a Gaussian scenario noise, that is uncompensated atmospheric retrieval and/or sensors errors used to obtain the library data set.

### 3. Simulations Examples

Several simulation tests were performed to assess the potential of the tool for the instrument image quality and applications evaluation in the framework of the study and the testing phases of the Selex Galileo SIMGA airborne hyper spectral camera and the HypSeo (ASI-PRISMA precursor [21]) spaceborne hyper spectral and panchromatic cameras phase A study.

Such activities allowed also the validation of the simulator by means of real SIMGA data acquired on clay soil targets during an airborne campaign of 2009 in Mugello (Tuscany, I)

test site, where ground truth data were collected simultaneously at the same time of overflights [16].

Some examples of simulation of a 3D map representation of the ISR function have been produced for the purpose of evaluating the instrument image quality, which is generally given from the FWHM of the instrument spatial response or by the ratio between the integral of the spatial response within a delimited spatial domain (e.g., 1 Spatial Sampling Interval) and the integral in all spatial domain, which is generally called integrated energy (in percentage unit).

A more detailed analysis based on another image quality parameter (SNR\*MTF) has been done to trade-off the image quality of a panchromatic camera as a function of some instrument parameters (e.g., pupil diameter and spatial sampling) for different atmospheric conditions (summer/winter and rural/urban aerosol) aiming to a better definition of the instrument requirements.

Finally VIS and SWIR radiance and reflectance simulated images have been generated for some specific targets related to civil (land use) and dual use applications for terrestrial and marine environments to the scope of understanding the instrument capabilities for targets' discrimination. These two dual use applications has been simulated during the testing phase of the airborne SG instrument (SIMGA) by means of targets of small green panels over vegetation cover and small grey panels under water, and then verified by means of an airborne campaign on a controlled area.

**3.1. SRF 3D Maps for Integrated Energy Calculations.** The simulator permits a 3D representation of the SRF map by using as input a delta function. As an example this representation has been done to evaluate the spatial resolution (defined in terms of percentage of integrated energy of SRF within a certain space domain) of the airborne SG SIMGA hyper-spectral camera by taking into account both the laboratory measurements and the smearing effect introduced from the detector integration which occurs during platform motion. The along and the across-track MTF and SRF contributions are displayed in Figures 6(a) and 6(b), respectively, for the VIS and the SWIR channels. The instrument parameters used in the simulations are reported in Tables 2(a) and 2(b). From the tables it appears that the ratio between the FWHM of the SRF and the Spatial Sampling Distance (SSD) is much lower for SWIR channels (0.87 along scan\*1.05 across scan) with respect to the VIS ones (2.70 along scan\*1.49 across scan), showing that the SRF of VIS channels has a larger width (in  $\pm 2/3$  pixels) with respect to that of the SWIR ones ( $\pm 1$  pixel) (see also Figures 6(a) and 6(b)).

The integrated energy calculation performed within an area of 1 SSD\*1 SSD of the VIS and SWIR 3D maps also confirms that the energy content within a pixel is much lower for VIS respect to SWIR channels (the same happens within the same ground size of 1.333 m\*1.333 m):

- (i) Integrated Energy in 0.706 m\*0.706 m for VIS (1 SSD\*1 SSD) = 19%,
- (ii) Integrated Energy in 1.333 m\*1.333 m for VIS (1.9 SSD\*1.9 SSD) = 51%,

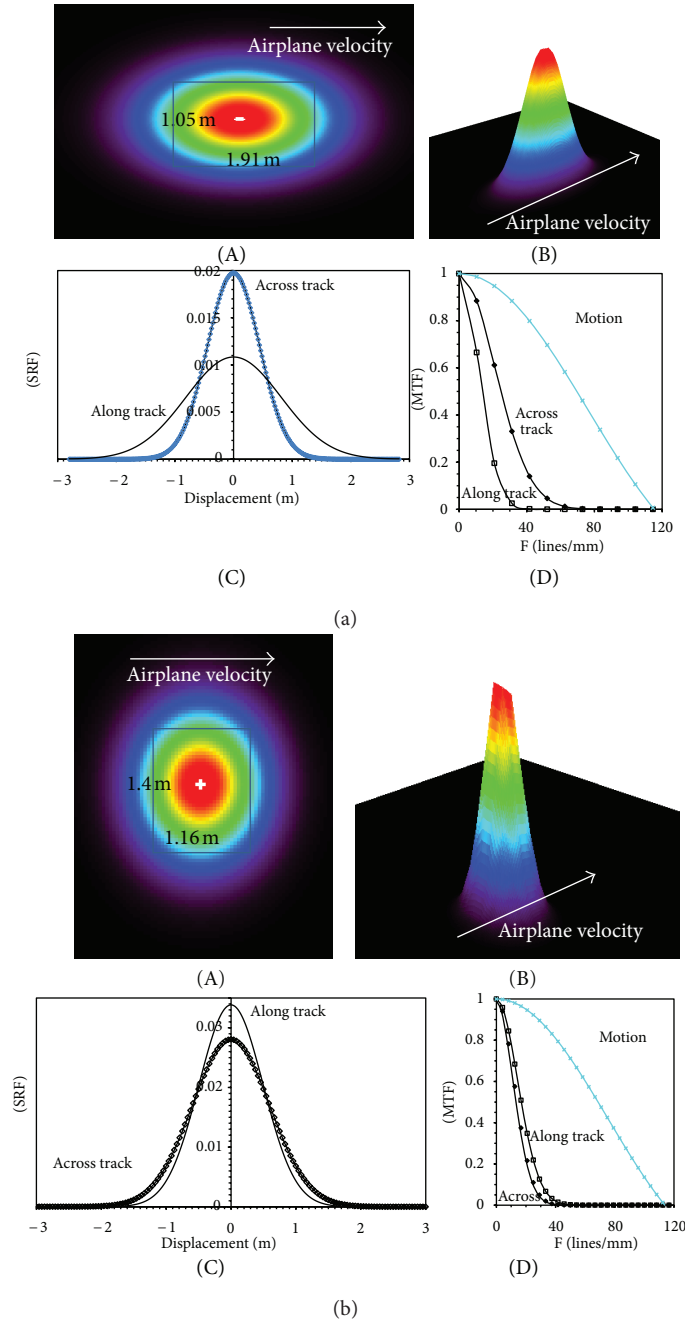


FIGURE 6: (a) Maps of Spatial Response Function (SRF) of SIMGA VIS channels ((a), (b)), plots of SRFs across and along-track (along and across-slit) for the central FOV pixel as a function of on-ground displacement (c). The simulation is obtained by using the static laboratory measurements after having introduced the smearing effect due to the along-track motion (Tables 2(a) and 2(b)). MTF motion and along/across-track components as a function of spatial frequency at detector level (d). (b) Maps of Spatial Response Function (SRF) of SIMGA SWIR channels (a), (b), plots of SRFs across and along-track (along and across-slit) for the central FOV pixel as a function of on-ground displacement (c). The simulation is obtained by using the static laboratory measurements after having introduced the smearing effect due to the along-track motion (Tables 2(a) and 2(b)). MTF motion and along/across-track components as a function of spatial frequency at detector level (d).

(iii) Integrated Energy in  $1.333 \text{ m} \times 1.333 \text{ m}$  for SWIR ( $1 \text{ SSD} \times 1 \text{ SSD}$ ) = 61%.

In conclusion the spatial resolution of VIS channels is coarser with respect to that of SWIR channels, also if the spatial sampling is better (0.706 m respect to 1.333 m).

A further exercise was done to simulate the 3D Hypseo SRF [16] by using the instrument parameter reported in Table 3 and the Hypseo MTF model [21]. The FWHM of the spatial response is  $24.4 \text{ m} \times 20.6 \text{ m}$  (along-scan\*across-scan) while the integrated energy in  $1 \text{ SSD} \times 1 \text{ SSD}$  ( $20 \text{ m} \times 20 \text{ m}$ ) is

TABLE 2

(a) Full Width Half Maximum (FWHM) values of SIMGA Spatial Response (across and along slit) obtained by static measurements performed in laboratory (Gaussian fit to data, [9]) and smearing effect due to integration during motion

	FWHM (m) at 1 Km Across-SLIT (along-scan)	FWHM (m) at 1 Km Along-SLIT (across-scan)
VIS	1.91 (1.88 static)	1.05
SWIR	1.16 (1.13 static)	1.40

(b) SIMGA detector and optical parameters used for simulation ( $V = 30$  m/s at 1 Km height)

	Detector pitch (micron)	Focal length (mm)	Pupil diameter (mm)	SSD (m) At $H = 1$ Km	FOV (deg)	$T_{dwell}$ (msec)	$T_{int}$ (msec)	$T_{int}/T_{dwell}$
VIS	12	17	7.08	0.706	$\pm 19$	23.5	17	0.72
SWIR	30	22.5	11.25	1.333	$\pm 12$	44.3	13	0.29

TABLE 3: Characteristics of HYPSEO Hyper-spectral and PAN cameras at 620 Km satellite altitude.

Parameters	Hyper-spectral camera		Pan camera			
	VNIR band	Swir band	Pan band			
Spectral Interval [nm]	400–1000	1000–2500	500–900			
Average Spectral sampling [nm]	10	10	500–900			
Swath [km]/FOV (°)		20/1.85	20/1.85	14/1.30	10/0.93	10/0.93
Spatial Sampling [m]	20	20	5	3.5	2.5	2.5
Useful Zone [km]		500	500			
Spectral channels (max)	$\approx 60$	$\approx 150$	1			
Aperture Diameter [mm]		150 ( $F/3.7$ )	150 ( $F/5.8$ )	150 ( $F/8.3$ )	150 ( $F/11.6$ )	300 ( $F/5.8$ )
Detector pixel dimension [ $\mu\text{m}$ ]	18	18	7			
Array dimension	1000 $\times$ 256	1000 $\times$ 256	4000 $\times$ 1			
FPA type	Si on Hybrid CMOS	Cooled CMT on Hybrid CMOS	Si CCD			
SNR at $\rho = 0.3$ and SZA = 60°	$\approx 200$	$\approx 50$	144	71	32	92

53%, which is a value substantially equal to that estimated for the airborne SIMGA instrument at 1.33 m  $\times$  1.33 m of pixel size.

**3.2. Satellite Panchromatic Image Quality Requirements.** The simulator permits to study the impact of system design parameters on the instrument image quality. To this scope a parametric analysis of the performance of the HypSEO-PAN Camera as a function of the pupil diameter dimension for different spatial sampling, atmospheric and illumination conditions was performed on the basis of simulated test images and instrument parameters (Table 4), to trade-off the instrument sizing with the image quality.

We have adopted as a first approximation of image quality criterion the Minimum Resolvable Contrast (MRC) at a certain spatial frequency  $f$ , which is equal to the inverse of the product  $[\text{MTF}(f) \cdot \text{SNR}]$ , where SNR is calculated for uniform scenes (spatial frequency  $f = 0$ ) [11]. As a rule of thumb, the adopted value of  $\text{MRC} = 10\%$  gives the following threshold relationship for target identification with spatial frequency  $f$ :

$$\text{MTF}(f) \cdot \text{SNR} > 10. \quad (11)$$

Two different kind of input images have been used for the simulations: a surface reflectance image, based on the

IKONOS panchromatic camera at  $\sim 1$  m spatial sampling and a bar synthetic image at a spatial sampling of 0.5 m.

In Figure 7 a comparison between simulations of the Hypseo panchromatic image, obtained from the IKONOS image, at different spatial sampling intervals and different Hypseo pupil diameters is shown for the low radiance case (case “B” in Table 4). The product  $\text{MTF}(f) \cdot \text{SNR}$  has been calculated and the results are displayed in Table 5. The simulation with a high pupil diameter of 300 mm (case (b) in Table 5) is better from image quality point of view (lower GSD, high  $\text{SNR} \cdot \text{MTF}$ , and optimum targets discrimination in Figure 7(b)) but it has a large impact on instrument sizing. All other images are strongly affected from diffraction, due to the pupil size of 150 mm, but the case with 5 m of GSD (case (d) in Table 5) seems better for  $\text{SNR} \cdot \text{MTF}$  parameter and targets discrimination (in case (a) and (c) of Figure 7 the instrument noise overlays all other possible image features).

Another simulation with synthetic bars has been done to verify the previous results, by changing the sampling and the illumination conditions avoiding any possible effect coming from the degraded characteristics of the IKONOS image quality. In Figure 8 an HypSEO PAN simulation, from a synthetic bar image, at different spatial resolution (GSD) and pupil diameter ( $D$ ) is shown for a high (case “A”) and a low (case “B”) radiance case, with parameters represented in

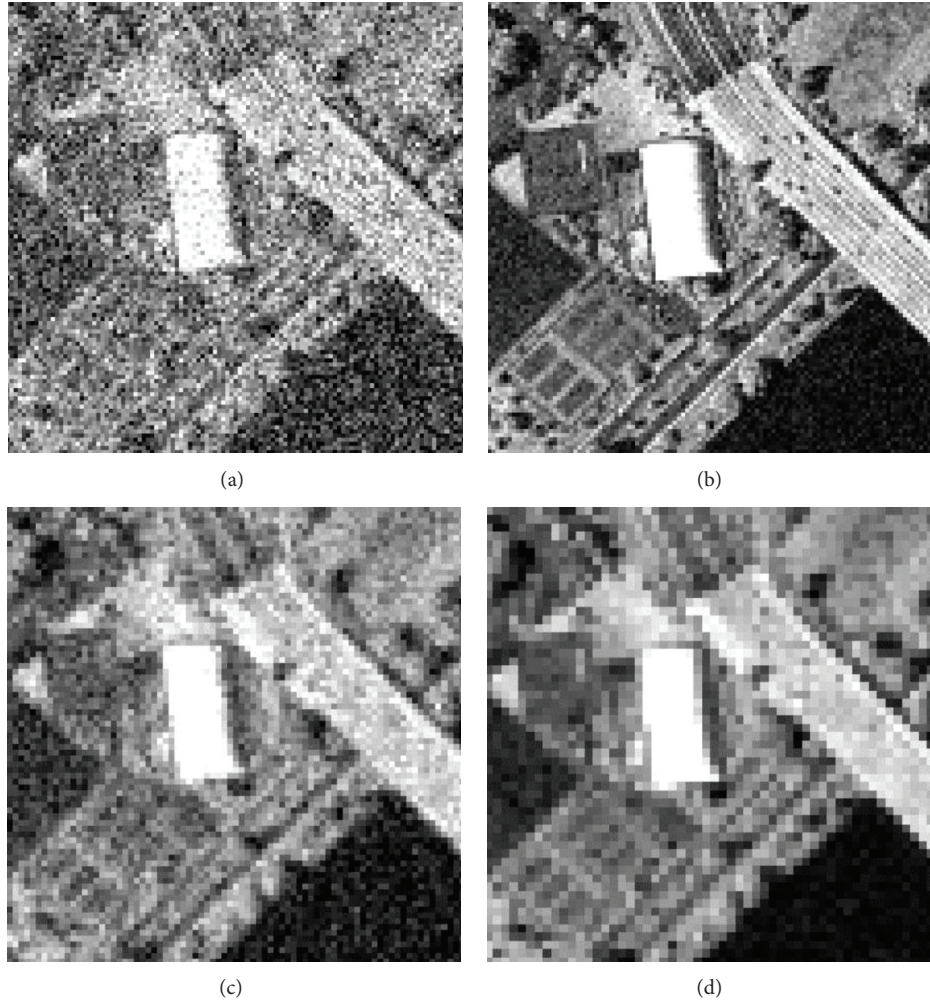


FIGURE 7: Simulated HypSEO Pan images (from IKONOS) for low TOA radiance ( $18 \text{ W} \cdot \text{m}^{-2} \cdot \text{sr}^{-1} \cdot \mu\text{m}^{-1}$  at albedo = 0.27, case “B” in Table 4), different spatial sampling (GSD) and pupil diameter ( $D$ ): (a) GSD = 2.5 m,  $D = 150$  mm (SNR = 11,  $\text{MTF}(f_{\text{Nyquist}}) = 0.09$ ); (b) GSD = 2.5 m,  $D = 300$  mm (SNR = 32,  $\text{MTF}(f_{\text{Nyquist}}) = 0.18$ ); (c) GSD = 3.5 m,  $D = 150$  mm (SNR = 27,  $\text{MTF}(f_{\text{Nyquist}}) = 0.17$ ); (d) GSD = 5 m,  $D = 150$  mm (SNR = 50,  $\text{MTF}(f_{\text{Nyquist}}) = 0.22$ ).

TABLE 4: Illumination/atmospheric parameters used in the Hypseo PAN camera simulations.

	Atmosphere	Visibility	Day	Hour	Lat.	Long.	Sun Zenith Angle (SZA)	Altitude
Case A	Midlatitude summer	Rural VIS 23 Km	174	10:00 a.m.	45°	0°	32°	620 Km
Case B	Midlatitude winter	Urban VIS 5 Km	355	10:00 a.m.	45°	0°	72°	620 Km

TABLE 5: Image quality parameters related to the simulations of Figure 7 with low illumination radiance (Case B in Table 4). The diffraction limit represents the Airy radius ( $\lambda = 1 \mu\text{m}$ ,  $H = 620$  Km) of Rayleigh criterion. Case (b) is better respect to case (d) because  $\text{SNR} \cdot \text{MTF}$  is related to a signal with lower Nyquist period.

Case	GSD	Pupil diameter	On ground diffraction limit	Nyquist period	$\text{SNR} \cdot \text{MTF}_{\text{Nyquist}}$	Image quality evaluation
(a)	2.5 m	150 mm	5.0 m	5 m	1	Low
(b)	2.5 m	300 mm	2.5 m	5 m	5.8	High
(c)	3.5 m	150 mm	5.0 m	7 m	4.6	Sufficient
(d)	5.0 m	150 mm	5.0 m	10 m	11	Sufficient

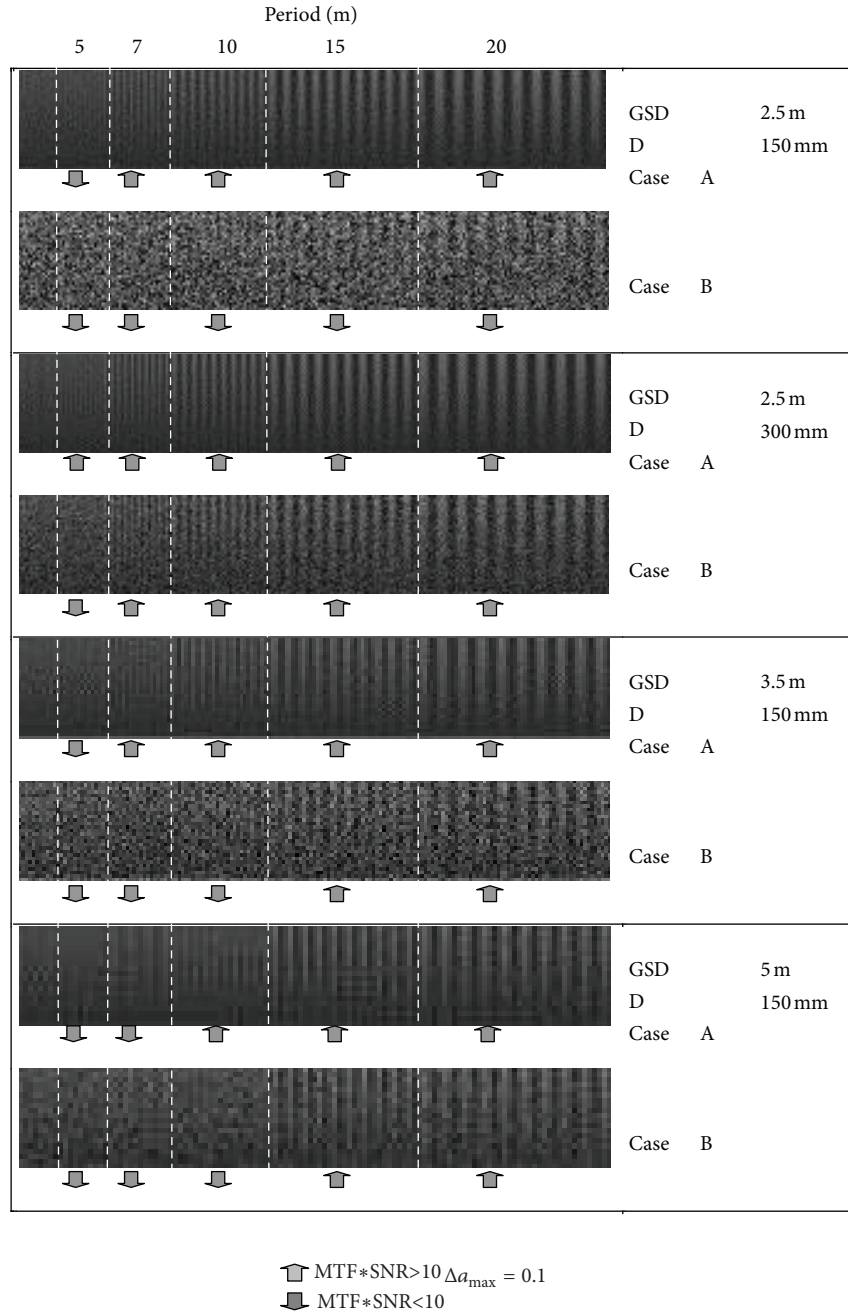


FIGURE 8: HypSEO PAN simulation (from synthetic bar image) at different spatial resolution (GSD), pupil diameter ( $D$ ), and illumination conditions (high radiance case “A” and low radiance case “B” in Table 4); the contrast along the vertical axis changes between 10% and 20%; the up and down arrows indicate the periods for which the criterion ( $SNR \cdot MTF > 10$ ) is satisfied or not.

Table 4. The input synthetic image in the horizontal direction is composed by 5 sequences of grey-black bars, each consisting of 10 cycles at fixed period (5, 7, 10, 15, and 20 m). In the vertical direction the albedo range of grey bars is between 10% and 20%, whereas the albedo of black bars is constant (10%). The up and down arrows in Figure 8 indicate the periods for which the criterion  $MTF(f) \cdot SNR > 10$  is satisfied or not.

The radiance ( $L$ ), the Signal to Noise Ratio (SNR), and the Modulation Transfer Function (MTF) values corresponding

to the extreme simulated albedo values are represented in Table 6 while the product  $MTF(f) \cdot SNR$  has been reported in Table 7.

The results confirm that image quality as defined from this kind of metric is improved by increasing pupil diameter (from 150 to 300 mm) at equal spatial sampling (GSD = 2.5 m), because of an increased SNR and a reduced diffraction effect on MTF. The image quality is also improved as spatial sampling decreases from 2.5 to 3.5 m (pupil diameter = 150 mm) because of an increased SNR.

TABLE 6: Radiance, SNR, and across-track MTF values corresponding to the extreme simulated albedo values, calculated for different ground spatial sampling (GSD), pupil diameter ( $D$ ) and the two simulation conditions reported in Table 4.

Simulation scenario			SNR at L at $a = 0.09$		SNR at L at $a = 0.20$		MTF across-track at period (m)				
Case/SZA	GSD (m)	$D$ (mm)	$L$ ( $W/m^2/sr/\mu m$ )	SNR	$L$ ( $W/m^2/sr/\mu m$ )	SNR	5	7	10	15	20
A/32°	2.5	150	40.0	22.5	73.4	37.7	0.09	0.26	0.46	0.65	0.74
B/72°			14.5	8.8	16.7	10.1					
A/32°	2.5	300	40.0	69.1	73.4	104.9	0.18	0.38	0.57	0.75	0.81
B/72°			14.5	31.0	16.7	34.9					
A/32°	3.5	150	40.0	52.0	71.5	79.8	0.04	0.17	0.37	0.58	0.68
B/72°			14.5	22.3	16.6	25.1					
A/32°	5	150	40.0	110.8	71.6	158.9	0.001	0.06	0.22	0.45	0.61
B/72°			14.5	54.0	16.6	60.0					

TABLE 7: Image quality parameter (SNR\*MTF) calculated at low and high illumination radiance (Table 4), 20% of on ground albedo and different spatial periods of Figure 8. The diffraction limit represents the Airy radius of Rayleigh criterion. Values with SNR\*MTF > 10 are bold.

Illumination	GSD	Pupil diameter	On ground diffraction limit	SNR*MTF at $r = 0.2$ at spatial period					Quality evaluation
				5 m	7 m	10 m	15 m	20 m	
High	2.5 m	150 mm	5.0 m	3.4	9.8	<b>17.3</b>	<b>24.5</b>	<b>27.9</b>	Low
Low				1.0	2.6	4.6	6.6	7.5	
High	2.5 m	300 mm	2.5 m	<b>18.9</b>	<b>39.9</b>	<b>59.8</b>	<b>78.7</b>	<b>85.0</b>	High
Low				6.3	<b>13.3</b>	<b>19.9</b>	<b>26.2</b>	<b>28.3</b>	
High	3.5 m	150 mm	5.0 m	3.2	<b>13.6</b>	<b>29.5</b>	<b>46.3</b>	<b>54.3</b>	Suff.
Low				1.0	4.3	9.3	<b>14.6</b>	<b>17.1</b>	
High	5.0 m	150 mm	5.0 m	0.2	9.5	<b>34.9</b>	<b>71.5</b>	<b>96.9</b>	Suff.
Low				0.1	3.6	<b>13.2</b>	<b>27.9</b>	<b>36.6</b>	

TABLE 8: Main parameters for Modtran simulations.

Latitude	44°
Longitude	11.4°
Time	10.6
Day	23/9/09
Atmospheric model	Midlatitude summer
Aerosol model	Rural
Vis	23 Km
Water Vapour	0.4 (standard)
Ground elevation	0.25 Km
Scattering model	Scaled DISORT 4 streams
CO <sub>2</sub>	390 ppm
Airplane altitude	1 Km

The HypSEO PAN nominal case Ground Spatial Sampling (GSD) of 5 m and pupil diameter ( $D$ ) of 150 mm seems a good compromise in terms of image quality with respect to the others, because the simulation results are not so different with respect to the case with GSD = 3.5 m ( $D = 150$  mm) (SNR\*MTF is higher for low radiance case) and from an instrument design point of view it appears more feasible with respect to the best case with GSD = 2.5 m ( $D = 300$  mm).

For PAN nominal case the above MTF( $f$ ) · SNR criterion is satisfied only for periods larger than the Nyquist period of 10 m at high radiances, but some oscillations affected by aliasing can also be observed at low periods as 7 m.

Finally an example of simulated Hypseo PAN image (GSD = 5 m,  $D = 150$  mm) obtained from airborne high resolution MIVIS data in a forest environment has been performed (Figure 9(c)) to the scope of testing image fusion methods based on the sharpening of hyperspectral image by means of panchromatic observations [22].

**3.3. Satellite Hyperspectral Land Use Classification.** Another important use of the simulator has regarded the demonstration of potential applications of the HYPSEO SG spaceborne hyperspectral camera.

A simulation of the HYPSEO SG space-borne hyperspectral camera was performed by using as input the airborne MIVIS reflectance images acquired on a Tuscany (I) test site (S. Rossore Park and Arno River mouth) at 2.5 m spatial resolution [23]. The instrumental parameters are reported in Table 3 [24].

A MIVIS reflectance image is transformed into the satellite HYPSEO radiance (Figure 9) ( $H = 620$  Km) by using the atmospheric model parameters of Table 4. Then the HYPSEO radiance image is obtained by means of a spectral resampling of the MIVIS image to the 210 spectral

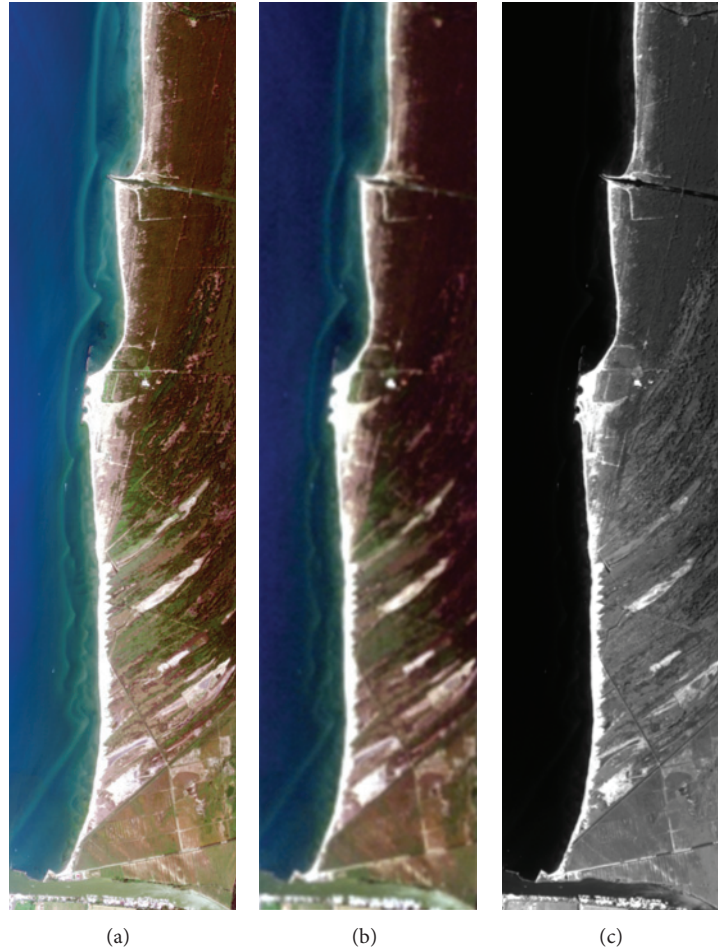


FIGURE 9: Airborne and simulated space-borne image on S. Rossore Park (I) test site: (a) MIVIS airborne reflectance (2.5 m), used as input; (b) simulated hyper-spectral HYPSEO radiance (20 m); (c) simulated PAN HYPSEO radiance (5 m) image.

bands of Hypseo, with a Gaussian Instrument Chromatic Response (with FWHM = 10 nm) and a spatial resampling to the HYPSEO spatial sampling interval of 20 m by using the simulated spatial response, and adding the noise by means of parameters coming from the HYPSEO radiometric model. Moreover an HYPSEO reflectance image has been obtained after removal of atmospheric effects introduced by MODTRAN code (Table 4).

A land use classification map based on the Spectral Angle Mapper (SAM) algorithm [25] from the HYPSEO simulated reflectance image is shown in Figure 10. The confusion matrix shows a good correlation between classified and ground truth data, compared with multispectral sensors [23], confirming the instrument capabilities for this kind of application.

**3.4. Target “Camouflage” in Rural Background.** The dual use capability for targets discrimination with camouflage panels embedded in vegetation has been evaluated during the testing phase of the SIMGA airborne hyperspectral instrument. To this scope some simulations was done during the SIMGA project phase. The simulated instrument SIMGA reflectance images been obtained by using the MODTRAN code in

a standard atmospheric condition (Table 8), the measured instrument spatial response (Figures 6(a) and 6(b) and Tables 2(a) and 2(b)) and the instrument noise [16]. In Figure 11 a SIMGA reflectance image of simulated green panels over vegetation after FLAASH inversion algorithm is shown. The result of simulation showed that green panels were clearly distinguished respect to vegetation, because of their higher reflectance in the SWIR bands (1.2 and 1.6 micron), so validating the utility of the hyperspectral sensor for this kind of application. Moreover a validation of the simulation was obtained during an airborne campaign performed in S. Rossore park (Tuscany, I), where different green panels were placed over green grass. In Figure 12 the green panels are clearly distinguished in the SWIR bands while the contrast in VIS bands is negligible.

**3.5. Underwater Submerged Targets.** Another dual use capability regarding the discrimination of underwater submerged targets was tested by means of SIMGA image simulations and verified with overflights in a controlled zone.

In order to test the detection capabilities of small grey panels under water a direct bathymetric model has been

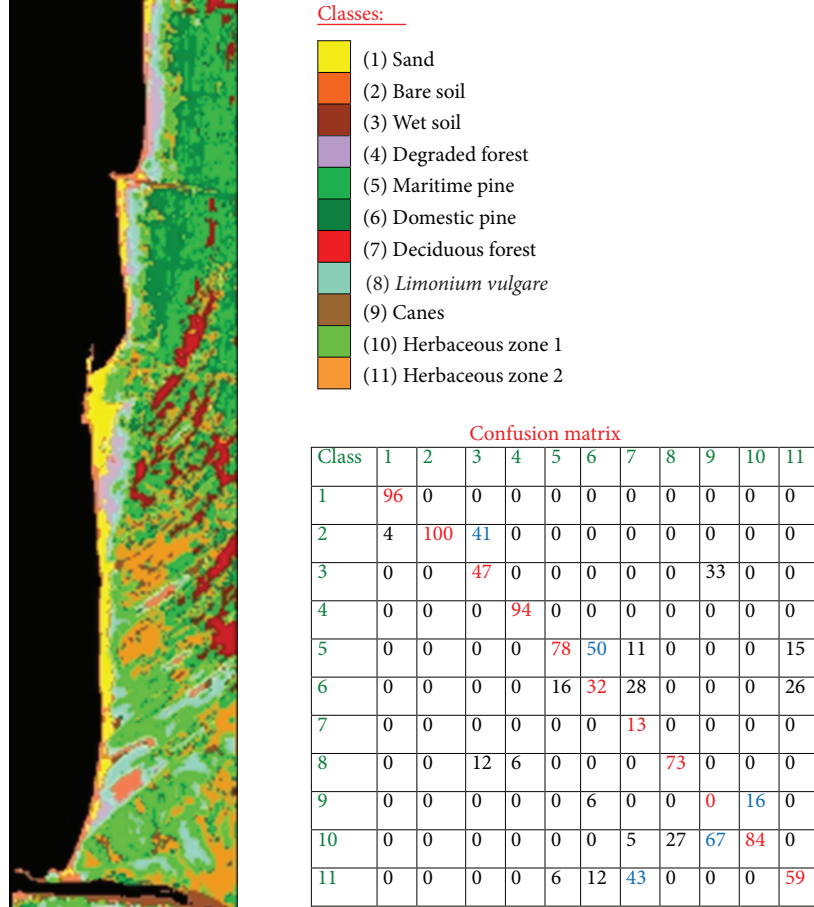


FIGURE 10: Example of forest SAM classification map of S. Rossore test site (Italy) based on simulated Hypseo hyper-spectral image (20 m). Confusion matrix shows a good correlation between classified and ground truth data.

developed to simulate the total reflectance of shallow waters on the basis of chlorophyll, sediment, and yellow substance content, the bottom and panel reflectance and the water depth height.

The total reflectance (Figure 13)  $R(\lambda)$  has been calculated by means of the surface  $R_{\text{surface}}(\lambda)$  and subsurface  $R_{\text{sub-surface}}(\lambda)$  reflectance with the following relationship [26]:

$$R(\lambda) = R_{\text{surface}}(\lambda) + R_{\text{sub-surface}}(\lambda) * \left[ \frac{1 - \rho_F(\vartheta')}{n^2} \right], \quad (12)$$

With

- (i)  $\rho(\theta')$  the Fresnel reflectivity at the interface air-water which takes into account the reflection of the subsurface radiance into the water ( $\sim 0.021$ ),
- (ii)  $\theta'$  is the incident angle of the radiation coming from below the water which generates a refraction in air at the angle  $\theta$  in the observation direction [ $n * \sin(\theta') = \sin(\theta)$  with  $n = 1.8368$  the water refraction index],
- (iii)  $R_{\text{surface}}$  reflectance depends from surface roughness and foam, but in this analysis has been taken constant and equal in first approximation to 0.021.

The subsurface reflectance is obtained by means of a two-flux algorithm (Figure 13) which yields the following analytical relationship [27] for a water layer of uniform optical properties and thickness  $H$  (m), above a reflecting bottom with reflectance  $\rho_{\text{bottom}}$ :

$$R(\lambda) = R^0(\lambda) + \left[ \frac{(\rho_{\text{bottom}}(\lambda) - R^0(\lambda)) \cdot (1 - R^0(\lambda)^2)}{R^0(\lambda) \cdot (\rho_{\text{bottom}}(\lambda) - R^0(\lambda)) + (1 - R^0(\lambda)) \rho_{\text{bottom}}(\lambda)} \cdot e^{2H \cdot \sqrt{(A(\lambda)^2 + 2A(\lambda)B(\lambda))}} \right], \quad (13)$$

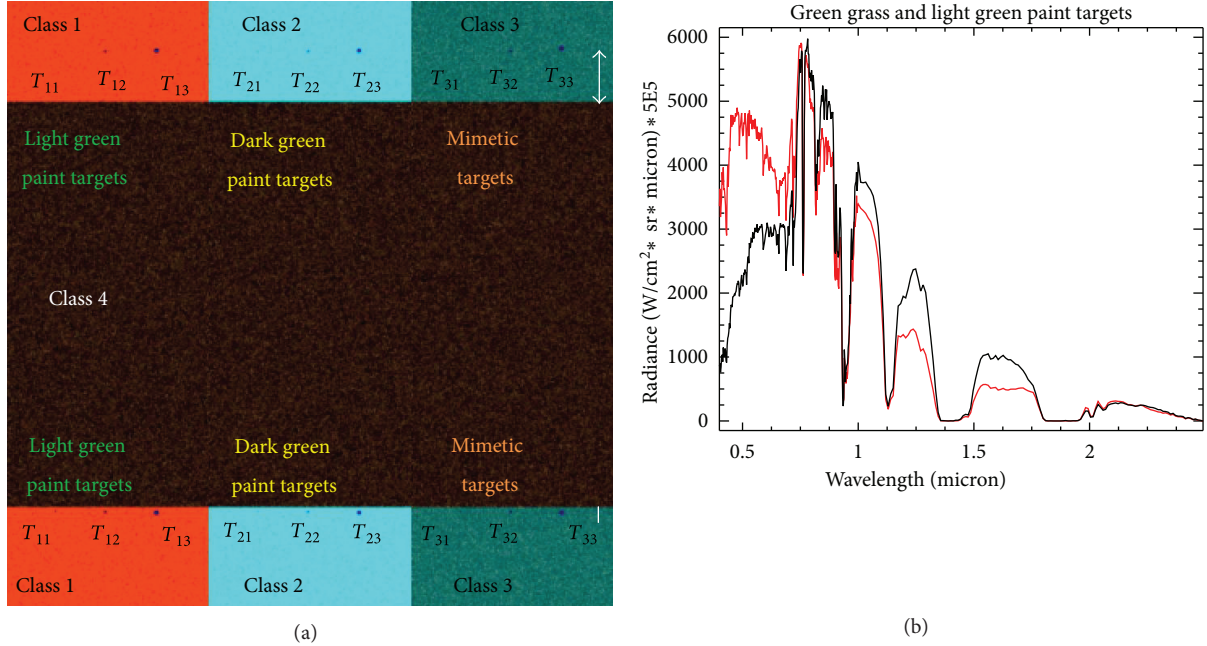


FIGURE 11: Simulated false color SIMGA radiance image (SWIR bands) of green panels over vegetation (a). The scenario has a dimension of  $740 \times 740 \text{ m}^2$  and it is composed of 4 classes of background scenario: class 1 = green grass, class 2 = bare soil, class 3 = linear mixing of green grass (1/3), dry grass (1/3), and bare soil (1/3); class 4 = pinewood [linear mixing of green (1/2) and dry (1/2) needles]. 18 targets are used grouping in three different sizes ( $T_1 = 1 \times 1 \text{ m}^2$ ,  $T_2 = 2 \times 2 \text{ m}^2$ , and  $T_3 = 4 \times 4 \text{ m}^2$ ) and three different types (light green paint, dark green paint, and mimetic paint). Mimetic paint is composed of 1/3 light green paint, 1/3 dark green paint, and 1/3 light grey paint. The same type and size of targets are disposed in the upper and in the lower part of the figure at different distances (resp., 40 m and 4 m) respect to the class 4 scenario. Green panels are clearly distinguished as little dark points respect to vegetation, because of their lower radiance in the SWIR bands (at 1.25 and 1.6 micron). Comparison between green grass (upper black curve in the SWIR bands) and light green paint panel (lower red curve in the SWIR bands) (b).

where

$$(i) R^0(\lambda) = B(\lambda) / (A(\lambda) + B(\lambda) + \sqrt{A(\lambda)^2 + 2A(\lambda)B(\lambda)}),$$

(ii)  $A(\lambda)$  and  $B(\lambda)$  represent, respectively, the total absorption and scattering coefficients, including that of water, chlorophyll, and yellow substance,

(iii) the range of validity is  $B/(A + B) \leq 0.6$ .

The total absorption and backscattering coefficients are calculated from a three component water colour model ([28, 29]), which has been adapted for class 1 and class 2 waters [30].

In this model the total absorption and backscattering coefficients ( $\text{m}^{-1}$ ) are obtained as a linear combination of that of water, chlorophyll, sediment, and yellow substance with the following relationships:

$$\begin{aligned} B(\lambda) &= 0.5 \cdot B_w(\lambda) + 0.005 \cdot B_c(\lambda) + 0.015 \cdot B_s(\lambda), \\ A(\lambda) &= A_w(\lambda) + a_c(\lambda) \cdot C + a_s(\lambda) \cdot S + A_Y(\lambda), \end{aligned} \quad (14)$$

where

(i) the suffix  $w, c, s, Y$  means, respectively, water, chlorophyll, sediment, and yellow substance,

(ii)  $C, S,$  and  $Y$  represent the chlorophyll, sediment, and yellow substance content ( $C$  in  $\text{mg}/\text{m}^3$ ,  $S,$  and  $Y$  in  $\text{g}/\text{m}^3$ ),

(iii)  $a_c, a_s, a_Y,$  respectively, the chlorophyll, sediment and yellow substance specific absorption coefficients ( $\text{m}^2/\text{mg}$  and  $\text{m}^2/\text{g}$ , resp.) shown in Figure 14 [30]

$$(iv) B_w(\lambda) = 0.002 \text{ m}^{-1} (\lambda(\text{nm})/550)^{-4.3},$$

$$(v) B_s(\lambda) = 1 (\text{m}^2/\text{mg}) * S (\text{g}/\text{m}^3) * [(\lambda(\text{nm})/550)^{-1}],$$

$$(vi) B_c(\lambda) = 0.12 C^{0.63} [a_c(550)/a_c(\lambda)] (\text{m}^{-1}),$$

$$(vii) a_c(550) = 0.0189 \text{ m}^2/\text{mg} \text{ if } C < 1 \text{ mg}/\text{m}^3,$$

$$(viii) a_c(550) = 0.00486 \text{ m}^2/\text{mg} \text{ if } C > 1 \text{ mg}/\text{m}^3,$$

$$(ix) A_Y(\lambda) = A_Y(443 \text{ nm}) * \exp[-0.014 * (\lambda(\text{nm}) - 443)] (\text{m}^{-1}),$$

$$(x) A_Y(443 \text{ nm}) = (0.12 \text{ m}^{-1}) * Y,$$

$$(xi) a_s(443 \text{ nm}) = 0.034 \text{ m}^2/\text{g},$$

$$(xii) a_c(443 \text{ nm}) = 0.07 \text{ m}^2/\text{mg} \text{ if } C < 1 \text{ mg}/\text{m}^3,$$

$$(xiii) a_c(443 \text{ nm}) = 0.018 \text{ m}^2/\text{mg} \text{ if } C > 1 \text{ mg}/\text{m}^3.$$

The concentration of the three water components can be divided in

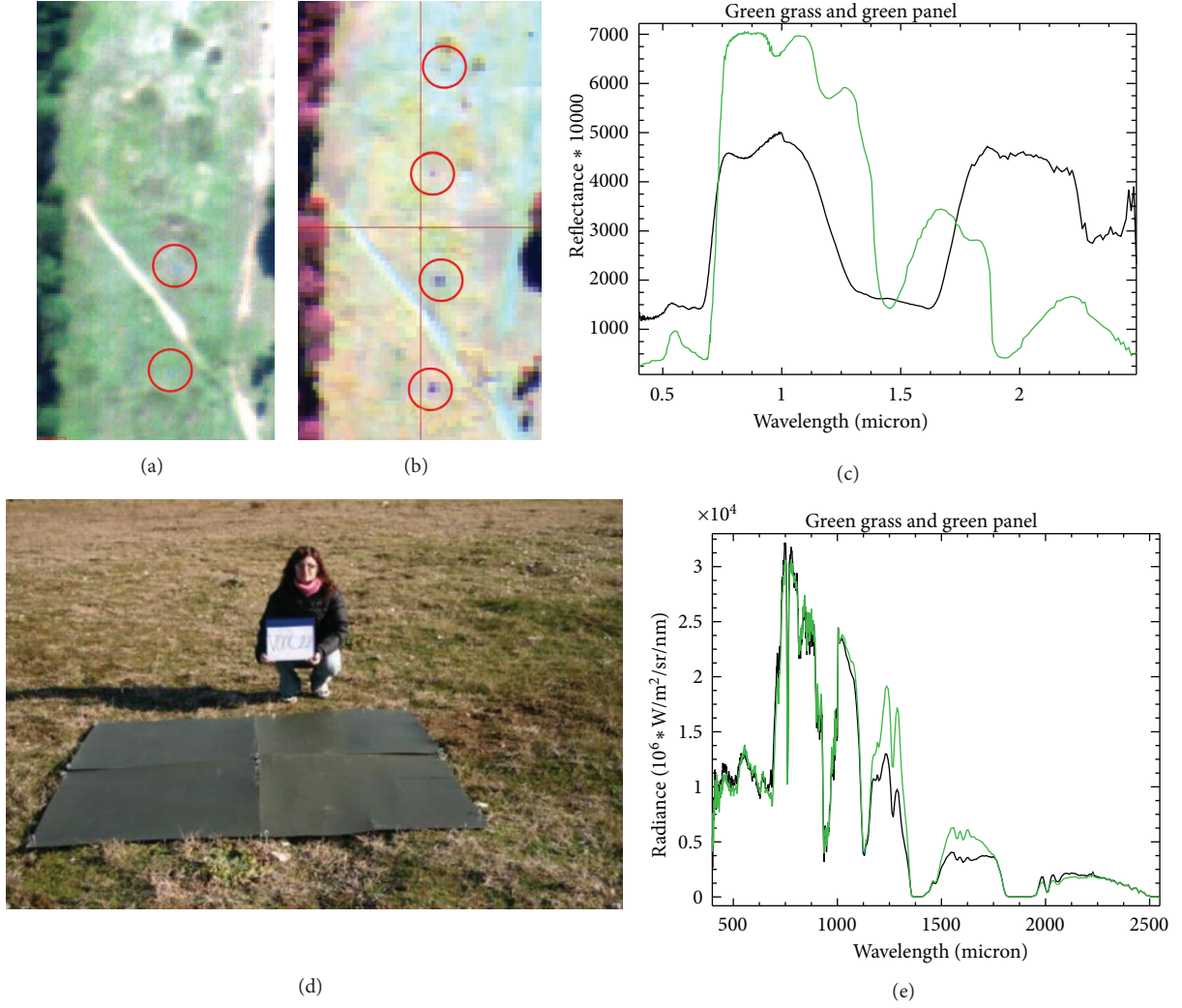


FIGURE 12: SIMGA false colour radiance images on panels over vegetation (S. Rossore park): VNIR false colour (a), SWIR false colour (b). Comparison between reflectance of green panel (lower black curve at 1.6 micron) and green grass (upper green curve at 1.6 micron) (c), photo of green panel over grass (d), and comparison between SIMGA radiance acquired on green grass (upper green curve at 1.6 micron) and green panel (lower black curve at 1.6 micron) (e). Panels are clearly distinguished in the SWIR bands, while the contrast respect to vegetation in VIS bands is negligible.

- (i) completely correlated type 1 waters characterised by a rather stable correlation between optically active substances, with phytoplankton concentration as dominant, in this case the yellow substance backscattering and sediment absorption coefficients has been considered as related to the chlorophyll with the following relationships [12, 29]:

$$B_s(550 \text{ nm}) = 0.2 \cdot C^{0.63} \cdot \text{m}^{-1},$$

$$A_Y(443 \text{ nm}) = \frac{0.2}{0.8} [A_w(443 \text{ nm}) + a_c(443 \text{ nm}) \cdot C + a_s(443 \text{ nm}) \cdot S],$$

$$S(\text{g/m}^3) = \left[ \frac{10^{-0.25}}{2} \right] \cdot C^{0.57} (\text{mg/m}^3), \quad (15)$$

- (ii) completely uncorrelated coastal type 2 waters, with no correlation between the three water components, when high concentration of sediments and yellow substances exist,
- (iii) partially correlated coastal type 2 waters for which it is possible to retrieve a partial correlation between the three water components [30]. Examples are given by the following relationships:

- (1) Gulf of Naples [31]

$$\begin{aligned} \text{Log}(S) &= -0.25 + 0.57 \cdot \text{Log}(C) \\ \text{Log}(A_Y(440)) &= -1.20 + 0.47 \cdot \text{Log}(C), \end{aligned} \quad (16)$$

- (2) Northern basin of the Adriatic Sea [32]

$$\begin{aligned} \text{Log}(S) &= -0.026 + 0.59 \cdot \text{Log}(C) \\ \text{Log}(A_Y(440)) &= -1.28 + 0.38 \cdot \text{Log}(C), \end{aligned} \quad (17)$$

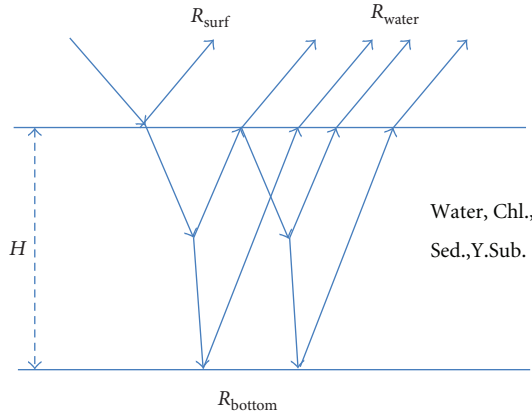


FIGURE 13: Two fluxes direct bathymetry reflectance model ( $R_{surf}$  = surface reflectance due to roughness and foam,  $R_{bulk}$  = Sub-surface water reflectance due to particulate concentration  $C$  = Chlorophyll,  $S$  = sediment,  $Y$  = yellow substance, and  $R_{bottom}$  = reflectance of bottom).

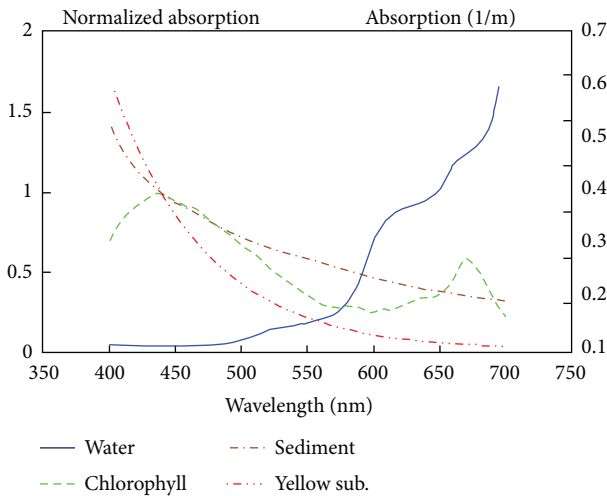


FIGURE 14: Specific absorption spectra of chlorophyll a, suspended sediment, and yellow substance normalized to the value at the 440 nm wavelength (left scale). Absorption spectrum of water is in  $m^{-1}$  (right scale) [12].

(3) Tirrenian Sea near Migliarino-S. Rossore (Tuscany) [33]

$$\text{Log}(C) = \text{Log}(0.0206) + 2.0615 \cdot \text{Log}(S), \quad (18)$$

A reflectance simulation of S. Rossore waters at 1 m of bottom depth obtained by means of the two flux model is displayed in Figure 15. The Total Reflectance represents simulations of correlated waters type 2 model ( $C = 3 \text{ mg/m}^3$ ,  $S = 1.8 \text{ g/m}^3$ ,  $Y = 0.6 \text{ g/m}^3$ ), with the S. Rossore (I) bottom sand and grey panels reflectance measurements performed with a Field Spec portable spectrometer.

Finally simulated SIMGA radiance and radiance images of a marine environment (sand, waters with sand bottom at 2 m and 8 m of depths, panels of  $1 \text{ m} \times 1 \text{ m}$  and  $2 \text{ m} \times 2 \text{ m}$  under water at 1 m and 0.2 m of depth) have been performed

(Figure 16). SIMGA radiance has been simulated at 1.5 km airborne altitude with MODTRAN code and at the SIMGA spatial (1 m for VIS and 2 m for SWIR bands) and spectral resolution (2.4 nm for VIS and 10.8 nm for SWIR). The simulated SIMGA reflectance image has been obtained through the inversion of MODTRAN parameters used for the direct simulation and results show that all grey panels (both at 0.2 m or 1 m depth) can be clearly distinguished both in low (2 m) and high (8 m) depth waters (Figure 16).

This result was validated (Figure 17) by means of SIMGA overflights on the Morto mouth river (S. Rossore park in Tuscany, I), where two different grey panels were submerged. The two panels are clearly detectable in the visible part of the spectrum, so demonstrating the capability of the SIMGA hyperspectral instrument for this kind of application.

#### 4. Conclusions

An end-to-end software tool (SG\_SIM) for the simulation of airborne/satellite optical sensors images has been implemented in ENVI-IDL environment. Input images can be either high resolution airborne or synthetic data. The simulator features three separate modules: the reflectance scenario, which generates a desired reflectance image with spectral mixtures, the atmosphere module, which converts the input reflectance map into the at-sensor radiance image, and the instrument module, which simulates the main degradations introduced by the instrument (ISR, MTF, ICR and noise). As other end-to-end simulators the SG\_SIM Simulator integrates a complete atmospheric radiative transfer modelling which could easily refined through the implementation of most MODTRAN options and it includes all main functions and features necessary for a complete hyperspectral image simulation such as ISR&MTF, ICR and noise sources. Compared to the other simulators (e.g., SENSOR, [4]), SG\_SIM allows also the control of spectral mixing and the generation of synthetic scenario, but is lacking of MWIR/LWIR spectral bands, 3D reflectance simulation, and DEM ray-tracing functions as included in CAMEO [5]. The implementation and further development of the SG\_SIM approach was boosted significantly by the Selex Galileo S.p.A. airborne imaging system SIMGA and by other phase 0/A studies carried out for preliminary evaluations of image quality and product accuracy from new classes of space-borne optical sensors. The validation of the simulator is reported in [16], whereas in this paper the simulator's theoretical basis and some simulation examples have been described. For the simulated cases the following results can be outlined:

- (i) the 3D representation of the SRF allows the visual inspection of the spatial pixel response for image quality analysis,
- (ii) the potentials of the simulator for the HYPSEO Pan-chromatic camera trade-off analysis between project parameters (pupil diameter, optics degradations, detector noise, etc.) and system performances (SNR, spatial resolution, etc.) have been demonstrated by

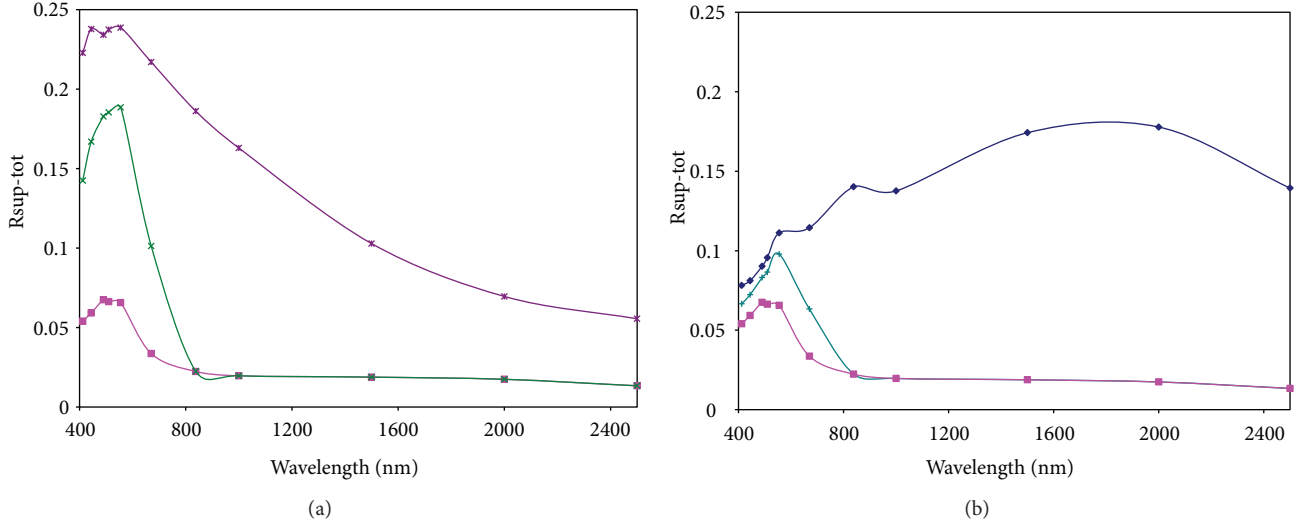


FIGURE 15: Total Reflectance curves (green curves in the middle part of Figures 15(a) and 15(b)) from the two fluxes direct bathymetry reflectance model obtained from simulations with different type of S. Rossore bottom targets: grey panel (upper maroon part of Figure 15(a) (a) sand (upper blue part of Figure 15(b)) (b). The simulation is performed at a bottom depth ( $H$ ) of 1 m with partially correlated waters type 2 model ( $C = 3 \text{ mg/m}^3$ ,  $S = 1.8 \text{ g/m}^3$ ,  $Y = 0.6 \text{ g/m}^3$ ) (lower pink reflectance curves in Figures 15(a) and 15(b)).

- using as inputs synthetic bars and an IKONOS images with different radiance and surface albedo levels,
- (iii) the potentials of the HYPSEO hyperspectral camera for vegetation mapping has been demonstrated on the basis of a MIVIS airborne scene rescaled at satellite level and ground truth data,
- (iv) the potentials for detection of camouflaged targets in a rural background has been demonstrated in the SWIR bands by means of a simulation of a synthetic scenario with green panels at different size,
- (v) the potentials for the identification of submerged targets in the visible spectral range at airborne level (1 m of spatial resolution) have been demonstrated by means of the simulation of a synthetic scenario with submerged grey panels and the implementation of a direct bathymetric-water color model to generate surface reflectance as input to the scene simulator,
- (vi) real airborne data on submerged and camouflaged targets have confirmed the results from simulations performed before the flight campaign,

These results demonstrate the potentials of the proposed simplified end-to-end simulator as a preliminary aid tool (during phase 0/A) for the dimensioning of new optical instruments to trace the link between user and instrument requirements.

## 5. Annex

The formulation of the following MTF components implemented in the SG\_SIM model are described in the following paragraphs:

- (i) Detector pixel size

- (ii) Detector cross talk
- (iii) CCD detector charge transfer
- (iv) Image motion during integration time
- (v) Electronic filtering
- (vi) Focal plane random jitter during integration time
- (vii) Optics diffraction and aberrations.

**5.1. Detector Pixel Size.** The finite size of detector pixel permits the spatial integration of the signal coming from a finite spatial region on ground and this introduces a sort of degradation of the original high resolution image. This effect is analogous to a spatial filter windowing with a rect function which is 1 within a certain spatial rectangular domain and 0 outside:

$$\text{PSF}_{\text{pixel}}(x, y) = \text{rect}(\Delta x, \Delta y) = \text{rect}_x(\Delta x) \cdot \text{rect}_y(\Delta y). \quad (19)$$

The transfer function of this function obtained by its Fourier Transform is represented with the following relationship:

$$\text{MTF}_{\text{pixel}}(k_x, k_y) = \text{sinc}_x(\pi \cdot k_x \cdot \Delta x) \cdot \text{sinc}_y(\pi \cdot k_y \cdot \Delta y), \quad (20)$$

where

- (i)  $k_x, k_y$  are the spatial frequencies along the  $x$  and  $y$  direction,
- (ii)  $\Delta x, \Delta y$  are the detector size along  $x$  and  $y$  directions,

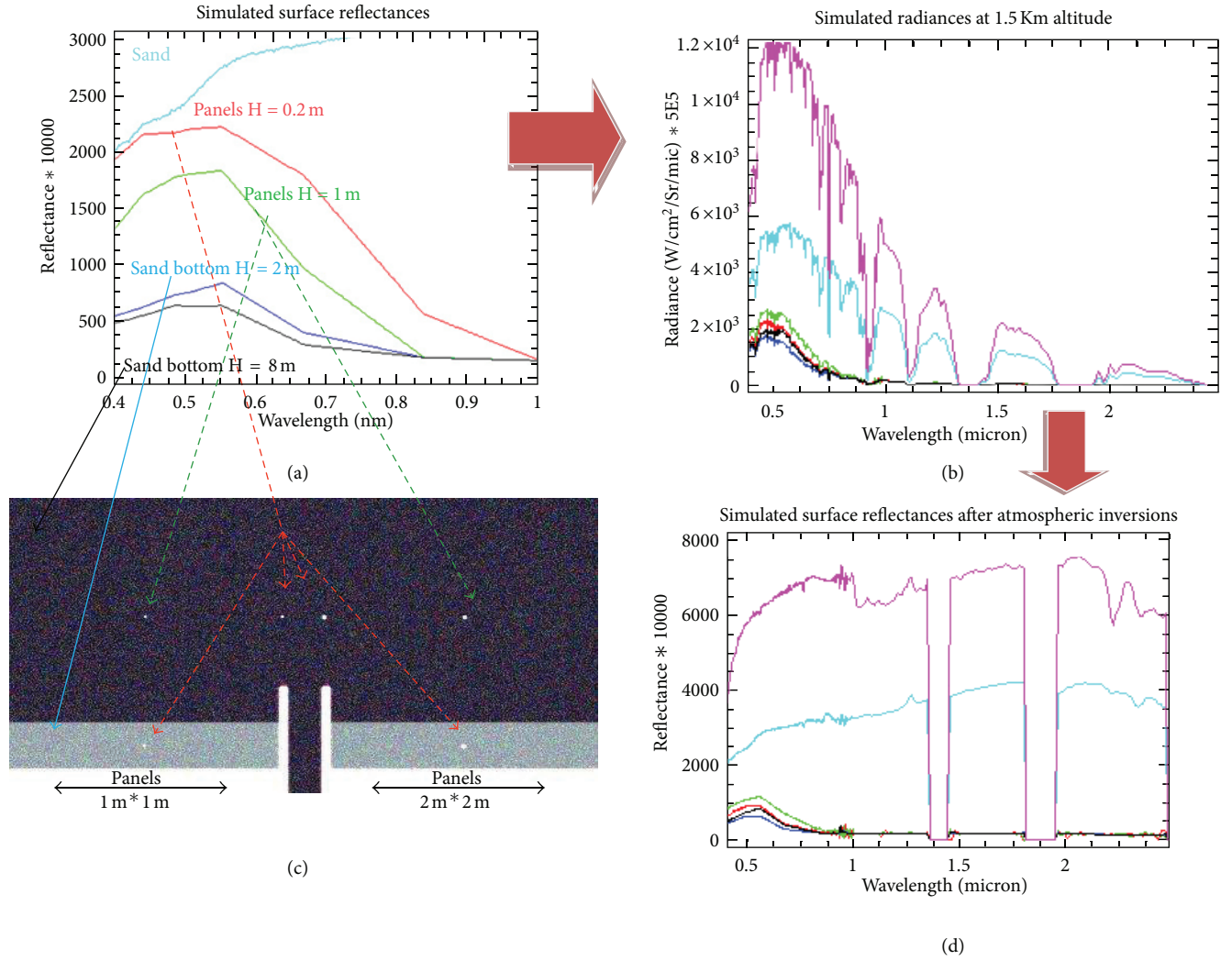


FIGURE 16: Simulated radiance/reflectance image of marine environment (sand, waters with sand bottom at 2 m & 8 m depths, panels of 1 m \* 1 m & 2 m \* 2 m under water at 2 m & 0.2 m depth, chlorophyll of 3 mg/m<sup>3</sup>, sediment of 1.8 g/m<sup>3</sup>, and yellow substance of 0.6 g/m<sup>3</sup>) obtained with SIMGA model at 1.5 km altitude (spatial resolution 1 m VIS, 2 m SWIR, spectral resolution 2.4 nm VIS, 10.8 nm SWIR). Simulated synthetic reflectance (waters with sand bottom at 2 m or 8 m of depth, panels under water at 0.2 m and 1 m of depth, beach surface sand) from two-fluxes model (a), radiances at 1.5 Km altitude (b), surface reflectance (also beach sand and concrete pier are represented in the upper part of Figures 16(b) and 16(d)) after atmospheric inversion algorithm based on Modtran code with the same parameters as the direct simulation (d), and RGB synthetic radiance image representing the simulated scenario (c).

(iii) the sinc functions are expressed from the following relationships:

$$\begin{aligned} \sin c_x(\pi \cdot k_x \cdot \Delta x) &= \frac{\sin(\pi \cdot k_x \cdot \Delta x)}{(\pi \cdot k_x \cdot \Delta x)}, \\ \sin c_y(\pi \cdot k_y \cdot \Delta y) &= \frac{\sin(\pi \cdot k_y \cdot \Delta y)}{(\pi \cdot k_y \cdot \Delta y)}. \end{aligned} \quad (21)$$

**5.2. Detector Cross Talk.** The detector cross talk between two successive pixels is taken into account as a first approximation by assuming a trapezoidal spatial windowing filter, instead of a rectangular one, which can be obtained by means of a convolution between two rect functions, one representing the detector size ( $\Delta x, \Delta y$ ) and the other representing the

cross talk size ( $\delta x, \delta y$ ) between two successive pixels ( $\delta x < \Delta x, \delta y < \Delta y$ ):

$$\begin{aligned} \text{PSF}_{\text{pixel-2}}(x, y) &= \text{rect}(\Delta x, \Delta y) \otimes \text{rect}(\delta x, \delta y) \\ &= [\text{rect}_x(\Delta x) \otimes \text{rect}_x(\delta x)] \\ &\quad \cdot [\text{rect}_y(\Delta y) \otimes \text{rect}_y(\delta y)]. \end{aligned} \quad (22)$$

The Transfer function is obtained from the following relationship:

$$\begin{aligned} \text{MTF}_{\text{pixel-2}}(k_x, k_y) &= [\sin c_x(\pi \cdot k_x \cdot \Delta x) \cdot \sin c_x(\pi \cdot k_x \cdot \delta x)] \\ &\quad \cdot [\sin c_y(\pi \cdot k_y \cdot \Delta y) \cdot \sin c_y(\pi \cdot k_y \cdot \delta y)]. \end{aligned} \quad (23)$$

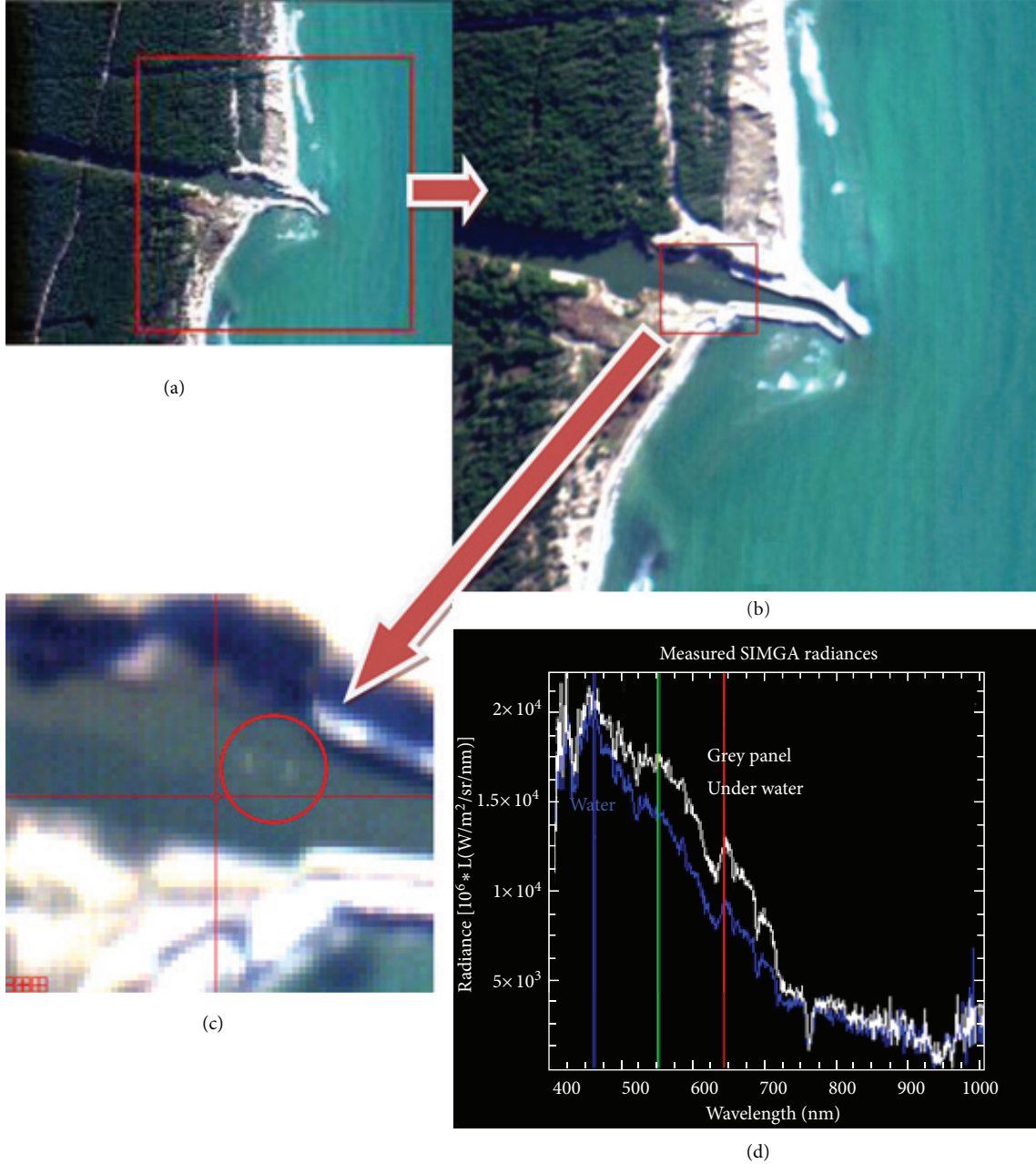


FIGURE 17: SIMGA RGB radiance images ((a), (b), (c)) on panels under water (S. Rossore park, Fiume Morto river), comparison between radiance measurements of grey panel under water and water (d).

5.3. *CCD Detector Charge Transfer.* For a CCD (Charge Capacitance Device) detector the reading of electrons acquired in each pixel of the matrix is performed by mean of a charge transfer from a pixel to the other. In this way the total transfer efficiency is related to the pixel-to-pixel Charge Transfer Efficiency (CTE) and the total number of transfers  $N_{\text{trans}}$ . As the CTE is not 1 some losses are present at the end of the reading time which implies a reduction of image contrast and then an MTF less than 1 in the direction of output register:

$$\text{MTF}_{\text{CCD-CTE}}(k, k_{\text{Nyq}}) = e^{-N_{\text{trans}} \cdot (1-\text{CTE}) \cdot [1 - \cos(\pi \cdot k / k_{\text{Nyq}})]}. \quad (24)$$

With

- (i) CTE the pixel Charge Transfer Efficiency (greater than 99,99%),
- (ii)  $N_{\text{trans}}$  the total number of charge transfers,
- (iii)  $k$  the spatial frequency and  $k_{\text{Nyq}}$  the Nyquist frequency of the system (half of the sampling frequency  $k_{\text{Nyq}} = 1/(2p)$ , with  $p$  the detector pitch).

5.4. *Image Motion During Integration Time.* The effect of temporal acquisition (integration time  $t_{\text{int}}$  greater than zero) during the image motion (with velocity  $v$ ), which happens

along the scan direction (the satellite velocity in a push broom system) introduces an image blur, which can be taken into account with a PSF similar to a rect function, which represents the temporal aperture along the motion:

$$\text{PSF}_{\text{temporal}}(x) = \text{rect}_x(v \cdot t_{\text{int}}). \quad (25)$$

With the following MTF:

$$\text{MTF}_{\text{along-motion}}(k_x, k_y) = \sin c_x(\pi \cdot k_x \cdot v \cdot t_{\text{int}}). \quad (26)$$

The worst case happens when the integration time is equal or larger than the dwell time, that is, the spatial displacement equivalent to a pixel size, while the best case ( $\text{MTF} \cong 1$ ) is for a short integration time.

**5.5. Electronic Filtering.** An electronic system can introduce a temporal smoothing due to a finite frequency bandwidth and thus a reduced space/temporal response. This effect has been simulated by using a general formulation based on the following Butterworth filter response:

$$\text{MTF}_{\text{filter}}(f) = \frac{1}{\sqrt{1 + (f/(N_f \cdot f_{\text{Nyq}}))^{2 \cdot N_b}}}. \quad (27)$$

With

- (i)  $f$  the frequency,
- (ii)  $f_{\text{Nyq}}$  the Nyquist frequency,
- (iii)  $N_b$  the order of Butterworth filter,
- (iv)  $N_f$  the ratio between the 3 dB filter frequency and the Nyquist frequency  $N_f = f_{3\text{dB}}/f_{\text{Nyq}}$ ; this ratio should be between 2.2 and 3 for a good reproduction of a square wave.

The above equation correctly reproduces the behaviour of the classical low-pass filter for  $N_b = 1$ .

**5.6. Focal Plane Random Jitter during Integration Time.** For high frequencies random vibration of the focal plane a Gaussian spatial response (PSF) can be taken into account. The Fourier Transform of PSF is still a Gaussian function, representing the MTF, with the following relationship:

$$\text{MTF}_{\text{jitter-random}}(f) = e^{-2 \cdot \pi^2 \cdot [\text{jitter} \cdot p \cdot f]^2}. \quad (28)$$

With

- (i)  $p$  the detector pitch,
- (ii)  $\text{jitter} * p$  the fraction of pixel representing the rms values of random fluctuations,
- (iii)  $f$  the spatial frequency at detector level.

**5.7. Optics Diffraction and Aberrations.** The MTF related to diffraction from optics has been evaluated by using the O'Neill formulas, valid for diffraction in presence of a telescope with central obscuration.

The following formulation for MTF diffraction term is used [34]:

$$\text{MTF}_{\text{diffraction}}(f) = \frac{(A + B + C)}{(1 - \eta^2)}, \quad (29a)$$

with  $\eta$ ,  $f$ , and other parameters defined as follows:

- (i)  $\eta$  = obscuration factor = ratio between the obscuration diameter and the pupil diameter,
- (ii)  $f$  = spatial frequency at detector level ( $\text{cm}^{-1}$ ),
- (iii)  $\omega = f/f_{\text{cut-off}}$ ,
- (iv)  $f_{\text{cut-off}}$  = optics cut-off ( $\text{cm}^{-1}$ ) at detector level =  $1/(\lambda * f\text{-number})$ ,
- (v)  $\lambda$  = wavelength;
- (vi)  $f\text{-number} = F/D$ , ratio between the focal length  $F$  and the pupil diameter  $D$ .

The  $A$ ,  $B$ , and  $C$  parameters are defined from the following relationships:

$$\omega \leq 1, \quad A = \frac{2}{\pi} \cdot [\arccos(\omega) - \omega \sqrt{1 - \omega^2}] \quad (29b)$$

$$\omega > 1, \quad A = 0,$$

$$\eta = 0, \quad t = 0, \quad \phi = 0, \quad B = 0;$$

$$\eta \neq 0, \quad t = \frac{\omega}{\eta}, \quad \phi = \arccos\left[\frac{1 + \eta^2 - 4\omega^2}{2\eta}\right]$$

$$t > 1, \quad B = 0 \quad (29c)$$

$$t \leq 1, \quad B = 2\eta^2 \frac{[\arccos(t) - t \sqrt{1 - t^2}]}{\pi} - 2\eta^2$$

$$\omega \leq \frac{1 - \eta}{2}, \quad C = -2\eta^2$$

$$\omega < \frac{1 + \eta}{2}, \quad C = \left\{ 2\eta \sin(\phi) + (1 + \eta^2) \phi \right.$$

$$\left. - 2(1 - \eta^2) \arctan\left[\left(\frac{1 + \eta}{1 - \eta}\right) \tan\left(\frac{\phi}{2}\right)\right] \right\}$$

$$\cdot \frac{1}{\pi} - 2\eta^2,$$

$$\omega \geq \frac{1 + \eta}{2}, \quad C = 0. \quad (29d)$$

The above MTF formulation for optics diffraction can be simplified to the following well known diffraction relationship in

absence of central obscuration, which is zero for  $f \geq f_{\text{cut-off}}$  :

$$f \leq f_{\text{cut-off}}$$

MTF

$$= \frac{2}{\pi} \cdot \left[ \arccos\left(\frac{f}{f_{\text{cut-off}}}\right) - \left(\frac{f}{f_{\text{cut-off}}}\right) \sqrt{1 - \left(\frac{f}{f_{\text{cut-off}}}\right)^2} \right],$$

$$f > f_{\text{cut-off}} \quad \text{MTF} = 0,$$

$$f_{\text{cut-off}} = \frac{1}{\lambda \cdot f_{\text{number}}}. \quad (29e)$$

Regarding possible optics aberrations the model takes into account, as a first approximation, the following exponential fitting function:

$$\text{MTF}_{\text{aberration}}(f) = e^{-k \cdot (f/f_{\text{cut-off}})^x}, \quad (30)$$

with  $k$  and  $x$  representing two empirical parameters used to approximate all optics degradation effects.

## Acknowledgments

The authors wish to thank L. Tommasi of Selex Galileo, R. Bonsignori of Eumetsat (formerly with Selex Galileo) and F. Pecchioni of University of Florence for the useful technical discussions and contributions. The authors also wish to acknowledge the ASI HYPSEO Phase A/B study under ASI/CSM/vdc/299/00 Contract for instrument specification and modelling.

## References

- [1] J. S. Pearlman, P. S. Barry, C. C. Segal, J. Shepanski, D. Beiso, and S. L. Carman, "Hyperion, a space-based imaging spectrometer," *IEEE Transactions on Geoscience and Remote Sensing*, vol. 41, no. 6, pp. 1160–1173, 2003.
- [2] ENVI software Exelis Visual Information Solutions, <http://www.exelisvis.com/language/en-us/products/services/envi.aspx>.
- [3] MODTRAN software, <http://modtran5.com/>.
- [4] A. Börner, L. Wiest, P. Keller et al., "SENSOR: a tool for the simulation of hyperspectral remote sensing systems," *ISPRS Journal of Photogrammetry and Remote Sensing*, vol. 55, no. 5-6, pp. 299–312, 2001.
- [5] I. R. Moorhead, M. A. Gilmore, A. W. Houlbrook et al., "CAMEO-SIM: a physics-based broadband scene simulation tool for assessment of camouflage, concealment, and deception methodologies," *Optical Engineering*, vol. 40, no. 9, pp. 1896–1905, 2001.
- [6] S. A. Cota, C. J. Florio, D. J. Duvall, and M. A. Leon, "The use of the general image quality equation in the design and evaluation of imaging systems," in *Remote Sensing System Engineering II*, vol. 7458 of *Proceedings of SPIE*, 2009.
- [7] S. A. Cota, J. T. Bell, R. H. Boucher et al., "PICASSO: an end-to-end image simulation tool for space and airborne imaging systems," *Journal of Applied Remote Sensing*, vol. 4, no. 1, Article ID 043535, 2010.
- [8] S. A. Cota, T. S. Lomheim, C. J. Florio et al., "PICASSO: an end-to-end image simulation tool for space and airborne imaging systems: II. Extension to the Thermal Infrared—equation and methods," in *Imaging Spectrometry XVI*, vol. 8158 of *Proceedings of SPIE*, p. 81580, 2011.
- [9] D. Labate, F. Butera, L. Chiarantini, and M. Dami, "SIMGA HYPER: Hyperspectral Avionic System Calibration Results," Technical note Galileo Avionica, 19 February 2007.
- [10] J. W. Goodman, *Introduction to Fourier Optics*, McGraw-Hill, New York, NY, USA, 1968.
- [11] G. C. Holst and T. S. Lomheim, *CMOS/CCD Sensors and Camera Systems*, JCD Publishing and SPIE Press, 2007.
- [12] S. Tassan, "SeaWiFS potential for remote sensing of marine Trichodesmium at sub-bloom concentration," *International Journal of Remote Sensing*, vol. 16, no. 18, pp. 3619–3627, 1995.
- [13] L. Alparone, M. Selva, B. Aiazzi, S. Baronti, F. Butera, and L. Chiarantini, "Signal-dependent noise modelling and estimation of new-generation imaging spectrometers," in *Proceedings of the 1st Workshop on Hyperspectral Image and Signal Processing: Evolution in Remote Sensing (WHISPERS '09)*, pp. 1–4, Grenoble, France, August 2009.
- [14] L. Alparone, M. Selva, L. Capobianco, S. Moretti, L. Chiarantini, and F. Butera, "Quality assessment of data products from a new generation airborne imaging spectrometer," in *Proceedings of the IEEE International Geoscience and Remote Sensing Symposium (IGARSS '09)*, vol. 4, pp. 422–425, July 2009.
- [15] B. Aiazzi, L. Alparone, S. Baronti, F. Butera, L. Chiarantini, and M. Selva, "Benefits of signal dependent noise reduction for spectral analysis of data from advanced imaging spectrometers," in *Proceedings of the Workshop on Hyperspectral Image and Signal Processing: Evolution in Remote Sensing (WHISPERS '11)*, Lisbon, France, June 2011.
- [16] P. Coppo, L. Chiarantini, and L. Alparone, "Design and validation of an end-to-end simulator for imaging spectrometers," *Optical Engineering*, vol. 51, no. 11, Article ID 111721, 2012, Special session on Hyperspectral Imaging Systems.
- [17] ENVI FLAASH atmospheric correction software and Exelis Visual Information Solutions, [http://www.exelisvis.com/portals/0/pdfs/envi/Flaash\\_Module.pdf](http://www.exelisvis.com/portals/0/pdfs/envi/Flaash_Module.pdf).
- [18] S. Adler-Golden, A. Berk, L. S. Bernstein et al., "FLAASH, a MODTRAN4 atmospheric correction package for hyperspectral data retrievals and simulations," in *Proceedings of the 7th Jet Propulsion Laboratory (JPL) Airborne Earth Science Workshop*, JPL Publication 97-21, pp. 9–14, 1998.
- [19] C. Ann Bateson, G. P. Asner, and C. A. Wessman, "Endmember bundles: a new approach to incorporating endmember variability into spectral mixture analysis," *IEEE Transactions on Geoscience and Remote Sensing*, vol. 38, no. 2, pp. 1083–1094, 2000.
- [20] J. M. P. Nascimento and J. M. B. Dias, "Does independent component analysis play a role in unmixing hyperspectral data?" *IEEE Transactions on Geoscience and Remote Sensing*, vol. 43, no. 1, pp. 175–187, 2005.
- [21] D. Labate, M. Ceccherini, A. Cisbani et al., "The PRISMA payload optomechanical design, a high performance instrument for a new hyperspectral mission," *Acta Astronautica*, vol. 65, no. 9-10, pp. 1429–1436, 2009.
- [22] A. Garzelli, B. Aiazzi, S. Baronti, M. Selva, and L. Alparone, "Hyperspectral image fusion," in *Proceedings of the Hyperspectral 2010 Workshop*, pp. 17–19, Frascati, Italy, March 2010, (ESA SP-683, May 2010).

- [23] P. Coppo, L. Chiarantini, F. Maselli, S. Migliorini, I. Pippi, and P. Marcoionni, "Application test of the OG-HYC hyperspectral camera," in *Sensors, Systems, and Next-Generation Satellites V*, vol. 4540 of *Proceedings of SPIE*, pp. 147–158, September 2001.
- [24] A. Bini, D. Labate, A. Romoli et al., "Hyperspectral earth observer (HYPSEO) program," in *Proceedings of the 52nd International Astronautical Federation (IAF '01)*, Toulouse, France, October 2001.
- [25] ENVI Spectral Angle Mapper (SAM) algorithm and Exelis Visual Information Solutions, [http://www.exelisvis.com/portals/0/tutorials/envi/SAM\\_SID\\_Classification.pdf](http://www.exelisvis.com/portals/0/tutorials/envi/SAM_SID_Classification.pdf).
- [26] I. S. Robinson, *Satellite Oceanography*, John Wiley & Sons, New York, NY, USA, 1985, Ellis Orwood Lim.
- [27] S. Tassan, "An algorithm for the identification of benthic algae in the Venice Lagoon from thematic mapper data," *International Journal of Remote Sensing*, vol. 13, no. 15, pp. 2887–2909, 1992.
- [28] A. Morel and Prieur, "Analysis of variations in ocean colour," *Limnology and Oceanography*, vol. 22, pp. 709–722, 1977.
- [29] S. Sathyendranath, L. Prieur, and A. Morel, "A three-component model of ocean colour and its application to remote sensing of phytoplankton pigments in coastal waters," *International Journal of Remote Sensing*, vol. 10, no. 8, pp. 1373–1394, 1989.
- [30] S. Tassan, "Local algorithms using SeaWiFS data for the retrieval of phytoplankton, pigments, suspended sediment, and yellow substance in coastal waters," *Applied Optics*, vol. 33, no. 12, pp. 2369–2378, 1994.
- [31] S. Tassan and M. Ribera d'Alcalá, "Water quality monitoring by thematic mapper in coastal environments. A performance analysis of local biooptical algorithms and atmospheric correction procedures," *Remote Sensing of Environment*, vol. 45, no. 2, pp. 177–191, 1993.
- [32] B. Sturm, "Ocean colour remote sensing: a status report," in *Satellite Remote Sensing for Hydrology and Water Management*, E. C. Barret, Ed., pp. 243–277, Gordon and Breach Science Publishers, New York, NY, USA, 1990.
- [33] P. Coppo, L. Chiarantini, F. Maselli et al., "Test Applicativi della camera Iperspettrale Cosmo-Skymed," Contratto ALS-US-SBC-0058/99, doc. N. SKC-GAL-TN-008, Dicembre 2000.
- [34] E. L. O'Neill, "Transfer function for an annular aperture," *The Journal of the Optical Society of America*, vol. 46, pp. 285–288, 1956.

## Research Article

# Heat Diffusion in Klinker Facade: The Study Case of a Gio Ponti Building

**N. Ludwig,<sup>1</sup> E. Rosina,<sup>2</sup> S. Caglio,<sup>3</sup> M. Gargano,<sup>1</sup> and V. Redaelli<sup>3</sup>**

<sup>1</sup>Department of Physics, University of Milan, via Celoria 16, 20133 Milano, Italy

<sup>2</sup>B.E.S.T Department, Politechnic of Milan, via Bonardi 9, 20133 Milano, Italy

<sup>3</sup>DERALAB srl, v. C. Correnti 14-20831 Seregno (MB), Italy

Correspondence should be addressed to E. Rosina, [elisabetta.rosina@polimi.it](mailto:elisabetta.rosina@polimi.it)

Received 18 August 2012; Revised 8 November 2012; Accepted 22 November 2012

Academic Editor: Marija Strojnik

Copyright © 2012 N. Ludwig et al. This is an open access article distributed under the Creative Commons Attribution License, which permits unrestricted use, distribution, and reproduction in any medium, provided the original work is properly cited.

The researchers focus on the IRT procedure of heat diffusion in ceramic finishing materials of contemporary architecture. The aim of the research is the development of a method for the thermal characterization of clinkers, a very common ceramic finishing material of buildings. The first experimental phase was performed in laboratory on clinkers of different shapes, thickness, colors, and glazing surface. The researchers determined two characteristic parameters related to thickness and thermal conductivity, by the interpolation of the heating curve in function of time with an analytical curve (resulted from a particular solution of Fourier's equation). This curve allows to obtain a parameter characteristic of the material of the specimens under investigation. At present time, the researchers have been studying the correlation between this parameter and the damage level in the specimens; they will be testing the model on real-scale study cases in the second experimental phase.

## 1. Introduction

The use of clinker tiles for finishing the facades of contemporary architecture has been a common practice since the 50–60s.

The durability of the ceramic materials, their low cost, their stainless and apparently low sensitivity to pollution effects, and finally the low requirement for maintenance are some of the reasons of their diffused application in the Middle-Southern region of Europe, as an effective alternative to brick-faced masonry, timber cladding, and stucco.

After more than 50 years from its first use, most of the ceramic finishing shows damage due to weathering/pollution in the mortar joints and the mortar underneath the tiles [1–3] that cause the tiles detachment.

Since 2010, an articulate and widespread research has been developed at Politecnico of Milano and State University of Milan, entitled “Sustainable Campus Leonardo.” The focus of the research is to involve scientists on the study, analysis, survey, assessment, management, repair, and enhancement of the universities' campus in the Eastern area of Milano.

Among these research lines, the authors developed a methodology to assess the state of conservation of the facades, especially ceramic finishing. In the present paper, the authors show the improvement of the preliminary tests based on the solution of the mathematical model of heat transfer in the ceramic medium. The preliminary test had its validation by softly hammering both the sound zone and the delaminated areas of the finishing. The different sounds revealed the detachment of the finishing. The method has been applied on historical buildings, dating back to the beginning of XX century up to the 60's. The more recent buildings, built with contemporary techniques and materials, were designed by one of the most famous architect of that time, Gio' Ponti, and they are included in the preservation office list of monuments (Figure 1).

Therefore, the assessment of facade in Campus Leonardo is an important issue both for economical aspects related to the costs of maintenance and for the project of repair, dealing with high historical and artistic valued contemporary buildings. From this side, the critical point is to preserve the authenticity of a building, of which materials

could be perfectly replaced with new ones, thanks to the possibility of reproducing industrial tiles (and the other elements).

It is unanimously accepted in the current debate on restoration of historical building that the repair should be clearly identified, although it should not affect the aesthetical unit of the work of art, and that a *mimetic* solution, with the substitution of materials and elements with new ones *à l'identique*, has been a banned practice starting from the third decade of the XX century. Nevertheless, the common practice is to replace the damaged parts with new elements that have the same apparel of the original ones. As an example, the recent renovation of the historical site of Bauhaus, where the architects provided a consistent refurbishment, including the substitution of the finishing [4]. This approach could not have been applied in Campus Leonardo on Gio' Ponti buildings, because the architect designed special polyhedral tiles for his buildings, and he applied the tiles with different orientation to create different effects of reflection/color during the day, depending on the inclination of sun rays hitting the surface. The design of the surface is completely connected with the concept design of the building, in a holistic view of the buildings and its technological elements. His projects and realizations are yet innovative, because the architect always followed his incredible interest for experimentation in new materials and pattern. Therefore, the most advanced approach indicates the need to limit as much as possible any substitution, preventing the damage by reducing risk factors (environment, wrong building repairs, inadequate use, lack of maintenance, etc.) and by means of a plan of conservation [5].

The durability of the facade of contemporary buildings is also an important issue for managing the building sector, as well as the identification of the risk factors and the evaluation of the buildings' technological components' life cycle [6–8]; the costs of fixing the ceramic finishing is a large part of the economic effort within the whole maintenance predictable costs. Nevertheless, only few nondestructive tests are available to assess the facades, most of these tests require the contact with the surface under investigation (knocking with a hammer or knuckles or the vibration test [9, 10]). Infrared thermography (IRT) is the only technique that ensures a no-contact investigation of the surface, and it has no competitor regarding costs (no scaffolding or forklift basket is required) or speed of inspection. Moreover, the expected results are a map that localizes and gives an approximated evaluation of the delaminated finishing's size.

Up to now, the common approach is the use of qualitative IRT allowing only an approximated mapping of defects and an evaluation of their size. False alerts in IRT are often the worst risk for the assessment, caused by the optical properties of tiles (colors, reflectance, and damage of the glazing surface), their geometric shape (i.e., Gio' Ponti designed polyhedral tiles, Figure 2, to enhance the effect of reflected light), the nonhomogeneous layer of mortar underneath, and the effects of aging [11].



FIGURE 1: Gio' Ponti's building, *La Nave*, located in Milan, in Campus Leonardo, after restoration. Clinker finishing is better shown in Figure 3 that recaptures a small area of the Northern façade.



FIGURE 2: The two series of *La Nave* tiles after a first repair and substitution. Original tiles are on the right and the lower part of the left corner; the new tiles are on the upper/middle of left part of the wall.

However, to increase the reliability of the investigation, a new approach is necessary. If investigation is supposed to be an enhancement for the program of conservation and maintenance, the assessment of the facade has to be done in the very preliminary phase of the project, by noncontact tests and without any verification at close distance (from the scaffolding) therefore, it is necessary to increase the reliability of the tests results, because up to now the results of IRT application can be misleading [12, 13].

Simplified mathematical models that are able to describe with good approximation the thermal behavior of sound and defected surface can be useful to this aim [14–16].

Scientific literature on the properties of ceramic materials is very poor [17, 18], and none of the listed properties deals with the on-site thermal characterization and detachment analysis.

Authors determined two characteristic parameters related to thickness and thermal conductivity of the tiles, by interpolating the time-dependent heating curve with an analytical expression, deduced from a solution of Fourier's heat diffusion equation [15]. In the first part of the work, a standard procedures was used in the laboratory to obtain the thermal characteristics of selected ceramic specimens.

## 2. Determination of the Function of Surface Heating

To determine the function that describes the surface heating of a wall, we have to consider the Fourier equation for the heat diffusion through a homogenous bulk

$$\nabla^2 T = \frac{1}{\alpha} \frac{\partial T}{\partial t}, \quad (1)$$

where  $\alpha$  is the thermal diffusivity. In laboratory tests, it is assumed that the heat propagation in the sample is one dimensional, namely, taking place only along one direction ( $z$ ), specifically the perpendicular one to the face hit by the solar irradiation.

The experimental results are in agreement with this approximation, allowing us to apply it to real cases of study. The researchers chose the heating by irradiation simulated in the laboratory by a pair of halogen lamps and generated by the sun during on-site investigations.

Called  $z$  the heat propagating dimension, the Fourier equation reduces to the following:

$$\frac{\partial^2 T(z, t)}{\partial z^2} = \frac{1}{\alpha} \frac{\partial T(z, t)}{\partial t}. \quad (2)$$

The independence of the spatial variable ( $z$ ) by the time ( $t$ ) allowed the researchers to apply the method of separation of variables, so we have two coupled equations, one for the spatial variable  $z$ , named  $\theta_z$ , and one for the time  $t$ ,  $\theta_t$ :

$$\begin{aligned} \frac{1}{\theta_z} \frac{\partial^2 \theta_z}{\partial z^2} &= \lambda^2, \\ \frac{1}{\alpha \theta_t} \frac{\partial \theta_t}{\partial t} &= \lambda^2, \end{aligned} \quad (3)$$

where  $\lambda$  is the unknown coupling term.

Seeking the function that describes the temporal evolution of the surface temperature of the wall,  $z = 0$  was set, and it was calculated the constants using boundary conditions deduced from the experimental curves, obtaining from the general solutions:

$$T_0(t) = -\Delta T e^{-\lambda^2 \alpha t} + T_{\text{Max}}, \quad (4)$$

where  $T_0$  is the surface temperature and  $T_{\text{max}} = T_0 (t = \infty)$ .

To determine the coupling parameter  $\lambda$ , the researchers used dimensional analysis, obtaining a relationship with a length  $L$  that has been called *limit of dimming*. Where  $\lambda = L^{-1}$  in [ $\text{m}^{-1}$ ]. The researchers defined the parameter  $L$  by means of experimental tests in the laboratory of heat diffusion in the materials.  $L$  depends on the material thermal characteristics, and it is the distance from the surface layer to the inner layer from which no thermal signal can be detected. It is not possible to detect any structure or void underneath the layer at depth  $\geq L$  from the surface.  $L$  depends on the kind and intensity of heating too, therefore the quantitative comparison between sound and detached areas has to be done at the same environmental conditions. In the case studies of clinker detachments, this parameter is used to infer the presence of thermal anomalies due to degradation.

TABLE 1: Values of mean emissivity of the samples, tested in the laboratory.

Board	Clinker	Emissivity
—	K2	0.96
—	K4	0.94
—	K6	0.92
CE004	A1	0.98
	A2	0.98
	A3	0.98
	B1	0.95
	B2	0.95
	B3	0.95
CE7	A	0.93
	B	0.87
	C	0.94
	D	0.96
	E	0.97
	F	0.95
CE007	A	0.96
	B	0.94
	C	0.89
	D	0.96
	E	0.96
	F	0.97
CE008	A	0.96
	B	0.90
	C	0.92
	D	0.93
	E	0.97

## 3. Laboratory Test

23 clinker specimens, with different shape and colors have been studied for the evaluation of heat transmission and emission. Three tiles were simply laid plain; other three were applied on brick solid masonries, simulating a detachment between the tile and the masonry for half of the specimens surfaces. The other 17 specimens were glued to some plywood tables, and a scheme of the experimental setup is in Figure 3. The experimental setup for the heat transmission evaluation allowed to obtain an extremely homogeneous and controlled increase of the temperature up to  $80^\circ\text{C}$  on one side of the tile (front), by using on the rear a heating surface controlled through hot water vapor flux. The first evaluation had the purpose to measure the heating differences on the sound and delaminated areas of the same specimens, therefore, to simulate a real case of damaged areas.

Emissivity measurement was obtained by the comparison with a target of known emissivity (black carbon powder) by lighting of both the specimens and the target with two halogen lamps (650 W) symmetrically placed at 1.5 m from the objects. Measurements were obtained by a LW camera (microbolometric sensor,  $0.08^\circ\text{C}$  thermal resolution at  $20^\circ\text{C}$ ). Results of laboratory tests (Table 1) were used for

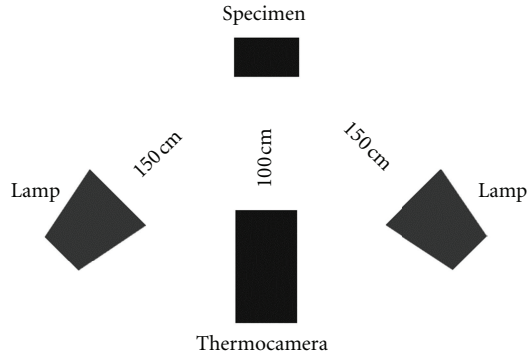


FIGURE 3: Plan of the experimental set-up in the laboratory.

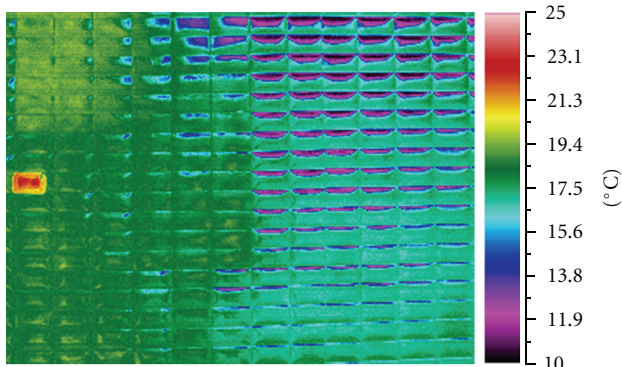


FIGURE 4: Infrared image of *La Nave* tiles. The recaptured area has a visualization in the visible range in Figure 2.

emissivity estimation in all on-site measurements, where emissivity values were unknown.

The experimental results of the laboratory tests give a 0.95 average value of emissivity. Values of emissivity distribution are shown in Figure 6. In the cases under study, the temperature variations, due to the differences of the emissivity values and those linked to the surface irregularities and colors, resulted smaller than the instrumental and experimental error, in particular, when the thermal gradient is taken into account instead of the temperature's absolute values.

Temperature differences between sound and damaged areas resulted to be 1–1.5°C. As for the detection of detachments on plaster [14], the analysis of the thermal maps allows to find out the detachment of tiles. As an example of laboratory tests, Figure 7 shows the higher heating in the detached areas (the red dotted curve) due to the air gap underneath the tiles, as it happens for plaster and plaster detachments. The following tests were set on site with the aim to verify the real feasibility of the procedure on the real study cases.

#### 4. On-Site Tests

The researchers chose a real-scale study case to examine the modalities of on-site monitoring and to test the laboratory procedure. A cavity wall of *La Nave*, an historical building at



FIGURE 5: Experimental setup, three infrared camera, mod. TVS 700.

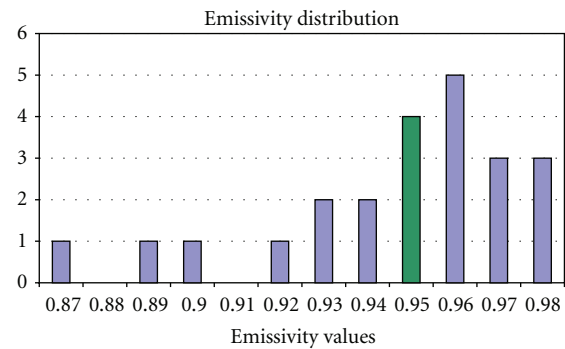


FIGURE 6: Emissivity distribution of samples based on the experimental recurrences.

Leonardo Campus, Politecnico di Milano (Figure 1), served as a mock up (*La Nave* is a Gio Ponti's listed building; it recently underwent restoration of the facades due to the clinker tiles detachment). The wall has a solid concrete structure of 8 cm thick, an interior cavity of 23 cm, a finishing of mortar (2.5 cm thick), and grey clinker tiles (3 mm). The examined side of the wall is the Southern elevation, ground level. Southern orientation was chosen with the aim to exploit the solar irradiation and obtain a relevant thermal gradient for the following data processing and analysis. Measurements were performed in reflection mode, in two consecutive days, with clear sky and similar environment temperature (air temperature ranging between 15 and 24°C; RH 40–64%), in the same location. Three thermocameras (TVS Avio 700 LW, the same model used in the laboratory tests) recorded a sequence of 420 images each, at the rate of 1 frame per minute, during 5 hours of sun irradiation and 2 hours of cooling, for the purpose to investigate a wide surface at the same natural heating conditions. The recaptured images have a spatial resolution of few mm, which is necessary to detect the mortar joints between the tiles. Furthermore, the use of three thermocameras allowed the researchers to study the effects of different angles of view and solar irradiation on nonplanar surfaces. In particular, the test area on *La Nave* wall surface shows the presence of both Gio'

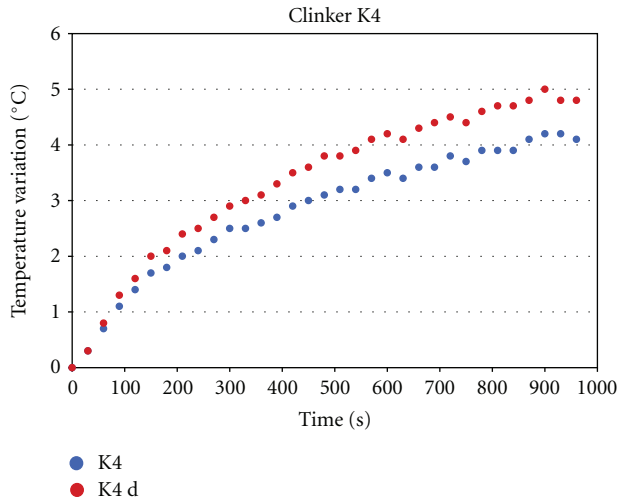


FIGURE 7: Heating of a sound area (K4) and delaminated one (K4 d) in clinker tile K4.

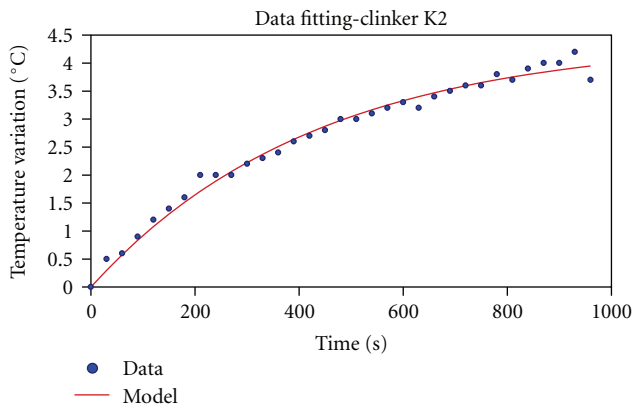


FIGURE 8: Fitting of the heating data obtained in the laboratory test with the mathematical model for K2 clinker.  $R^2 = 0.989$ .

Ponti tiles and new tiles, due to maintenance intervention. The new series of tiles have flat and smoother surface while the original ones have rounded polyhedral surface (Figure 2). All the tiles have similar grey colors therefore, it was possible to avoid the effects of the absorption of solar radiation due to the colors in the analysis of the heating curves.

The selected area under investigation has been analyzed by means of three thermocameras, set at 4.5 m from the surface, recapturing different areas of 2 sq m at 1.5–3 m from the ground level (Figure 5).

The thermocameras started the shooting 30 min before the direct solar irradiation and continued 1 hour after the shadowing, for a total time 7 hours, with a rate of 1 frame per minute. The first day, the lens axis of the three thermocameras was set perpendicularly to the surface (Figure 4).

The second day, the researchers set the lens axis with different inclination, with the aim to verify the influence on the measures of the inclination as an effect of the reflection of the solar irradiation on the tiles.

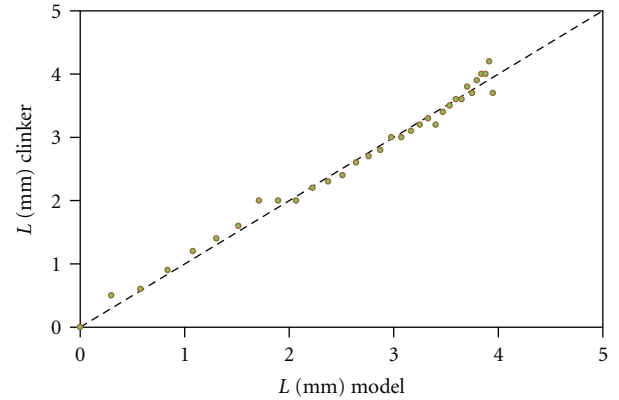


FIGURE 9: The relation between the calculated values and the experimental ones shows a close match in laboratory tests,  $R^2 = 0.989$ .

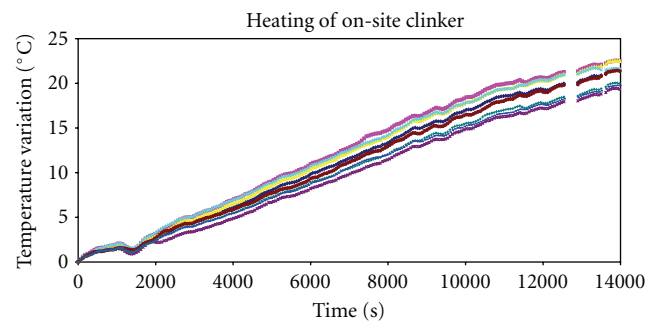


FIGURE 10: Experimental results of the on-site recaptures: the trend of the areas is similar and the differences of temperatures of the heating are very small at the end ( $<5^{\circ}\text{C}$ ).

### 5. On-Site Test: Data Analysis and Results

The data acquired on the second day showed a different thermal response on the rounded surface of tiles due to the shooting angle. The thermal analysis of the tiles with flat surface showed small differences when varying the shooting angle. Nevertheless, in the analysis of thermal gradient, the effect of the inclination of the recapture axis, and therefore of the reflected radiation, are *negligible* for such small differences.

A general suggested procedure is to capture the areas with different viewing angles, better if symmetrical.

As expected, the derived curves obtained by the laboratory tests (Figures 8, 9, and 10) fit better the mathematical model than the results of on-site tests. Errors of temperature evaluation have the same magnitude of incertitude of the thermocameras sensors ( $0.08^{\circ}\text{C}$ ). This is due to the higher irradiation necessary to heat the whole surface; in fact, the wall did not reach the equilibrium with the environment even after 5 hours of solar irradiation. On the contrary, during the laboratory tests, this steady condition was achieved after only 20 minutes of irradiation by halogen lamps.

Up to now, the researchers are acquiring new data on clinkers with different colors laid on concrete and stucco,

with the purpose to verify and extend the recording and analysis procedure.

Moreover, the authors are looking for relations between the parameters and the level of damage of the surface.

## 6. Conclusions

The results pinpoint that the IRT application study detecting delaminations of clinker finishing is similar to the well-known application of the investigation of stucco and plaster finishing, although tiles have a nonplanar, irregular, and reflective surface. The development of both an experimental methodology for homogenous heating of the samples and a data interpolation curve allowed to obtain two parameters characteristic of clinker tiles' thermal behavior in laboratory studies/tests. Experimental data fit with the function expressing the law of heat diffusion. The semiquantitative approach used in the definition of the damage level of the investigated areas is a novelty that can bring interesting results on real-scale experiments. At present, the researchers are testing the feasibility of the procedures on site, in addition to the verification of the calculation procedure that are so far robust and fitting of the experimental data. A further development is to reduce the amount of thermographic shootings necessary to extract the fitting parameters.

## References

- [1] F. Re Cecconi, *Metodologie e strumentazioni per la previsione della durabilità di componenti edilizi per edifici scolastici ai fini della loro programmazione manutentiva [Ph.D. thesis]*, 1996.
- [2] S. M. Cornick and M. A. Lacasse, "An investigation of climate loads on building façades for selected locations in the United States," *Journal of ASTM International*, vol. 6, no. 2, pp. 1–17, 2009.
- [3] R. Mačiulaitis, A. Kičaitė, D. Nagrockienė, and G. Kudabiene, "Evaluation of service frost resistance of ceramic facing tiles," *Journal of Civil Engineering and Management*, vol. 10, no. 4, pp. 285–293, 2004.
- [4] M. Markgraf, "Conservation and preservation of the bauhaus building in Dessau," *IV. World Heritage Sites of the 20th Century—German Case Studies*, pp. 108–111, 2006.
- [5] A. Canziani, *On the Edge of Modern Heritage Conservation (Conservare L'Architettura)*, Electa, Milano, Italy, 2009.
- [6] M. K. Kumaran, P. Mukhopadhyaya, S. M. Cornick et al., "An Integrated methodology to develop moisture management strategies for exterior wall systems," in *Proceedings of the 9th Canadian Conference on Building Science and Technology*, pp. 45–62, Vancouver, Canada, 2003.
- [7] H. Kunzel, H. M. Kunzel, and K. Sedlbauer, "Long-term performance of External Thermal Insulation Systems (ETICS)," *ACTA Architectura*, vol. 5, no. 1, pp. 11–24, 2006.
- [8] B. Daniotti, S. Lupica Spagnolo, and R. Paolini, "Climatic data analysis to define accelerated ageing for reference service life evaluation," in *Proceedings of the 11th Conference on Durability of Building Materials and Components (DBMC '08)*, Istanbul, Turkey, 2008.
- [9] E. Esposito, S. Copparoni, and B. Naticchia, "Recent progress in diagnostics of civil structures by laser vibrometry," in *Proceedings of the 16th World Conference on Nondestructive Testing*, Montreal, Canada, 2004.
- [10] P. Castellini, E. Esposito, B. Marchetti, E. Esposito, and E. P. Tomasini, "New applications of Scanning Laser Doppler Vibrometry (SLDV) to non-destructive diagnostics of artworks: mosaics, ceramics, inlaid wood and easel painting," *Journal of Cultural Heritage*, vol. 4, supplement 1, pp. 321–329, 2003.
- [11] M. A. Crippa, A. del Conte, E. Esposito, and P. Perrotta, "Applicazione di sistemi ottici per la Diagnostica dello stato di adesione di Rivestimenti superficiali: il caso dell'edificio "Tri-foglio" del Politecnico di Milano," in *Atti del 11th Conferenza Nazionale sulle Prove non Distruttive Monitoraggio Diagnostica e 11th Congresso Nazionale dell'AIPnD*, Milan, Italy, 2005.
- [12] E. Edis, I. Flores-Colen, and J. De Brito, "Passive thermography inspection of adhered ceramic claddings: limitation and conditioning factors," *Journal of Performance of Constructed Facilities*, pp. 258–268, 2012.
- [13] S. Striato, *Edificio 14 al Politecnico di Milano: indagini per la conservazione della compagine muraria [Dissertation thesis]*, Politecnico di Milano, AA, 2011/2012.
- [14] N. Ludwig, "Thermographic testing on buildings using a simplified heat transfer model," *Materials Evaluation*, vol. 61, no. 5, pp. 599–603, 2003.
- [15] S. Caglio, *Tecniche di termografia dinamica per lo studio di fenomeni di diffusione del calore in materiali di interesse archeometrico [M.S. thesis]*, faculty of Physics, State University of Milan, 2004/2005.
- [16] N. Ludwig and P. Teruzzi, "Heat losses and 3D diffusion phenomena for defect sizing procedures in video pulse thermography," *Infrared Physics and Technology*, vol. 43, no. 3-5, pp. 297–301, 2002.
- [17] D. Muez and T. Fett, *Ceramics, Mechanical Properties, Failure Behaviour, Materials Selection*, Springer, Berlin, Germany, 1999.
- [18] J. Stránský, J. Vorel, J. Zeman, and M. Šejnoha, "Mori-Tanaka based estimates of effective thermal conductivity of various Engineering materials," *Micromachines*, vol. 2, no. 2, pp. 129–149, 2011.

## Research Article

# Micro-Scale Thermal Imaging of Organic and Polymeric Materials with Cooled and Uncooled Infrared Cameras

J. Morikawa,<sup>1</sup> E. Hayakawa,<sup>2</sup> and T. Hashimoto<sup>1</sup>

<sup>1</sup> Tokyo Institute of Technology, 2-12-1, S8-29, Ookayama, Meguro-ku, Tokyo 152-8550, Japan

<sup>2</sup> ai-Phase Co., Ltd., 2-15-19, Kami-osaki, Shinagawa-ku, Tokyo 141-0021, Japan

Correspondence should be addressed to J. Morikawa, morikawa.j.aa@m.titech.ac.jp

Received 10 August 2012; Revised 19 November 2012; Accepted 22 November 2012

Academic Editor: Antoni Rogalski

Copyright © 2012 J. Morikawa et al. This is an open access article distributed under the Creative Commons Attribution License, which permits unrestricted use, distribution, and reproduction in any medium, provided the original work is properly cited.

The emissivity corrected thermal imaging combined with a real-time direct imposed-signal system on the freezing of biological cells is presented, which makes it possible to visualize the exothermic latent heat at a minus temperature. The applicability of the uncooled micro bolometer (thermal detector) to the micro-scale thermal analysis on the phase transitions of organic and polymeric materials is discussed in comparison with the photon detector, equipped with the optics originally designed.

## 1. Introduction

Noncontact thermal imaging methods are preferred in the characterization of materials in the increasing number of applications. Creating and monitoring thermal distributions with a spatial resolution of  $\sim 10\ \mu\text{m}$  is required, in particular, for the materials developed in the energy saving and renewable technology [1].

A recent advance in IR detectors arrays provides the enhanced applications [2]. Thermal imaging applied to the materials' characterization in a micro-scale is summarized with actual imaging results of organic, polymeric, and biological materials, using a cooled and an un-cooled infrared cameras equipped with the optics originally designed in this study. Examples of microscale thermal analysis and the lock-in thermography are presented. The latent heat generation and dissipation at minus temperatures during the freezing of biological cells are visualized that clarifies the thermal diffusion effect on crystallization and the vitrification [3–7]. On-lamellae thermal analysis of *n*-alkane visualizes the early stage of anisotropic lamella formation and the difference of thermal propagation in crystallizations and the rotator phase transitions [8]. The crystallization front of polymeric spherulite of poly(ethylene oxide) visualizes the temperature rise of  $\sim 100\ \text{mK}$  [9]. The basic results of lock-in thermography visualize the phase and amplitude image using a method of modulated spot heating with a diode laser that generates a thermal wave inside the specimen [10, 11].

A promising application of micro-bolometer sensor is additionally introduced [12].

## 2. Approach and Techniques

In order to visualize the material's thermal phenomena with a spatial resolution  $\sim 10\ \mu\text{m}$  and in a time scale  $\sim 10\ \text{ms}$ , the following techniques have been developed. The measurement is done preferably under the dynamic temperature field such as a constant rate heating/cooling and a temperature modulation.

**2.1. Optics.** Materials for optics suitable to the mid- and long-wave infrared cameras are chosen, respectively. Spatial resolutions  $4.3\ \mu\text{m}$  (calculated at  $\lambda = 5\ \mu\text{m}$ ,  $\lambda$ : wavelength) and  $11.1\ \mu\text{m}$  (at  $\lambda = 10\ \mu\text{m}$ ) have been achieved for the indium antimonide (InSb) and vanadium oxide (VOx) detectors of focal plane arrays (FPAs), in a good balance of modulation transfer function (MTF) and numerical aperture (NA).

**2.2. Precision Temperature Control.** Equipped with the microlens, the measuring area is  $1\ \text{mm}^2$ . Temperature control of the micro-scale area of the baseplate of a sample holder is required. The temperature is controlled with a precision of  $0.1\ \text{K}$  and a temperature scan at a constant rate of  $0.1\ \text{K}–500\ \text{K}/\text{min}$  is routinely used. Together with the micro-alignment of an *xyz* stage the temperature is controlled using a field programmable gate arrays (FPGAs).

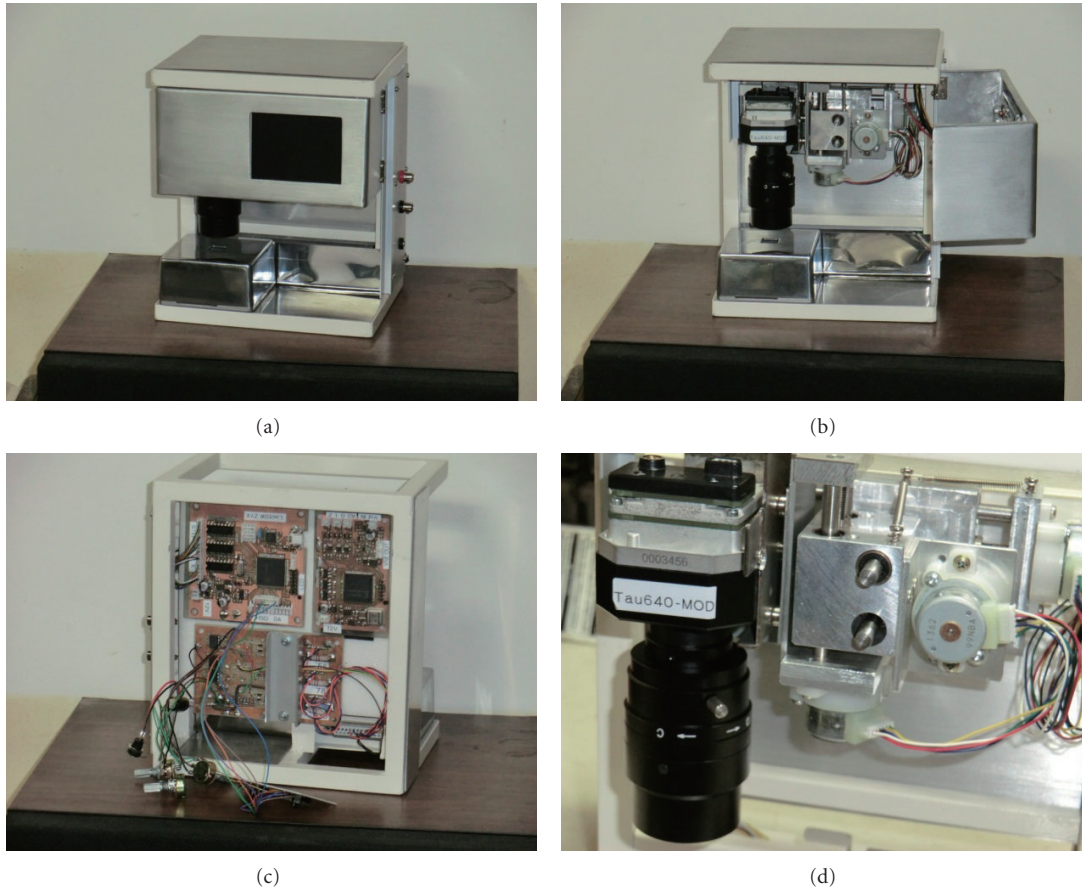


FIGURE 1: Photographical view of the experimental setup of a real-time direct signal imposing system with un-cooled IR FPA sensors equipped with a micro lens optical system. The height of the instrument system box is 20 cm.

**2.3. Modulated Laser Scanning System.** The excitation source was a laser diode (LD) of 0.1 W power emitting at 630 nm wavelength. The optical pick-up head was used to deliver light to inside/onto the sample by a PMMA lens of  $D = 4$  mm diameter and  $f$ -number = 1.0. The corresponding numerical aperture was  $NA = 0.5$  and the focal spot size on the sample is estimated to be  $d = 1.22 \lambda/NA \sim 1.5 \mu\text{m}$ . This is the size of a heat source.

**2.4. Phase Lock-In Algorithm.** It is based on the discrete cosine transform (DCT) and the inverse discrete cosine transform (IDCT). The heat source point is set as a reference point for the phase shift calculation.

**2.5. Time Differential Images.** It is calculated as a standard procedure as  $I'(t) = \partial I/\partial t = \min_{\Delta t > 0} (I(t) - I(t - \Delta t))/\Delta t$ , where  $I(t)$  is the intensity at a time moment  $t$  and  $\Delta t$  is a time interval between the captured images.

**2.6. Inverse Processing.** The method to estimate the local thermal diffusivity and a heat source distribution has been developed by Pradere et al. [7]. Considering the Laplacian terms, it enables to estimate the localized heat source and thermal diffusivity simultaneously.

**2.7. Superimpose for the Emissivity Corrections.** In spite of the improvement of the resolution of time and space with the techniques developed as above, the procedure for emissivity correction is still important, especially for the thermal phenomena including phase transitions. The emissivity change during phase transitions is not a simple function of temperature.

In order to calibrate the intensity of all pixels in FPA into temperature, the measured temperature data is directly imposed to the IR intensity signal [12]. The application of this approach to calibrate the emissivity into the temperature during the materials characterization is one of the purposes of this paper.

### 3. Experimental

The measuring instrument, including the signal imposing system, is designed as follows [12]:

- A: signal (composite video signal) capturing part,
- B: superimposer of video signal,
- C: timing trigger generator,
- D: synchronous IR camera with InSb or VOx FPA sensors,

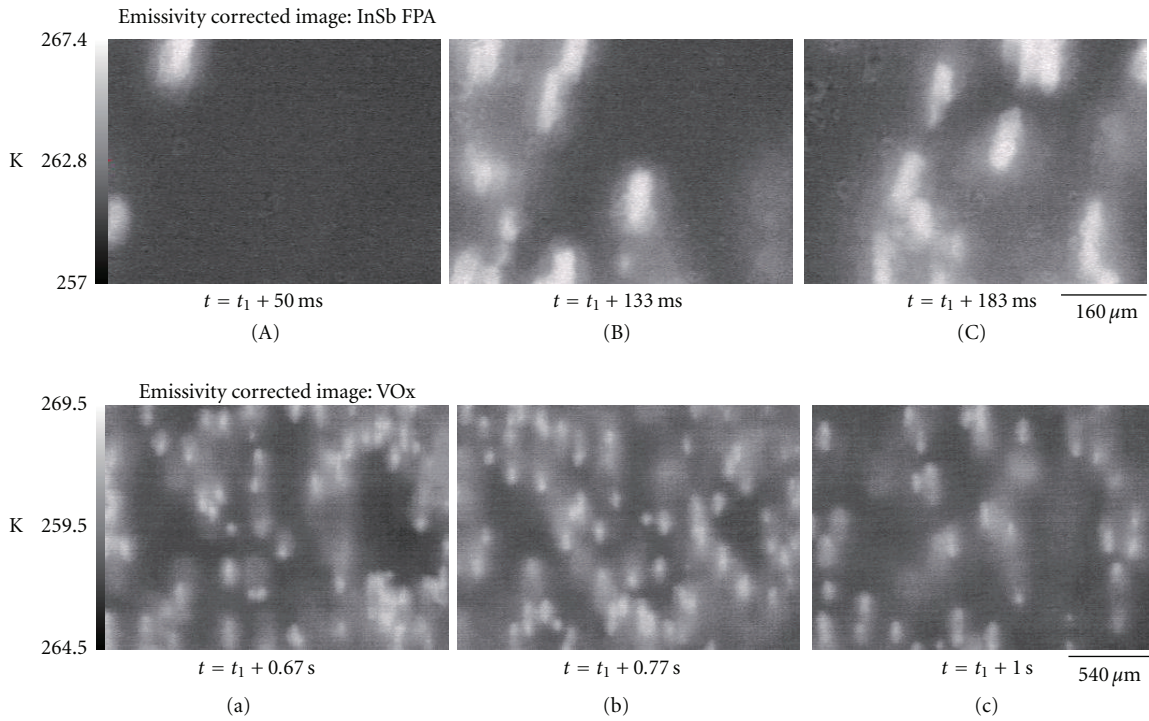


FIGURE 2: ((A),(B), and (C)) Sequence of the emissivity corrected image of freezing onion-skin cells at minus temperatures under a cooling scan observed with the InSb IR FPA ( $30 \mu\text{m}$  detector pitch) equipped with a  $\times 7.5$  magnification micro lens. ((a), (b), and (c)) Sequence of the emissivity corrected image of freezing leek cells ((a),(b),(c)) at minus temperatures under a cooling scan  $0.2 \text{ K/s}$  observed with the VOx IR FPA ( $17 \mu\text{m}$  detector pitch) equipped with a  $\times 2.5$  magnification micro lens. After the emissivity correction, temperature of each pixel is calibrated. The temperature is shown in the concentration bar in the left. The signal is captured via NTSC in the time interval as shown in the figures.

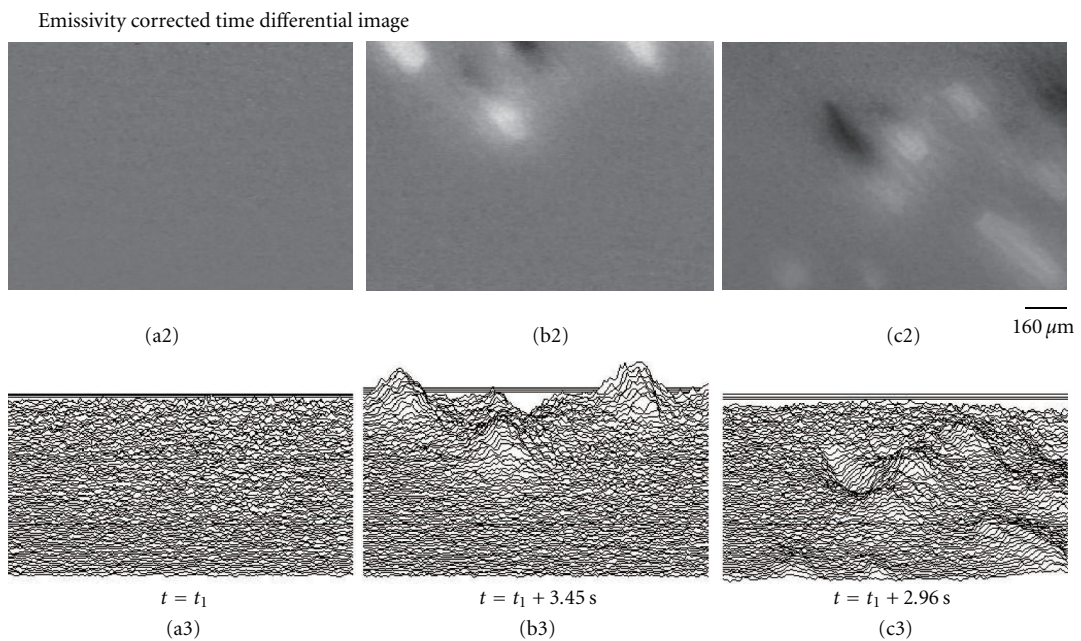


FIGURE 3: ((a2), (b2), and (c2)) Sequence of the time derivative thermal image of freezing biological cells captured with InSb IR FPA at minus temperatures and ((a3), (b3), and (c3)) the three-dimensional plot of time derivative image of (a2), (b2), and (c2).

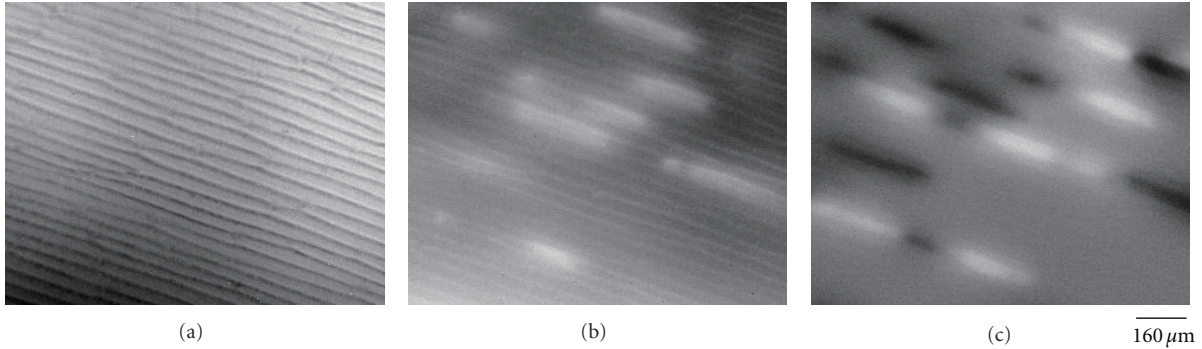


FIGURE 4: Thermal image of the freezing process of the cellular tissue of a leek observed with the InSb IR FPA equipped with a  $\times 7.5$  magnifications micro lens. (a) The subtracted image, (b) the raw image, and (c) the temporal derivative image at minus temperatures.

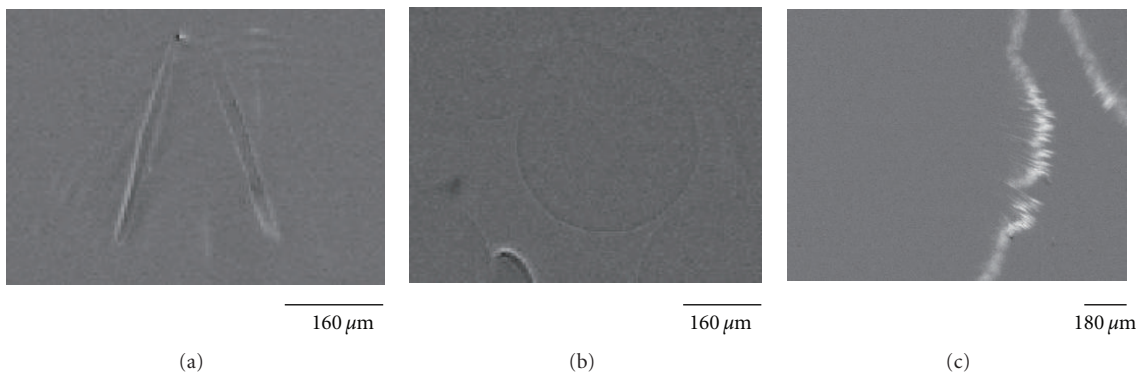


FIGURE 5: Thermal image in the crystallization of organic and polymeric materials; (a) *n*-pentacosane,  $C_{25}H_{52}$ , cooling at a rate of 0.6 K/min from 56.1°C to 55.8°C, (b) poly(ethylene oxide) at a cooling rate of 30 K/min from the molten state, and (c) stearic acid at a cooling rate of 10 K/min from the liquid state. The temporal derivative images are shown.

- E: high-precision/high-speed temperature controller,
- F: actuator and laser drive,
- G: stage scanners.

A handy size design is realized when VOx FPA is applied. The photographical view of the instrument is depicted in Figure 1.

The laser drive for generating a modulated spot heating with 630 nm diode laser and the  $xy$  positioning actuator are triggered with a timing signal synchronous to the video signal capturing. The video signal synthesizer makes it possible to record a direct signal of temperature or positioning data, simultaneously, with the imaging video signals. The imposed data are applied to the pixel emissivity corrections at one time under heating/cooling temperature scan. The Peltier-type dual heater is set to operate a heating and cooling scan of the specimens.

## 4. Results

**4.1. Pixel by Pixel Temperature Calibration with the Imposed Temperature Signal.** Figure 2 shows the thermal imaging of the biological tissues of onion-skin cells and leek cells in a cooling scan with the method of pixel by pixel temperature calibration with the imposed temperature signal. The

emissivity is corrected with the imposed signal, and the calibrated temperature is shown as a contrast of light and shade. Shortly after the surface water becomes frozen, the freezing of cell starts in one cell by one cell, and because of the localized temperature rise caused by thermal diffusion from the freezing cell next to another one, the freezing proceeds in a random way.

Figure 3 shows the temporal derivative image of the freezing onion-skin cells using the emissivity corrected intensity. The white and dark color corresponds to the positive and the negative temporal derivative coefficient of temperature. The adjacent cells do not freeze continuously. This is a characteristic phenomenon in the freezing process in tissues of plant cells. The cell wall plays an important role in the transfer of the excited heat.

Comparing the temporal derivative images calculated from the emissivity corrected and uncorrected images, no large differences are found. However, the Laplacian terms are influenced by the emissivity correction procedure. This is promising to diminish the measuring noise that affects the inverse processing.

**4.2. Crystallization of Organic and Polymeric Materials.** Typical examples of the crystallization front of organic materials are shown in Figures 4 and 5. The anisotropic propagation of

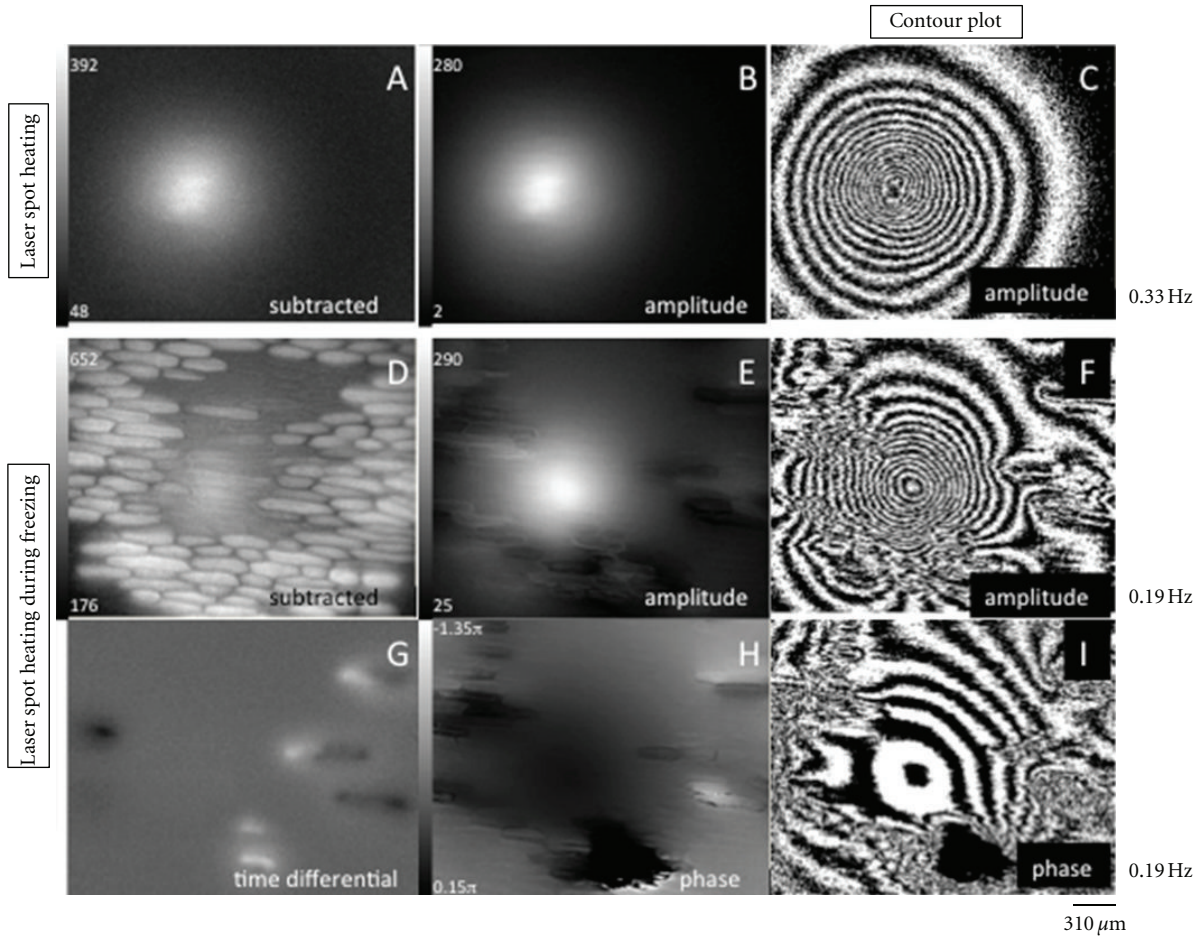


FIGURE 6: Phase-locked image in comparison with the subtracted image of onion-skin cells irradiated with a laser-modulated spot heating at r.t. ((A)–(C); 0.33 Hz) and under a cooling temperature control ((D)–(I); 0.19 Hz). A: subtracted image, B: amplitude image, (C): contour plot of (B), (D): subtracted image, (E): amplitude image, (F): contour plot of (E), (G): time differential image, (H): phase image, and (I): contour plot of (H). observed with the InSb IR FPA ( $25 \mu\text{m}$  detector pitch) equipped with a  $\times 8.3$  magnification micro lens.

excited heat generated in the phase change strongly correlates to the high structure of the materials. In the tissue of leek (Figure 4), in spite of the twice longer cell size, the freezing occurs one cell by one cell.

The excited heat in the different crystal morphology, a linear shape, a spherulite, and a radial pattern are found in Figure 5, respectively. The bidirectional anisotropic heat propagation is observed in the crystallization of *n*-alkane. The emissivity correction before and after the phase change is important when thermal propagation is precisely extracted from the data.

#### 4.3. Application of the Phase Lock-In Technique

**4.3.1. The Effect of Noncontact Laser-Modulated Spot Heating during the Freezing of Onion-Skin Cells.** Figure 6 shows the phase and amplitude image of onion-skin cells irradiated with a laser-modulated spot heating under a temperature control, kept at a room temperature (Figures 6(A)–6(C)) or cooled at a constant rate (Figures 6(D)–6(I)).

The bright-colored cells in the subtracted image of Figure 6(D) indicate that it has been frozen under cooling,

with a simultaneous irradiation of a laser spot heating. The exothermic heat disturbs the modulated temperature field and the contour lines in the amplitude and phase image of Figures 6(F) and 6(I) are distorted in comparison with the contour image in Figure 6(C), where no exothermic heat is generated. The image in Figure 6 is captured with an InSb FPAs equipped with a micro lens.

A micro-scale laser-modulated spot heating is also captured with the uncooled IR camera systems (VOx FPAs) equipped with a micro lens. Figure 7 shows the examples of phase and amplitude thermal image of the polyimide film base copper clads laminates for flexible printed wiring boards scanned with a modulated laser irradiation.

The regular intervals of the contour lines in the phase image in Figures 7(B) and 7(C) indicate the homogeneous in-plane thermal diffusivity on the polyimide film region. On the other hand, if the spot heating is scanned between the copper wiring area (Figure 7(D)), the intervals of the phase contour lines become denser because of the higher and anisotropic thermal diffusivity of the copper leads area (Figure 7(E)). The higher the frequency is, thermal wave

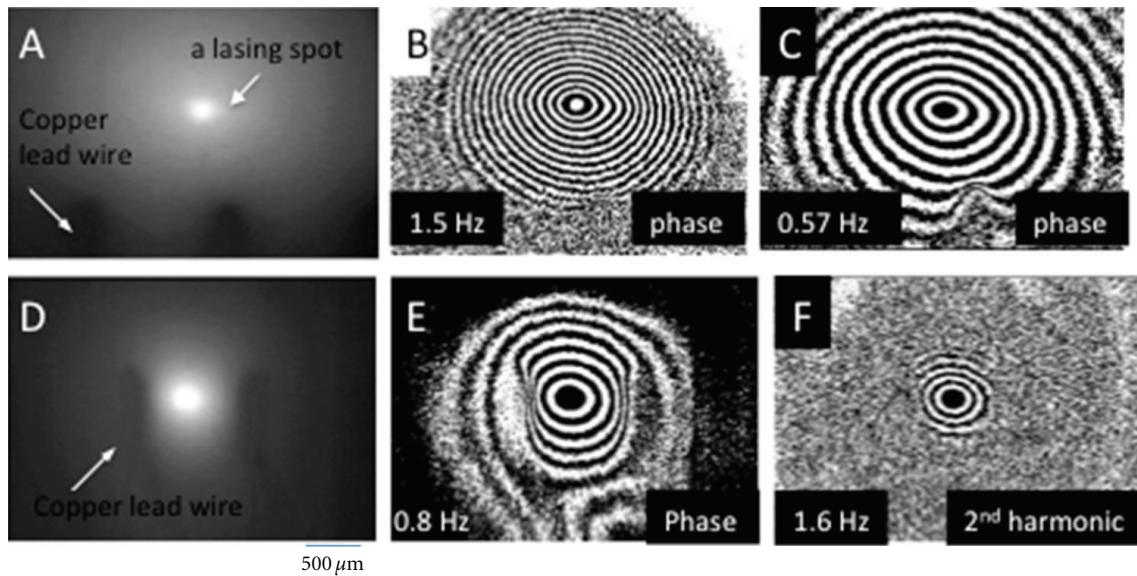


FIGURE 7: Phase-locked image with a contour line ((B), (C), (E), and (F)) in comparison with the raw image ((A), (D)) of the polyimide film base copper clads laminates for flexible printed wiring boards. The modulated frequencies are (B): 1.5 Hz, (C): 0.57 Hz, (E): 0.8 Hz, and (F): 1.6 Hz (2nd harmonic image of (E)), observed with the VOx IR FPA (25  $\mu\text{m}$  detector pitch) equipped with a  $\times 2.5$  magnification micro lens.

diminishes inside the wiring area and does not expand in the whole area of the film. The results in Figure 7 indicate the applicability of the micro-bolometer systems combined with the phase lock-in technique for the in-plane thermal characterization of the composite film.

## 5. Conclusion

The emissivity correction procedure and the phase-locked analysis are examined for the materials' thermal characterization both with the photon type and the thermal type IR detectors using the originally developed measuring systems. It will be of use to apply these results to mathematical processing to analyze the micro-scale thermal phenomena in order to develop the advanced materials.

## Acknowledgment

Support via a Grant from Japan Science and Technology Agency (Development of System and Technology for Advanced Measurement and Analysis) is gratefully acknowledged.

## References

- [1] O. Breitenstein, J. Bauer, K. Bothe et al., "Understanding junction breakdown in multicrystalline solar cells," *Journal of Applied Physics*, vol. 109, no. 7, Article ID 071101, 10 pages, 2011.
- [2] A. Rogalski, J. Antoszewski, and L. Faraone, "Third-generation infrared photodetector arrays," *Journal of Applied Physics*, vol. 105, no. 9, Article ID 091101, 44 pages, 2009.
- [3] T. Hashimoto and J. Morikawa, "Two-dimensional microscale thermal analysis of freezing of onion skin cells by high-speed infrared focal plane arrays," *Japanese Journal of Applied Physics*, vol. 42, no. 6, pp. L706–L708, 2003.
- [4] J. Morikawa, T. Hashimoto, E. Hayakawa, and H. Uemura, "Two-dimensional thermal analysis for freezing of plant and animal cells by high-speed microscopic IR camera," in *Thermosense XXV*, vol. 5073 of *Proceedings of SPIE*, pp. 148–153, April 2003.
- [5] J. Morikawa, T. Hashimoto, K. Yamamoto, and J. Ando, "Two-dimensional thermal analysis for freezing of endothelial cells by high-speed microscopic IR focal plane arrays," in *6th Conference on Biomedical Thermosacoustics, Optoacoustics, and Acousto-Optics—Photons Plus Ultrasound: Imaging and Sensing*, *Proceedings of SPIE*, pp. 282–290, January 2005.
- [6] J. Morikawa, T. Hashimoto, and T. Eto, "Two-dimensional thermal analysis of organic materials by IR thermography," in *Proceedings of the International Conference on Quantitative InfraRed Thermography (QIRT '06)*, Padua, Italy, June 2006, Paper no. 2006-036.
- [7] C. Pradere, J. Morikawa, J. C. Batsale, and T. Hashimoto, "Microscale thermography of freezing biological cells in view of cryopreservation," *Quantitative Infra Red Thermography Journal*, vol. 6, no. 1, p. 37, 2009.
- [8] J. Morikawa, T. Hashimoto, E. Hayakawa, and T. Eto, "Two-dimensional thermal analysis of organic materials by microscale thermography," in *International Conference on Quantitative InfraRed Thermography (QIRT '08)*, Krakov, Poland, July 2008.
- [9] J. Morikawa, E. Hayakawa, K. Ikuo, and T. Hashimoto, "Two-dimensional thermal analysis of organic molecular crystals and polymeric spherulites by microscale thermography," in *Thermosense XXXII*, vol. 7661 of *Proceedings of SPIE*, pp. 1–9, April 2010.
- [10] J. Morikawa, T. Hashimoto, E. Hayakawa, T. Eto, and R. Li Voti, "Thermal characterization of multi-layer polymer film by IR thermography," in *International Conference on Quantitative InfraRed Thermography (QIRT '08)*, Padua, Italy, June 2006, Paper no. 2006-020.

- [11] J. Morikawa, E. Hayakawa, and T. Hshimoto, "Thermal wave in a pulsed laser scanning system observed by a micro-scale thermography," in *Proceedings of the 1st Meditteranean International Workshop on Photoacoustic & Photothermal Phenomena*, Erice, Italy, July 2010.
- [12] J. Morikawa, E. Hayakawa, and T. Hashimoto, "Application of micro-scale thermography to the thermal analysis of polymeric and organic materials," in *Thermosense: Thermal Infrared Applications XXXIII*, vol. 8013 of *Proceedings of SPIE*, pp. 1–6, April 2011.

## Research Article

# Emissivity Measurement of Semitransparent Textiles

**P. Bison, A. Bortolin, G. Cadelano, G. Ferrarini, and E. Grinzato**

*ITC, CNR, Corso Stati Uniti 4, 35127 Padova, Italy*

Correspondence should be addressed to P. Bison, [paolo.bison@itc.cnr.it](mailto:paolo.bison@itc.cnr.it)

Received 10 August 2012; Revised 14 November 2012; Accepted 22 November 2012

Academic Editor: Laura Abbozzo Ronchi

Copyright © 2012 P. Bison et al. This is an open access article distributed under the Creative Commons Attribution License, which permits unrestricted use, distribution, and reproduction in any medium, provided the original work is properly cited.

In the textiles production industry it is more and more common to advertise new textiles, especially for sportswear, by claiming their ability to emit IR radiation in the long wave band at a higher degree with respect to normal clothes, that is highly beneficial to improve sporting performances. Three textiles are compared, one normal and two “special,” with  $\text{Ag}^+$  ions and carbon powder added, with different colors. The emissivity of the textiles has been measured to determine if it is increased in the “special” textiles with respect to the normal one. No substantial increase has been noticed. Nonetheless, the test implied some nonstandard procedures due to the semitransparent nature of the textiles, in comparison with the normal procedure that is commonly used on opaque surfaces.

## 1. Introduction

Two textiles are made of polypropylene (PP) and charged with  $\text{Ag}^+$  ions and Carbon powder. They differ from the color that is green for the first and blue for the second. They are compared with a third “normal” PP textile of green color and the same weft of the previous. The purpose is to demonstrate if the emissivity in the Infrared-Long Wave band (IR-LW) [1–3] of the charged textiles is increased or not due to the presence of the charging elements.

The measurement is carried out in the wavelength interval 8–14  $\mu\text{m}$ ; it is an integral measurement; that is, it represents the average value of the spectral emissivity in the considered interval [4].

The measurement is carried out by means of a microbolometric camera that exhibits an almost flat spectral response at the various wavelengths. Therefore, it is not taken into account any spectral response of the detector even because of the comparative nature of the measurement [5, 6].

Any evaluation of the taking angle is neglected and so the dependence of the emissivity with the view angle. The measurement is performed with a normal view with respect to the textiles [7].

The measurement technique consists in laying down the charged textiles, to be measured, and the “normal” (the reference) one, side by side and in contact with a thick

aluminum plate that is assumed to be as much isothermal as possible. Observing the two textiles (that own the same temperature) by an IR camera allows to evaluate the IR radiation emitted by their surfaces. The possible difference in the radiation collected by the IR camera in correspondence of the “measured” textiles and the “reference” one is due to the emissivity difference. In this case the measurement is more difficult than the one for an opaque surface in so far the textiles are semitransparent and the radiation collected by the camera is due to the contribution of the textiles themselves plus the background, each one emitted with its own emissivity and weighted by the surface fraction that it covers. Therefore, a preliminary assessment of the transmittance coefficient of the textiles is done in such a way to determine the percentage of radiation emitted by the textiles themselves and the percentage that they transmit, coming from the background.

## 2. Equations Related to the Emissivity Measurement

In case of an opaque object at temperature  $T_o$  and emissivity  $\epsilon_m$  and with a surrounding environment at temperature  $T_a$  the radiance measured by the IR camera is given by [8]

$$I_m = \epsilon_m I_o + (1 - \epsilon_m) I_a, \quad (1)$$

where  $\varepsilon_m I_o$  is the radiance emitted by the object surface and  $(1 - \varepsilon_m)I_a$  is the radiance generated by the environment and reflected by the object surface. In (1) the effect of the absorption and emission of radiation by the atmosphere is neglected due to the small distance between the camera and the object. In case of comparative measurement, in which one material is the reference (subscript  $r$ ) and the other is the measured one (subscript  $m$ ) the ratio between the two emissivities is given by

$$R = \frac{\varepsilon_m}{\varepsilon_r} = \frac{I_m - I_a}{I_r - I_a}, \quad (2)$$

where  $I_r$ ,  $I_m$ , and  $I_a$  are the radiances measured by the camera in correspondence of the reference material, the measured material, and the environment, respectively.

In case of semitransparent material, as it is the case of the textiles, (1) is transformed in

$$I_m = (1 - \tau_m)[\varepsilon_m I_o + (1 - \varepsilon_m)I_a] + \tau_m I_s, \quad (3)$$

where  $\tau_m$  is the transmittance coefficient of the textiles (that is the one's complement of the surface percentage covered by the textiles) and  $I_s$  is the radiance emitted by the surface of the metallic plate on which the textiles are laid down and that is heated at a constant temperature during the measurement. In case of the comparative measurement of semitransparent materials with transmittance coefficients  $\tau_m$  and  $\tau_r$ , respectively, for the measured and reference textiles, one obtains

$$R_{st} = \frac{\varepsilon_m}{\varepsilon_r} = \frac{1 - \tau_r}{1 - \tau_m} \frac{I_m - I_a - \tau_m(I_s - I_a)}{I_r - I_a - \tau_r(I_s - I_a)}. \quad (4)$$

### 3. Measurement Uncertainty Analysis

The evaluation of the ratio  $R_{st}$  by means of (4) requires the measurement of six quantities. Each one is measured many times (some tenths for transmittances to some thousands for radiances). The statistical evaluation of (4) is therefore necessary, together with its uncertainty by means of the uncertainties propagation:

$$\delta R_{st} = \sqrt{\left[ \left[ \frac{\partial R_{st}}{\partial \tau_r} \delta \tau_r \right]^2 + \left[ \frac{\partial R_{st}}{\partial \tau_m} \delta \tau_m \right]^2 + \left[ \frac{\partial R_{st}}{\partial I_r} \delta I_r \right]^2 \cdots \right.} \\ \left. \cdots \left[ \frac{\partial R_{st}}{\partial I_m} \delta I_m \right]^2 + \left[ \frac{\partial R_{st}}{\partial I_a} \delta I_a \right]^2 + \left[ \frac{\partial R_{st}}{\partial I_s} \delta I_s \right]^2 \right}, \quad (5)$$

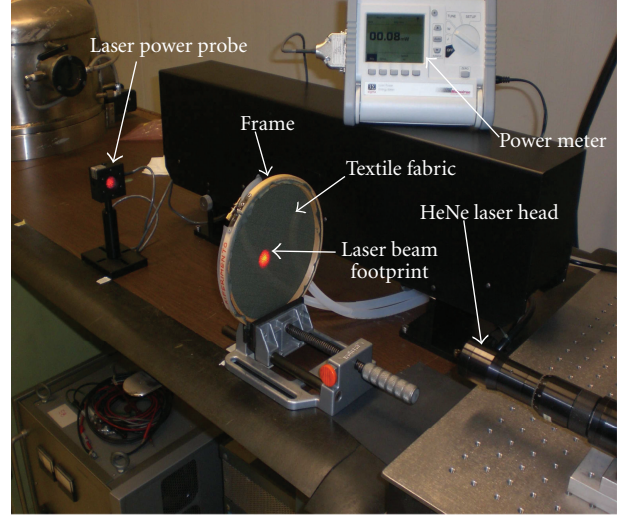


FIGURE 1: Experimental layout for the transmittance measurement in the optical wavelength range.

where the uncertainties  $\delta \tau_r, \delta \tau_s, \dots, \delta I_s$  have been estimated by their standard deviation and the partial derivatives of  $R_{st}$  are given by

$$\frac{\partial R_{st}}{\partial \tau_r} = R_{st} \left[ \frac{I_s - I_a}{I_r - (1 - \tau_r)I_a - \tau_r I_s} - \frac{1}{1 - \tau_r} \right],$$

$$\frac{\partial R_{st}}{\partial \tau_m} = R_{st} \left[ \frac{1}{1 - \tau_m} - \frac{I_s - I_a}{I_m - (1 - \tau_m)I_a - \tau_m I_s} \right],$$

$$\frac{\partial R_{st}}{\partial I_r} = R_{st} \frac{-1}{I_r - (1 - \tau_r)I_a - \tau_r I_s},$$

$$\frac{\partial R_{st}}{\partial I_m} = R_{st} \frac{1}{I_m - (1 - \tau_m)I_a - \tau_m I_s}, \quad (6)$$

$$\frac{\partial R_{st}}{\partial I_a} = R_{st} \left[ \frac{1 - \tau_r}{I_r - (1 - \tau_r)I_a - \tau_r I_s} - \cdots \right],$$

$$\frac{\partial R_{st}}{\partial I_s} = R_{st} \left[ \frac{\tau_r}{I_r - (1 - \tau_r)I_a - \tau_r I_s} - \cdots \right].$$

### 4. Experimental Apparatus for Transmittance Measurement

The measurement apparatus for the transmittance evaluation consists of a Continuous Wave HeNe laser with emission at the wavelength  $\lambda = 632.8$  nm, at a power of 10 mW. The beam is expanded to an FWHM of almost 2 cm. The power of the beam is measured by a suitable detector connected to a power meter, once without any obstacle in the optical path and then with the textiles in between. From the ratio of the measured power with and without the textiles, the transmittance is obtained. See Figure 1.

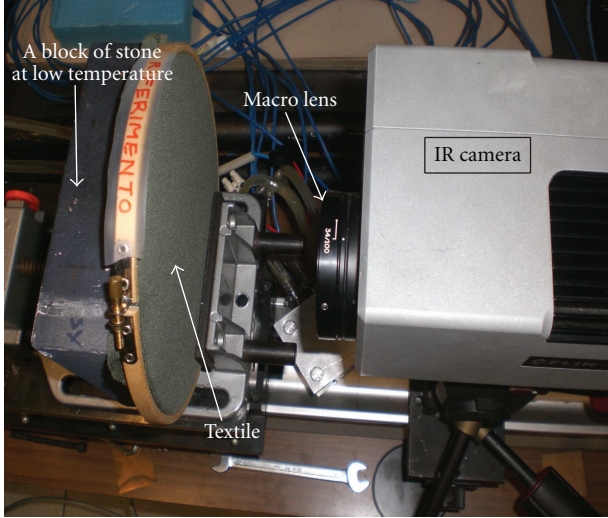


FIGURE 2: Experimental layout for the transmittance measurement in IR wavelength range.

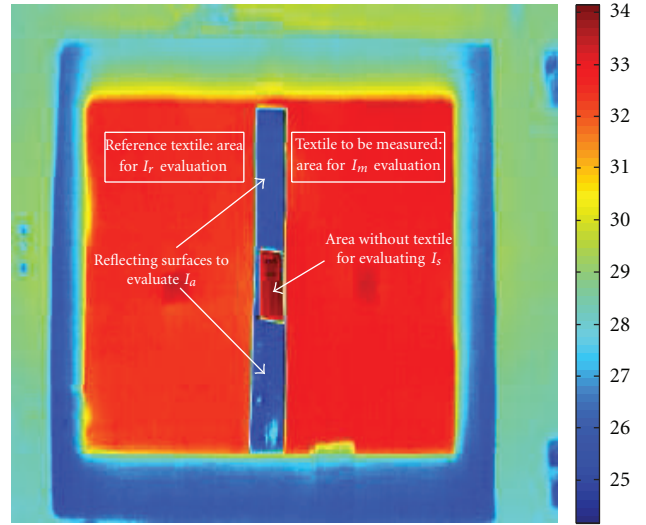


FIGURE 4: IR image relative to Figure 3. See the indication of the areas utilized to evaluate (4).

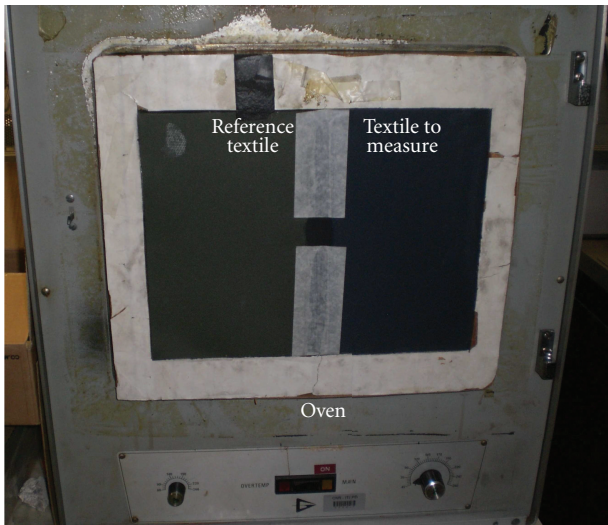


FIGURE 3: Experimental layout for the emissivity measurement.

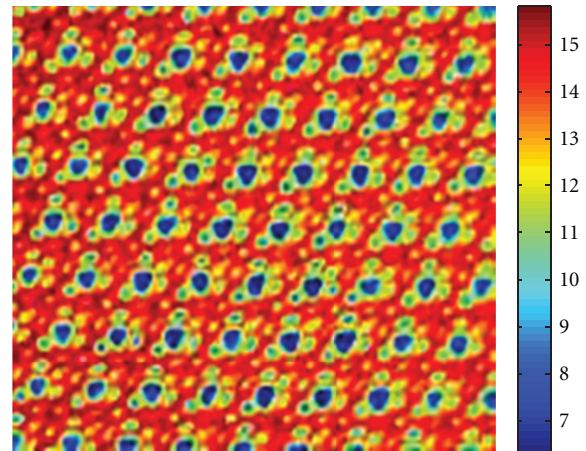


FIGURE 5: Results of the transmittance measurement in the IR. Notice the regular appearance of the cold background areas.

TABLE 1: Results of the transmittance measurement by laser attenuation.

Textiles	Transmittance Mean $\pm$ standard dev.
RV	0.13 $\pm$ 0.02
CV	0.14 $\pm$ 0.02
CB	0.15 $\pm$ 0.02

A possible objection to the assessment of the transmittance as described above is connected to the wavelength of the laser source that is 20 times smaller of the radiation considered in the emissivity evaluation. On purpose a second experimental layout has been prepared. An IR camera with a macro lens ( $\sim 100 \mu\text{m}/\text{pixel}$ ) observes a cold background

through the textiles at ambient temperature. The background object has no contact with the textiles, avoiding any conduction effect. See Figure 2.

### 5. Experimental Apparatus for Emissivity Measurement

The measurement apparatus is composed of an aluminum plate 2 cm thick, on which the reference and measured textiles are laid down side by side. The plate is successively inserted on the opening of an oven from which it receives heat. The aluminum plate guarantees the uniformity of the temperature of the textiles. An IR camera observes the textiles that are heated at a temperature of 35-36°C, around the human body temperature. See Figure 3.

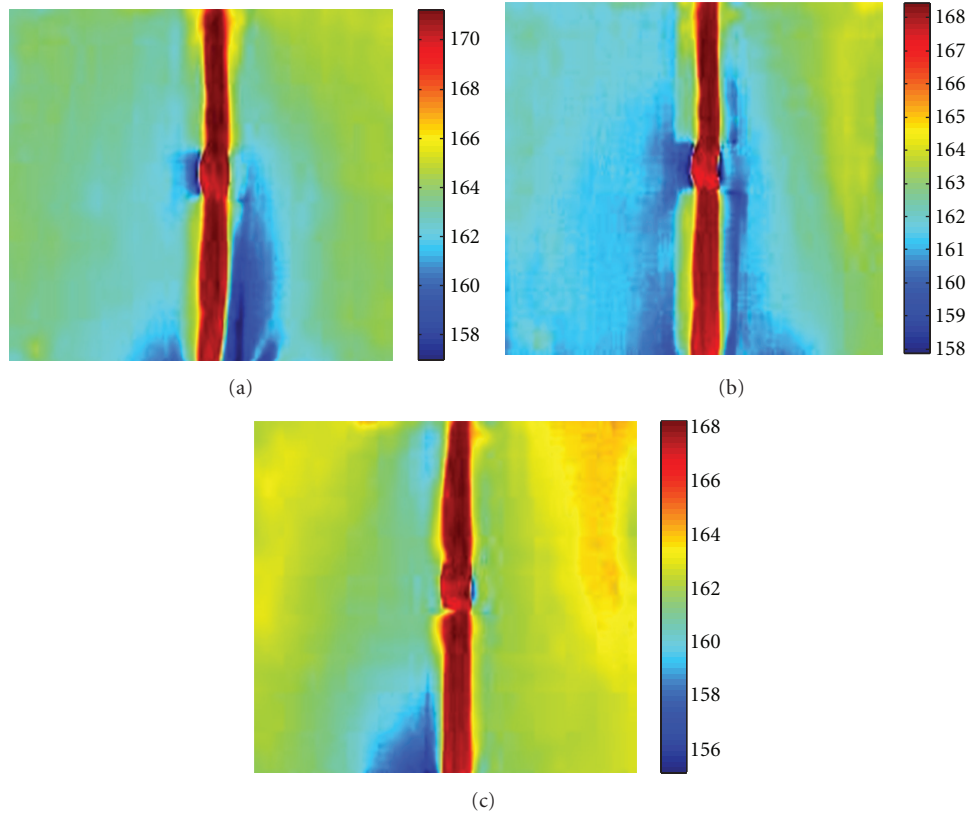


FIGURE 6: (a) Textiles RV on left and CV on right; (b) textiles RV on left and CB on right; (c) textiles CV on left and CB on right.

In the successive Figure 4 the IR image relative to Figure 3 is shown. The areas utilized for the radiance measurements, according to (4) are indicated.

## 6. Measurements of Transmittance by Laser

The measurements have been carried out on three textiles: the reference one of green color RV, the charged one of green color CV, and the charged one of blue color CB. Each textile has been positioned at 1/4, 1/2, and 3/4 of the laser beam optical path between the laser head and the detector. For each position the measurement has been repeated four times, for a total of 12 measurements. The results with mean values and standard deviations are reported in Table 1.

A second transmittance measurement has been carried out in the IR. Figure 5 shows the IR image of the textiles with some cold areas regularly disposed in the image. The measurement in this case consists in determining the percentage of cold areas in comparison with the total area. The weakness of this technique is related to the arbitrary threshold that should discriminate between cold and hot areas. By varying the threshold between 10.0 and 11.0°C one obtains a transmittance value between 0.116 and 0.170. By choosing a threshold at 10.5°C one obtains a transmittance of 0.142 close to the values obtained with the laser attenuation technique.

TABLE 2: Results of the emissivity ratio according to (4).

Textiles	$R_{st}$
	Mean $\pm$ standard dev.
RV-CV	$1.036 \pm 0.065$
RV-CB	$1.061 \pm 0.053$
CV-CB	$1.059 \pm 0.065$

## 7. Emissivity Measurement

Three experiments have been carried out:

- (i) in the first, the reference textile RV is on the left and the charged green textile CV is on the right, see Figure 6(a);
- (ii) in the second, RV is on the left while the charged textile of blue color is on the right, see Figure 6(b);
- (iii) in the third, two charged textiles are directly compared: CV on the left and CB on the right, see Figure 6(c).

The IR images and the computations are done in Object Signal, units furnished directly by the IR camera software, before the transformation in temperature unit, and proportional to radiance.

In Table 2 the results are reported.

## 8. Conclusion

The CV textile shows an emissivity 3.6% higher than the RV. The CB textile presents an emissivity 5.3% higher than RV. The measurements are affected by an uncertainty of about 5%, that means the differences in emissivity are comparable to the measurement error. The last test, that directly compares the two charged textiles, shows that the blue textile has an emissivity higher than the green one. From these considerations one could guess that the colors used in the textiles affect emissivity more than the charging elements.

## Acknowledgment

This work has been financed by the fabrics company IDEE PER IL TESSILE.

## References

- [1] Wikipedia Contributors, *Emissivity*—*Wikipedia, the Free Encyclopedia*, 2010.
- [2] X. P. V. Maldague, *Theory and Practice of Infrared Technology for Nondestructive Testing*, Wiley-Interscience, 2001.
- [3] X. P. V. Maldague, Ed., *Infrared and Thermal Testing*, American Society for Nondestructive Testing, 3rd edition, 2001.
- [4] R. Siegel and J. R. Howell, *Thermal Radiation Heat Transfer*, Hemisphere, 1981.
- [5] F. Bertrand, J. L. Tissot, and G. Destefanis, "Second generation cooled infrared detectors state of the art and prospects," in *Proceedings of the 4th International Workshop on Advanced Infrared Technology and Applications*, L. Ronchi Abbozzo, Ed., Fondazione Vasco Ronchi, 1997.
- [6] W. D. Rogatto, Ed., *Electro-Optical Components*, vol. 3 of *The Infrared and Electro-Optical Systems Handbook*, ERIM and SPIE Optical Engineering Press, 1993.
- [7] H. C. Hottel and A. F. Sarofim, *Radiative Transfer*, McGraw-Hill Book Company, 1967.
- [8] R. P. Madding, "Emissivity measurement and temperature correction accuracy considerations," in *Thermosense XXI*, vol. 3700 of *Proceedings of SPIE*, pp. 393–401, April 1999.

## Research Article

# Infrared Camera Analysis of Laser Hardening

**J. Tesar, P. Vacikova, O. Soukup, and S. Houdkova**

*New Technologies-Research Centre, University of West Bohemia, Univerzitni 8, 30614 Plzeň, Czech Republic*

Correspondence should be addressed to J. Tesar, tesar@ntc.zcu.cz

Received 10 August 2012; Accepted 5 November 2012

Academic Editor: Antoni Rogalski

Copyright © 2012 J. Tesar et al. This is an open access article distributed under the Creative Commons Attribution License, which permits unrestricted use, distribution, and reproduction in any medium, provided the original work is properly cited.

The improvement of surface properties such as laser hardening becomes very important in present manufacturing. Resulting laser hardening depth and surface hardness can be affected by changes in optical properties of material surface, that is, by absorptivity that gives the ratio between absorbed energy and incident laser energy. The surface changes on tested sample of steel block were made by engraving laser with different scanning velocity and repetition frequency. During the laser hardening the process was observed by infrared (IR) camera system that measures infrared radiation from the heated sample and depicts it in a form of temperature field. The images from the IR camera of the sample are shown, and maximal temperatures of all engraved areas are evaluated and compared. The surface hardness was measured, and the hardening depth was estimated from the measured hardness profile in the sample cross-section. The correlation between reached temperature, surface hardness, and hardening depth is shown. The highest and the lowest temperatures correspond to the lowest/highest hardness and the highest/lowest hardening depth.

## 1. Introduction

Laser hardening is one of the modern possibilities of improving surface properties of the metallic materials. It is a characteristic of the laser surface hardening process that the material is rapidly heated to a high temperature by guiding the laser beam across the workpiece surface. Short times of interaction between the laser beam and the workpiece surface cause that the absorbed energy is concentrated only at the workpiece surface, whereas the core remains cold. The removal of heat from the surface layer to the colder unaffected metal of a machine part permits rapid cooling and formation of a hardened microstructure required at the workpiece surface.

Parts of hardened surface can be manufactured separately each with different final properties. The final hardness and hardening depth depend primarily on the beam irradiance on the surface of the workpiece, the processing rate, and the thermophysical properties of the material. A low interaction time and a high power result in a shallow hardening depth whereas the converse results in a deeper hardening depth [1]. The parameter that can affect the final properties is the amount of energy accepted from the incident laser beam. This can be changed by corrections of optical properties of

the surface absorptivity. The influence of different types of absorbing coatings on specimen surfaces and measurement of IR radiation with a photodiode was presented in [2]. The depth of hardening with and without different coatings was compared in [3]; the connection between surface temperature and absorptivity was emphasized. An infrared camera was used in [4] for process characterization, control, and temperature field monitoring.

An infrared camera ThermaCAM SC3000 was used in [5] for temperature fields measurements during hardening of a cylinder rotating under a laser beam (CO<sub>2</sub>, 1.5 kW, 10.6 μm). The view of the camera was under angle of 30° from the laser beam. The emissivity was set to the value of 0.88, corresponding to the applied surface coating, which was used to improve absorptivity.

The same camera but under angle of 53° from the laser beam of direct diode laser (Nuvonix ISL-4000L, 4 kW, and 805 nm) was used in [6]. The emissivity of the sample was estimated during the heating with the propane torch in order to see how emissivity changes with temperature.

In this work an engraving laser is used to obtain surfaces with different optical properties that depend on the parameters of the engraving laser—its wavelength, energy, repetition frequency, and scanning velocity (velocity of laser

moving). The emissivity for the IR camera measurement is estimated after experiment from an image of infrared camera (thermogram) of the sample that is heated on a hot plate.

The aim of this work is to demonstrate that due to different parameters of engraving laser (repetition frequency and scanning velocity) are reached different surface temperatures by laser hardening caused by different absorptivity on engraved surfaces. The surface temperature has a direct connection with hardening depth and hardness distribution [2, 3, 5]. This way is possible to control surface hardness and hardening depth without change of hardening laser power, for example, for precise hardening of small details on the processed surface.

## 2. Theoretical Assumptions

Incident, reflected, absorbed, and transmitted fluxes are connected together by energy conservation law. From this fact can be deduced that the sum of optical properties reflectivity ( $\rho$ ), absorptivity ( $\alpha$ ), and transmissivity ( $\tau$ ) equals one [7]:

$$\rho + \alpha + \tau = 1. \quad (1)$$

For an opaque object without transmission ( $\tau = 0$ ) the relation (1) simplifies

$$\rho + \alpha = 1. \quad (2)$$

Kirchhoff's law provides a link between the absorption and emission processes and thus between emissivity and absorptivity

$$\varepsilon = \alpha. \quad (3)$$

These relations are valid for similar spectral or total spectral condition.

In this case there are three sets of optical properties (three different wavelengths) for that Kirchhoff's law is valid. The three wavelengths are wavelength of engraving laser 1064 nm, wavelength of hardening laser 808 nm, and the range of infrared camera 7.5–13  $\mu\text{m}$ . This means that, for example, emissivity of surface in range of infrared camera  $\varepsilon_{\text{IR}}$  has no direct connection with absorptivity on wavelength of hardening laser  $\alpha_{\text{HPDD}}$ .

## 3. Experimental Settings

The investigated sample is a block of steel 95MnWCr5 of dimensions 105  $\times$  65  $\times$  15 mm with 30 squares of size 5  $\times$  5 mm made by laser engraving on the surface of the largest side. The engraving was made with different repetition frequency of laser and scanning velocity. Marking-Laser System BLS-100 (SHT) was used. It contains pulsed Nd:YAG laser of wavelength 1064 nm. The parameters of engraving make a matrix with repetition frequencies  $f$  of 2, 5, 7, 15, 30, and 80 kHz and scanning velocities  $v$  of 20, 50, 100, 300, and 500 mm/s—see Figure 1.

This sample then undergoes laser hardening with continuous HPDD (high power direct diode) laser HighLight

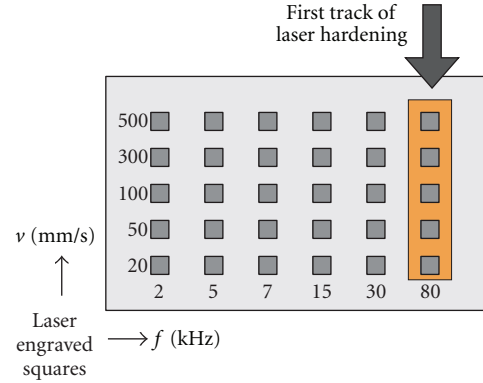


FIGURE 1: Arrangement of engraved squares on the sample surface.

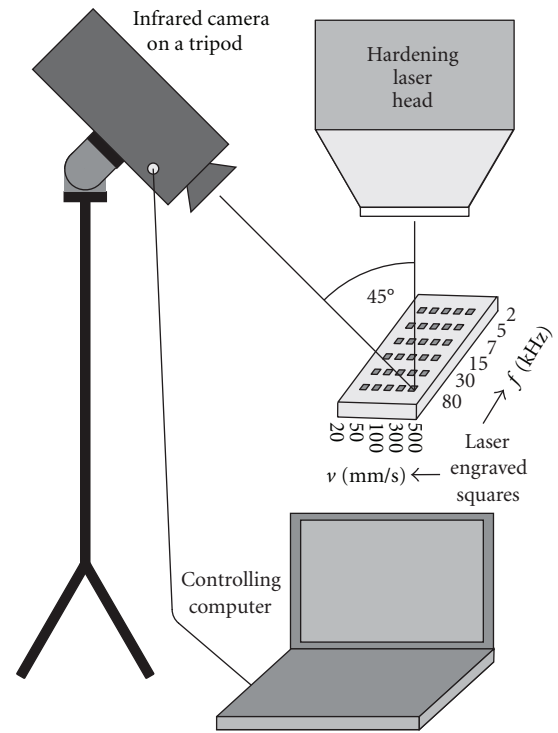


FIGURE 2: Scheme of laser hardening arrangement—laser head on the robotic arm, computer controlled infrared camera on a tripod, and investigated sample.

ISL-4000L (Coherent). The laser working head is placed on the robotic arm (Figure 2, photo on Figure 3). It works on wavelength 808  $\pm$  10 nm and the maximal possible power is 4 kW. The laser spot has rectangular shape of dimensions 6  $\times$  12 mm with Gaussian energetic profile on the 6 mm long side and uniform energetic profile on the longer side. The distance between laser head and sample is 12 cm. The laser treating consists of six tracks. The first track begins on square made with highest repetition frequency (80 kHz) and scanning velocity of engraving (500 mm/s) and continues with squares of lower scanning velocity—see Figure 1. Next tracks are columns of lower repetition frequencies.

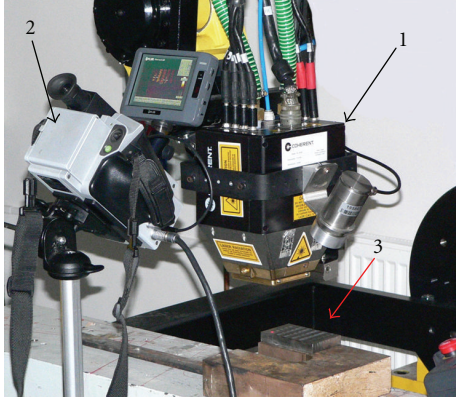


FIGURE 3: Photo of laser hardening arrangement—(1) laser head on the robotic arm, (2) infrared camera, and (3) investigated sample.

The process of laser hardening is measured with computer controlled infrared camera system ThermoCAM SC2000 by company FLIR—photo in Figure 3. It measures emitted infrared radiation in the wavelength range 7.5–13  $\mu\text{m}$  and depicts it in a form of temperature field of measured object surface with resolution  $320 \times 240$  pixels (uncooled microbolometer FPA detector). The infrared camera has measurement accuracy  $\pm 2\%$ , temperature resolution  $0.1^\circ\text{C}$ , and range from  $-40^\circ\text{C}$  up to  $+2000^\circ\text{C}$  divided into three regions. The first region, intended for room temperatures, ranges from  $-40^\circ\text{C}$  to  $+120^\circ\text{C}$ , the middle from  $80^\circ\text{C}$  to  $500^\circ\text{C}$  and region for very high temperatures from  $350^\circ\text{C}$  up to  $2000^\circ\text{C}$ . The camera is placed on a tripod mount and grips with the laser beam angle approximately of  $45^\circ$ . This position is chosen to prevent damaging IR camera by the laser beam reflected from the sample. Another reason is that the laser spot and hot trace are clearly seen and the laser head is not visible in the infrared image.

#### 4. Measurement

Each engraved square has a different value of emissivity and these values are not known so the emissivity value of the whole image is set to  $\varepsilon = 1$  in the infrared camera. Emissivities are set to correct values by postprocessing. The filter (temperature range) from  $350^\circ\text{C}$  to  $2000^\circ\text{C}$  is selected. The value of distance between camera and sample is set to 0.5 m and atmospheric and ambient temperatures to  $23^\circ\text{C}$ . The recording of thermograms (images captured by infrared camera) runs with frequency of 50 Hz. After the end of laser hardening one image is captured with a filter suitable for room temperatures. The treating laser moves with velocity 1200 mm/min and works with power of 60% in the first column (80 kHz of engraving laser) and with 70% in other cases. The sample surface after laser hardening of all columns is shown in Figure 4.

After laser hardening the emissivity of all engraved squares was measured using a method of known (constant) temperature. The surface in surroundings of engraved squares was painted with a color of known emissivity and



FIGURE 4: The sample surface after laser hardening.

TABLE 1: Emissivities of engraved areas in the range of infrared camera 7.5–13  $\mu\text{m}$ .

$f$ (kHz)/ $v$ (mm/s)	2	5	7	15	30	80
500	0.80	0.71	0.70	0.79	0.90	0.16
300	0.75	0.71	0.75	0.73	0.86	0.21
100	0.69	0.80	0.84	0.83	0.75	0.40
50	0.77	0.82	0.85	0.88	0.80	0.60
20	0.85	0.89	0.92	0.95	0.90	0.79

the sample was placed on electrically heated plate. After temperature stabilizing (at  $220^\circ\text{C}$ ) a thermogram was captured and the emissivities of engraved areas were determined from equality of temperatures. This proved that every engraved square has different emissivity strongly dependent on parameters of engraving (Table 1).

The whole sample was cut to 30 pieces according to engraved squares after the determination of emissivity and analyzed on automatic microhardness testing system OmniMet MHT (Buehler). Surface hardness HV10 was analyzed and the hardening depth was determined from the profile of microhardness HV0.3 in the sample cross-section.

#### 5. Postprocessing

The infrared images of laser hardening were recorded and saved in the form of sequences and one single IR image of hot sample after laser hardening. All sequences and images were evaluated in software ThermoCAM Researcher. The postprocessing procedure started with the single image that was captured with a filter suitable for room temperatures immediately after the end of laser hardening. The sample remained a little hot so the engraved squares with different emissivities and all details were clearly seen (Figure 5).

It was much easier to place single analyzed points with corresponding emissivities to correct places (into the centre of engraved squares) in this picture than in picture of laser hardening made with filter for high temperatures.

With correctly placed analyzed points were loaded six sequences of laser hardening (Figure 6). Each sequence corresponds to one column (engraving laser repetition frequency) and was evaluated separately.

The temporal dependence of temperatures from these points for the second run of hardening laser (30 kHz of

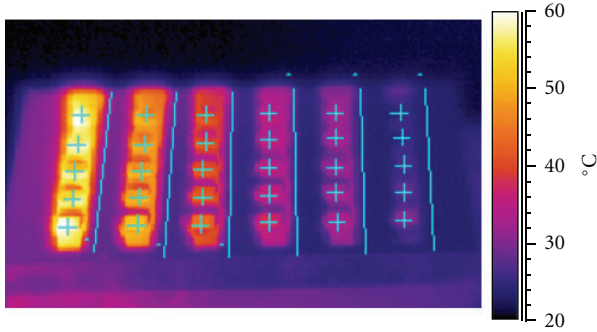


FIGURE 5: The thermogram of the sample captured with filter for room temperatures immediately after laser hardening.

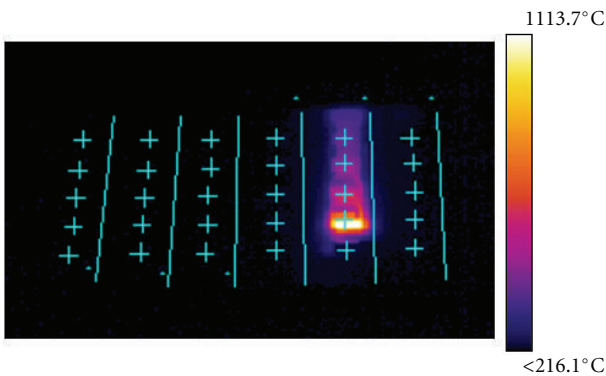


FIGURE 6: Thermogram of the sample during second track of laser hardening, analyzed points.

engraving laser) is shown in Figure 7. The time consequence of temperature peaks of analyzing points in centers of engraved squares is clearly seen. Each temperature temporal dependence curve begins with increase of temperature then continues short peak and then with an exponential decrease of temperature. The minimum of temperature that can be measured with IR camera using measurement range for region of high temperatures is  $215^{\circ}\text{C}$ .

From curves of Figure 7 (500–50 mm/s) could be seemed that the maximal values of temperature increase with decreasing emissivity of the engraved squares shown in Table 1. But it is not true. The maximal temperature depends on the amount of absorbed energy brought in the material by hardening laser that is not equal for all squares because of different absorptivity on the wavelength of 808 nm. This absorptivity has no direct connection with emissivity on the wavelength range of infrared camera  $7.5\text{--}13\ \mu\text{m}$ .

### 6. Results

In Figure 8 is shown that the maximal temperature  $1505^{\circ}\text{C}$  was reached on the square with parameters of engraving laser of 20 mm/s and 15 kHz and the lowest temperature  $1070^{\circ}\text{C}$  with parameters 500 mm/s and 30 kHz.

Absolutely the lowest temperature  $901^{\circ}\text{C}$  was reached with parameters 300 mm/s and 80 kHz but whole this

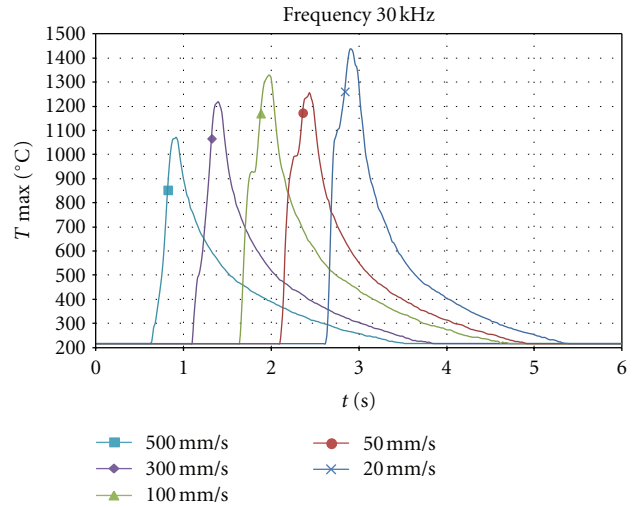


FIGURE 7: Temporal dependence of maximal temperatures in engraved areas for second run of hardening laser.

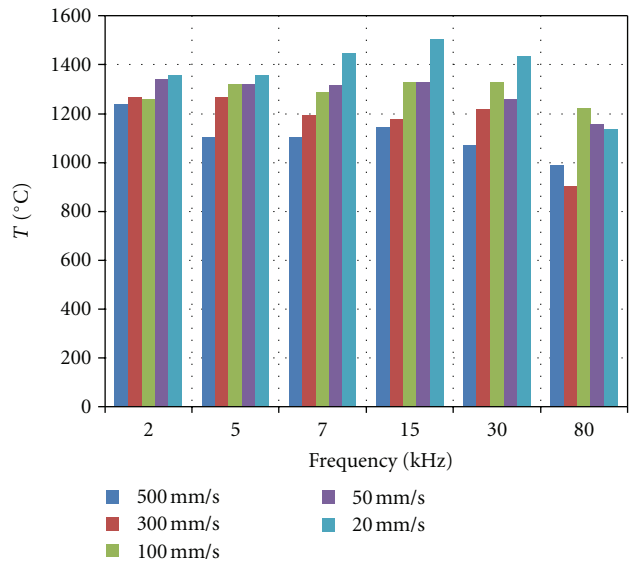


FIGURE 8: Maximal temperatures reached on the engraved squares during run of hardening laser.

column (80 kHz) was made with power of hardening laser 60% and other columns with power 70%. From Figure 8 it can be also seen that maximal temperature is reached on the squares that were made with the lowest scanning velocity of engraving laser 20 mm/s and the minimal temperature on squares made with scanning velocity 500 mm/s. This is valid with exception of the run of hardening laser with lower power.

The measured surface hardness HV10 and the hardening depth of analyzed squares made with repetition frequency of engraving laser 30 kHz (second track of hardening laser) are depicted in Figure 9. The maximal reached temperatures are written above each column corresponding to the scanning velocity of engraving laser.

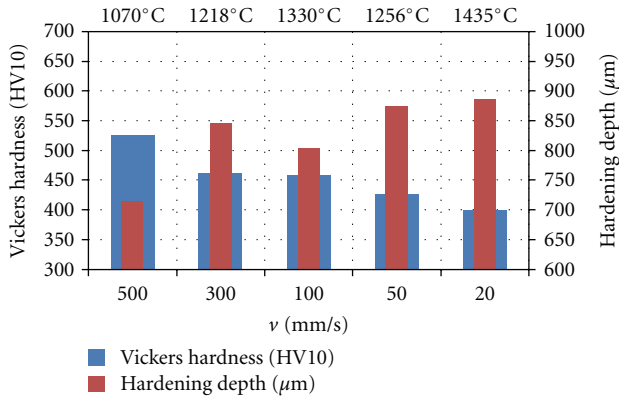


FIGURE 9: The dependence of surface hardness and hardening depth after HPDD laser hardening on scanning velocity of engraving laser by repetition frequency of 30 kHz.

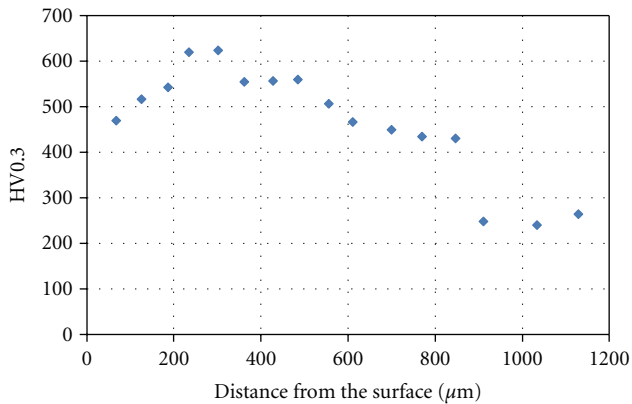


FIGURE 10: The microhardness depth profile on the sample cross-section of the square that was engraved with parameters 30 kHz and 300 mm/s.

Surface hardness was determined from averaging of five measurements on different places of hardened square surface. The hardening depth was estimated according to big change of hardness values in depth profile (Figure 10) and verified with visual measurement of the sample cross-section on digital microscope Hirox KH-7700 (Hirox) (Figure 11).

The value of hardening depth (square with parameters 30 kHz and 300 mm/s) was estimated to 846 μm because in this depth occurred a big decrease of microhardness HV0.3 from value 431 (depth 846 μm) to value 239 (depth 910 μm).

The hardening depth correlates with the reached temperature; higher temperature means bigger depth of hard material [2, 3]. The results of hardness measurement and measurement of hardening depth in connection with surface temperature measured during laser hardening by infrared camera agree with conclusions stated in [2, 3]. Exception makes only temperature 1330°C (square 100 mm/s) when the Vickers hardness should be lower and hardening depth higher than in case of temperature 1256°C (square 50 mm/s) (Figure 12).

The higher surface hardness by lower surface temperatures (Figure 12) is caused by higher cooling rate to bulk

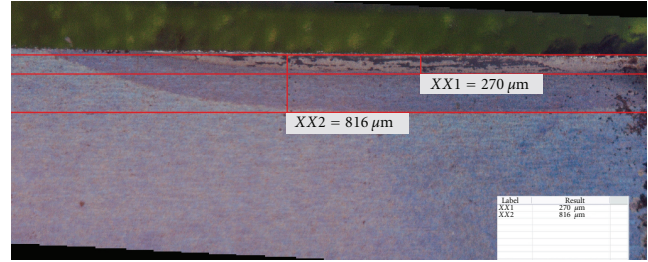


FIGURE 11: The enlarged picture of the sample cross-section through the square with parameters 30 kHz and 300 mm/s made by optical microscope Hirox. There are marked depths of regions with changed structure (270 μm) and temperature affected area (816 μm).

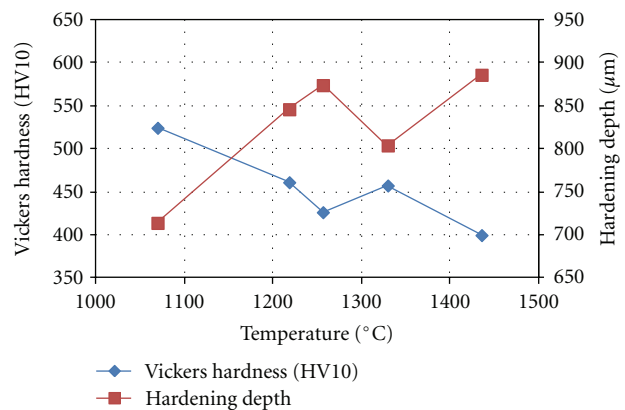


FIGURE 12: The dependence of surface hardness and hardening depth on the temperature reached on squares made by engraving laser by repetition frequency of 30 kHz.

material. The cooling rate by higher surface temperatures is lower because the bulk material has higher temperature in the same depth due to bigger amount of absorbed laser energy. Higher temperature in the depth of material results in higher hardening depth by higher surface temperatures.

## 7. Conclusion

The possibilities of using engraving laser to affect surface absorption of hardening laser were shown in this contribution. The differences in absorptivity cause big differences in surface temperature that is measured with an infrared camera during laser hardening process. Reached surface temperature is directly connected with hardness and hardening depth. Maximal temperatures of all squares are determined and compared together. The result is that the maximal temperature increases with decreasing scanning velocity of engraving laser. The column with repetition frequency of engraving laser 30 kHz was selected for detailed analysis. Hardness and hardening depth estimated from the hardness profile in the sample cross-section were evaluated. The hardening depth was verified by optical microscope. The results prove that the higher surface temperature reached by

laser hardening means bigger depth of hard material and lower surface hardness.

## Acknowledgments

This paper is based upon work sponsored by the Project no. SGS-2010-083 of the University of West Bohemia in Pilsen. The result was developed within the CENTEM Project, reg. no. CZ.1.05/2.1.00/03.0088, that is cofunded from the ERDF within the OP RDI program of the Ministry of Education, Youth and Sports of Czech Republic. The authors of the paper do not have a direct financial relation with the mentioned commercial identities.

## References

- [1] E. Kennedy, G. Byrne, and D. N. Collins, "A review of the use of high power diode lasers in surface hardening," *Journal of Materials Processing Technology*, vol. 155-156, no. 1–3, pp. 1855–1860, 2004.
- [2] J. Grum and T. Kek, "The influence of different conditions of laser-beam interaction in laser surface hardening of steels," *Thin Solid Films*, vol. 453-454, pp. 94–99, 2004.
- [3] V. S. Kovalenko and D. F. Dauw, "Ways to intensify laser hardening technology," *CIRP Annals*, vol. 47, no. 1, pp. 133–136, 1998.
- [4] H. Attia, S. Tavakoli, R. Vargas, and V. Thomson, "Laser-assisted high-speed finish turning of superalloy Inconel 718 under dry conditions," *CIRP Annals*, vol. 59, no. 1, pp. 83–88, 2010.
- [5] R. Patwa and Y. C. Shin, "Predictive modeling of laser hardening of AISI5150H steels," *International Journal of Machine Tools and Manufacture*, vol. 47, no. 2, pp. 307–320, 2007.
- [6] S. Skvarenina and Y. C. Shin, "Predictive modeling and experimental results for laser hardening of AISI 1536 steel with complex geometric features by a high power diode laser," *Surface and Coatings Technology*, vol. 201, no. 6, pp. 2256–2269, 2006.
- [7] X. P. V. Maldague, *Theory and Practise of Infrared Technology for Nondestructive Testing*, Wiley Interscience, 2001.

## Review Article

# Infrared: A Key Technology for Security Systems

**Carlo Corsi**

*Centro Ricerche Elettro Ottiche, SS.17 Località Boschetto, 67100 L'Aquila, Italy*

Correspondence should be addressed to Carlo Corsi, [corsi@romaricerche.it](mailto:corsi@romaricerche.it)

Received 26 September 2012; Accepted 23 October 2012

Academic Editor: Ovidio Salvetti

Copyright © 2012 Carlo Corsi. This is an open access article distributed under the Creative Commons Attribution License, which permits unrestricted use, distribution, and reproduction in any medium, provided the original work is properly cited.

Infrared science and technology has been, since the first applications, mainly dedicated to security and surveillance especially in military field, besides specialized techniques in thermal imaging for medical diagnostic and building structures and recently in energy savings and aerospace context. Till recently the security applications were mainly based on thermal imaging as surveillance and warning military systems. In all these applications the advent of room temperature, more reliable due to the coolers avoidance, low cost, and, overall, completely integrable with Silicon technology FPAs, especially designed and tailored for specific applications, smart sensors, has really been impacted with revolutionary and new ideas and system concepts in all the infrared fields, especially for security applications. Lastly, the advent of reliable Infrared Solid State Laser Sources, operating up to the Long Infrared Wavelength Band and the new emerging techniques in Far Infrared Submillimeter Terahertz Bands, has opened wide and new areas for developing new, advanced security systems. A review of all the items with evidence of the weak and the strong points of each item, especially considering possible future developments, will be reported and discussed.

## 1. Historical Introduction

Infrared, as part of e.m. spectrum, was discovered by Sir William Herschel as a form of radiation beyond red light. These “calorific rays” renamed infrared rays or infrared radiation (the prefix *infra* in latin means “below”) were mainly devoted to thermal measurement and for a long time the major advances were due to infrared thermal imaging based on radiometric measurements [1].

The basic laws of IR radiation (Kirchhoff’s law, Stefan-Boltzmann’s law, Planck’s law, and Wien’s displacement law) have been developed many years after the discovery of IR radiation.

In 1859, Gustave Kirchhoff found that a material that is a good absorber of radiation is also a good radiator. Kirchhoff’s law states that the ratio of radiated power and the absorption coefficient (1) is the same for all radiators at that temperature, (2) is dependent on wavelength and temperature, and (3) is independent of the shape or material of the radiator. If a body absorbs all radiation falling upon it, it is said to be “black.” For a blackbody the radiated power is equal to the absorbed power and the emissivity (ratio of emitted power to absorbed power) equals one.

In 1884, L. E. Boltzmann, starting from the physical principles of thermodynamics, derived the theoretical formula of Black Body Radiation Law, stated empirically in 1879 by J. Stefan’s, by developing the Stefan-Boltzmann’s Law

$$W = \sigma \cdot T^4, \quad (1)$$

where  $W$  is the radiation power,  $T$  is the absolute temperature, and  $\sigma$  is the Stefan-Boltzmann’s constant.

In 1901, Nobel Prize Max Karl Ernst Ludwig Planck developed the Planck’s law which stated that the radiation from a blackbody at a specific wavelength can be calculated from

$$I(\nu)d\nu = \frac{2h\nu^3}{c^2} \frac{1}{\exp(h\nu/kT) - 1} d\nu, \quad (2)$$

where  $I(\nu)d\nu$  is the radiation power emitted per unit of surface and solid angle unit, in the frequency interval  $(\nu \div \nu + d\nu)$ ,  $T$  is the Absolute Temperature,  $c$  is the speed of light, and  $h$  is the Planck’s constant.

Soon after Wilhelm Wien (Nobel prize 1911) established the Wien’s Displacement Law taking the derivative of the

Planck's law equation to find the wavelength for maximum spectral radiance at any given temperature:

$$\lambda_{\text{Max}} \cdot T = 2897.8 \mu\text{m} \cdot \text{K}. \quad (3)$$

IR detectors' development, even after the discovery of Infrared Radiation by Sir H. Herschel in 1798, was mainly based on the use of thermometers/bolometers which dominated IR applications till the 1st World War, although in 1821 J. T. Seebeck had already discovered the thermoelectric effect. In the area of bolometer/thermometers L. Nobili had fabricated the first thermocouple in 1829, allowing in 1833 the multielement thermopile development by Macedonio Melloni, who was able to show that a person 10 meters away could be detected by focusing the thermal energy on the thermopile. In 1878 Langley invented the bolometer, a radiant-heat detector that was declared sensitive to differences in temperature of one hundred thousandth of a degree Celsius. Composed of two thin strips of metal, a Wheatstone bridge, a battery, and a galvanometer, this instrument enabled him to study solar irradiance (light rays from the sun) far into its infrared region and to measure the intensity of solar radiation at various wavelengths. Langley's bolometer was a device capable of accurately measuring thermal radiation and was so sensitive that it could detect the thermal radiation from a cow from 400 meter away [2] (Figures 1 and 2).

Between the years 1900 and 1920, the inventors of the world "discovered" the infrared. Many patents were issued for devices for security applications to detect personnel, artillery, aircraft, ships, and even icebergs. The first operating systems, in the modern sense, began to be developed during the 1914–18 War, when both sides had research programs devoted to the military exploitation of the infrared.

First advanced application of IR technology to security in civil area was probably the "Infrared Eye" of Bellingham: a device to detect the presence of icebergs and steamships by using a mirror and an original thermopile, perhaps developed one year before, but proposed for Patent in May 1913 (after the Titanic tragedy in April 1912) [3] (Figure 3).

"The infra-red eye, which in this case is a thermopile, is mounted laterally in tube 2 preferably of stout copper and of a diameter of about 10 inches or example, and near the window end of the same. Window 3 may have a diameter of about 6 inches and consists of a material transparent to infrared radiations. The infrared eye is prevented from directly receiving the radiation in question by being shielded by shield 4 and by being mounted close behind the opaque portion of mount 5 containing said window. At the other end of the tube there is arranged mirror 6 which is preferably of copper, the reflecting surface being gilt. The reflecting surface of mirror 6 is supposed to be toroidal, the toroidal surface being of such curvatures in the vertical and horizontal planes, respectively, as to produce on the sensitive surface of the thermopile sharply localized images in a horizontal plane, the rays in the vertical plane on the other hand being distributed over an angle of several degrees below to several degrees above the horizontal, and the object being to prevent loss of the image by pitching of the ship when the apparatus is in use at sea."

Similarly Parker in the same period of time was patenting an advanced sensor using the high sensitivity of "Delta zero measurement" by means of a Wheatstone Bridge [4] (Figure 4).

"This invention relates to thermic balances or radiometers and has for its object an improved capable of detecting the presence of a body by its sensitiveness to the ethereal radiation produced by that body consists in improvements in radiometers as well as in a novel adaptation thereof to produce an instrument sensitive only to the energy radiated by bodies and also rugged enough to be used as a commercial instrument with particular reference to its use as a detector of the presence of cold bodies, as icebergs. I accomplish this and the other objects by the apparatus herein after described."

So between the years 1900 and 1920, many inventions in the world were based on the infrared with patents issued for devices to detect personnel, artillery, aircraft, ships, and even icebergs. The first operating systems, in the modern sense, began to be developed during the 1914–18 War, when both sides had research programs devoted to the military exploitation of the infrared. These programs included experimental systems for enemy intrusion/detection, remote temperature sensing, secure communications, and "flying torpedo" guidance. An infrared search system tested during this period was able to detect an approaching airplane at a distance of 1.5 km, or a person more than 300 meters away. The most sensitive systems up to this time were all based upon variations of the bolometer idea, but the period between the two World Wars saw the development of two revolutionary new infrared detectors: the image converter and the photon detector. In fact early thermal detectors, mainly thermocouples and bolometers, were sensitive to all infrared wavelengths and operating at room temperature and normally, until few years ago, they were with relatively low sensitivity and slow response time.

The first photon detectors (based on photoconductive effect discovered by Smith [5] in 1873 in Selenium and, later on, by Bose in photovoltaic lead sulphide, but not applied for many years) were developed by Case in 1917 [6]. In 1933, Kutzscher developed IR PbS detectors (using natural galena found in Sardinia): these sensors were widely used during the 2nd War. These detectors have been extensively developed since the 1940s. Lead sulfide (PbS) was the first practical IR detector, sensitive to infrared wavelengths up to  $\sim 3 \mu\text{m}$ . In the mean time Cashman developed TaS, PbSe, and PbTe IR detectors with high performances supporting the developments in England and US.

At first, the image converter received the greatest attention by the military, because it enabled an observer to literally "see in the dark." However, the sensitivity of the image converter was limited to the near infrared wavelengths, and the most interesting military targets (i.e., enemy soldiers) had to be illuminated by infrared search beams. (Since this involved the risk of giving away the observer's position to a similarly-equipped enemy observer, it is understandable that military interest in the image converter eventually faded).

The tactical military disadvantages of so-called "active" thermal imaging systems provided impetus following the 1939–45 War for extensive secret military IR-research

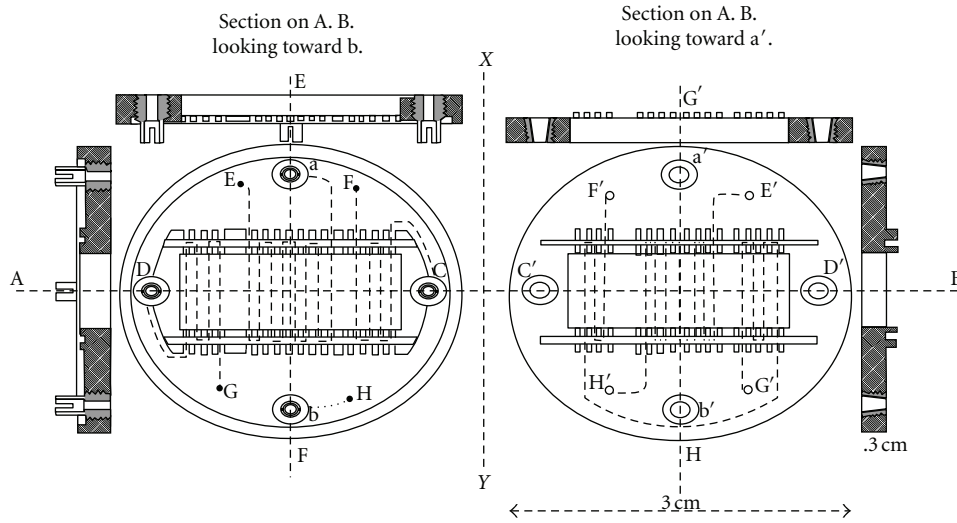


FIGURE 1: The Langley Bolometer.

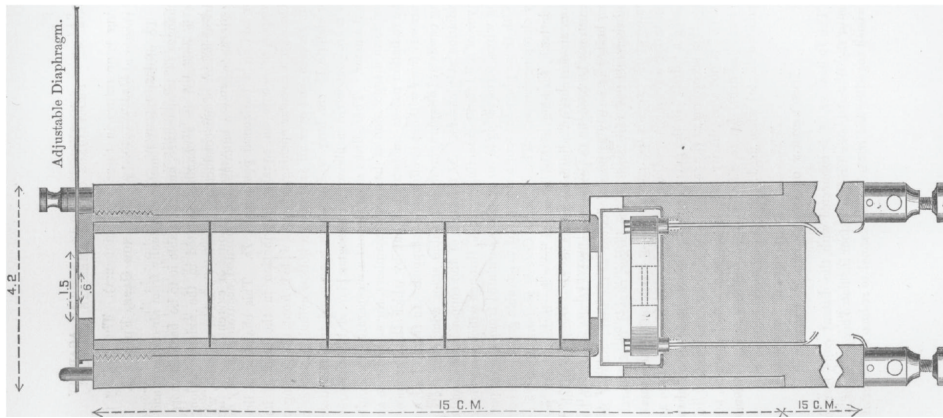


FIGURE 2: Section of the Bolometer case and Bolometer.

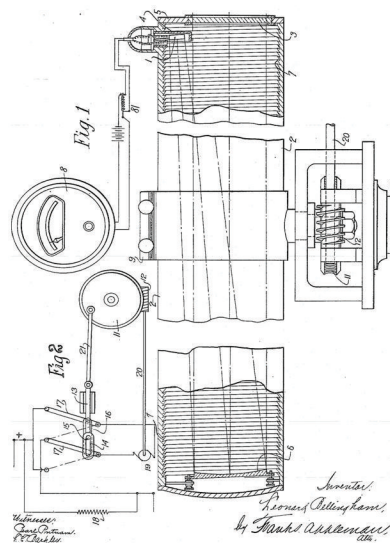


FIGURE 3: Bellingham. Means for detecting the presence at a distance of icebergs, steamships, and other cool or hot objects. Filed May 1, 1913; patented November 2, 1915.

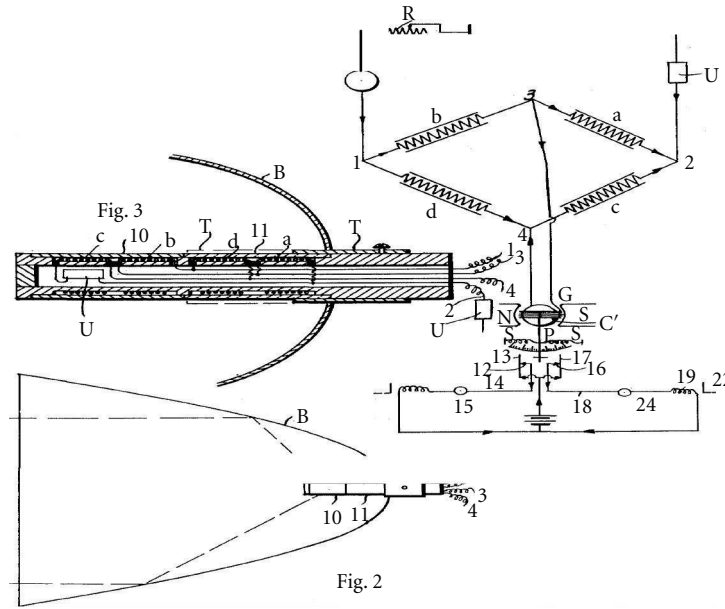


FIGURE 4: Parker, Thermic balance or radiometer application, filed July 31, 1912; patented June 9, 1914.

Infrared: military applications 2° war



FIGURE 5: Infrared: military applications 2° War.

programs into the possibilities of developing “passive” (no search beam) systems based on the extremely sensitive photon detector. During this period, military secrecy rules completely prevented disclosure of the status of IR-imaging technology. This secrecy only began to be lifted in the middle of the 1950s, and adequate thermal imaging devices began to be available to civilian science and industry (Figure 5).

High level results were achieved in the 1940s, especially in lead salts (PbSe and PbTe) good stable cells were developed by OSRD, Office of Scientific Research and Development in co-operation with the MIT, Harvard, and the British TRE Telecommunication Research Establishment, Great

Malvern). The history of IR detector developments has been therefore almost coincident with optoelectronics for military applications for many decades, strongly conditioning the cultural behavior of the IR industry and in some way of R&D labs.

## 2. Focal Plane Array (FPA)

The basic strategic device in infrared technology is the sensor that in its historical evolution has been growing from single detector with an optical-mechanical scan of the acquired scene and then, starting from the middle of

1970s, multipixel sensor Focal Plane staring Arrays (FPA). Infrared technology starting from the 1950s was enjoying a great growth, especially in the development of solid state IR sensors. Almost contemporarily lead selenide (PbSe), lead telluride (PbTe), and indium antimonide (InSb) cooled detectors extended the spectral range beyond that of PbS, providing sensitivity in the 3–5  $\mu\text{m}$  medium wavelengths (MWIR) atmospheric window. (Extrinsic photoconductive germanium detectors were allowing to reach long wavelength spectral region, needing very low temperature with the use of liquid helium). But we had to wait till the 1960s to see the first advanced developments coming out thanks to direct gap photon materials based on ternary semiconductor compounds (HgCdTe and PbSnTe) [7, 8]. This was a real breakthrough, because after the discovery of solid state transistors (1948) and the explosion of solid state electronics, microelectronic was offering new advanced manufacturing technologies like photo-masking and integrated microsoldering and assembly allowing multielements structure (first Linear Arrays and then in the 1970–80s years Bidimensional Focal Plane arrays FPAs) with the highest number of pixels. After the 1980s strong efforts were put to developing integrated electronics for signal readout and elaboration, with working temperature close to room temperature with the main task of achieving high optoelectronic FPA's performances with smaller and lighter structures, with possibilities of applications in civil area thanks to cost reduction and civilization by eliminating optomechanical scanning and cryogenic low-temperature cooling.

The recent development of advanced IR FPA (with  $>10^6$  pixels in the 8–12  $\mu\text{m}$ ) working at room temperature allows to forecast an incredible growth of uses besides the evident growth of advanced applications of IR based on thermal measurements. The choice, supported by US industries, of concentrating efforts and resources in a specific technology produced the “first generation of linear detector arrays,” which allowed to obtain BLIP detectors at liquid nitrogen temperature (this first generation of CMT linear arrays was the basis for the “Common Modules” LWIR FLIR systems with a number of pixels from 60 up to 180, each detector connected with feed-throughs to the room temperature read out electronics). The invention of Charge Coupled Devices (CCDs) in 1969 [9] made it possible to start the developing of the “second generation” FPAs detector arrays coupled with on-focal-plane electronic analogue signal readouts which could multiplex the signal from a very large array of detectors. In the middle 1970s, while the 1st Common Module IR Arrays were produced, the first CCD IR bidimensional arrays [10, 11] were appearing in USA and, the first Smart Sensors based on LTT RF sputtered thin films, using X-Y addressing readout, were developed in Italy [12]. In 1975 the first CCD TV camera was realized and this was allowing to forecast the “2nd generation FPAs” capable of a staring vision, although the necessity of very high spatial resolution and high reliability even in complex structures, with extremely high number of pixels (up to one million pixels), were pushing towards alternative solutions, with materials less difficult than CMT, in the manufacturing process (e.g., extrinsic silicon detectors). The high quantum

yield of CMT and the top performances required by the military anyhow allowed to improve the performances of sensor linear arrays by integrating time delay and integration inside the detectors' structure itself (SPRITE detector [13]).

In the late 1970s through the 1980s, CMT technology efforts focused almost exclusively on PV device development because of the need for low power and high impedance for interfacing to readout input circuits in large arrays (photoconductive CMT was not suitable due to its low impedance). This effort has been concretized in the 1990s with the birth of “second generation IR detectors” which provides large 2D arrays with the number of pixels up to many hundred thousands thanks to hybrid integration (indium bumps or loopholes soldering) of CMT bidimensional arrays in silicon substrate with CCD and more recently CMOS readout. At the same time, other significant detector technology developments were taking place. Silicon technology generated novel platinum silicide (PtSi) detector devices which have become standard commercial products for a variety of MWIR high-resolution applications. Monolithic extrinsic silicon detectors were demonstrated first in the mid 1970s [14, 15]. Thanks to PtSi Schottky barrier IR properties, great attention was dedicated to FPA arrays based on integrated silicon Schottky sensors which were showing reliable monolithic silicon CMOS-integrated technology and high uniformity in detectivity, but were operating in the short wavelength region and with the limitation of low working temperatures. Similar considerations can be made for the long wavelength GaAs/GaAlAs Multi-Quantum Well IR FPA arrays [16], which, although if with lower quantum efficiency, are close to CMT performances even showing higher homogeneity and stability in sensitivity thanks to a more reliable manufacturing process, but with the strong limitation of working at lower temperatures ( $<77\text{ K}$ ). This requires the use of Cryogenic structures with high cost of purchasing and maintenance, therefore improving the restriction of the main use to military applications, limiting the market size, and, as consequence, the product growth. In all the latest developments the really driving key technology has been the integration of the IR technology with silicon microelectronics and it was, more and more, emerging the importance to free IR from the constraints of the cooling requirements due to its high cost (almost 1/3 of the total cost) and low reliability and heavy need for maintenance. For the above reasons, work on uncooled infrared detectors has shown an impressive growth since the first developments, allowing the real expectation for a production of low cost, high performance detector arrays which finally should follow the rules of a real global market, opening a real market for civil applications following the winning rules of silicon microelectronics. For these reasons the emerging room temperature detectors in the 1970s by the use of pyroelectric materials [17, 18], which shows the limitations of not being fully monolithic, but the innovative room temperature silicon microbolometers appearing on the IR scene in 1990 [19], seem to be a real breakthrough for future IR sensors.

In Table 1 are reported the highlights of the IR Sensor developments since the Herschel's discovery.

TABLE 1: History of IR detectors.

1800	IR radiation Sir W. Herschel
1821	Thermoelectric effect Seebeck
1829	Thermocouple G. Nobili
1833	Thermopile Macedonio Melloni
1836	Optical pyrometer Becquerel
1873	Photo-detection (Selenium) Smith
1884	IR radiation law Boltzmann
1902	Photoconductivity effect Bose
1917	Lead sulphide Case
1933	Lead sulphide (galena) Kutzsher
1940	TI2S Cashman
1942	Golay cell Golay—Queen Mary College
1948	Transistor Bardeen-Brattain-Shockley
1950s	PbS, PbSe, PbTe T. Moss RRSE
1959	HgCdTe W. Lawson, J. Putley
1960s	Ge: X, InSb
1969	CCD Boyle-Smith (Bell Labs)
1970s	PbSnTe/HgCdTe, Si: X Lincoln Labs, SBRCHughes, Honeywell, Rockwell, Mullard
1973	Common modules Night vision Lab
1975	IR Fly Eye Smart Sensors: C. Corsi, Elettronica SpA
1978	Si: X/CCD/PtSi/CCDHgCdTe/CCD RCA Princeton Lab W. F. Kosonocky, F. Shepherd D. Barbee-F. Milton-J. Steckel
1980s	HgCdTe SPRITE InGaAs QWIP T. Elliott RSE, F. Capasso L. Esaki, B. FLevine, M. Razeghi, L. J. Kozlowski
1990s	Pyroelectric FPAs/MicroBolometer FPAs/Multi-colour FPAs/Advanced FPAs RRSE-BAE,. R. A. Wood, J. L. Tissot, P. R. Norton, A. Rogalski, H. Zogg S. D. Gunapala, D. Z. Ting
2000	MEMS FPAs—Cantilever IR Nanotubes/Nanowires B. Coole, S. R. Hunter, X. Zhang, J. M. Xu, S. Huang, Y. Zhao, J. Xu, Maurer, G. Jiang, D. J. Zook

### 3. Smart Sensors

The most important applications for security systems have been developed in military fields evidencing a consistent growth in the system concepts especially for the capabilities of intelligent evaluation of the signal detection and warning for threats' presence. So starting from the late 1970s [20–23] and the beginning of 1980s under the pushing of USA Strategic Defence Initiative for achieving outstanding performances in sensors systems a new class of infrared sensors systems called “Smart Sensors” were appearing on the infrared stage. “Smart Sensors” integrate the sensing function with the signal extraction, processing, and “understanding” particularly in application fields such as remote sensing where minimum size and high level multifunction performances were considered as the main achievements to be reached. So the term “Smart Sensors” has been originated to indicate sensing structures capable of gathering in an

“intelligent” way and of preprocessing the acquired signal to give aimed and selected information [24].

In a broad sense, they include any sensor systems covering the whole electromagnetic spectrum: this paper deals specifically with a new class of smart sensors in infrared spectral bands whose developments started some years ago [20, 21] when the integrated processing capabilities based on advanced readout integrated with signal processing were still far from the complexity needed in advanced IR surveillance and warning systems because of the enormous amount of unwanted signals emitted by operating scenario especially in military applications [23].

Later on, thanks to the CCD readout technology, it was recognized that the rapid advances of “very large scale integration” (VLSI) processor technology and mosaic infrared detector array technology could be combined to develop new generations of Smart Sensor systems with much improved performances. Therefore, sophisticated signal processing operations have been developed in these new systems by integrating microcomputers and other VLSI signal processors within or next to the sensor arrays on the same focal plane avoiding complex computing located far away from the sensors. These developments were later widespread on too many applications and the term “Smart Sensors” was used and “abused” to identify and define sensors with some integrated type of processing and even to erroneously define “Smart Sensors” that are supplying aimed information.

In conclusion there are two main classes of IR Smart Sensors: the first one supported by the impressive growth of integrated microcircuitry which, thanks to the CCD/CMOS integrated readout, can allow sophisticated preprocessing using the Smart Sensing techniques (these devices known as “vision chips” in the visible range have been recently strongly investigated and successfully developed) [25], and the other one, more oriented to specific applications, in which most of the intelligence of preprocessing is inside the design and structure of the sensor itself [23, 25].

The Smart Sensor technology in fact should allow integrating technical design and development from optics, detector materials, electronics, and algorithms into the sensor's structure and function rather than trying to get the required performance by relying on massive improvements in just the aspect of the number of pixels and related electronics readout and processing technology. Therefore, the performance of the Smart Sensor can be achieved with lower technological risk and with integrated structure which allows smaller size and higher reliability and often higher performances for specific applications like, for example, warning and alarm systems. The “Smart Sensor” design concept is based on the processing capabilities, at least at some stage of threshold, inside the sensors structure itself. Such new family of sensor, defined in a broad sense, intelligent sensors, or Smart Sensors are the result of an optoelectronics analogue processing which in some way are simulating some functions of signal pattern extraction information selection for pattern recognitions, as it happens in the dynamic link between the human eye and brain or,

more truly, in the primitive visual structures of some insects (fly-eye) [26].

The main task is to satisfy better or even to substitute the highly complex elaboration of signal output deriving from the enormous mass of data coming from the high number of sensing pixels by implementing an elaboration prefiltering capability in the sensor structure itself. This prefiltering capability associated to an integrated electronic processing can allow implementing correlations in the spectral, temporal, and spatial domains, so that it is possible to contain the flux of acquired data extracting only those with higher information content. Examples of such correlations can be exemplified by some well-defined signal extractions (Point Source Detection, Edge Enhancement, and Morphological Structure Recognition).

These correlations associated to appropriate temporal signatures can allow to discriminate and identify the targets, like that performed by an insect eye thanks to a spatial-temporal correlation. (Figure 6). One of the simplest feature extraction and in the same time most appealing for the numerous applications is the discrimination of point sources from extended background emissions and/or of fast events (moving targets or changeable emissions) for static or slow moving scenario. In this case a reticle structured detector, which is electronically modulated to obtain a spatial-temporal correlation of the focused spot target, buried within the diffused background emission, can allow the detection of point source or a well-defined-shaped target improving the signal to clutter ratio. This dynamic spatial filtering can be implemented with special feature structure which is capable of preferable detection for selectable forms (e.g., point sources, linearly structured objects, etc.). These correlations associated to appropriate temporal signatures can allow discriminating and identifying the targets, like that performed by an insect eye thanks to a spatial-temporal correlation. One of the simplest feature extraction applications is the discrimination of point sources from extended background emission and/or of fast events (moving targets or changeable emissions) from static or slow moving scenarios. Normally this is obtained by an external chopper (mechanical or optical) which modulates the incoming signal depending from its collimated spot size. This signal processing can be done by emulating the fly-eye structure that is a sensor with a finger-type electrodes structure which, thanks to an electronic modulation in a differential way between two adjacent subpixels, can detect spot size almost cancelling the signal due to a diffused irradiation source (e.g., clouds and diffused sun irradiation) which are widespread in more than one single sub-pixel (a third electrode structure can be inserted for avoiding the missing of the detection of point target in case that the focused spot is falling just in the middle of two adjacent electrodes [23]).

Associated with the pushing towards highest number of pixels ( $>10^6$ ) and the highest working temperatures (close to room temperature), the general trends of future detectors will show more and more increasing of the “intelligence” of the sensors which will integrate the sensing function with the signal extraction, processing/“understanding” (Smart

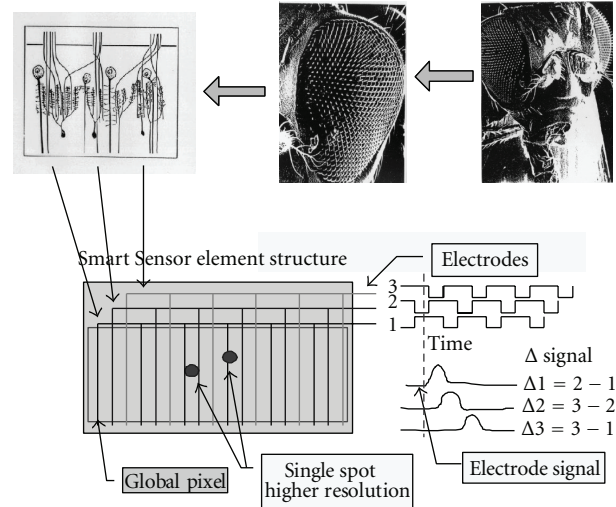


FIGURE 6: Smart Sensor emulating fly-eye recognition structure with an integrated 3 electrodes modulation.

Sensors). The basic objectives of new IR smart sensors are much more demanding because significant improvements in the performance of VLSI processors and infrared mosaic detector arrays are being achieved. Especially in the prethreshold stage, target signals are expected to be deeply buried in background clutter noise which can be much higher than the target intensity. Therefore, imaginative pattern recognition processing techniques using all spatial, temporal, and/or spectral information of both targets and background clutter should be developed for suppressing background clutter and unwanted signal, but maintaining or ever enhancing the target signal. At last, it is important to underline that the important recent developments of neural networks for advanced computing allow foreseeing an impressive growth of the “Smart Sensor” concept especially for those detector technologies which will take advantage of the possibility of integrating processing devices [27].

#### 4. Infrared Technology System Applications

For a long time infrared was confined to military applications especially based on thermovision, technology that is “infrared: to see the invisible” (Figures 7, 8, and 9).

In the end of 1990s the crisis originated by the solving of Soviet Union and the consequent the end of “Cold War” was pushing the use of infrared towards civil applications (the famous slogan “from military to civil” and “the dual-use mode” with the explosion of thermovision technology applied to environmental control, building/art masterpieces analysis, medical functional diagnostics\*, and recently car guidance/collision avoidance systems)\* [26, 28–35].

The developments were so great that, thanks to simultaneous lowering of costs due to mass production of advanced room temperature FPAs sensors, there was emerging a dual way use from civil to military markets [36, 37].

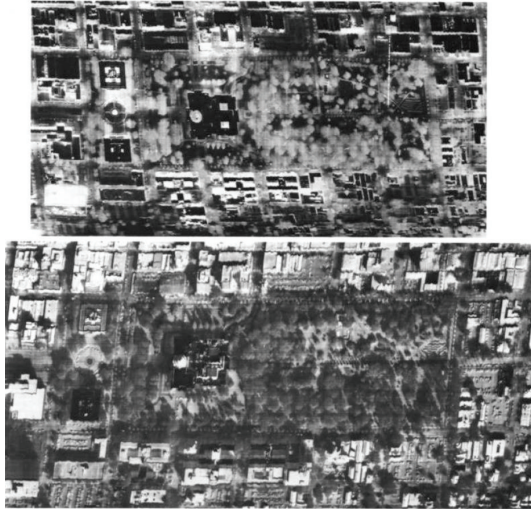


FIGURE 7: High-resolution visible and infrared aerial photos.



FIGURE 8: Visible and infrared photos of a wood. Both photos (FLIR System Inc.) are evidencing targets in the infrared photos not detectable in the visible.

**4.1. Smart Sensors for Collision Avoidance in the Fog.** An important application of the IR Smart Sensors for civil security is an IR system for driving assistance in low visibility due to fog/smokes as “collision avoidance in low visibility.”

In fact thanks to the better visibility through fog in IR field in respect to visible many systems proposals have been done by car producers for the use of thermal viewers to be installed on board. These IR systems up to now have shown heavy limits for the sensible cost also if using the IR room temperature microbolometers and for maintenance and reliability and over all for “man interface” (it is evident that few car drivers can use an helmet-type display or can have enough skillfulness to look at a display while driving in very low visibility).

For these reasons a new generation of simple, reliable, Smart Sensors operating at room temperature with no costly



FIGURE 9: Aerial infrared photo of “Kennedy Aircraft Carrier”: aircrafts parked or just landed can be recognized.

thermocontrol, which supply a sound and light alarm in case of presence of an obstacle on the road, could be a winning solution. In the presence of fog, air is more transparent to IR radiation than to VIS light. CREO developed a low-cost smart sensor, based on a  $32 \times 2$  bilinear microbolometer array, to be fixed close to the car headlamps, and capable to perform radiometric identification of hot objects and deliver an audible alarm to the driver.

In Figure 10 is shown a high-resolution thermal image of two possible obstacles in a winter environment: a car parked for more than 10 minutes and a running car. In Figure 11 is shown the signal detected by the IR Smart Sensor structure supplying automatic alarm in both cases.

**4.2. Toxic Gas Sensing.** Owing to the increasing demand for security in civilian crowded areas, both for the risk of accidents in dangerous materials transportation and in industrial toxic substances processing and recently of terrorist threat, the development of novel large-scale applicable technologies and methodologies for quick detection and identification of extremely toxic compounds is strongly advised. Particularly, in military battlefield operations or in case of terrorist attacks, high detection capability coupled to low false alarm rate and identification capability, at least for classes, are required. The alarm systems should be compact and small size, even expendable in case of military battlefield operations. In fact due to the presence of dense smokes and powders besides toxic gases, the environment of a battlefield is normally turbid; therefore, it needed a stand-off point detection system which should operate in the dangerous selected areas and delivered by special launcher systems or put on board of URPV (Unmanned Remote Pilot Vehicle).

Moreover, most of the CWAs (Chemical Warfare Agents) are heavier than air and are spreading in the atmosphere when there is ground movement: therefore, it needed a point stand-off detection system to detect the presence of toxic gases. Last but not least the system should be unattended without the need of any intervention by human operators.

Existing technologies are based on two main classes of sensors: one based on simple physical-chemical sensors which are modifying their electronic properties in presence of some gases and the other based on complex sensor subsystems which are correlating the physical-chemical properties detected by specific measurements. Both may be high sensitive although the first class type is confined to be used only for specific gases and with performances changing with time and up to now is unable to supply gas identification. The second class type (e.g., surface acoustic

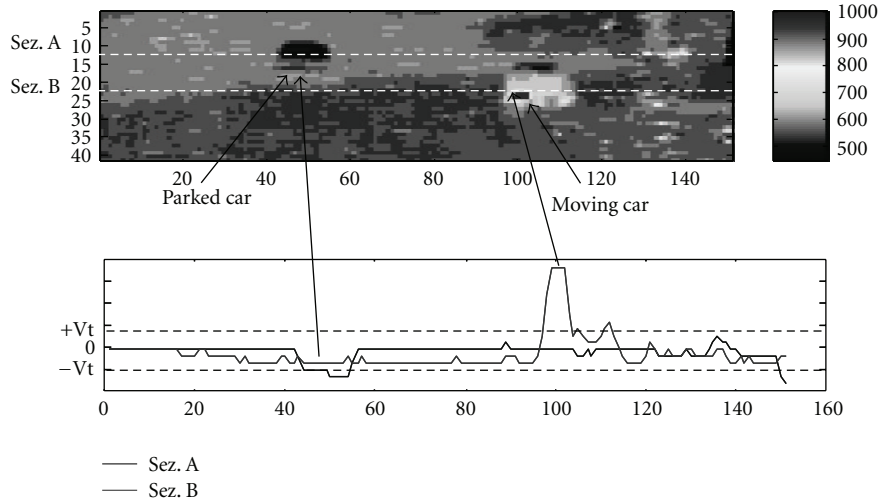


FIGURE 10: Thermal imaging—Smart Sensors signals.

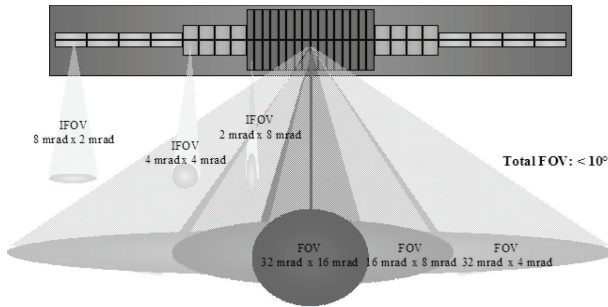


FIGURE 11: Smart Sensor structure for collision avoidance.

wave, ion mobility spectrometry, and mass spectrometry), can achieve high sensitivity and selectivity, but most of these technologies cannot give both at the same time and not in unattended way needing human intervention in their use 1-3. Best performing systems usually require costly and sophisticated laboratory equipments (e.g., FTIR spectrometry, gas chromatography, and mass spectrometry [38–40]). Furthermore, they often require ancillary operations, such as sample preparation and preconcentration, thus requiring long time for analysis, not operationally acceptable.

**4.2.1. Toxic Gas Sensing Based on NDIR Multichannel Absorption Spectroscopy.** Best performing systems are costly and sophisticated laboratory equipments (e.g., FTIR spectrometry, gas chromatography, and mass spectrometry) and are recently substituted by innovative system, based on consolidated technique of nondispersive infrared spectroscopy (NDIR) with Bidimensional Multipath Multi-Spectral Staring Smart Sensors in the IR ( $3 \div 5$  and  $8 \div 12$  micron) using a MEMS Multielement Blackbody Source optically coupled to a Multipass Cell/Spectrally Linear Variable Filter. A new Sensor Staring Array Structure, designed to perform multispectral measurements for Gas Detection, Identification, and Alarm, has been developed. (Resolution of 0.3 microns

spectral resolution allows not only to detect but even to identify, at least for classes, even a small amount (down to few parts per million) of toxic gases operating at room temperature and pressure, even if unattended).

Innovative systems, although based on the consolidated technique of nondispersive infrared spectroscopy (NDIR), performing a fast multispectral measurement of the radiation emitted from a thermal blackbody source in the IR spectral range, particularly between 8 and 12 micron wavelength region, have been recently developed [41].

The detection and identification of absorbing species is achieved by analyzing the spectroscopic signal variation. The novel technical approach consists in the implementing of a low cost source and a microbolometer room temperature sensor array with smart 6 architecture coupled to a spectrally linear variable filter by using a high throughput efficiency optical system 7 to increase the path length and make simultaneous acquisition of several spectral bands within a reasonably compact size. The linear variable filter is a narrow band pass filter in which the wavelength of peak transmittance changes linearly along one direction of the filter surface.

The optical resolution of each detection channel is optimized in width to be matched at the best between resolving power and integrating absorption signal in the widest band as possible, so it has to be not too narrow and not too large. Also, considering technological constrains associated to the filter feasibility, a good tradeoff is around 0.1 micron bandwidth. The system is working at room temperature, small, portable, low cost, and low power consumption device, in order to allow easy operation and large scale distribution both for environmental and security applications.

A new Sensor Staring Array Structure has been developed and designed to perform multispectral measurements for gas detection, identification, and alarm. Resolution of 0.1 microns spectral resolution allows not only to detect but even to identify, at least for classes, even a small amount

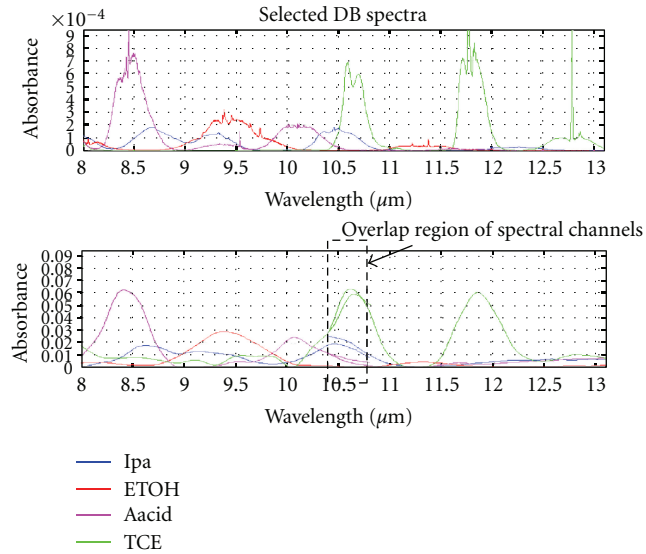


FIGURE 12: Spectra of 4 vapour organic compounds: from high-resolution database (top); as measured by the NDIR-CANARIO sensor (bottom). CANARIO-EDA Italy-Spain Project. Similar results available for CWAs [41].

(down to few parts per million) of toxic gases operating at room temperature and pressure, even if unattended [41] (Figure 12).

Application security: detection of toxic gases by IR spectroscopy: the vast majority of TICs and CWAs show strong absorption bands in the MID-IR.

This system aimed at developing a compact point sensor for providing early warning in the presence of chemical agents in the air. Battlefields and urban areas at risk of terroristic attack were the foreseen application scenarios. Wide chemical range and effective identification of targets and rejection of other vapours were given as the key performance objectives.

The sensor is based on Active Multispectral InfraRed Absorption Spectroscopy in the gas phase and uses 42 spectral channels to represent molecular fingerprints across the Medium and Long Wave IR spectrum (MWIR and LWIR). The heart of the sensor is an advanced detector device operability (self-calibration capability); the system is showing sensitivity for most Toxic Industrial Compounds and Chemical Warfare Agents with a limit of detection to Nerve Agents around 500 ppb.

The NDIR system matches very well the requirements of an early warning system for toxic gases, that could be implemented both as an autonomous unit and as the node of a sensor network; key assets are its ability to detect and correctly identify a huge number chemicals of different nature and class of risk (CWAs, TICs, solvents, and perfumes.), with minimal false alarm rate; other crucial assets are its compact and simple design, cost-effectiveness, unattended, and continuous operability (self-calibration capability).

Moreover, it shows identification capacity and high rejection of interferents and it is suitable for surveillance

and warning in the presence of toxic gases intentionally or accidentally released in the air.

4.2.2. *Standoff Detection.* Infrared/microwaves techniques and Imaging Hyperspectral Sensors are mostly developed for their selectivity and specificity to detect differences in the spectra of two or more species of chemical warfare agents (CWA) allowing detection of explosives with high sensitivity and very low false alarm rate. Infrared transmission spectroscopy is an analytical tool to detect and identify chemicals in the gas phase.

Open-path Fourier transform infrared (FTIR) spectroscopy is an established method to monitor environmental pollutants (1), for example, aircraft exhaust gases (2), detect toxic gas emissions at industrial plants (3), and even detect chemical warfare agents (CWA). Thus, open-path FTIR is a potential method for explosive detection too. A major drawback of open-path FTIR is the long integration time needed to collect a spectrum because of the low power of the thermal radiation sources usually employed. This is especially the case if trace compounds have to be detected, which only show up in tiny spectral features in the spectra.

The sensitivity of infrared spectroscopy is linked to the measurement of small relative transmission changes of for example, less than  $10^{-3}$ . Selectivity and specificity are linked to the ability to detect differences in the spectra of two or more.

A major drawback of open-path FTIR is the long integration time needed to collect a spectrum because of the low power of the thermal radiation sources usually employed. This is especially the case if trace compounds have to be detected, which only show up in tiny spectral features in the spectra.

The sensitivity of infrared spectroscopy is linked to the measurement of small relative transmission changes of for example, less than  $10^{-3}$  at one or more spectral positions. Selectivity and specificity are linked to the ability to detect differences in the spectra of two or more species. If spectral features of two compounds overlap at one wavelength, at another wavelength a difference may occur which could be used to discern between the two species. As is the case with chemical warfare agents (CWA) for detection of explosives very good sensitivity and a very low false alarm rate, that is, specificity, are a must.

Recently integration of multispectral IR spectroscopy with quantum cascade lasers and hollow-waveguides is promising improved sensitivity and area coverage allowing fast and effective detection at public places like airports, railway, or coach stations [42].

In fact infrared laser spectroscopy, an established method to measure gas concentrations, due to the high power of the laser and its higher optical collimation compared to the thermal emitters used in FTIR equipment sensitive, allows to make long distance measurements. Especially for small molecules with single rotational-vibrational lines in the infrared laser spectroscopy methods are extremely sensitive and relative transmission changes of  $10^{-4}$  and below have been measured even in industrial in situ applications.

**4.2.3. QC-Laser Spectroscopy.** The stronger and more specific infrared absorptions of most chemicals/toxic gases are in the mid/far infrared range between  $3\ \mu\text{m}$  and  $20\ \mu\text{m}$  wavelength, making this region interesting for infrared spectroscopy, for this reason, although most work on laser spectroscopy is performed in the near infrared, where suitable laser sources thanks to wide use in telecommunications wavelength bands, the quantum cascade lasers (QCL) in the middle/far IR are the ideal source for IR laser spectroscopy. After the first QCL spectroscopic applications made with pulsed QCL operation, most of the developments are using CW sources at room temperature, nowadays available for many wavelengths in the mid/far infrared [43–46].

Recently QCL system for gas detection operating in the pulse mode, driven by a short pulse in the 10–100 ns range with pulse repetition rates in the low 10–100 kHz range, are allowing enough time to get consistent absorption features of the sample gas within the pulse duration.

Advanced QCL laser system has detection capability of hidden explosives and other items on personnel. As is the case with chemical warfare agents (CWA) for detection of explosives, very good sensitivity and a very low false alarm rate, that is, specificity, are a must. Fast and effective detection of explosives is a key security issue against possible terrorist attacks. Especially at public places like airports, railway, or coach stations efficient detection systems are needed. Usual methods at airport security checks are wiping carry-on baggage/laptop computers, and so forth to collect samples which are analyzed subsequently by, for example, gas chromatography mass spectroscopy (GC-MS); gas chromatography chemo luminescence (GC-CL) ion mobility spectrometers (IMS) (Figure 13).

## 5. Terahertz THz Systems

Recent events have led to dramatic changes to the methods employed in security screening. For example, following the failed shoe bombing, it is now common for shoes to be removed and X-rayed at airport checkpoints. There is therefore an increasing focus on new technologies that can be applied to security screening, either to simplify or speed up the checking process, or to provide additional functionality. Terahertz (THz) technology is a promising, emerging candidate.

**5.1. Terahertz Radiation and Its Properties.** The “terahertz gap” due to the fact that until recently there was a lack of high power sources and high sensitivity detectors can be allocated between 100 GHz ( $3\ \text{mm}$ ) and 10 THz ( $30\ \mu\text{m}$ ) that is between the millimeter-microwave part of the e.m. spectrum and the far infrared. Concerning microwave sources till now few sources (recently solid state) are capable of generating enough power radiation efficiently produced at frequencies above hundred gigahertz, whereas solid state laser sources have been limited by thermal effects in their performances in the far infrared region. However, in recent years, several approaches have been developed that enable the efficient generation and detection of terahertz radiation

truly commercially viable. The most mature technology uses ultrafast pulsed laser technology and produces very short terahertz pulses. As a pulsed technique, with picosecond timescales, the method is intrinsically broadband.

Radiation at terahertz frequencies has unique properties that may be advantageous for security applications. It penetrates many nonconducting materials, but unlike X-rays is nonionizing. The short pulses produced by laser techniques also allow radar-like imaging in three dimensions, as well as the simultaneous collection of spectroscopic information as in magnetic resonance imaging (MRI) or optical spectroscopy. This is important because many substances have characteristic intermolecular vibrations at far infrared/terahertz frequencies that can be used to characterize them as molecules.

Terahertz technology, which is a nonionizing radiation, is really a powerful technique in security screening applications thanks to the following properties [48–50].

- (i) Spectroscopy allows detecting and identifying different chemicals, thanks to their characteristic spectral signatures, even when hidden inside dress clothing.
- (ii) 2D terahertz imaging capable of making visible metals and even plastics and ceramic, materials that are hard to be detected using backscatter X-ray.
- (iii) High-resolution 3D imaging thanks to the extremely short pulses used in pulsed terahertz techniques like in the radar technology. (e.g., layers of powder can be detected and resolved inside a mail envelope).

In synthesis Multispectral (IR-Thz) Systems for security applications will have high growth especially coupled to new solid state tunable laser sources with innovative, new technologies for Multispectral Pluridomain Smart Sensors:

- (i) to IR/THz Imaging/Pattern Security Applications,
- (ii) to IR/THz Spectroscopy for Security Applications,
- (iii) to Stand-Off Laser Detection IR/THz Spectroscopy.

**5.2. Security Applications of THz Technology.** Recently terrorist events, based on new types of threats and explosives, have pushed towards the developments of new techniques of detection and alarm employing different parts of the electromagnetic spectrum, particularly extending from infrared to terahertz radiation, that is, the e.m. band between infrared and microwave. Also in these new developments there is a priority to the developing of imaging systems, at least for the know-how originated in infrared technologies, while spectroscopic detection is mostly developed by microwaves techniques.

Radiation at terahertz frequencies has unique properties that may be advantageous for security applications; in fact, it can penetrate many nonconducting materials, but unlike X-rays is nonionizing, and can allow radar-like imaging in three dimensions thanks to the extremely short pulses used in pulsed terahertz techniques, as well as the simultaneous collection of spectroscopic information like infrared. This is important because many substances have characteristic

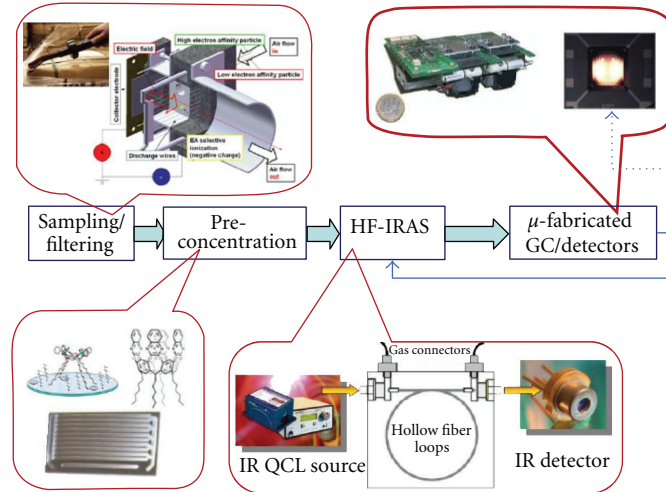


FIGURE 13: DIRAC system architecture: EC-FP7 Project [47].

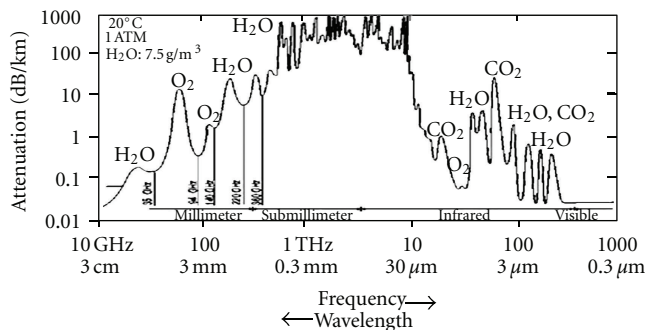


FIGURE 14: Absorption bands in atmospheric transmission.

intermolecular vibrations at Far IR-THz frequencies that can be used to characterize them as molecules like IR spectroscopy that can detect bond vibrations of single molecules (Figure 14).

5.3. *Surveillance; Detection and Warning Systems: Past, Present, and Future Trends.* Standoff detection is showing hidden explosives and other items on personnel.

- (i) Selectivity and specificity are linked to the ability to detect differences in the spectra of two or more species. If spectral features of two compounds overlap at one wavelength, at another wavelength a difference may occur which could be used to discern between the two species. As is the case with chemical warfare agents (CWA) for detection of explosives very good sensitivity and a very low false alarm rate, that is, specificity, are a must.
- (ii) Fast and effective detection of explosives is a key security issue against possible terrorist attacks. Especially at public places like airports, railway, or coach stations efficient detection systems are needed. Usual methods at airport security checks are wiping carry-on baggage/laptop computers, and so forth to collect

samples which are analyzed subsequently [51] by; for example

- (a) gas chromatography mass spectroscopy (GC-MS);
- (b) gas chromatography chemo luminescence (GC-CL);
- (c) ion mobility spectrometers (IMS).

Multispectral (IR-THz) Systems for security applications will have high growth especially coupled to new solid state tuneable laser sources with innovative, new technologies for Multispectral Pluridomain Smart Sensors.

Thermography, associated to functional diagnostics with high filtering correlation in time and spectral domain, will stay as the main market and system application associated to an impressive development of high number, fast, multispectral, room temperature sensors (microbolometers).

## 6. Synthesis Historical Technology Evolution

The main application for IR technology was in the past and will be in the future surveillance and warning and more specifically for military applications that conditioned for a long time the development of IR devices and systems. The highlights of this application field are quite well known and have allowed to develop an impressive know-how either in the systems' performances.

The first historical lesson, missed for lack of knowledge of the users, was the underestimation of the strategic value of IR surveillance systems (at that time the RADAR was not yet operating although in 1904 Christian Hülsmeyer [50] had used radio waves for detecting "the presence of metallic distant objects," only in 1922 Guglielmo Marconi [52] proposed the idea of a Radio Telemeter for localizing metallic objects at distance and therefore the remote sensing was mainly just optical). In fact Bellingham, probably in 1910, had developed a method to detect the presence

of icebergs and steamships by using a mirror and the original thermopile: he patented this device later in 1913 [3]. His infrared radiometer's primary advantage over the disappearing-filament optical pyrometer was that it was able to detect temperatures substantially lower than ambient. If this device was installed on the Titanic ship avoiding that grave tragedy, probably the efforts in developing IR surveillance systems would have been much greater. During World War 2 great efforts have been dedicated to the development of IR surveillance systems especially in the Army with both parties capable of IR detection of enemy's tanks and support to night moving.

After the 1970s R&D developments of IR surveillance systems, especially for navy applications, were done in advanced Countries (especially US, UK, France, and Italy, where the first Modular FPAs Staring Omni-Directional Surveillance System prototype was designed and realized) [20]. In the 1980s the SDI Program for Ballistic Missile Defense by US was originating highly advanced E. O. Surveillance System with performances close at BLIP limits. Nowadays the main efforts are dedicated to the multispectral detection capability. Lastly, wide application of IR warning is expected in automotive for Smart Collision Avoidance Systems in poor visibility conditions: room temperature. Smart IR Receivers could be installed with high reliability and simple, immediate man-machine interface in any type of motor vehicles [53].

Future trends of infrared detectors are linked to the development of new emerging technologies of sensor fabrication for mass production especially for civil applications, with a strong two-way synergy between civil and military. New markets (automotive, intelligent building, and environmental control) and consolidated markets (biomedical and medical, energy control, and surveillance and warning) will get strong benefits from Microsystem Technologies (sensors, control and actuators) especially in automotive applications, with a real possibility of high level products at contained cost feeding a double-way of technology transfer between civil and military in the future more and more towards new military market applications (especially portable equipments). The competition among various technologies and "technical schools" has been strong with unforeseeable emerging new actors in the last years (overall, room temperature microbolometers for future, and extremely valid applications in the civil field). Operational requirements (mainly of maintenance and reliability) were pushing IR science to look for new advanced sensors which could avoid the cryogenic needs. The new microbolometers technology, because of the micro size of thin films bolometers, completely integrable with silicon technology and therefore often named silicon microbolometers, have been emerging in the last years with a very high promising for future IR sensors market growth. For extremely high sensitivity sensors especially for military and space applications the technologies actually with major possibility of future development are mainly based on photon sensors (Intrinsic and Quantum Well). Multispectral and hyperspectral capabilities with spatial-temporal filtering capabilities are also emerging especially in military and space applications for target identification. The key emerging

factor for future IR FPAs technologies is the room working temperature for uncooled imaging systems and the complete integrability with silicon microcircuits technology especially because integrated signal processing (Smart Sensors) will play a fundamental role in future applications where mass production could allow consisting cost reduction (huge markets are expected especially for automotive applications for unit cost of few hundreds Euros). So, for the first time, thanks also to the elimination of cryogenic cooling, wide use of I.R., Smart Sensors are emerging on the international market, becoming strategic components for the most important areas, like transports, (especially cars, aircrafts, and helicopters), security, environment and territory control, biomedicine.

### 6.1. Infrared Systems Evolution

- (i) From Thermography to Digital Functional Imaging.
- (ii) From Imaging to Pattern Analysis and Detection.
- (iii) From Detection to Smart Sensors Alarm Systems.
- (iv) Computational Methods in Gas Fluidodinamics.
- (v) Energy/Structure Building Control, Electricity-Mechanics Control, Medical-Veterinary Diagnostics, and Art Restoration.
- (vi) To Multispectral/Hyperspectral Patterns Systems.
- (vii) To IR/Thz Imaging/Pattern Security Applications.
- (viii) To IR/THz Spectroscopy for Security Applications.
- (ix) To Stand-Off Laser Detection IR/THz Spectroscopy.

## 7. Conclusions

Terroristic events, based on new types of threats and explosives, have pushed towards the developments of new techniques of detection and alarm employing different parts of the electromagnetic spectrum, particularly extending from infrared to terahertz radiation, that is, the E.M. band between infrared and microwave. Also in these new developments there is a priority to the developing of imaging systems, at least for the know-how originated in infrared technologies, while spectroscopic detection is mostly developed by microwave techniques. Recently the emerging terahertz technologies [11], thanks to their nonionizing radiation and their detection capability of hidden objects in clothing and in packaging containers and luggage, coupled to the spectroscopic detection of plastic explosives and other chemical and biological agents, are the most promising technologies for integrated, efficient systems for security screening and counterterrorism. Radiation at terahertz frequencies has unique properties that may be advantageous for security applications; in fact, it can penetrate many nonconducting materials, but unlike X-rays is nonionizing, and can allow radar-like imaging in three dimensions thanks to the extremely short pulses used in pulsed terahertz techniques as well as the simultaneous collection of spectroscopic information like infrared. This is important because many substances have characteristic intermolecular vibrations at

Far IR-THz frequencies that can be used to characterize them as molecules like IR spectroscopy that can detect bond vibrations of single molecules. Terahertz technologies, thanks to their nonionizing radiation and their detection capability of hidden objects in clothing and in packaging containers and luggage, coupled to the spectroscopic detection of plastic explosives and other chemical and biological agents, are very promising technologies for integrated, efficient systems for security screening and counterterrorism attacks. Far-infrared/microwaves techniques and Imaging Hyperspectral Sensors will be mostly developed for their selectivity and specificity to detect differences in the spectra of two or more species of chemical warfare agents (CWA) allowing detection of explosives with high sensitivity and very low false alarm rate. Recently integration of multispectral IR spectroscopy with quantum cascade lasers and hollow waveguides is improving sensitivity and area coverage allowing fast and effective detection at public places like airports, railway, or coach stations. In future, an evolution from Infrared Thermography to Digital Functional Imaging and from Imaging to Pattern Analysis and from Detection to Smart Sensors Alarm Systems is expected. Multispectral (IR-THz) Systems for security applications will have high growth especially coupled to new solid state tunable IR laser sources with innovative, new technologies for Multi-Spectral Multi-Domain Smart Sensors.

## References

- [1] W. Herschel, "Experiments on the refrangibility of the visible rays of the sun," *Philosophical Transactions of the Royal Society of London*, vol. 90, pp. 284–292, 1800.
- [2] S. P. Langley, "The bolometer," in *Vallegheny Observatory*, The Society Gregory, New York, NY, USA, 1880.
- [3] L. Bellingham, "Means for detecting the presence at a distance of icebergs, steamships, and other cool or hot objects," US patent no. 1, 158, 967.
- [4] R. D. Parker, "Thermic balance or radiometer," US patent no. 1.099, 199, 1914.
- [5] W. Smith, "Effect of Light on Selenium during the passage of an electric current," *Nature*, vol. 7, p. 303, 1873.
- [6] T. W. Case, "Notes on the change of resistance of certain substances in light," *Physical Review*, vol. 9, no. 4, pp. 305–310, 1917.
- [7] W. D. Lawson, S. Nielson, E. H. Putley, and A. S. Young, "Preparation and properties of HgTe and mixed crystals of HgTe-CdTe," *Journal of Physics and Chemistry of Solids*, vol. 9, no. 3-4, pp. 325–329, 1959.
- [8] I. Melngailis and T. C. Harman, *Semiconductors and Semimetals*, vol. 5, Academic Press, 1970.
- [9] W. S. Boyle and G. E. Smith, "Charge coupled semiconductor devices," *Bell System Technical Journal*, vol. 49, pp. 587–593, 1970.
- [10] D. F. Barbe, "Imaging devices using the charge-coupled concept," *Proceedings of the IEEE*, vol. 63, no. 1, pp. 38–67, 1975.
- [11] A. J. Steckl, R. D. Nelson, B. T. French, R. A. Gudmundsen, and D. Schechter, "Application of charge-coupled devices to infrared detection and imaging," *Proceedings of the IEEE*, vol. 63, no. 1, pp. 67–74, 1975.
- [12] C. Corsi, "Infrared detector arrays by new technologies," *Proceedings of the IEEE*, vol. 63, no. 1, pp. 14–26, 1975.
- [13] C. T. Elliot, D. Day, and D. Wilson, "An integrating detector for serial scan thermal imaging," *Infrared Physics*, vol. 22, no. 1, pp. 31–42, 1982.
- [14] F. Shepherd, "Schottky Diode Infrared Detectors," *Proceedings of SPIE*, vol. 443, p. 42, 1983.
- [15] W. Kosonocky, "Schottky Barrier IR CCD e Arrays," *SPIE*, vol. 443, p. 167, 1983.
- [16] S. D. Gunapala and K. M. S. V. Bandara, "Recent developments in quantum-well infrared photodetectors," *Thin Films*, vol. 21, pp. 113–237, 1995.
- [17] R. Watton, "Ferroelectric materials and devices in infrared detection and imaging," *Ferroelectrics*, vol. 91, no. 1, pp. 87–108, 1989.
- [18] R. W. Whatmore, "Pyroelectric devices and materials," *Reports on Progress in Physics*, vol. 49, no. 12, pp. 1335–1386, 1986.
- [19] R. A. Wood, C. J. Han, and P. W. Kruse, "Integrated uncooled infrared detector imaging arrays," in *Proceedings of the IEEE Solid State Sensors & Actuators Workshop*, Hilton Head Island, SC, USA, June 1992.
- [20] C. Corsi, "Infrared surveillance and warning systems," in *Proceedings of the International NATO Electronics Warfare Conference*, 1978.
- [21] C. Corsi, G. Di Nola, G. Marangoni, and G. Salcito, "Elemento Ottico Integrato per filtraggio spaziale incorporante un modulatore di ampiezza di segnali di frequenza spaziale desiderata," Tech. Rep. PT-79, Elettronica S.p.A., 1979.
- [22] T. F. Tao, D. Minler, B. Eversor, and D. Jaloshna, *Smart Sensors*, vol. 178, SPIE, 1979.
- [23] C. Corsi, G. DiNola, G. Marangoni, and G. Salcito, National patent no. 47722/80.
- [24] C. Corsi, "Smart sensors," *Microsystem Technologies*, pp. 149–154, 1995.
- [25] A. Moini, "Vision chips or seeing silicon," Tech. Rep. 8, Department Electrical & Electronics Engineering, The University of Adelaide, Adelaide, Australia, 1998.
- [26] C. Corsi, "History highlights and future trends of infrared sensors," *Journal of Modern Optics*, vol. 57, no. 18, pp. 1663–1686, 2010.
- [27] C. Corsi, "Smart Sensors," in *Infrared Spaceborne Remote Sensing XIV*, Strojnik, Ed., vol. 6297 of *Proceedings of SPIE*, 2006.
- [28] C. Corsi, "Rivelatori IR: stato dell'arte e trends di sviluppo futuro," *Atti della Fondazione Giorgio Ronchi*, vol. XLVI, no. 5, pp. 801–810, 1991.
- [29] L. J. Kozlowski and W. F. Kosonocky, "Infrared detector arrays," in *Hand-Book of Optics*, M. Bass, Ed., chapter 23, Williams, W. L. Wolfe, and McGraw-Hill, 1995.
- [30] C. Corsi, "Future trends and advanced development in I.R. detectors," in *Proceedings of 2nd Joint Conference IRIS-NATO*, London, UK, June 1996.
- [31] P. R. Norton, "Status of infrared detectors," in *Infrared Detectors and Focal Plane Arrays V*, vol. 3379 of *Proceedings of SPIE*, pp. 102–114, April 1998.
- [32] M. Razeghi, "Current status and future trends of infrared detectors," *Opto-Electronics Review*, vol. 6, no. 3, pp. 155–194, 1998.
- [33] P. Norton, J. Campbell, S. Horn, and D. Reago, "Third-generation infrared imagers," in *Infrared Technology and Applications XXVI*, vol. 4130 of *Proceedings of SPIE*, pp. 226–236, August 2000.

- [34] A. Rogalski, "IR detectors: the next millennium," in *International Conference on Solid State Crystals 2000 Epilayers and Heterostructures in Optoelectronics and Semiconductor Technology*, vol. 4413 of *Proceedings of SPIE*, pp. 307–322, October 2000.
- [35] A. Rogalski, "IR detectors: status trends," *Progress in Quantum Electronics*, vol. 27, pp. 59–210, 2003.
- [36] C. Corsi, "Infrared and the others," *Giorgio Ronchi Foundation Atti*, vol. 57, pp. 363–369, 2002.
- [37] C. Corsi, "History lessons and future trends in advanced IR detectors," *Atti della Fondazione Giorgio Ronchi*, vol. 53, pp. 11–20, 1998.
- [38] S. Harden, "Ion mobility spectrometry for detection of chemical warfare agents 1960's to the present," in *Proceedings of the 13th International Conference on Ion Mobility Spectrometry*, Gatlinburg, Tenn, USA, July 2004.
- [39] J. Xu, W. B. Whitten, and J. M. Ramsey, "A miniature ion mobility spectrometer," *International Journal for Ion Mobility Spectrometry*, vol. 5, no. 2, pp. 207–214, 2002.
- [40] J. Stach and J. I. Baumbach, "Ion mobility spectrometry—basic elements/applications," *International Journal for Ion Mobility Spectrometry*, vol. 5, no. 1, pp. 1–21, 2002.
- [41] C. Corsi, N. Liberatore, S. Mengali, A. Mercuri, R. Viola, and D. Zintu, "Advanced applications to Security of IR smart microbolometers," in *Electro-Optical Remote Sensing, Detection, and Photonic Technologies and Their Applications*, vol. 6739 of *Proceedings of SPIE*, September 2007.
- [42] J. Hildenbrand, J. Herbst, J. Wöllenstein, and A. Lambrecht, "Explosive detection using infrared laser spectroscopy," Fraunhofer Institute for Physical Measurement Techniques (IPM), Heidenhofstr. 8, D-79110 Germany.
- [43] J. Faist, F. Capasso, D. L. Sivco, C. Sirtori, A. L. Hutchinson, and A. Y. Cho, "Quantum cascade laser," *Science*, vol. 264, no. 5158, pp. 553–556, 1994.
- [44] A. A. Kosterev and F. K. Tittel, "Chemical sensors based on quantum cascade lasers," *IEEE Journal of Quantum Electronics*, vol. 38, no. 6, pp. 582–591, 2002.
- [45] B. G. Lee, M. A. Belkin, R. Audet et al., "Widely tunable single-mode quantum cascade laser source for mid-infrared spectroscopy," *Applied Physics Letters*, vol. 91, no. 23, Article ID 231101, 2007.
- [46] A. Lambrecht, S. Hartwig, J. Herbst, and J. Wöllenstein, "Hollow fibers for compact infrared gas sensors," in *Photonic Crystal Materials and Devices VII*, *Proceedings of SPIE*, January 2008.
- [47] S. Mengali, N. Liberatore, and R. Viola, "DIRAC," in *Proceedings of the 1st National Conference on Sensors*, F. Baldini, A. D'Amico, C. Di Natale, P. Siciliano, and R. Seeber, Eds., vol. 162 of *Lecture Notes in Electrical Engineering*, Rome, Italy, 2013.
- [48] M. C. Kemp, P. F. Taday, B. E. Cole, J. A. Cluff, A. J. Fitzgerald, and W. R. Tribe, "Security applications of terahertz technology," in *Terahertz for Military and Security Applications*, vol. 5070 of *Proceedings of SPIE*, pp. 44–52, April 2003.
- [49] K. Kawase, Y. Ogawa, Y. Watanabe, and H. Inoue, "Non-destructive terahertz imaging of illicit drugs using spectral fingerprints," *Optics Express*, vol. 11, no. 20, pp. 2549–2554, 2003.
- [50] The Telemobiloscope, *Electrical Magazine*, vol. 2, 1904.
- [51] H. Sekiguchi, K. Matsushita, S. Yamashiro et al., "On-site determination of nerve and mustard gases using a field-portable gas chromatograph-mass spectrometer," *Forensic Toxicology*, vol. 24, no. 1, pp. 17–22, 2006.
- [52] G. Marconi Conference, "American Institute of Electrical Engineers/Institute of Radio Engineers," 1922.
- [53] C. Corsi, European patent PCT/IT99/00327-Int.Publ.N.WO, 00596.

## Research Article

# Nanoscale Biomolecular Detection Limit for Gold Nanoparticles Based on Near-Infrared Response

Mario D'Acunto,<sup>1,2</sup> Davide Moroni,<sup>2</sup> and Ovidio Salvetti<sup>2</sup>

<sup>1</sup>Istituto di Struttura della Materia, Consiglio Nazionale delle Ricerche, Via Fosso del Cavaliere 100, 00133 Roma, Italy

<sup>2</sup>Istituto di Scienze e Tecnologia dell'Informazione, Consiglio Nazionale delle Ricerche, Via Moruzzi 1, 56124 Pisa, Italy

Correspondence should be addressed to Mario D'Acunto, mario.dacunto@ism.cnr.it

Received 27 July 2012; Accepted 31 October 2012

Academic Editor: Carlo Corsi

Copyright © 2012 Mario D'Acunto et al. This is an open access article distributed under the Creative Commons Attribution License, which permits unrestricted use, distribution, and reproduction in any medium, provided the original work is properly cited.

Gold nanoparticles have been widely used during the past few years in various technical and biomedical applications. In particular, the resonance optical properties of nanometer-sized particles have been employed to design biochips and biosensors used as analytical tools. The optical properties of nonfunctionalized gold nanoparticles and core-gold nanoshells play a crucial role for the design of biosensors where gold surface is used as a sensing component. Gold nanoparticles exhibit excellent optical tunability at visible and near-infrared frequencies leading to sharp peaks in their spectral extinction. In this paper, we study how the optical properties of gold nanoparticles and core-gold nanoshells are changed as a function of different sizes, shapes, composition, and biomolecular coating with characteristic shifts towards the near-infrared region. We show that the optical tenability can be carefully tailored for particle sizes falling in the range 100–150 nm. The results should improve the design of sensors working at the detection limit.

## 1. Introduction

The development of biosensors devices requires sophisticated approaches to detect and to identify the analytes [1–3]. Because the sensor signal-to-noise ratio increases with decreasing size for many devices, many researchers are expending considerable effort for miniaturizing sensing devices down to nanoscale size [3–7]. In the past decade several authors have analyzed the effect of flow, size, and adsorption isotherms on biomolecular adsorption and in a limited way the effects at nanometer length scales. The role of nanoscale size can be shown examining a simple sensor geometry (e.g., hemisphere) that absorbs the analyte [6, 8, 9]. The maximum number of molecules,  $N(t)$ , that can accumulate on a sensor due to irreversible adsorption may be determined by

$$N(t) = \int_0^t F(\tau) d\tau = \int_0^t \int_A f d\sigma d\tau, \quad (1)$$

where  $F$  is the total flux (molecule  $s^{-1}$ ),  $f$  is the flux at the sensors (molecules  $s^{-1}m^{-2}$ ),  $\sigma$  is the unit area,  $A$  is the sensor

area, and  $t$  is time. Time dependence in (1) involves a crucial question for clinical applications; that is, if any analyte molecule that contacts the sensor surface can be detected, what is the minimum detectable concentration for a given accumulation time? Sheehan and Whitman [6] showed that DNA microarrays with a 200  $\mu m$  diameter hemisphere can detect  $\sim 1$  fM in  $\sim 1$  min, which is actually very close to the actual DNA detection limit,  $\sim 20$  fM. Analogously, from (1) is possible to deduce the accumulation events

$$N(t) = 4DN_A c_0 a t, \quad (2)$$

where  $N_A$  is Avogadro's number,  $c_0$  is the initial solution concentration,  $a$  is the radius of the sensing surface, and  $D$  is a diffusion constant. It is remarkable that (2) is linear in both radius and time. This implies that when reducing the size of the absorbing surface, the time for a critical accumulation of events increases consequently. The advent of nanotubes and nanowires as biosensors introduces new geometries into the sensing activity with some changes to accumulation events as in (2).

The use of nanotechnologies for diagnostic applications meets the rigorous demands of clinical standards sensitivity with cost effectiveness. Today, main nanodiagnostic tools include quantum dots (QDs), gold nanoparticles, and cantilevers [10]. The effectiveness of nanoparticles as biomedical imaging contrast and therapeutic agents depends on their optical properties. Biosensing applications based on surface plasmon resonance shifts need strong resonance in the wavelength sensitivity range of the instrument as well as narrow optical resonance line widths. For actual *in vivo* imaging and therapeutic applications, the optical resonance of the nanoparticles is strongly desired to be in the near-infrared (NIR) region of the biological water window, where the tissue transmissivity is the highest [11–15].

The optical properties of gold nanoparticles in the visible and near-infrared (vis-NIR) domains are governed by the collective response of conduction electrons. These form an electron gas that moves away from its equilibrium position when perturbed by an external light field, thus creating induced surface polarization changes that act as a restoring force on the electron gas. This results in a collective oscillatory motion of the electrons similar to the vibrations of a plasma and characterized by a dominant resonance band lying in the vis-NIR for gold and called plasmon excitations. Thus the surface of gold nanoparticles can be used as a sensing element because when biomolecules attach to such surface the binding event can be revealed by optical changes. In addition, it is possible to calculate the maximum number of possible binding events and the consequent optical response when the shape and size of the gold particles are known.

In this paper, we will calculate and simulate the optical tunability of gold nanoparticles and core-gold nanoshells (optical changes with nanoparticles sizes) using the classical Mie theory and discrete dipole approximation (DDA). We will show that when biomolecules bind to gold surface optical shifts toward the near-infrared region are produced, and wavelengths changes can be accurately quantified. The accurate knowledge of the optical tunability could allow for improving sensing performance, sensitivity, and figure of merit of biosensors operating at detection limit in short time as requested in clinical applications.

## 2. Nanoscale-Sized Systems for Detection Limit

The increased demand for sensitivity requires that a diagnostically significant interaction occurs between analyte molecules and signal-generating particles, thus enabling detection of a single analyte molecule. Nanotechnology has enabled one-to-one interaction between analytes and signal-generating particles such as QDs and gold nanoparticles. Here, we review briefly the most important nanoscale tools for detection limit, such as QDs, cantilevers, and gold nanoparticles [10, 16].

QDs are semiconductor nanocrystals, characterized by strong light absorbance, that can be used as fluorescent labels for biomolecules. A typical QD has a diameter of 2–10 nm

and is usually composed of a core consisting of a semiconductor material enclosed in a shell of another semiconductor material with a larger spectral bandgap. When a QD absorbs a photon with energy higher than the bandgap energy of the composing semiconductor, an exciton (electron-hole pair) is created. As a result, a broadband absorption spectrum occurs because of the increased probability of absorption at shorter wavelengths. The recombination of the exciton, generally characterized by a long lifetime  $>10$  ns, to a lower energy state leads to emission of a photon with a narrow symmetric band [17–19]. QDs are reported to emit with lifetimes of 5–40 ns, whereas conventional dyes emit in a time less than 2 ns. This characteristic produces a strong and stable fluorescence signal. In addition, due to quantum confinement effect a direct relationship exists between the QD size and the values of the quantized energy levels. Methods for tracking and detecting QDs are numerous and include fluorometry and several types of microscopy, such as fluorescence, confocal, total internal reflection, wide-field epifluorescence, near-field optical microscopy, and multiphoton microscopy. The choice of detection techniques depends on the emission of wavelengths; for example, QDs composed by CdSe/NzS emit in the 530–630 nm range and InP and InAs QDs emit in the NIR range, while PbS emits in the 850–950 nm range and PbSe QD in the mid-infrared range.

Another nanoscale detection technique is based on cantilevers [20–22]. Cantilevers are small beams similar to those used in atomic force microscopy and they operate detection by use of nanomechanical deflections. An instructive example of operating cantilevers is the detection of DNA hybridization. The cantilever surface holds a particular DNA sequence capable of binding to a specific target. When the hybridization occurs with the cantilever single-stranded DNA, mechanical stress produced by the rebinding process underlying the hybridization deflects the cantilever, with a measurable deflection by the optical lever method proportional to the amount of DNA hybridized. This technique can be used as a microarray, allowing for multiple analyses. However, this method currently needs further development to solve the problem of nonspecific binding [23].

Gold nanoparticles and gold nanoshells provide great sensitivity for the detection of DNA antibodies and proteins [24–28]. The instrumental platform for the detection of biomolecules including gold particles is based on surface plasmon resonance (SPR). SPR is an optical technique that measures the refractive index of very thin layers of material adsorbed on a metal. It offers real-time *in situ* analysis of dynamic surface events and is capable of defining rates of adsorption and desorption for surface interactions. Plasmon-plasmon resonance, resulting from the interaction of locally adjacent gold nanoparticle labels that have bound to a target, produces changes in optical properties that can be used for detection. It is known that the characteristic red color of gold colloid changes to a bluish-purple color on colloid aggregation because of this effect. Analogously, the reduction of gold particle sizes involves shifts toward the NIR region [29]. Raman spectroscopy is a favored detection method using silver in the visualization process. In this case, gold nanoparticles can be coated with silver shells;

silver-coated gold particles less than 100 nm in size have strong light-scattering properties and can easily be detected by optical microscopies operating at the detection limit for oligonucleotides down to  $\sim 10$  fM, that is, nearly 50-fold lower than conventional fluorophore-based methods. Gold nanoshells could allow direct, rapid, and economically feasible analysis of whole blood samples. Generally, a nanoshell consists of concentric spherical nanoparticles with a dielectric core, meanly consisting of gold sulfide or silica, surrounded by a thin gold shell. Variations in the relative thickness of the core and outer shell allow the optical resonance of gold to go into the midinfrared region. Other relative surface properties can be used to focus the absorption wavelength range into the near-infrared, just above the absorption of hemoglobin and below that of water [30]. This characteristic aids in avoiding interference from hemoglobin giving the possibility to do a direct analysis of whole blood. An additional advantage of gold nanoshells is the excellent biocompatibility.

The optical tunability of gold nanoparticles and core-gold nanoshells resides in plasmon resonance properties. It is well known that the plasmon resonance of metal nanoparticles is strongly sensitive to the nanoparticles' size and shape and the dielectric properties of the surrounding environments. We will simulate the optical tunability of gold nanoparticles and gold nanoshells (optical changes with nanoparticles' sizes and surface biomolecular coating) using the classical Mie theory and DDA-modified approach. Finally, we will obtain the wavelength shift as a function of different size dimension, environments, and biomolecular coating layer of the gold nanoparticles. The accurate knowledge of the optical tunability and wavelength shifts should allow for development of biosensors operating at detection limit in short time as requested in clinical applications.

The design of biosensors working at the detection limit must attempt to compare sensing performance, sensitivity, and figure of merit (FOM) [31]. The sensitivity  $S$  is defined as the ratio of the resonant wavelength shift  $\partial\lambda_{\text{res}}$  to the variation of the surrounding refractive index  $\partial n_s$ , while the FOM is defined as the ratio of the refractive index sensitivity to the resonance width  $\Delta\lambda$ :

$$S = \frac{\partial\lambda_{\text{res}}}{\partial n_s}, \quad \text{FOM} = \frac{S}{\Delta\lambda}. \quad (3)$$

Resolution is typically defined as the minimum detection limit. In addition, sensitivity and thence resolution can be modified by size and geometry of the gold nanoparticles and nanostructure environment. In general, the adsorbed mass on the sensor surface can be approximated by the De Freijter's formula, which is based on the refractive index change [32]

$$\gamma = \frac{d\Delta n}{\partial n/\partial c}, \quad (4)$$

where  $d$  is the dimension of the adsorbed species (biomolecule) falling in the range of nanometers,  $\Delta n$  is the refractive index difference between the medium and the species, and  $\partial n/\partial c$  is the correspondent biomolecular

refractive increment. Analogously, the spectral response of the refractometric nanoplasmonic sensors can be described by

$$\Delta\lambda = m(n_{\text{eff}} - n_{\text{medium}}), \quad (5)$$

where  $m$  is the refractive index sensitivity, expressed in plasmon resonance peak shift per refractive index unit (RIU), and  $n_{\text{eff}}$  is the effective refractive index of the adsorbate layer. In the simplest approximation, the surface plasmon resonance-induced evanescent field decays exponentially from the surface as  $E(z) = \exp(-z/l_d)$  with a decay length  $l_d$ . The effective refractive index of the adsorbate layer is described as

$$n_{\text{eff}} = \frac{2}{l_d} \int_0^d n(z)E^2(z)dz. \quad (6)$$

Using (5)-(6) into (4) we obtain a relationship of the surface plasmon resonance peak shift with the surface coverage of the adsorbate:

$$\gamma(t) = \frac{d\Delta\lambda(t)}{m(1 - \exp(-2d/l_d))\partial n/\partial c}. \quad (7)$$

In the next section, we will provide the accurate calculation of wavelength shifts due to increased size of gold nanoparticles and coating of gold surface in core-gold nanoshells. Equation (7) establishes that the accurate knowledge of such shifts gives the possibility to design gold nanoparticles based sensors working at the biomolecular detection limit.

### 3. Optical-Infrared Response of Gold Nanoparticles and Core-Gold Nanoshells: Calculation and Simulation Methods

The complexity of the electromagnetic field in the presence of arbitrarily shaped nanoparticles is such that Maxwell's equations must be solved using numerical methods [33]. The far-field performance of a nanoparticle is summarized in the wavelength-dependent absorption and scattering cross sections, and as a consequence, the optical properties of gold nanospheres and silica-gold nanoshells will be quantified in terms of their calculated absorption and scattering efficiency. The light intensity transmitted through a dilute dispersion  $I$  (assuming no more than one photon-particle collision per photon) is  $I = I_0 \exp[-(\sigma_{\text{abs}} + \sigma_{\text{sc}})NL]$ , where  $I_0$  is the incident light intensity,  $N$  is the number of particles per unit volume,  $L$  is the path length inside the dispersion, and  $\sigma_{\text{abs}}$  and  $\sigma_{\text{sc}}$  are the wavelength-dependent absorption and scattering cross sections, respectively. The optical modeling of nanoparticles thus relies on the solution of Maxwell's equations for each specific geometry and set of illumination conditions, assuming a local dielectric function,  $\epsilon(\omega)$ , and description of the materials involved. When dipolar contribution in plasmon excitation is prominent, then the far-field cross sections can be obtained from the polarizability  $\alpha$  using the following expressions [34]:

$$\sigma_{\text{abs}} + \sigma_{\text{sc}} = \frac{2\pi}{\lambda\sqrt{\epsilon_m}} \text{Im}\{\alpha\}, \quad \sigma_{\text{sc}} = \frac{8\pi^3}{3\lambda^4} |\alpha|^2, \quad (8)$$

where  $\varepsilon_m$  is the environmental permittivity of the medium outside the particle and  $\lambda$  is the light wavelength.

To simulate the optical properties of gold nanoparticles, many methods can be found. Mie theory is one of such methods [35]. Mie scattering theory begins with Maxwell's equations and the necessary boundary conditions, which are then transformed into spherical polar coordinates with a solution of the wave vector equation emerging. The coefficients for scattering arise and the theory is extended to the far-field solution based on a plane constructed from the incident and scattered waves. At this point, the Stokes parameters that are the measurable quantities and the formulation of matrix plane can be quantified. From Mie theory, once scattering matrices have been derived, information about the direction and polarization dependence of the scattered light can be extracted, so that absorption, scattering, and extinction cross sections for any arbitrary spherical particle with dielectric function  $\varepsilon$  can be calculated. Since extincted power is the sum of the scattered and absorbed power, the absorption cross section is simply  $\sigma_{\text{abs}} = \sigma_{\text{ext}} - \sigma_{\text{sca}}$ , while the scattering and extinction cross sections can be calculated from the total cross section of a spherical particle, that can be written as

$$\sigma = \frac{\lambda_m^2}{2\pi} \sum_{l=1}^{l=\infty} (2l+1) \left[ \text{Im}\{\varphi_l^E\} + \text{Im}\{\varphi_l^M\} \right], \quad (9)$$

where  $\varphi_l^{E,M}$  are the electric and magnetic scattering coefficients, respectively, and  $l$  is the orbital momentum number (e.g.,  $l = 1$  for a dipole). These coefficients admit analytical expressions in terms of spherical Bessel and Hankel functions for a homogeneous sphere [33]

$$\begin{aligned} \varphi_l^E &= \frac{-\varepsilon_m j_l(\rho_m) \left[ j_l(\rho) + \rho j_l'(\rho) \right] + \varepsilon \left[ j_l(\rho_m) + \rho_m j_l'(\rho_m) \right] j_l(\rho)}{\varepsilon_m h_l(\rho_m) \left[ j_l(\rho) + \rho j_l'(\rho) \right] - \varepsilon \left[ h_l(\rho_m) + \rho_m h_l'(\rho_m) \right] j_l(\rho)} \\ \varphi_l^M &= \frac{-\rho j_l(\rho_m) j_l'(\rho) + \rho_m j_l'(\rho_m) j_l(\rho)}{\rho h_l(\rho_m) j_l'(\rho) - \rho_m h_l'(\rho_m) j_l(\rho)}, \end{aligned} \quad (10)$$

where  $\rho = (2\pi R/\lambda)\sqrt{\varepsilon}$ ,  $\rho_m = (2\pi R/\lambda)\sqrt{\varepsilon_m}$ , and the prime represents the first differentiation with respect to the argument in parentheses. It should be noted that plasmon modes are related to the poles of  $\varphi_l^E$ . In fact, the magnetic contribution to scattering produces only resonances for particle sizes comparable to the wavelength. The multipolar polarizability is proportional to  $\varphi_l^E$ , and in particular, the dipolar polarizability reads  $\alpha = (3\lambda^3/4\pi^2)\varphi_{l=1}^E$ , where the dipolar electric scattering coefficient can be readily calculated using  $j_1(x) = \sin x/x^2 - \cos x/x$  and  $h_1(x) = (1/x^2 - i/x) \exp(ix)$ , so that (8) can be used instead of (9). The value of  $\alpha$  obtained is really accurate for describing gold spheres

with diameters up to 200 nm and simplified expression can be found as, for example,

$$\begin{aligned} \alpha &= 3V\varepsilon_m \\ &\times \frac{1 - 0.1(\varepsilon + \varepsilon_m)\theta^2/4}{(\varepsilon + 2\varepsilon_m)/(\varepsilon - \varepsilon_m) - (0.1\varepsilon + \varepsilon_m)\theta^2/4 - i(2/3)\varepsilon_m^{3/2}\theta^3}, \end{aligned} \quad (11)$$

where  $V$  is the particle volume,  $\varepsilon$  and  $\varepsilon_m$  are the permittivities of the particle and the surrounding medium, and  $\theta = 2\pi R/\lambda$  is the size parameters that recover the electrostatic limit for  $\theta = 0$ . Analogously, the dipolar polarizability of a coated gold nanosphere is given by

$$\begin{aligned} \alpha &= 3V\varepsilon_m \\ &\times \frac{(R_0/R_i)^3(2\varepsilon_{\text{coat}} + \varepsilon)(\varepsilon_{\text{coat}} - \varepsilon_m) - (\varepsilon_{\text{coat}} - \varepsilon)(2\varepsilon_{\text{coat}} + \varepsilon_m)}{(R_0/R_i)^3(2\varepsilon_{\text{coat}} + \varepsilon)(\varepsilon_{\text{coat}} + 2\varepsilon_m) - 2(\varepsilon_{\text{coat}} - \varepsilon)(\varepsilon_{\text{coat}} - \varepsilon_m)}, \end{aligned} \quad (12)$$

where  $R_i$  is the internal radius of the core material described by  $\varepsilon$ , the coating of permittivity  $\varepsilon_{\text{coat}}$  extends up to a radius  $R_0$ , and the medium outside the particle has permittivity  $\varepsilon_m$ . An analogous formula can be derived for a barium titanate core particle with a gold nanoshell. Calculations of the optical absorption and scattering efficiency of gold nanospheres and barium titanate-gold nanoshells will be presented below. The required parameters for the code were the value of the core and shell radii  $R_1$  and  $R_2$ , the complex refractive indices for the core, shell, and biomolecular coating, and the surrounding medium  $n_c$ ,  $n_s$ ,  $n_b$ , and  $n_m$ , respectively, Figure 1.

The discrete-dipole approximation (DDA) has been used as a complimentary method to Mie theory [36]. DDA is a flexible and powerful technique for computing scattering and absorption by targets of arbitrary geometry. DDA calculations require choices for the locations and the polarizabilities of the point dipoles that represent the targets. To approximate a certain geometry (e.g., a sphere or a core-shell-environment system, where the shell is made by gold) with a finite number of dipoles, we might consider using some number of closely spaced, weaker dipoles in regions near the target boundaries to do a better job of approximating the boundary geometry. For a core-shell system, we use the following algorithm to generate the dipole array. Given a coordinate reference system, (1) we generate a trial lattice defined by a lattice spacing  $d$  and coordinates of the lattice point nearest the origin. (2) All lattice sites are located within the volume  $V$  of the core-shell-surrounding system (where the surrounding is considered as a sphere enveloping the core-shell system). (3) Try different values of  $d$  and dipoles coordinates and maximize some goodness-of-fit criterion for a list of occupied sites  $i = 1, \dots, N$ . Each of these occupied sites represents a cubic subvolume  $d^3$  of material centered on the site. Particular efforts have been addressed to distinguish between lattice sites near the surface and those in the interior. (4) We therefore rescale the array

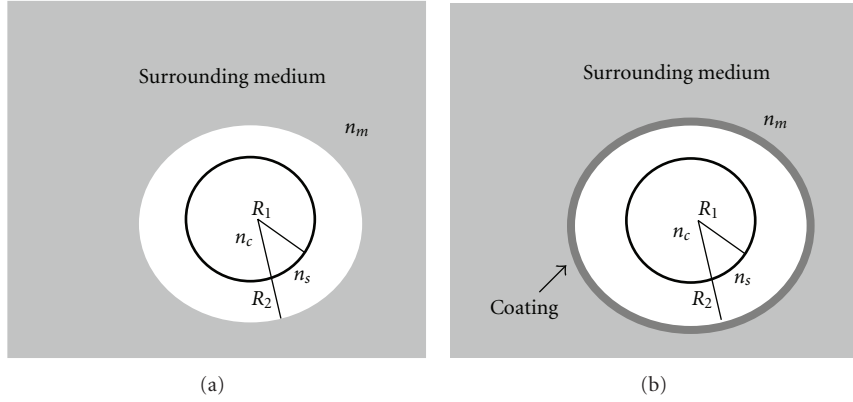


FIGURE 1: (a) Schematic sketch of a gold nanoshell,  $R_1$  and  $R_2$  are the core and shell radii, and the complex refractive indices for the core, shell, and the surrounding medium are  $n_c$ ,  $n_s$ , and  $n_m$ , respectively. (b) The same gold nanoshell with a biomolecular absorbed coating layer. Note that the shell radius is defined as the total radius minus the core radius.

by requiring that  $d = (V/N)^{1/3}$ , so that the volume  $Nd^3$  of the occupied lattice sites is equal to the volume  $V$  of the original target. (5) For each occupied  $N$  sites, assign a dipole polarizability  $\alpha_i$ .

The assignment of dipole polarizabilities is a crucial question in a DDA method. Following the seminal paper of Draine and Flatau [37], the polarizability  $\alpha(\omega)$  can be found analytically in the long-wavelength limit  $|n|kd \ll 1$  as a series expansion in the powers of  $kd$ , with the criterion that  $N > (4\pi/3)|n|^3(kr_{\text{eff}})^3$  where  $n$  is the refractive index and  $r_{\text{eff}} = (3V/4\pi)^{1/3}$  is the effective radius of the nanoparticles of volume  $V$ . As a consequence, for materials with higher refractive indexes the DDA method can overestimate absorption cross sections. A customized code for the DDA calculations of gold nanoshells has been written adapting DDSCAT program that is a freely available code [38, 39].

The finiteness of the speed of light has important consequences that affect the response of gold nanoparticles. First of all, the electromagnetic field cannot penetrate beyond a certain depth inside the metal, the so-called skin depth, which is of the order of 15 nm in the vis-NIR. But more importantly, redshifts take place as the particles size increases, and retardation effects play a significant role when the diameter is a consistent fraction of the mode wavelength  $\lambda_m$  in the surrounding medium, which is related to the free-space wavelength through  $\lambda_m = \lambda/\sqrt{\epsilon_m}$ . In particular, opposite charges are separated by roughly one particle diameter in a dipole mode, so that the reaction of one end of the particle to changes produced in the other end takes place with a phase delay of the order of  $4\pi R/\lambda_m$ , and consequently, the period of one mode oscillation increases to accommodate this delay. Analogously, quadrupoles and higher-order modes produce more nodes in the distribution of the polarization charges induced on the surface of the particle, which reduce the effective interaction distance.

Figure 2 shows the shift towards the NIR region for the efficiency of the absorption calculated using the Mie theory and DDA approach for a gold nanoparticle (radius 120 nm, black line) and a barium titanate (BaTiO<sub>3</sub>)-gold nanoshell

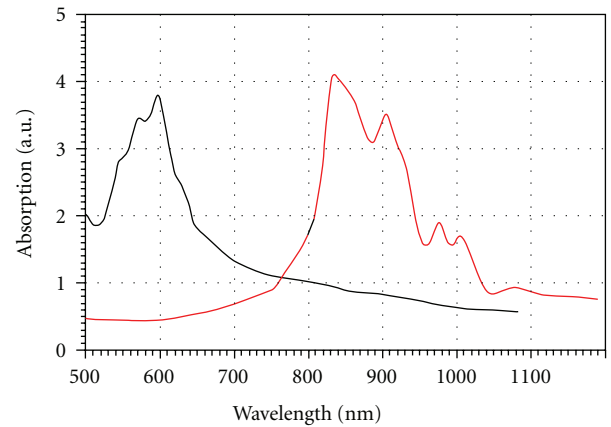


FIGURE 2: Calculated spectra of the efficiency of absorption as a function of the wavelength for gold nanoparticle (120 nm, black line) and barium titanate-gold nanoshell (100 + 20 nm, red line).

(core 100 nm, gold 20 nm, red line). The barium titanate refractive index was taken to follow the dispersion formula as  $n^2 - 1 = 4.187\lambda^2/(\lambda^2 - 0.223^2)$ . The refractive index of the surrounding medium was considered to be  $n_m = 1.34 + 0i$  at all wavelengths, close to the water.

Optical tunability plays a fundamental role for the identification of size, shape, and core-shell composition of the nanoparticles for biomedical sensors and detection limit definition. In order to define the optical tunability, the red shifts must be carefully identified. In Figure 3, the tunability of the extinction cross section of a gold nanoparticle as a function of the diameter size is reported, while in Figure 4, the same quantity for a core-gold nanoshell (core = BaTiO<sub>3</sub>, gold shell = 20 nm) is reported as a function of different core/gold ratios. In the case of a gold nanosphere, the total extinction cross section increases linearly as the nanosphere size increases, with an initial value of  $\sigma_{\text{ext}} (\text{nm}^2) = 4871$  for a gold nanosphere diameter of 40 nm. Approximately, linear behavior of total extinction cross section is waited for core/shells systems, Figure 4.

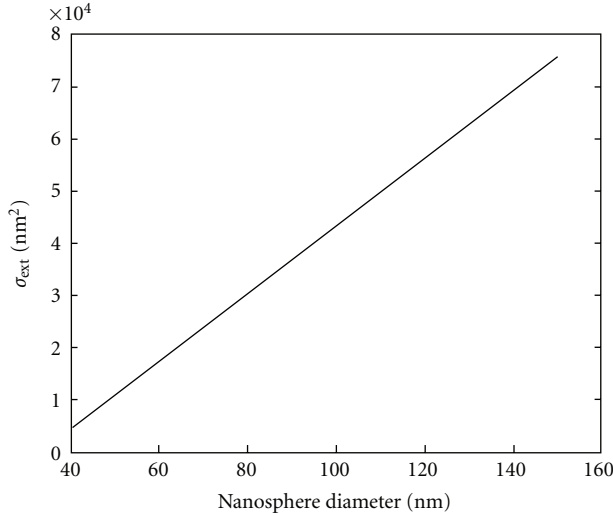


FIGURE 3: Tunability of the extinction cross section of nanoparticles. Variation of the total extinction cross section as a function of the nanosphere diameter size. The extinction cross section changes linearly with the gold nanosphere diameter giving the possibility of direct tuning of optical response with gold nanosphere dimension.

The increase in the extinction scattering with the nanoparticle volume has been related to increased radiative damping in larger nanoparticles based on experimental scattering spectra of gold nanospheres and core-gold systems [29–33]. This behavior suggests that larger nanoparticles of high core/shell ratios would be more suitable for biological sensors applications based on light scattering. In the case of nanoshells, the relative core-shell dimensions vary linearly the magnitude of light extinction. This implies that a decrease in the core/shell ratio can be seen to be an effective handle in increasing the scattering contribution to the total extinction. The next calculated quantity is the effect of a biomolecular adsorbed layer on the gold surface for a core/shell system with fixed ratio (80 nm for BaTiO<sub>3</sub> and 20 nm for gold surface) on wavelength shifts  $\Delta\lambda$  for different layer dimensions. This quantity is particularly important for the definition of sensitivity response and FOM of a biosensor, as described by (3). In Figure 5, the progressive plasmon resonance maximum wavelength red-shift is shown as a function of increased homogeneous layers of adsorbed bovine serum albumin (BSA, 170 mg/mol). The calculation was made, as in the previous case, using (8) and (12), but including in the DDA approach progressive 1-to-3 supplemental layers with a known refractive index [40]. It is interesting to note that when increasing the size of the nanoparticle (from left black line to cyan line on right) an increasing wavelength red-shift is observed. The reduction of the peaks is an artifact effect and the absorption quantity should be normalized including the increasing nanoparticle volume.

Figure 5 represents the most important result of the present paper. In fact, once the red-shift,  $\Delta\lambda$ , is accurately known, it should be possible to quantify the refractive index

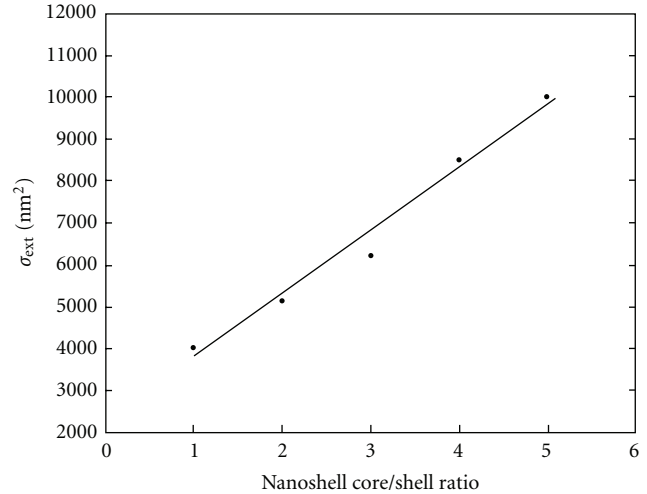


FIGURE 4: Tunability of the extinction cross section as a function of nanoshells core/shell ratios. As in the case of nanospheres, the extinction cross section shows a behavior close to be linear with core/shell ratio increments (gold shell = 20 nm).

changes,  $\gamma$ , (7), to design high sensitive biosensors operating at detection limit with effective optimal  $\partial n/\partial c$  factor. The absolute magnitude of the optical cross section provides a limited reliable measure of the optical properties of a population of nanoparticles employed in the biomedical sensing activity or other real-life biomedical applications because broad size nanoparticle population can have a different optical response with respect to few nanoparticles but with higher sizes. The red-shifts as a function of nanoparticles diameter size, shown in Figure 5, are one quantity that can be measured in scanning near optical microscopy (SNOM) technique, measurements that will provide the next development of the present paper.

#### 4. Conclusions

The development of biosensors devices requires sophisticated approaches to detect and to identify the analytes. Because the sensor signal-to-noise ratio increases with decreasing size for many devices, many researchers are expending considerable effort for miniaturizing sensing devices down to nanoscale size. Gold nanoparticles have been widely used during the past few years in various technical and biomedical applications. In particular, the resonance optical properties of nanometer-sized particles have been employed to design biochips and biosensors used as analytical tools. The optical properties of nonfunctionalized gold nanoparticles and core-gold nanoshells play a crucial role for the design of biosensors where gold surface is used as a sensing component. Gold nanoparticles exhibit excellent optical tunability at visible and near-infrared frequencies leading to sharp peaks in their spectral extinction. In this paper, we have simulated how the optical properties of gold nanoparticles are changed as a function of different sizes, shapes, and composition. We have shown that the optical

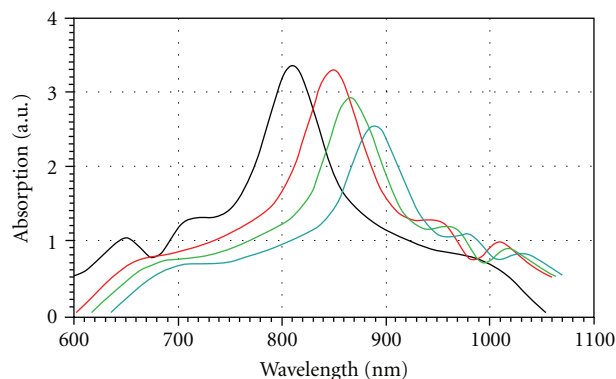


FIGURE 5: Plasmon resonance maximum red-shift for the absorption in a core/shell nanoparticle (BaTiO<sub>3</sub> 80 nm, Au 40 nm) with a different number of coating layers of BSA biomolecules (170 mg/mol). Black line represents the uncoated nanoshell, red line represents the coating with a uniform BSA layer, the green line represents two layers and, finally, the cyan line shows the effect of the third layer.

tunability can be carefully tailored for particle sizes falling in the range 100–150 nm. Nanoshells made by a barium titanate core have been considered and the optical response of gold surfaces coated by 1-to-3 layer of BSA was taken in consideration. The simulated results will help experimental optical tests that will be performed using nanoscale optical scanning technology.

## Acknowledgment

M. D'Acunto wishes to acknowledge the NanoICT Project for useful support.

## References

- [1] J. M. Ramsey and A. van der Berg, *Micro Total Analysis Systems*, Kluwer Academic Publisher, Boston, Mass, USA, 2001.
- [2] D. R. Reyes, D. Iossifidis, P. A. Auroux, and A. Manz, "Micro total analysis systems. 1. Introduction, theory, and technology," *Analytical Chemistry*, vol. 74, no. 12, pp. 2623–2636, 2002.
- [3] P. A. Auroux, D. Iossifidis, D. R. Reyes, and A. Manz, "Micro total analysis systems. 2. Analytical standard operations and applications," *Analytical Chemistry*, vol. 74, no. 12, pp. 2637–2652, 2002.
- [4] J. Kong, N. R. Franklin, C. Zhou et al., "Nanotube molecular wires as chemical sensors," *Science*, vol. 287, no. 5453, pp. 622–625, 2000.
- [5] Y. Cui, Q. Wei, H. Park, and C. M. Lieber, "Nanowire nanosensors for highly sensitive and selective detection of biological and chemical species," *Science*, vol. 293, no. 5533, pp. 1289–1292, 2001.
- [6] P. E. Sheehan and L. J. Whitman, "Detection limits for nanoscale biosensors," *Nano Letters*, vol. 5, no. 4, pp. 803–807, 2005.
- [7] E. S. Jeng, A. E. Moll, A. C. Roy, J. B. Gastala, and M. S. Strano, "Detection of DNA hybridization using the near-infrared band-gap fluorescence of single-walled carbon nanotubes," *Nano Letters*, vol. 6, no. 3, pp. 371–375, 2006.
- [8] P. R. Nair and M. A. Alam, "Screening-limited response of NanoBiosensors," *Nano Letters*, vol. 8, no. 5, pp. 1281–1285, 2008.
- [9] L. Soleymani, Z. Fang, E. H. Sargent, and S. O. Kelley, "Programming the detection limits of biosensors through controlled nanostructuring," *Nature Nanotechnology*, vol. 4, no. 12, pp. 844–848, 2009.
- [10] H. M. E. Azzazy, M. M. H. Mansour, and S. C. Kazmierczak, "Nanodiagnosics: a new frontier for clinical laboratory medicine," *Clinical Chemistry*, vol. 52, no. 7, pp. 1238–1246, 2006.
- [11] R. Weissleder, C. H. Tung, U. Mahmood, and A. Bogdanov, "In vivo imaging of tumors with protease-activated near-infrared fluorescent probes," *Nature Biotechnology*, vol. 17, no. 4, pp. 375–378, 1999.
- [12] W. C. W. Chan and S. Nie, "Quantum dot bioconjugates for ultrasensitive nonisotopic detection," *Science*, vol. 281, no. 5385, pp. 2016–2018, 1998.
- [13] S. M. Bachilo, M. S. Strano, C. Kittrell, R. H. Hauge, R. E. Smalley, and R. B. Weisman, "Structure-assigned optical spectra of single-walled carbon nanotubes," *Science*, vol. 298, no. 5602, pp. 2361–2366, 2002.
- [14] X. Y. Wu, H. J. Liu, J. Q. Liu et al., "Immunofluorescent labeling of cancer marker Her2 and other cellular targets with semiconductor quantum dots," *Nature Biotechnology*, vol. 21, no. 4, pp. 41–43, 2003.
- [15] C. L. Amiot, S. Xu, S. Liang, L. Pan, and J. X. Zhao, "Near-infrared fluorescent materials for sensing of biological targets," *Sensors*, vol. 8, no. 5, pp. 3082–3105, 2008.
- [16] H. M. E. Azzazy, M. M. H. Mansour, and S. C. Kazmierczak, "From diagnostics to therapy: prospects of quantum dots," *Clinical Biochemistry*, vol. 40, no. 13–14, pp. 917–927, 2007.
- [17] X. Michalet, F. F. Pinaud, L. A. Bentolila et al., "Quantum dots for live cells, in vivo imaging, and diagnostics," *Science*, vol. 307, no. 5709, pp. 538–544, 2005.
- [18] Y. Xing and J. Rao, "Quantum dot bioconjugates for in vitro diagnostics & in vivo imaging," *Cancer Biomarkers*, vol. 4, no. 6, pp. 307–319, 2008.
- [19] Z. Jin and N. Hildebrandt, "Semiconductor quantum dots for in vitro diagnostics and cellular imaging," *Trends in Biotechnology*, vol. 30, no. 7, pp. 394–403, 2012.
- [20] J. Fritz, M. K. Baller, H. P. Lang et al., "Translating biomolecular recognition into nanomechanics," *Science*, vol. 288, no. 5464, pp. 316–318, 2000.
- [21] R. McKendry, J. Zhang, Y. Arntz et al., "Multiple label-free biodetection and quantitative DNA-binding assays on a nanomechanical cantilever array," *Proceedings of the National Academy of Sciences of the United States of America*, vol. 99, no. 15, pp. 9783–9788, 2002.
- [22] J. Mertens, C. Rogero, M. Calleja et al., "Label-free detection of DNA hybridization based on hydration-induced tension in nucleic acid films," *Nature Nanotechnology*, vol. 3, no. 5, pp. 301–307, 2008.
- [23] R. Datar, S. Kim, S. Jeon et al., "Cantilever sensors: nanomechanical tools for diagnostics," *MRS Bulletin*, vol. 34, no. 6, pp. 449–454, 2009.
- [24] C. A. Mirkin, R. L. Letsinger, R. C. Mucic, and J. J. Storhoff, "A DNA-based method for rationally assembling nanoparticles into macroscopic materials," *Nature*, vol. 382, no. 6592, pp. 607–609, 1996.
- [25] C. C. You, O. R. Miranda, B. Gider et al., "Detection and identification of proteins using nanoparticle-fluorescent polymer 'chemical nose' sensors," *Nature Nanotechnology*, vol. 2, no. 5, pp. 318–323, 2007.

- [26] P. Baptista, E. Pereira, P. Eaton et al., "Gold nanoparticles for the development of clinical diagnosis methods," *Analytical and Bioanalytical Chemistry*, vol. 391, no. 3, pp. 943–950, 2008.
- [27] J. A. A. Ho, H. C. Chang, N. Y. Shih et al., "Diagnostic detection of human lung cancer-associated antigen using a gold nanoparticle-based electrochemical immunosensor," *Analytical Chemistry*, vol. 82, no. 14, pp. 5944–5950, 2010.
- [28] A. Kumar, B. M. Boruah, and X. J. Liang, "Gold nanoparticles: promising nanomaterials for the diagnosis of cancer and HIV/AIDS," *Journal of Nanomaterials*, vol. 2011, Article ID 202187, 17 pages, 2011.
- [29] P. K. Jain, K. S. Lee, I. H. El-Sayed, and M. A. El-Sayed, "Calculated absorption and scattering properties of gold nanoparticles of different size, shape, and composition: applications in biological imaging and biomedicine," *Journal of Physical Chemistry B*, vol. 110, no. 14, pp. 7238–7248, 2006.
- [30] J. Wang, M. O'Toole, A. Massey et al., "Highly specific, MIR fluorescent contrast agent with emission controlled by gold nanoparticle," *Advances in Experimental Medicine and Biology*, vol. 701, no. 4, pp. 149–154, 2011.
- [31] T. Chung, S. Y. Lee, E. Y. Song, H. Chun, and B. Lee, "Plasmonic nanostructures for nano-scale bio-sensing," *Sensors*, vol. 11, no. 11, pp. 10907–10929, 2011.
- [32] S. Chen, M. Svedendahl, M. Käll, L. Gunnarsson, and A. Dmitriev, "Ultrahigh sensitivity made simple: nanoplasmonic label-free biosensing with an extremely low limit-of-detection for bacterial and cancer diagnostics," *Nanotechnology*, vol. 20, no. 43, Article ID 434015, 2009.
- [33] V. Myroshnychenko, J. Rodríguez-Fernández, I. Pastoriza-Santos et al., "Modelling the optical response of gold nanoparticles," *Chemical Society Reviews*, vol. 37, no. 9, pp. 1792–1805, 2008.
- [34] J. D. Jackson, *Classical Electrodynamics*, Wiley, New York, NY, USA, 1999.
- [35] G. Mie, "Beiträge zur optik trüber medien, speziell kolloidaler metallösungen," *Annalen der Physik*, vol. 330, no. 3, pp. 377–445, 1908.
- [36] H. De Voe, "Optical properties of molecular aggregates. I. Classical model of electronic absorption and refraction," *The Journal of Chemical Physics*, vol. 41, no. 2, pp. 393–400, 1964.
- [37] B. T. Draine and P. J. Flatau, "Discrete-dipole approximation for scattering calculations," *Journal of the Optical Society of America A*, vol. 11, no. 4, pp. 1491–1499, 1994.
- [38] <http://code.google.com/p/ddscat/>.
- [39] <http://arxiv.org/pdf/1202.3424v3.pdf>.
- [40] Y. W. Jung, J. J. Yoon, Y. D. Kim, and D. Woo, "Study of the interaction between biomolecule monolayers using total internal reflection ellipsometry," *Journal of the Korean Physical Society*, vol. 58, no. 42, pp. 1031–1034, 2011.

## Research Article

# Porosity and Inclusion Detection in CFRP by Infrared Thermography

C. Toscano,<sup>1,2</sup> C. Meola,<sup>3</sup> M. C. Iorio,<sup>3</sup> and G. M. Carlomagno<sup>4</sup>

<sup>1</sup>C.I.R.A. Italian Aerospace Research Centre, via Maiorise snc, 81043 Capua, Italy

<sup>2</sup>Department of Aerospace Engineering, University of Naples Federico II, 80125 Naples, Italy

<sup>3</sup>Department of Aerospace Engineering (DIAS), University of Naples Federico II, Via Claudio, 21 80125 Naples, Italy

<sup>4</sup>Department of Aerospace Engineering (DIAS), University of Naples Federico II, P.le Tecchio, 21 80125 Naples, Italy

Correspondence should be addressed to C. Meola, carmeola@unina.it

Received 6 August 2012; Accepted 22 October 2012

Academic Editor: Laura Abbozzo Ronchi

Copyright © 2012 C. Toscano et al. This is an open access article distributed under the Creative Commons Attribution License, which permits unrestricted use, distribution, and reproduction in any medium, provided the original work is properly cited.

The ever wide use of composite materials in the aeronautical industry has evidenced the need for development of ever more effective nondestructive evaluation methodologies in order to reduce rejected parts and to optimize production costs. Infrared thermography has been recently enclosed amongst the standardized non destructive testing techniques, but its usefulness needs still complete assessment since it can be employed in several different arrangements and for many purposes. In this work, the possibility to detect slag inclusions and porosity is analyzed with both lock-in thermography and pulse thermography in the transmission mode. To this end, carbon-fiber-peinforced polymers different specimens are specifically fabricated of several different stacking sequences and with embedded slag inclusions and porosity percentages. As main results, both of the techniques are found definitely able to reveal the presence of the defects above mentioned. Moreover, these techniques could be considered complementary in order to better characterize the nature of the detected defects.

## 1. Introduction

In the last thirty years a huge employment of carbon-fiber-reinforced polymers (CFRPs) has characterized the production of components in the aerospace industry [1]. Indeed, since their introduction in the civil aviation in the eighties, CFRPs have gained a progressive interest due to their versatility (e.g., perfectly matching the design requirements) as well appreciable low weight and high stiffness with costs saving.

However, due to the many parameters involved in the CFRP manufacturing process, special care must be devoted to production control [2], in order to reduce rejected parts, and to detect, at the onset stage, buried defects, which may, unpredictably, grow once the structure is under load. Moreover, the intrinsic nonhomogeneities of the components and their properties, which are strictly dependent on the fiber quantity and orientation, make them susceptible to damage if impacted, also at low energy. This is why strong efforts have

been paid by the industries to develop ever more effective non destructive testing and evaluation techniques [3].

Great attention was devoted, in the last twenty years, to the use of infrared thermography, (IRT) for non destructive evaluation (NDE) of materials and, recently, it was included amongst the standardized NDE techniques in the aeronautical field [4]. The main advantages of IRT are related to its contactless character and fast rate of inspection of large components. It can be used as complement to, or substitute, of the most common techniques.

Infrared thermography for NDE is basically used in the so-called *active* mode [5], which means that the inspected part is heated (or cooled) with respect to the ambient temperature, by an external source. The presence of an inhomogeneity in the inspected material affects the heat propagation and causes a local surface temperature variation. Halogen lamps are mostly used for heating the inspected parts, but also mechanical loading, such as ultrasound waves, could be applied to induce mechanical friction in materials

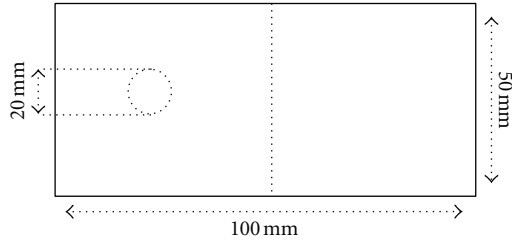


FIGURE 1: Schematic of the coupon with the Teflon disk embedded.

discontinuities [6]. This causes the generation of heat in the discontinuity, which is revealed by an infrared camera. It has been proven by several authors that infrared thermography is very effective for porosity detection. Amongst the used techniques, the measure of thermal diffusivity, or thermal effusivity, of the material was addressed [7–10].

In this work, CFRP coupons with induced porosity, through the curing cycle and buried slag inclusions are inspected with lock-in Thermography (LT) [11] and Pulse thermography (PT), both used in the transmission mode.

## 2. Fabrication of CFRP Coupons

A set of coupons was manufactured by hand lay up of prepreg laminas. In order to induce a controlled porosity level, curing in autoclave was performed by applying a temperature-pressure cycle, modified with respect to that suggested by the row material provider. In particular, to generate porosity, just only a partial pressure was used with respect to the prescribed one (7 bar gauge); specifically, a value of 100%, 75%, 50%, 25%, and 0% of the total prescribed pressure was applied during the autoclave curing. For each curing pressure level, four different lamination sequences (see Table 1) were considered in order to study any possible influences the specific fiber alignment may have on the porosity distribution. Therefore, 20 coupons were fabricated (i.e., 4 coupons involving the four different stacking sequences for each curing pressure level).

Moreover, a thin Teflon disk, 20 mm in diameter, was inserted in the middle of the stacking sequence to simulate delamination or inclusion of the bagging film; the thickness of the Teflon disk is of the same order of that of a single prepreg lamina. As sketched in Figure 1, each coupon is 50 mm large and 100 mm long; the thickness may be evaluated owing to the number of plies.

The presence of entrapped gas in the coupons (i.e., porosity), which increases with decreasing the applied pressure, was assessed through density measurements. More specifically, small samples were cut from each type of coupons and subjected to density measurements through the volumetric method (i.e., using a digital balance and the Archimedes push). The obtained density values are plotted against the curing pressure in Figure 2. As expected, on the whole, the density increases with the pressure.

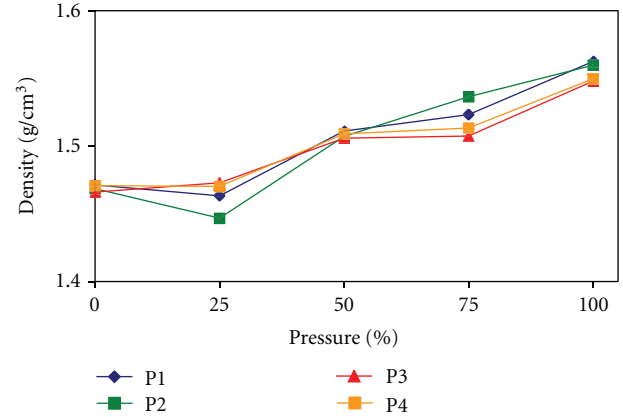


FIGURE 2: Density values versus the curing pressure percentage (used in autoclave).

## 3. Inspection with Infrared Thermography

As already stated, the inspection of the manufactured coupons was carried out with LT and PT in the transmission mode; thermal stimulation was performed with a halogen or a flash lamp, respectively. To screen the camera, which is the SC5000 (Flir systems), from the direct intense flash light, coupons were mounted in a proper housing. A test setup is shown in Figure 3; the position of the camera is opposite with respect to that of the lamp.

For LT tests, the infrared camera frames the thermal images and acquires the amplitude/time temperature variations over the rear surface of the coupon. Then, by the provided software, the phase differences between the modulated heating source and the out coming thermal waves are elaborated and represented in false color maps. Of course, the local color variations indicate the presence of inhomogeneities in the material. Then, the presence of the inclusion and/or porosity clusters could be alternately represented with lighter or darker colors in the phase maps. In order to rapidly get an idea about the inner coupons structures, the same excitation frequency was used for testing all the coupons.

The pulse thermography involves a similar test arrangement (Figure 3). The flash lamp is a Hensel MH6000, which is able to emit up to 6000 Joules, and it is driven by a Hensel TRIA6000S power pack producing a flash duration of 1/440 s at the maximum power. The heating of the rear surface of the coupon is recorded by the infrared camera. The time-temperature distribution is characterized by an increase in temperature from the initial one  $T_i$  until a maximum  $T_M$  is reached, as shown in Figure 4.

It can be demonstrated, under proper hypothesis, that if the surface of a finite slab of a homogeneous material is instantaneously heated up [12], then, if  $t = 0$  is the time when the flash is enforced (on the slab opposite side), the instant  $t_{1/2}$ , corresponding to  $T_{M/2}$  (the half of  $T_M - T_i$ ) can

TABLE 1: Stacking sequences and number of plies of the coupons.

Coupon	Stacking sequence	No. plies
P1	[0°]	24
P2	[90°]	24
P3	[(45°/-45°) <sub>6</sub> ] <sub>S</sub>	24
P4	[45/0/-45/90/45/0/-45/90/90/-45/0/45/90/-45/0/45] <sub>S</sub>	32



FIGURE 3: Experimental setup for the lock-in thermography in transmission mode. For the pulsed thermography, the halogen lamp is replaced with the flash lamp.

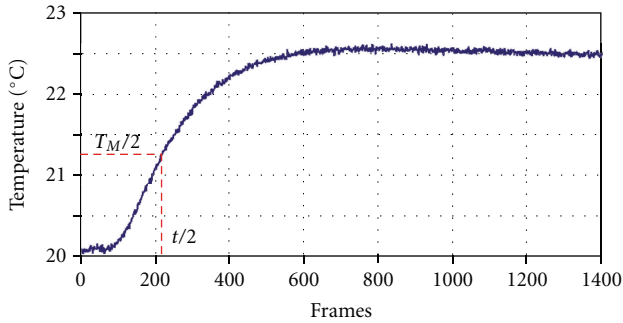


FIGURE 4: Typical temperature plot during flash heating.

be put in relation with the thermal diffusivity coefficient  $\alpha$  and the thickness  $L$  of the slab through the following relation:

$$\alpha = \frac{1.38L^2}{\pi^2 t_{1/2}}. \quad (1)$$

Of course, the thermal diffusivity has to be considered as a mean value across each specimen thickness. Thanks to the use of the infrared camera, the thermal “history” of the coupon can be easily recorded and successively analyzed. Then, by neglecting tangential conduction effects, from (1), the thermal diffusivity of the coupon can be calculated point by point over its entire surface. All the calculations, for each coupon, were done by an *ad hoc* tool developed in the Matlab environment, which is able to read the sequence of images

accounting for the “thermal history” and to calculate and map the thermal diffusivity.

#### 4. Discussion of Results

In the following Figures 5, 6, 7, 8, and 9 are reported some of the obtained results. For the same coupon, a phase map, obtained by the LT technique, and a thermal diffusivity map, obtained with the Matlab routine from PT sequences, are shown together in the same figure to allow for a direct comparison. In particular, each pair of maps is related to a coupon representing a specific lamination sequence and curing pressure. A color scale with values expressed in  $10^{-3} \text{ cm}^2/\text{s}$  is added to each diffusivity map.

By comparing phase and diffusivity maps, it can be noted, in general, a good matching of data regarding the slag inclusion detection. In particular, from phase maps, it is possible to distinguish not only the buried defects, but also the fiber orientation. On the other side, the map of thermal diffusivity is helpful to better distinguish areas of the material with different thermal behavior. Thus, on the whole, the application of both techniques can lead to a more comprehensive knowledge of the materials inner defects.

However, to a closer view some differences appear, which mainly reside in the position of the detected inclusion. This is due to some differences in the field of view used for the two different tests carried out with LT and PT. In addition, it has to be noted that some phase maps appear quite blurred making difficult distinguishing the Teflon disk; this occurs mainly for the coupon P4 cured at 50% (Figure 7(a)) and the P3 cured at 0% (Figure 9(a)). This is explicable by looking at the diffusivity maps; in fact, it can be noted that the thermal diffusivity in a high porosity area and in the inclusions attains almost the same value, which is smaller than that of the more dense material. Thus, the dampening down of the contrast with decreasing the curing pressure is obviously due a more diffuse presence of porosity, within the whole coupon volume, which masks the thin Teflon disk. This is what happens for the P3 coupon cured at 0% pressure (Figure 9(b)). More difficult to explain appears, at first sight, the poor contrast displayed by the phase map for the coupon P4 at 50% (Figure 7(a)) with respect to that of the coupon P3 at 25% (Figure 8(a)), which, instead, shows a well-contoured defect. However, this may be due to many different factors; the main ones being as follows.

- (i) The stacking sequence—the coupon P3 involves fibers at  $\pm 45^\circ$ , while the P4 one is characterized by the  $[45/0/-45/90/45/0/-45/90/90/-45/0/45/90/-45/0/45]<sub>S</sub>$  sequence. Of course, the more complex

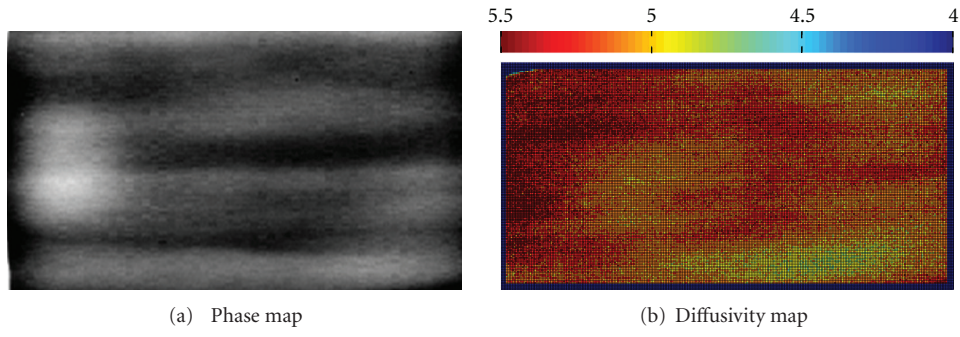


FIGURE 5: Phase map (a) and diffusivity map (b) of the P1 coupon cured with 100% of the pressure.

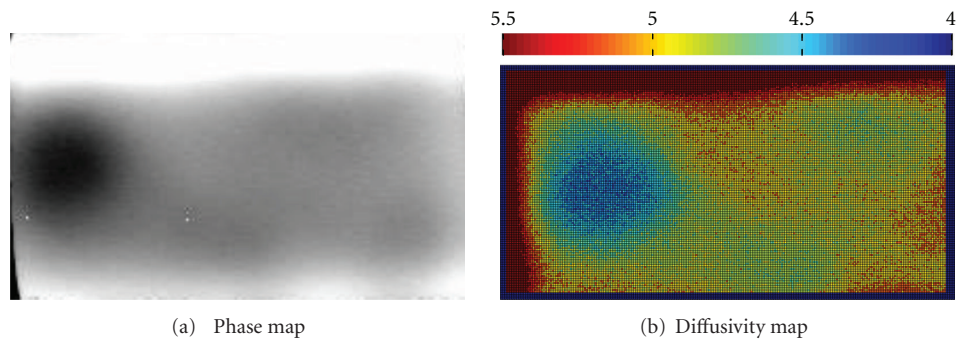


FIGURE 6: Phase map (a) and diffusivity map (b) of the P3 coupon cured with 75% of the pressure.

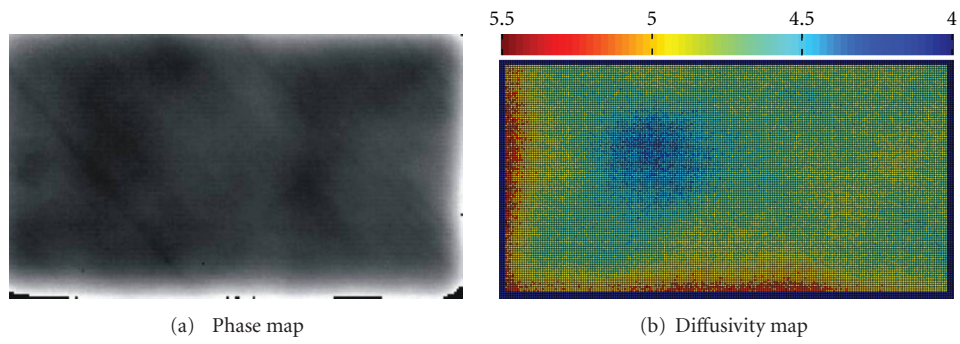


FIGURE 7: Phase map (a) and diffusivity map (b) of the P4 coupon cured with 50% of the pressure.

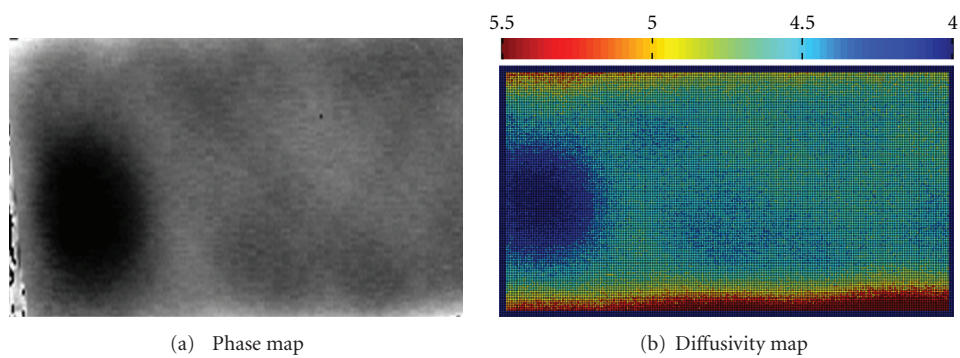


FIGURE 8: Phase map (a) and diffusivity map (b) of the P3 coupon cured with 25% of the pressure.

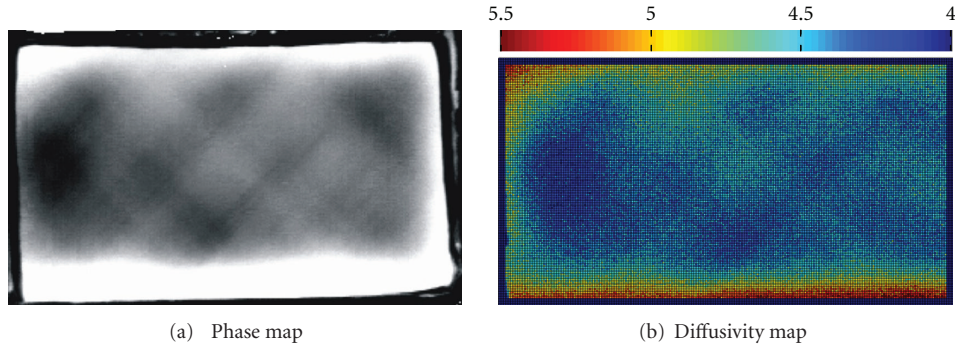


FIGURE 9: Phase map (a) and diffusivity map (b) of the P3 coupon cured with 0% of the pressure.

stacking sequence hinders the passage of air during application of the vacuum bag, then favouring the formation of air bubbles and of porosity clusters.

- (ii) The thickness—the coupon P4 includes a greater number of plies. The contrast generally decreases with increasing the defect depth.
- (iii) Manufacturing errors—something wrong is likely to occur during any process.

To better quantify the influence of the curing pressure, an average value  $\alpha_M$  of the thermal diffusivity is calculated in a given area relating to the sound half part of the coupon (i.e., the half part without the buried defect). These  $\alpha_M$  values are plotted against the curing pressure  $p_c$  in Figure 10. As can be seen, the trend of  $\alpha_M$  versus  $p_c$  is in very good agreement with that of the measured density already shown in Figure 2. By the way, the density is measured by weighting only a very small part of the coupon, while the average thermal diffusivity is measured over a large coupon surface. In the present case, the average was restricted to the coupon sound part (excluding the part with buried the Teflon disk); in a more general way, the thermal diffusivity can be calculated by considering a desired larger area and accounting also for a data deviation to include maxima and minima for a better material characterization. And so, it may be claimed that the indirect porosity estimation, obtained with infrared thermography and the flash method, is more effective and reliable with respect to that measured by the balance method.

As known, thermal diffusivity is higher along the carbon fibers than in the perpendicular direction, where the heat diffusion is principally due to the matrix of the composite. It seems, from Figure 10, that present data, considering data relative to P1 (fibers at  $0^\circ$ ) and P2 (fibers at  $90^\circ$ ) coupons, are in general agreement with the previous assertion. Instead, data for the P3 and P4 coupons present a quite similar trend, which might mean that, in a complex lamination sequence, the fibers orientation and the number of plies do not have an appreciable influences on the whole trend of the average thermal diffusivity. However, looking at Table 1, it is possible to see that for both P3 and P4 coupons, the external surface is characterized by fibers at  $45^\circ$ ; so, this may justify the obtained thermal diffusivity values. On the other side, data obtained

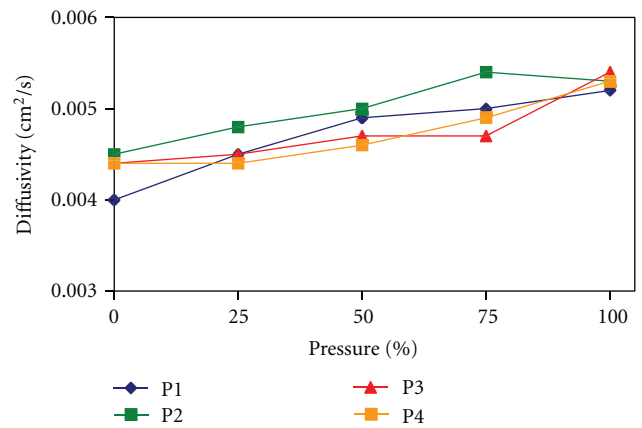


FIGURE 10: Average diffusivity versus applied curing pressure as percentage of the prescribed one.

with infrared thermography are generally affected by the characteristics of the viewed surface.

### 5. Conclusion

An experimental investigation was performed in order to gain new information on the application of infrared thermography in the inspection of CFRP for aeronautical use. Several *ad hoc* coupons with both porosity and slag inclusions were fabricated and then inspected with LT and PT techniques; results were presented in terms of phase images and thermal diffusivity maps.

Firstly, results highlight the capability of both techniques to detect the two types of defects. In particular, a smaller diffusivity value was found in a defective zone with respect to the almost homogeneous material. So, the comparison between the phase maps and the diffusivity maps allows gaining more exhaustive and clear information on the nature of the detected inhomogeneities. The obtained results demonstrate the advantage of using both LT and PT in the transmission mode because of the possibility of using the same set-up arrangement for both detection of defects and measurement of thermal diffusivity as well as the possibility for a direct comparison between phase angle and thermal

diffusivity values. In addition, testing in the transmission mode is helpful in the inspection of thick parts, which cannot always be resolved in the reflection mode.

The main drawbacks of both techniques are related to specific experimental conditions. In the case of IT in transmission, proper excitation frequencies must be investigated, as well as their relation with the obtained phase maps, which could lead to improve the knowledge about the porosity distribution and to distinguish inhomogeneities of different nature. Moreover, measurements of thermal diffusivity with PT needs further investigation to improve the signal to noise ratio for more quantitative measurements. What it is clear, is that the two techniques could be combined in order to draw a more clear picture of the conditions of the inspected part.

In the future, these approaches will be deeply investigated in order to define the optimum setup and test parameters so as to enhance the technique ability to detect specific defects and to obtain quantitative information.

## Acknowledgment

A special thank goes to Flir systems, Italy, for supplying the Flash lamp.

## References

- [1] A. A. Baker, S. Dutton, and D. Kelly, *Composite Materials for Aircraft Structures*, AIAA Education Series, 2nd edition, 2004.
- [2] [http://ntrs.nasa.gov/archive/nasa/casi.ntrs.nasa.gov/20090014807\\_2009014230.pdf](http://ntrs.nasa.gov/archive/nasa/casi.ntrs.nasa.gov/20090014807_2009014230.pdf).
- [3] C. Beine, C. Boller, U. Netzelmann et al., “NDT for CFRP aeronautical components a comparative study,” in *Proceedings of the NDT in Aerospace*, Hamburg, Germany, November 2010.
- [4] C. Meola and G. M. Carlomagno, “Infrared thermography in non-destructive inspection: theory and practice,” in *Recent Advances in Non Destructive Inspection*, C. Meola, Ed., pp. 89–123, Nova Science Publisher, 2010.
- [5] X. Maldague, *Nondestructive Evaluation of Materials by Infrared Thermography*, Springer, New York, NY, USA, 1993.
- [6] J. Rantala, D. Wu, A. Salerno, and G. Busse, “Lock-in thermography with mechanical loss angle heating at ultrasonic frequencies,” in *Proceedings of the Eurotherm Seminar*, vol. 50, Stuttgart, Germany, September 1996.
- [7] E. Grinzato, S. Marinetti, and P. G. Bison, “NDE of porosity in CFRP by multiple thermographic techniques,” in *Thermosense XXIV*, vol. 4710 of *Proceedings of SPIE*, pp. 588–598, April 2002.
- [8] A. Ciliberto, G. Cavaccini, O. Salvetti et al., “Porosity detection in composite aeronautical structures,” *Infrared Physics and Technology*, vol. 43, no. 3-5, pp. 139–143, 2002.
- [9] G. Hendorfer, G. Mayr, G. Zauner, M. Haslhofer, and R. Pree, “Quantitative determination of porosity by active thermography,” in *Review of Progress in Quantitative Nondestructive Evaluation*, vol. 894, pp. 702–708, August 2006.
- [10] G. Mayr and G. Handorfer, “Porosity determination by pulsed thermography in reflection mode,” in *Proceedings of the 10th International Conference on Quantitative InfraRed Thermography*, Quebec, Canada, July 2010.
- [11] C. Meola, “Nondestructive evaluation of materials with rear heating lock-in thermography,” *IEEE Sensors Journal*, vol. 7, no. 10, pp. 1388–1389, 2007.
- [12] W. J. Parker, R. J. Jenkins, C. P. Butler, and G. L. Abbott, “Flash method of determining thermal diffusivity, heat capacity, and thermal conductivity,” *Journal of Applied Physics*, vol. 32, no. 9, pp. 1679–1684, 1961.

## Research Article

# Contribution of Series Resistance in Modelling of High-Temperature Type II Superlattice p-i-n Photodiodes

Jarosław Wróbel, Piotr Martyniuk, and Antoni Rogalski

*Institute of Applied Physics, Military University of Technology, 2 Kaliskiego Street, 00-908 Warsaw, Poland*

Correspondence should be addressed to Jarosław Wróbel, jarekwrobel@wat.edu.pl

Received 24 August 2012; Accepted 23 October 2012

Academic Editor: Ovidio Salvetti

Copyright © 2012 Jarosław Wróbel et al. This is an open access article distributed under the Creative Commons Attribution License, which permits unrestricted use, distribution, and reproduction in any medium, provided the original work is properly cited.

We analyze some of the consequences of omitting series resistance in InAs/GaSb p-i-n T2SL photodiode dark current modelling, using simplified p-n junction model. Our considerations are limited to generation-recombination and diffusion-effective carrier lifetimes to show the possible scale of over- or underestimating photodiodes parameters in high-temperature region. As is shown, incorrect series resistance value might cause discrepancies in  $\tau_{gr}$  and  $\tau_{diff}$ 's estimations over one order of magnitude.

## 1. Introduction

Type II superlattices (T2SLs), especially InAs/GaSb, are very promising materials for both uncooled as well as cooled mid-wavelength infrared (MWIR) and long wavelength infrared (LWIR) photodetectors [1]. Relative easiness of controlling band offset causes them to be used in different types of structures [2]. Especially, introducing unipolar barriers in various designs based on type II SLs drastically changed the architecture of infrared detectors. At present, the InAs/GaSb T2SLs are considered to be an alternative to the HgCdTe IR material systems [1] and a candidate for the third-generation IR detectors [3]. However, InAs/GaSb T2SL is in an early stage of development. Problems exist in material growth, processing, substrate preparation, and device passivation [4–6]. Moreover, correct interpretations of measured detector characteristics are often difficult due to fact that T2SLs' band structures are much more complicated than bulk materials [7]. From this reason, there have been developed many simplified models [8–13], which assume that T2SL electrical parameters are mainly dependent on energy difference between first conduction and heavy hole miniband (which is treated as an effective bandgap). For an approximative describing of the detector transport mechanisms, the well-known standard theory of p-n junction is used [2, 14]. Recently published results of our group show that usage of this method can give very good fitting between theoretical

predictions and experimental data in a wide range of bias voltage (from  $-1.6$  to  $+0.3$  V) and temperature (from 77 to 240 K) for p-i-n and nBn devices [15–17]. It appears that good agreement between both types of results is possible if the influence of series resistance ( $R_{series}$ ) is taken into consideration, what might be essential in a thermoelectrically cooled (TE) photodetectors (in temperature range above 180 K).

In this paper we present the consequences of  $R_{series}$  omitting in the dark current modelling of p-i-n T2SL junctions, often met in literature. These consequences are shown on an example of temperature dependence of two fitting parameters—generation-recombination ( $\tau_{gr}$ ) and diffusion ( $\tau_{diff}$ )-effective carrier lifetimes. Both two mechanisms have decisive influence on current-voltage characteristics of TE-cooled p-i-n T2SL junctions in near-zero bias voltages [17].

## 2. Experimental Results

In the studies we have chosen representative sample of 10/10 ML InAs/GaSb T2SL in a p-i-n structure, fabricated in the Center for High Technology Materials, University of New Mexico, Albuquerque, NM, USA. The photodiode cutoff wavelength is roughly equal to  $5.6 \mu\text{m}$  at 120 K and  $6.2 \mu\text{m}$  at 230 K [18]. The detector architecture design and measurement details of current-voltage characteristics of

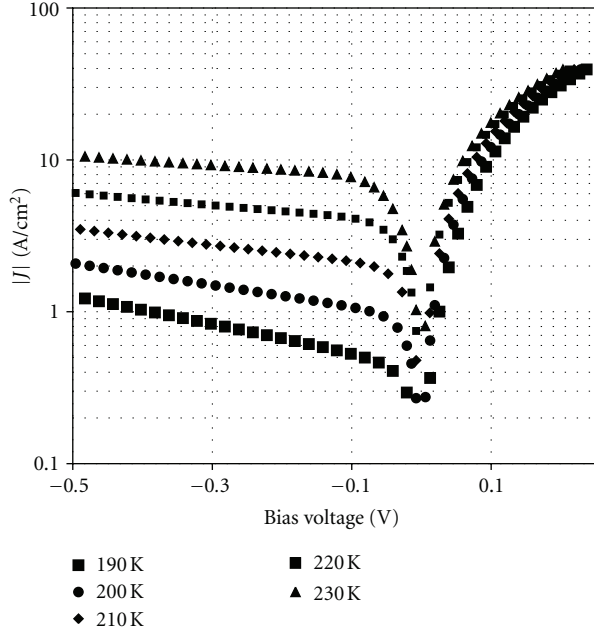


FIGURE 1: Experimental dark current density-voltage characteristics of p-i-n T2SL photodiode at different temperatures (after [17]).

these samples were presented elsewhere [16, 17]. Here we present only a few of the results (see Figures 1 and 2), indispensable for presenting the main goal of the paper.

### 3. Modelling of Current-Voltage Characteristics

In order to explain current-voltage characteristics of the MWIR type-II SLS photodiodes a bulk-based model with an effective band gap of SL material is used. It is well recognized that the photodiode dark current can be found as a superposition of several mechanisms (see Figure 3):

$$I_{\text{dark}} = I_{\text{diff}} + I_{\text{gr}} + I_{\text{btb}} + I_{\text{tat}} + I_{\text{Rshunt}}, \quad (1)$$

including four main mechanisms: diffusion ( $I_{\text{diff}}$ ), generation-recombination ( $I_{\text{gr}}$ ), band-to-band tunnelling ( $I_{\text{btb}}$ ), and trap-assisted tunnelling ( $I_{\text{tat}}$ ). The remaining mechanism is current due to the shunt resistance ( $I_{\text{Rshunt}}$ , originates from the surface and bulk leakage current and shows the presence in the reverse bias region).

The relation between the applied voltage,  $V$ , and the diffusion current density,  $J_{\text{diff}}$ , is given by

$$J_{\text{diff}} = J_s \left[ \exp\left(\frac{qV}{kT} - 1\right) \right], \quad (2)$$

where  $q$  is the electron charge,  $k$  is the Boltzmann's constant, and  $T$  is the absolute temperature. In the case of our devices, due to a gradient doping profile at the contacts, we apply the reflective contact configuration, and then the saturation current density  $J_s$  can be expressed as

$$J_s = qn_i^2 \left( \frac{D_e}{N_a L_e} \tanh \frac{x_p}{L_e} + \frac{D_h}{N_d L_h} \tanh \frac{x_n}{L_h} \right), \quad (3)$$

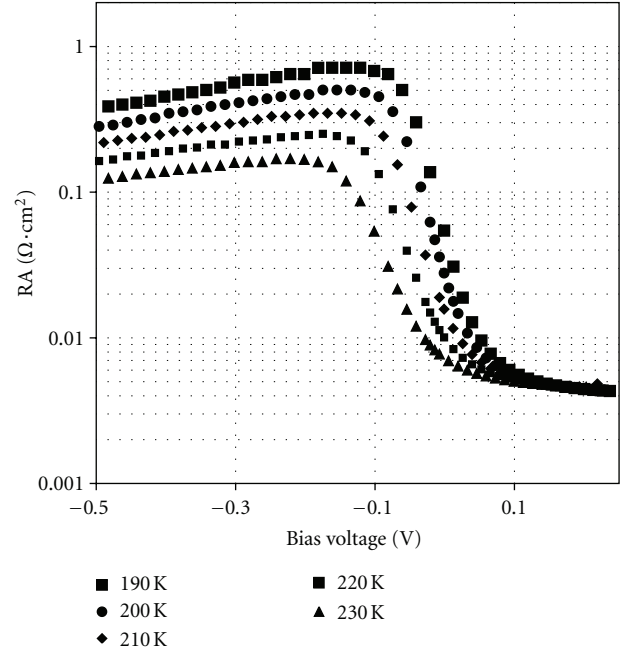


FIGURE 2: Experimental resistance-area product versus bias voltage of p-i-n T2SL photodiode at different temperatures (after [17]).

where  $n_i$  is the intrinsic carrier concentration,  $N_{a,d}$  is acceptor/donor doping concentrations,  $\mu_{e,h}$  is minority electron/hole mobility, and  $x_{n,p}$  is the device thicknesses ( $x_n$  is the thickness of  $n$ -type region, instead  $x_p$  is the thickness of  $p$ -type region). Additionally,  $L_{e,h}$  means electron/hole diffusion current length, and  $D_{e,h}$  diffusivity (with diffusion lifetime  $\tau_{e,h}$ ), where

$$D_{e,h} = \frac{kT}{q} \mu_{e,h}, \quad L_{e,h} = \sqrt{D_{e,h} \tau_{e,h}}. \quad (4)$$

The g-r current density under reverse-bias voltage and for forward-bias voltage values, that are less than  $V_b$  by several  $kT/q$ , is derived as

$$J_{\text{gr}} = \frac{qn_i w}{(\tau_{e0} \tau_{h0})^{1/2}} \frac{2 \sinh(qV/2kT)}{q(V_b - V)/kT} f(b), \quad (5)$$

where  $\tau_{e0}$  and  $\tau_{h0}$  are the carrier lifetimes for electrons and holes within the depletion region ( $w$  is the depletion width). In our estimation we also assumed that  $\tau_{e0} = \tau_{h0} = \tau_{\text{gr}}$  and  $\tau_e = \tau_h = \tau_{\text{diff}}$ . The function  $f(b)$  is a complicated expression involving a trap level and an applied voltage [2]. The values of parameters used in a device modelling are taken from published literature [19–21] and are gathered in Table 1 [16].

The description of other mechanisms, essential in high reverse bias voltage condition and detailed discussion of fitting procedure (including simple method of avoiding difficulties connected with the influence of series resistance), can be found in [16].

### 4. Results and Discussions

In some of the recently published papers related to high operating temperature (HOT) T2SL devices (see, e.g., Cervera et al. [12]) is mentioned the difficulties connected with

TABLE 1: Parameters taken in modelling of MWIR InAs/GaSb superlattice photodiodes.

Device geometry	
thickness of $p$ -type region, $x_p$	$0.27 \mu\text{m}$
thickness of $n$ -type region, $x_n$	$2.25 \mu\text{m}$
electrical area	$2.03 \times 10^{-3} \text{cm}^2$
Donor concentration, $N_d$	$1 \times 10^{16} \text{cm}^{-3}$
Acceptor concentration, $N_a$	$1 \times 10^{18} \text{cm}^{-3}$
Trap concentration, $N_T$	$8 \times 10^{14} \text{cm}^{-3}$
Minority electron mobility, $\mu_e$	$10000 \text{cm}^2/\text{Vs}$
Minority hole mobility, $\mu_h$	$1000 \text{cm}^2/\text{Vs}$
Electron-effective mass, $m_e^*$	$0.015m_0$
Hole effective mass, $m_h^*$	$0.4m_0$

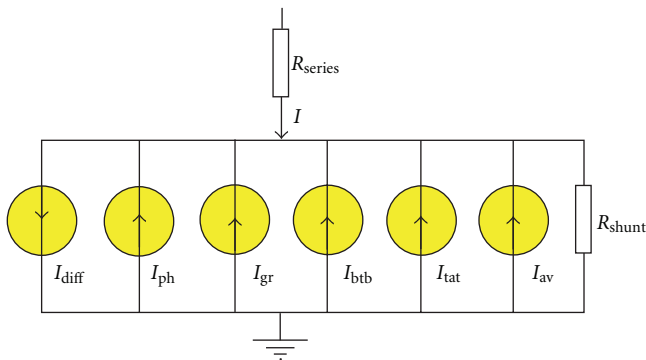


FIGURE 3: Possible currents operating in the photodiode.  $I_{\text{diff}}$  is ideal diffusion current,  $I_{\text{ph}}$  is the photocurrent,  $I_{\text{gr}}$  is due to a generation-recombination mechanism,  $I_{\text{tbt}}$  is due to a band-to-band tunnelling,  $I_{\text{tat}}$  is due to a trap-to-band tunnelling, and  $R_{\text{shunt}}$  is due to a surface and bulk leakage shunt resistance. Limiting currents act in opposition to diffusion current.

fitting procedure between measured  $I$ - $V$  characteristics and theoretical predicted results above 200 K. In our opinion these difficulties are strictly connected with the influence of series resistance in high-temperature region. Because  $R_{\text{series}}$ -value is connected in a series to all generation-recombination mechanisms (see Figure 3), we should solve the nonlinear problem to obtain voltage drops on both whole device except series resistance and a series resistance separately (see discussion in [16]). Omitting this problem causes it to be impossible to fit to measured dynamic resistance-voltage characteristics,  $R_d(V)$ , under HOT conditions. It is caused by the fact that voltage drop on device except  $R_{\text{series}}$  might be essentially lower than measured voltage, what causes considerable changes in shapes of  $RA$ -product curves (see Figure 4), and, in consequence, great difficulties in theoretical fitting procedure to the experimental  $R_d(V)$  characteristics.

At the beginning, we present a comparison of two simulation results, which were made using the same input parameters, except  $R_{\text{series}}$ . As we can see on Figure 4, the difference in a bias-dependent peak positions of dynamic resistance is nearly equal to 0.1 V, what in consequence causes significance discrepancy in an effective lifetimes estimations from (2) and (5).

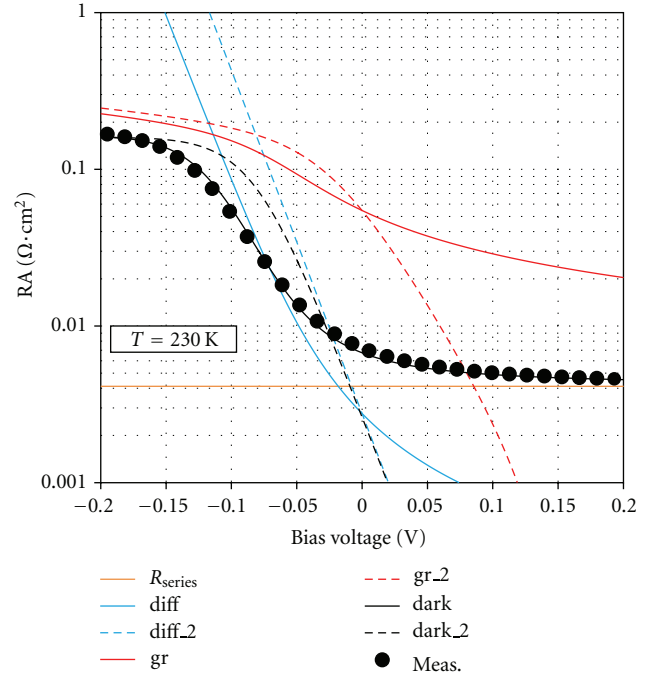


FIGURE 4: The comparison of two simulation results at 230 K, assuming the same input parameters except  $R_{\text{series}}$ . Curves with 2-index are calculated assuming zero value of  $R_{\text{series}}$ . Plots with no additional indexes are calculated assuming that  $R_{\text{series}} \approx 2 \Omega$  obtained from the fitting to the measured dynamic resistance (see Figure 2) under the forward bias voltage condition (at  $\approx 0.2 \text{V}$ ).

Second aspect, previously mentioned, is the fact that influences of  $R_{\text{series}}$  on shapes of different dark current components are effective if the  $R_{\text{series}}$  value is comparable with dynamic resistance contributions of respective dark current components. This is especially visible for g-r mechanism. As a result, estimating of  $\tau_{\text{gr}}$  and  $\tau_{\text{diff}}$  data assuming incorrect  $R_{\text{series}}$  value causes significant over- or underestimation in the effective current lifetimes.

Assuming the consideration above, we should underline that it is impossible to fit to measured  $RA(V)$  characteristics using (2) and (5), and omitting  $R_{\text{series}}$ . It causes many researchers to try to fit roughly only to the  $I$ - $V$  characteristics, without analysing first derivative of it ( $RA(V)$  dependence). In a consequence, for avoiding overestimation of dark current in a near zero-bias voltage region, it is needed to increase  $\tau_{\text{diff}}$  and decrease  $\tau_{\text{gr}}$  at bias voltage about  $-0.2 \text{V}$  in our case (this value depends on sample, temperature, and  $R_{\text{series}}$ ) shown in Figure 5. Curves with no additional index are calculated using parameters obtained from the correct fitting, but with zero value of  $R_{\text{series}}$ . Plots with 2 indexes are calculated using incorrect procedure.

As we can see on Figure 6, discrepancies between fitting results, made with and without including  $R_{\text{series}}$ , increase with temperature. It is caused by the fact that ideal photodiode resistance of p-i-n T2SL photodiode (with  $R_{\text{series}} = 0$ ) decreases with temperature and becomes comparable with weak temperature-dependent series resistance at high-temperature operation. In a consequence, a voltage drop

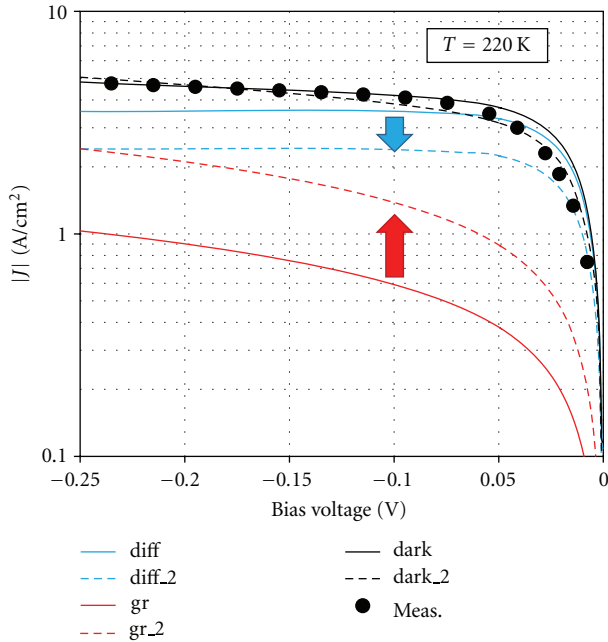


FIGURE 5: Explanation of incorrect fitting procedure (for more details—see text). Arrows show tendencies in change components of dark current to obtain good fitting to experimental data.

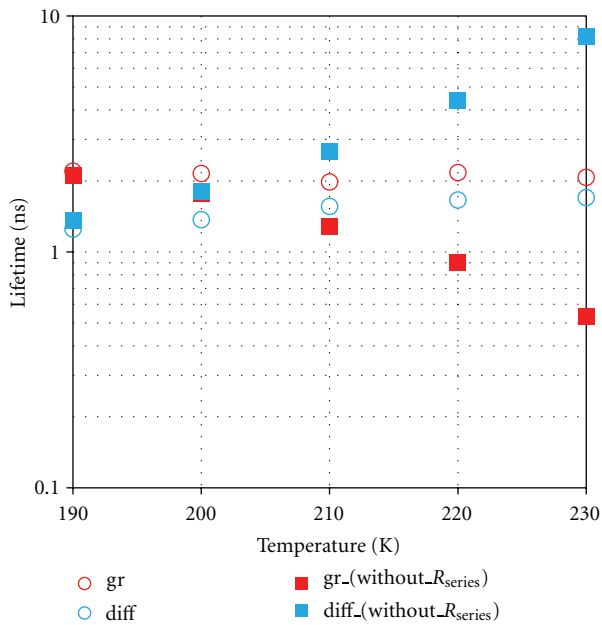


FIGURE 6: Comparison of g-r and diff. effective current lifetimes estimated theoretically for two cases: with including  $R_{series}$  and without it (see additional description in the text).

on an ideal diode and on series resistance are comparable, and  $I$ - $V$  characteristics essentially change their shapes. This results in under- or overestimations in key photodiode fitting parameters, like  $\tau_{gr}$  or  $\tau_{diff}$ . Our results for the MWIR photodiode seem to be confirmed by more direct measurements [22], where effective current lifetimes are weekly temperature dependent over 200 K.

## 5. Conclusions

In this paper we analyze some of the consequences of omitting series resistance in InAs/GaSb p-i-n T2SL photodiode dark current modelling, using simplified p-n junction model. Our considerations are limited to generation-recombination and diffusion-effective carrier lifetimes to show the possible scale of over- or underestimating photodiodes parameters. As is shown, incorrect series resistance value might cause discrepancies between  $\tau_{gr}$  and  $\tau_{diff}$  over one order of magnitude. Our results seem to be good explanation of difficulties in the estimation of parameters of MWIR T2SL photodiodes operated in high-temperature region.

## Acknowledgment

This paper has also been done under financial support of the Polish Ministry of Sciences and Higher Education, Key Project POIG.01.03.01-14-016/08 “New Photonic Materials and their Advanced Application.”

## References

- [1] A. Rogalski and P. Martyniuk, “InAs/GaInSb superlattices as a promising material system for third generation infrared detectors,” *Infrared Physics & Technology*, vol. 48, no. 1, pp. 39–52, 2006.
- [2] A. Rogalski, *Infrared Detectors*, CRC Press, Boca Raton, Fla, USA, 2nd edition, 2010.
- [3] A. Rogalski, “HgCdTe infrared detector material: history, status and outlook,” *Reports on Progress in Physics*, vol. 68, no. 10, pp. 2267–2336, 2005.
- [4] H. S. Kim, E. Plis, A. Khoshakhlagh et al., “Performance improvement of InAs/GaSb strained layer superlattice detectors by reducing surface leakage currents with SU-8 passivation,” *Applied Physics Letters*, vol. 96, no. 3, Article ID 033502, 3 pages, 2010.
- [5] H. S. Kim, *Investigation of InAs/GaSb superlattice based nBn detectors and focal plane arrays [Ph.D. thesis]*, Optical Science and Engineering, University of New Mexico, 2010.
- [6] H. S. Kim, E. Plis, N. Gautam et al., “SU-8 passivation of type-II InAs/GaSb strained layer superlattice detectors,” in *Infrared Technology and Applications 36*, vol. 7660 of *Proceedings of SPIE*, 76601U-1–9, April 2010.
- [7] F. Szmulowicz, H. J. Haugan, G. J. Brown et al., “Interfaces as design tools for short-period InAs/GaSb type-II superlattices for mid-infrared detectors,” *Opto-Electronics Review*, vol. 14, no. 1, pp. 71–77, 2006.
- [8] D. R. Rhiger, R. E. Kvaas, S. F. Harris, and C. J. Hill, “Characterization of LWIR diodes on InAs/GaSb type-II superlattice material,” *Infrared Physics & Technology*, vol. 52, no. 6, pp. 304–309, 2009.
- [9] J. Nguyen, D. Z. Ting, C. J. Hill, A. Soibel, S. A. Keo, and S. D. Gunapala, “Dark current analysis of InAs/GaSb superlattices at low temperatures,” *Infrared Physics & Technology*, vol. 52, no. 6, pp. 317–321, 2009.
- [10] C. L. Canedy, E. H. Aifer, J. H. Warner et al., “Controlling dark current in type-II superlattice photodiodes,” *Infrared Physics & Technology*, vol. 52, no. 6, pp. 326–334, 2009.
- [11] I. Vurgaftman, C. L. Canedy, J. A. Nolde, C. A. Affouda et al., “Analysis and performance of type-II superlattice infrared detectors,” *Optical Engineering*, vol. 50, no. 6, Article ID 061007, 2011.

- [12] C. Cervera, K. Jaworowicz, H. Ait-Kaci et al., "Temperature dependence performances of InAs/GaSb superlattice photodiode," *Infrared Physics & Technology*, vol. 54, no. 3, pp. 258–262, 2011.
- [13] V. Gopal, E. Plis, J. B. Rodriguez, C. E. Jones, L. Faraone, and S. Krishna, "Modeling of electrical characteristics of midwave type II InAs/GaSb strain layer superlattice diodes," *Journal of Applied Physics*, vol. 104, no. 12, Article ID 124506, 6 pages, 2008.
- [14] C.-T. Sah, R. N. Noyce, and W. Shockley, "Carrier generation and recombination in P-N junctions and P-N junction characteristics," *Proceedings of the Institute of Radio Engineers*, vol. 45, no. 9, pp. 1228–1243, 1957.
- [15] P. Martyniuk, J. Wróbel, E. Plis et al., "Performance modeling of MWIR InAs/GaSb/B-Al<sub>0.2</sub>Ga<sub>0.8</sub>Sb type-II superlattice nBn detector," *Semiconductor Science and Technology*, vol. 27, no. 5, Article ID 055002, 2012.
- [16] J. Wróbel, E. Plis, P. Madejczyk et al., "Analysis of temperature dependence of dark current mechanisms for mid-wavelength infrared InAs/GaSb superlattice photodiodes," submitted.
- [17] J. Wróbel, P. Martyniuk, E. Plis et al., "Dark current modeling of MWIR type-II superlattice detectors," in *Infrared Technology and Applications 38*, vol. 8353 of *Proceedings of SPIE*, 835316, April 2012.
- [18] B. Klein, E. Plis, M. N. Kutty et al., "Varshni parameters for InAs/GaSb strained layer superlattice infrared photodetectors," *Journal of Physics D*, vol. 44, no. 7, Article ID 075102, 5 pages, 2011.
- [19] T. V. Chandrasekhar Rao, J. Antoszewski, J. B. Rodriguez, E. Plis, S. Krishna, and L. Faraone, "Quantitative mobility spectrum analysis of carriers in GaSb/InAs/GaSb superlattice," *Journal of Vacuum Science and Technology B*, vol. 26, no. 3, pp. 1081–1083, 2008.
- [20] F. Szmulowicz, H. J. Haugan, S. Elhamri, G. J. Brown, and W. C. Mitchel, "Transport studies of MBE-grown InAs/GaSb superlattices," *Opto-Electronics Review*, vol. 18, no. 3, pp. 267–270, 2010.
- [21] D. Z.-Y. Ting, A. Soibel, L. Höglund et al., "Type-II superlattice infrared detectors," in *Semiconductors and Semimetals*, S. D. Gunapala, D. R. Rhiger, and C. Jagadish, Eds., vol. 84, pp. 1–57, Elsevier, Amsterdam, The Netherlands, 2011.
- [22] E. C. F. da Silva, D. Hoffman, A. Hood, B. M. Nguyen, P. Y. Delaunay, and M. Razeghi, "Influence of residual impurity background on the nonradiative recombination processes in high purity InAs/GaSb superlattice photodiodes," *Applied Physics Letters*, vol. 89, no. 24, Article ID 243517, 3 pages, 2006.

## Review Article

# High-Quality Growth of GaInNAs for Application to Near-Infrared Laser Diodes

**Masahiko Kondow and Fumitaro Ishikawa**

*Graduate School of Engineering, Osaka University, 2-1 Yamada-oka, Suita, Osaka 565-0871, Japan*

Correspondence should be addressed to Masahiko Kondow, kondow@eei.eng.osaka-u.ac.jp

Received 27 June 2012; Accepted 4 September 2012

Academic Editor: Marija Strojnik

Copyright © 2012 M. Kondow and F. Ishikawa. This is an open access article distributed under the Creative Commons Attribution License, which permits unrestricted use, distribution, and reproduction in any medium, provided the original work is properly cited.

GaInNAs was proposed and created in 1995. It can be grown pseudomorphically on a GaAs substrate and is a light-emitting material with a bandgap energy that corresponds to near infrared. By combining GaInNAs with GaAs, an ideal band lineup for laser-diode application is achieved. This paper presents the reproducible growth of high-quality GaInNAs by molecular beam epitaxy. Examining the effect of nitrogen introduction and its correlation with impurity incorporation, we find that Al is unintentionally incorporated into the epitaxial layer even though the Al cell shutter is closed, followed by the concomitant incorporation of O and C. A gas-phase-scattering model can explain this phenomenon, suggesting that a large amount of N<sub>2</sub> gas causes the scattering of residual Al atoms with occasional collisions resulting in the atoms being directed toward the substrate. Hence, the reduction of the sublimated Al beam during the growth period can suppress the incorporation of unintentional impurities, resulting in a highly pure epitaxial layer.

## 1. Introduction to GaInNAs for Application to Near-Infrared Laser Diodes

GaInNAs was proposed and created in 1995 by Kondow et al. [1, 2]. It is a member of the family of dilute nitrides and III-N-V alloys, such as GaNP and GaNAs, which are novel semiconductor materials developed in the 1990s. A couple of research groups reported on III-N-V alloy semiconductors before 1994 [3–6]. However, these reports have been limited to crystal growth and measurements of physical properties. Kondow et al. proposed application of dilute nitrides to optoelectronic devices [1, 2] because the exceptional physical properties of III-N-V alloy semiconductors, such as their huge degrees of bandgap bowing, facilitate devices with levels of performance greatly superior to those of current devices. The unusual physical properties are consequences of the exceptional chemical characteristics of N as compared to the other elements in groups III and V. However, these chemical characteristics lead to difficulties in the creation of alloys of N and III-V crystals, that is, in the growth of III-N-V alloys. A strongly nonequilibrium method of growth and highly reactive N precursor are essential to overcome

the immiscibility of N in III-V alloys. For this reason, no one had succeeded in growing any such material before the early 1990s. Kondow et al. proposed and developed a growth method for III-N-V alloys in 1994 [7]. They adopted molecular beam epitaxy (MBE) with N supplied in the form of radicals. Their method has subsequently been widely used as a standard method for growing III-N-V alloys with excellent crystallinity. In 1996, S. Sato et al. succeeded in growing GaInNAs with excellent crystallinity by conventional organometallic vapor-phase epitaxy (OMVPE) [8], despite the failure of several groups. In general, the advantages of OMVPE are its applicability to the fabrication of complex layered structures, good reproducibility of growth from run to run, and suitability for use in mass production. The availability of both growth methods has accelerated research in III-N-V alloys and the development of devices based on these materials.

GaInNAs is a light-emitting material with a bandgap energy suitable for near-infrared laser diodes (LDs) (1.3–1.55  $\mu\text{m}$  and longer wavelengths) and can be grown pseudomorphically on a GaAs substrate. Combining GaInNAs with GaAs or any other wide-gap materials that can be grown

on a GaAs substrate results in a type I band lineup for applying a material to the quantum-well active layer of an LD. A type I band lineup is essential for both electrons and holes to be confined to the quantum-well layer. This allows the fabrication of very deep quantum wells, especially in the conduction band. Deep quantum wells provide many advantages in terms of LD performance, as shown later.

In this section, we start by examining the bandgap structure of GaNAs and GaInNAs. Next, we explain the band lineup of GaNAs and GaInNAs. Then we present quantum levels in a GaInNAs/GaAs well. Finally, we discuss the advantages of GaInNAs in the application of LDs.

Figure 1 shows the experimentally obtained relationship between the N content and bandgap energy of GaNAs epilayers grown on a GaAs substrate [7]. The N content was estimated using X-ray diffraction, and the bandgap energy was measured by photoluminescence (PL). As for GaNAs with a low N content, the PL peaks of the GaNAs epilayer and the GaAs substrate overlapped when measurement was taken at room temperature. Therefore, PL was also observed at the very low temperature of 77 K. The bandgap energy decreased monotonically with increased N content. The energy difference between room temperature and 77 K measurements hardly varied, remaining at approximately 70 meV. The lines denoting room temperature and 77 K measurement thus run parallel in this figure. The slope of each line is 0.184 eV/% N. The GaNAs epilayers grown on a GaAs substrate were under tensile strain, which lowers the bandgap energy. To determine the relationship between the N content and bandgap energy of free standing, that is, stress-free, GaNAs, the bandgap energy was calibrated using the deformation potential parameters for GaAs. The results are shown as broken lines having a slope of 0.156 eV/% N in Figure 1.

Figure 2 shows the relationship between the lattice constant and bandgap energy in various III-V alloy semiconductors, including GaNAs and GaInNAs [9]. The bowing parameter of GaNAs was derived from the above experimental results for GaNAs with a small N content [7], assuming a parabolic curve [10]. With conventional alloy semiconductors, the results for which lie in the shaded area of Figure 2, the tendency is for the bandgap energy to increase with a decreasing lattice constant. On the other hand, the result for GaNAs departs from the shaded area to which conventional alloy semiconductors are restricted. Until N comes to make up half of the GaNAs, an increase in N content leads to a monotonic decrease in bandgap energy rather than an increase towards the value for cubic GaN (3.2 eV). This curious behavior is supported by both experimental results [6] and theoretical predictions [10]. The responsible factor is the large discrepancy between the electronegativity values for N and the other constituent atoms [10]. Phillips states that the electronegativity of N is 3.00, while the values for P, As, and Sb are from 1.31 to 1.64 [11]. Since one property of III-N-V alloy semiconductors is that a decrease in the lattice constant leads to a decrease in the bandgap energy, they provide operation over a dramatically broader area than conventional III-V alloy semiconductors, as shown in Figure 2. This leads to significantly greater freedom in the

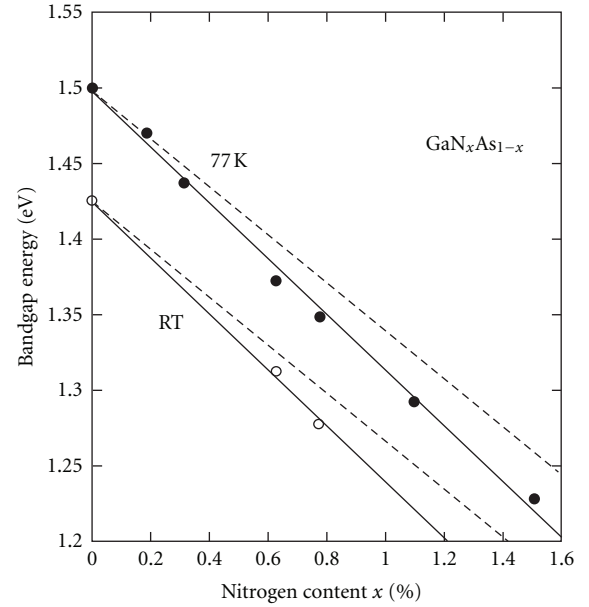


FIGURE 1: The relationship between N content and bandgap energy of GaNAs epilayers grown on a GaAs substrate [7]. The solid lines are experimental results. Broken lines are the result of calibration to remove the effect of strain.

design of semiconductor devices, to the extent that novel devices and dramatic improvements in the performance of current devices become possible. This figure includes results for GaNAs, which might possibly have a negative bandgap energy for large N concentrations. This might mean that GaNAs can act as a metal or semiconductor, according to the N content. While such behavior is very interesting, there is no reliable experimental data on this region because of phase separation. Furthermore, there is no guarantee that bandgap theory can be expanded to cover this region. Thus, the middle range of III-N-V alloy composition remains unexplored.

Let us focus on the bandgap energy of GaInNAs. Adding In to GaAs, that is, making a GaInAs-alloy semiconductor, increases the lattice constant, while adding N to GaAs, that is, making a GaNAs-alloy semiconductor, decreases the lattice constant. GaInNAs can thus be lattice matched to GaAs by adjusting the contents of In and N. Adding In to GaAs decreases the bandgap, and in the same way, adding N to GaAs also decreases the bandgap, as shown in Figure 2. Since both GaInAs and GaNAs are direct-transition-type semiconductors, GaInNAs is also of this type. Thus, GaInNAs is a light-emitting material that has a bandgap energy suitable for near-infrared laser diodes (0.8–1.0 eV) and is suitable for formation on a GaAs substrate.

Figure 3 shows the N-content dependence of the band-discontinuity energy in the valence band ( $\Delta E_v$ ) for GaNAs/GaAs measured using X-ray photoelectron spectroscopy (XPS) [12]. The rather large experimental error was due to the limited energy resolution in this measurement. The center value of  $\Delta E_v$  for GaNAs decreased as the N content increased. This suggests the formation of a type

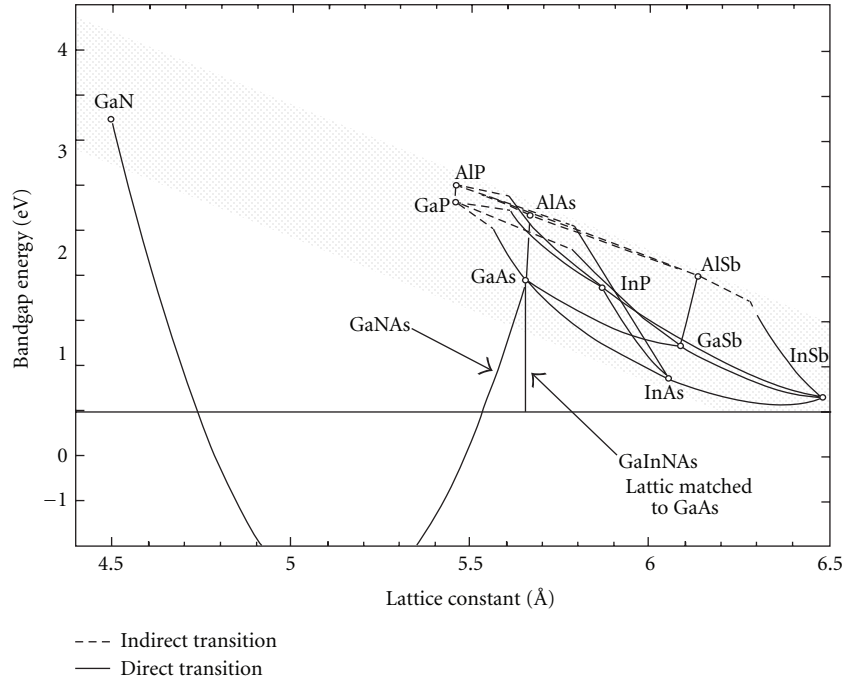


FIGURE 2: The relationship between lattice constant and bandgap energy in III-V alloy semiconductors [9].

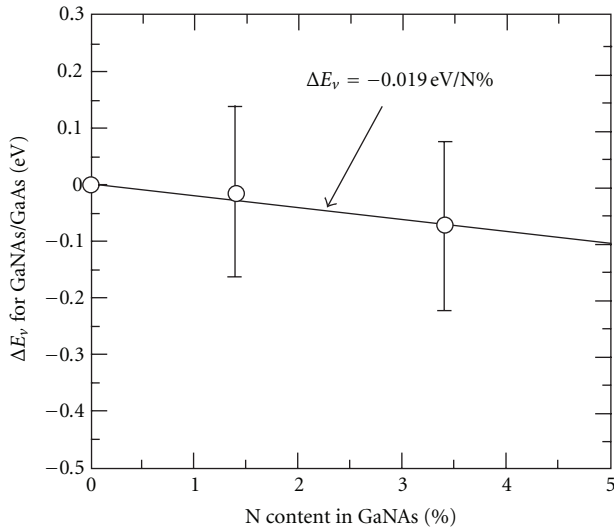


FIGURE 3: Dependence of  $\Delta E_v$  on the content of N in GaNAs/GaAs [12].

II band lineup in GaNAs/GaAs. From the slope,  $\Delta E_v$  for GaNAs/GaAs was estimated as  $-(0.019 \pm 0.053)$  eV/%N (the large experimental error means that there is still a possibility that a type I band lineup will form in GaNAs/GaAs). Ding et al. reported  $\Delta E_v$  of  $-1.84$  eV in cubic-GaN/GaAs based on XPS measurement [13]. If the  $\Delta E_v$  of cubic-GaN/GaAs is linearly interpolated,  $\Delta E_v$  of GaNAs/GaAs can be calculated as  $-0.0184$  eV/%N. This is in good agreement with the above measured value of  $-0.019$  eV/%N. Thus, bandgap bowing

seems to have little effect on the  $\Delta E_v$  of GaNAs, and this result supports the theoretical prediction by Sakai et al. in which bowing of the valence band of GaNAs is negligible [14].

Next, the band lineup of the GaInNAs materials system is examined from the viewpoint of application to an LD because a type I band lineup is essential for both electrons and holes to be confined to the quantum-well layer in order to apply a material to the quantum-well active layer of an LD.

A schematic diagram of the bandgap for GaInAs is shown in the right half of Figure 4, and the bandgap of GaNAs is shown in the left half. The horizontal axis shows strain, which allows us to draw the diagrams for GaInAs and GaNAs in the same figure. GaAs is therefore located in the center. In Figure 4, bowing of the valence band of GaNAs is assumed to be zero on the basis of the experimental results cited previously [12]. As a result, both the conduction band and bandgap have the same bowing parameter in the GaNAs system. Thus, the bowing of the conduction band is very large. Increasing the In content in GaInAs, that is, increasing the compressive (+) strain, lowers the conduction band and raises the valence band. On the other hand, increasing the N content in GaNAs, that is, increasing the tensile (-) strain, lowers both the conduction and valence bands. Since the conduction band falls more steeply than the valence band, increasing the N content decreases the bandgap. If a small amount of N is added to GaInAs to form GaInNAs, the conduction and valence bands will be moved from A to B and from D to E (Figure 4). When the composition is such that GaInNAs is lattice-matched with GaAs, the conduction band will be at C and the valence band will be at F. Note that the valence bands of the GaInNAs and GaAs are at almost the same energy level. Therefore, by combining GaInNAs with

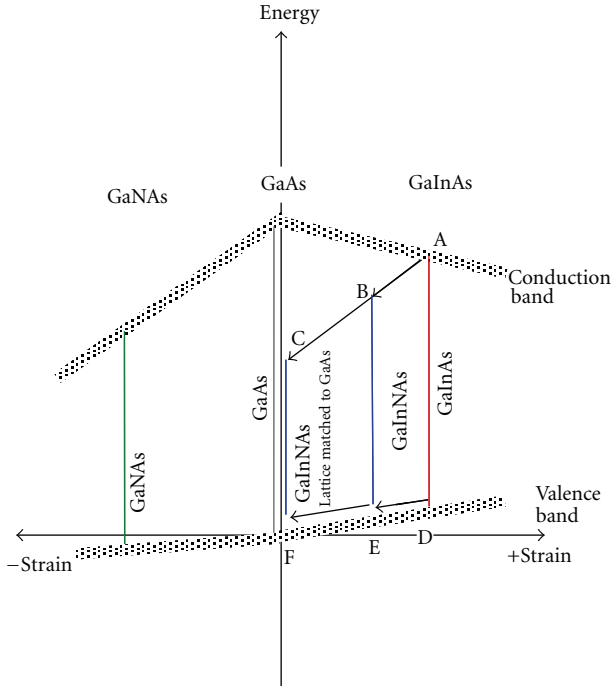


FIGURE 4: Schematic diagram of bandgap of GaInAs, GaNAs, and GaInAs. For lattice matching of GaInNAs to GaAs, In concentration is required to be approximately 3 times of N concentration. For example,  $\text{Ga}_{0.90}\text{In}_{0.10}\text{N}_{0.035}\text{As}_{0.965}$  is lattice-matched.

wide-gap materials, such as AlGaAs, a type I band lineup is easily achieved. Compressively (+) strained GaInNAs can also have a type I band lineup in combination with GaAs. In general, a  $\Delta E_v$  of more than 50 meV is required to confine holes to the quantum-well layer. Since the GaInAs quantum-well layer in a  $0.98 \mu\text{m}$  range laser diode formed on a GaAs substrate is strained by approximately 1% and has a  $\Delta E_v$  as high as 50 meV, compressively strained GaInNAs has to be strained by at least 1% to achieve good hole confinement (in this case, the GaInNAs should be grown as a strained quantum-well layer that is thinner than the critical thickness where misfit dislocations start to appear). The conduction band of GaInNAs, whether it is lattice-matched to GaAs or compressively strained, has a large discontinuity energy ( $\Delta E_c$ ).

Next, we discuss the quantum levels in GaInNAs/GaAs wells. Knowledge of the effective masses of individual holes and electrons is necessary if we are to determine these levels. As mentioned above, alloying Ga (In) As with N strongly affects the conduction band but has little effect on the valence band. Therefore, we may assume the effective mass of a hole in GaInNAs to be the same as that of a hole in GaInAs with the same In content. On the other hand, the effective mass of an electron in GaInNAs differs greatly from that of an electron in GaInAs. Figure 5 shows this effective mass as a function of the N content. This result was obtained by analyzing the optical transitions between the ground levels [17] and high-order quantum levels [15, 18] in GaInNAs/GaAs quantum wells. Note that the transition

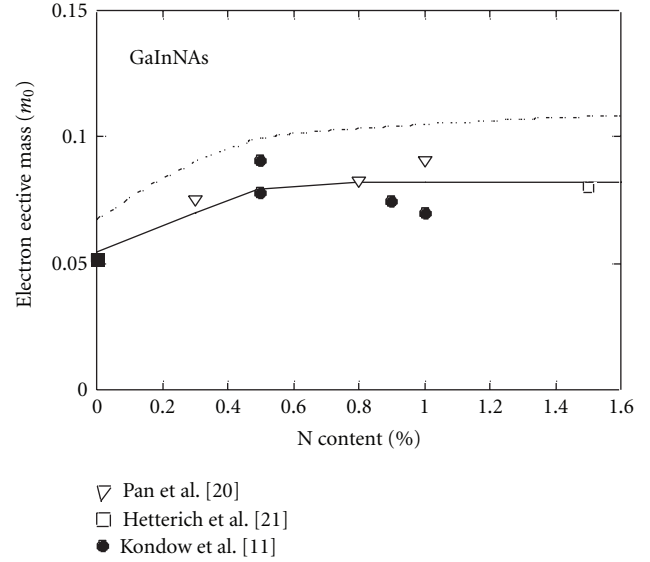


FIGURE 5: The effective mass of an electron in GaInNAs as a function of the content of N [15]. Broken line denotes a theory for GaNAs [16].

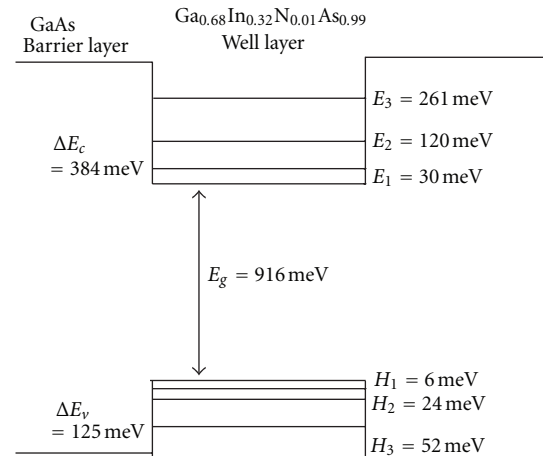


FIGURE 6: The quantum levels in a 10 nm thick  $\text{Ga}_{0.68}\text{In}_{0.32}\text{N}_{0.01}\text{As}_{0.99}/\text{GaAs}$  well with an emission wavelength of  $1.31 \mu\text{m}$ .

energies between the high-order quantum levels are sensitive to the mass value. Therefore, we can thus obtain precise values through this approach. The effective mass remains in the range  $0.08 \pm 0.01 m_0$  (where  $m_0$  is the mass of a free electron) almost independently of the N content. This behavior is in good agreement with a theoretical prediction for GaNAs [16]. An electron has a 60% larger effective mass in  $\text{Ga}_{0.7}\text{In}_{0.3}\text{NAs}$  than in  $\text{Ga}_{0.7}\text{In}_{0.3}\text{As}$ .

Figure 6 is a sketch of the quantum levels in a  $\text{Ga}_{0.68}\text{In}_{0.32}\text{N}_{0.01}\text{As}_{0.99}/\text{GaAs}$  well, a system that produces emission at  $1.31 \mu\text{m}$ . The well is 10 nm thick. The strain of the well is about +2%. The energy difference between electrons at the first and second quantum levels is 90 meV. Thus, most

electrons are on the ground level. This leads to a large optical gain for the LD.

Deep quantum wells provide many advantages in terms of LD performance, including high operating speeds and excellent temperature stability of threshold current ( $I_{th}$ ) and lasing wavelength. GaInNAs is also promising as a material for use in near-infrared vertical-cavity surface-emitting lasers (VCSELs), because a GaInNAs active layer can be grown on a highly reflective GaAs/AlAs distributed Bragg reflector (DBR) mirror over a GaAs substrate in a single stage of epitaxial growth [19]. GaInNAs can be grown by both OMVPE and MBE. However, LDs with a long lifetime is limited to MBE-grown devices [20, 21]. Therefore, from the viewpoint of industry use, MBE growth is important for GaInNAs. Currently MBE-grown GaInNAs VCSELs are on the market [21].

## 2. Unintentional Al Incorporation during GaInNAs Growth

*2.1. Background.* The features of GaInNAs material may come from the large electron negativity difference between III-nitride compounds and other III-V compounds. However, the large electron negativity and large atomic size differences also make obtaining a high-quality crystal difficult. Researchers worldwide have devoted much effort to improving the crystallinity of this novel material [22]. As a result, the threshold current density ( $J_{th}$ ) of 1.3  $\mu\text{m}$  range GaInNAs LDs has been reduced to as low as that of LDs made of conventional materials [23, 24]. However, this is still higher than that of LDs made of GaInAs, that is, the host material of GaInNAs. Therefore, the maximum performance of GaInNAs LDs has not yet been achieved. Some experimental studies have revealed that GaInNAs LDs still exhibit serious nonradiative recombination [25, 26].

Nonradiative recombination may be related to intrinsic and extrinsic defects. GaInNAs is thermodynamically metastable or unstable. Therefore, careful optimization of both growth and postannealing is necessary. Much effort by many researchers worldwide has been devoted to such optimization to reduce intrinsic defects [22]. However, the results have not been satisfactory, as mentioned above. Therefore, extrinsic defects in GaInNAs should now be studied. Aluminum was detected in OMVPE-grown GaInNAs grown over an AlGaAs layer [27–29]. According to Takeuchi et al. [27], Al generates three-dimensional growth and degrades the crystallinity of a GaInNAs active layer and LD performance.

GaInNAs can be grown by both OMVPE and MBE. However, LDs with a long lifetime are limited to MBE-grown devices [20, 21]. Therefore, from the viewpoint of industry use, MBE growth is important for GaInNAs. Kondow et al. investigated extrinsic impurities in MBE-grown GaInNAs [30]. They used 1.3  $\mu\text{m}$  range GaInNAs LDs with  $\text{Al}_{0.3}\text{Ga}_{0.7}\text{As}$  cladding layers as specimens. Thus, the  $\text{Ga}_{0.7}\text{In}_{0.3}\text{N}_{0.01}\text{As}_{0.99}$  active layer was grown over an AlGaAs layer. The LDs were grown using a solid-source MBE system with an N plasma cell [31]. Their  $\text{N}_2$  gas line from an  $\text{N}_2$  cylinder to a plasma cell did not have any material containing Al. It had two

inline purifiers, MILLIPORE Waferpure, which remove  $\text{H}_2\text{O}$ ,  $\text{O}_2$ , CO, and  $\text{CO}_2$  from  $\text{N}_2$  gas. The gas line was kept in a high vacuum at around  $1 \times 10^{-8}$  Torr using a vent/run system when  $\text{N}_2$  gas was not introduced. Figure 7 shows a cross section of the LDs they studied. The active layer had a single quantum well (SQW) with a thickness of 7 or 10 nm sandwiched between two 150 nm thick GaAs layers. The cladding layers were each 1.5  $\mu\text{m}$  thick and had a carrier density of approximately  $1 \times 10^{18} \text{ cm}^{-3}$ . A p-GaAs contact layer ( $p = 1 \times 10^{19} \text{ cm}^{-3}$ ) was formed to decrease the contact resistance. The ridge mesa width was approximately 2  $\mu\text{m}$ , and the cavity length was 400  $\mu\text{m}$ . Facets were as cleaved. This LD structure is likely one standard for the GaInNAs LD. The typical  $I_{th}$  of GaInAs LDs grown using their MBE system is 10 mA. This value is quite reasonable as a GaInAs LD under this LD structure. On the other hand, the GaInNAs LDs Kondow et al. investigated had an  $I_{th}$  of 60–70 mA.

To examine what residual molecules exist in their MBE chamber, experiments using quadrupole-mass spectrometry (QMS) were conducted under high sensitivity when  $\text{N}_2$  gas was not introduced into the chamber. The peaks corresponding to the residual molecules of  $\text{H}_2$ ,  $\text{H}_2\text{O}$ , CO,  $\text{N}_2$ , or  $\text{CO}_2$  were observed at 2, 18, 28, and 44 a.m.u., respectively, rather than those related to As at 37, 38 and 75 a.m.u. More specifically, the peaks at 2 and 18 a.m.u. accompanied peaks at 1 and at 16 and 17 a.m.u., respectively, because  $\text{H}_2$ ,  $\text{H}_2\text{O}$  were cracked in a QMS analyzer. Hence, the candidates of the extrinsic impurities in the GaInNAs crystal are H, C, and O. Note that no signal corresponding to  $\text{O}_2$  was detected at 32 a.m.u. Considering the lack of  $\text{O}_2$  and the typical  $I_{th}$  value for GaInAs LDs, their MBE system was prepared well and had no problem at least in growing conventional III-V materials.

The concentrations of impurities in the GaIn(N)As active layer were measured using secondary ion mass spectrometry (SIMS). Figure 8 shows the relationship between the impurity concentrations and  $I_{th}$  of the LDs. The  $I_{th}$  does not depend on H or C concentration. Since the respective concentrations for H and C at  $1 \times 10^{17}$  and  $1 \times 10^{16} \text{ cm}^{-3}$  were the detection limit in the SIMS measurement for their study, actual concentrations for H and C might be lower than these values. While we cannot determine the real relationship between  $I_{th}$  and H or C concentration, it is likely that the respective concentrations for H and C at  $1 \times 10^{17}$  and  $1 \times 10^{16} \text{ cm}^{-3}$  are too low to affect  $I_{th}$ . On the other hand,  $I_{th}$  increased as the O concentration increased (concentration of O at  $2 \times 10^{16} \text{ cm}^{-3}$  is the detection limit.). The O concentration dependence of  $I_{th}$  in the figure means that O is the main impurity that must be reduced to  $2 \times 10^{16} \text{ cm}^{-3}$  or less.

Although the O concentrations in the GaInAs and GaInNAs active layers are the same at  $4 \times 10^{16} \text{ cm}^{-3}$ , there is a considerable difference in  $I_{th}$  among these LDs. Therefore, some other impurity may exist in GaInNAs. When Kondow et al. considered the QMS results and the fact that the precursors used in the MBE were extremely pure, it was hard to believe that any atoms other than the precursors for the LDs could provide the unknown impurity. Thus, they checked for Al by using SIMS. They prepared samples of which the upper cladding layer was mostly etched off because it was

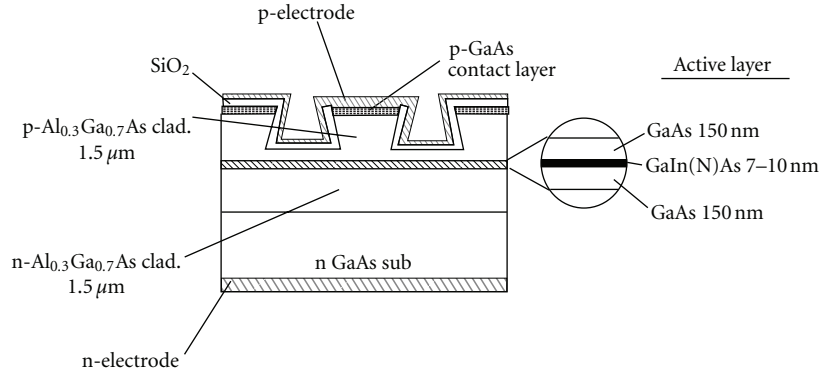


FIGURE 7: Cross section of the GaIn(N)As LDs used in the study [30].

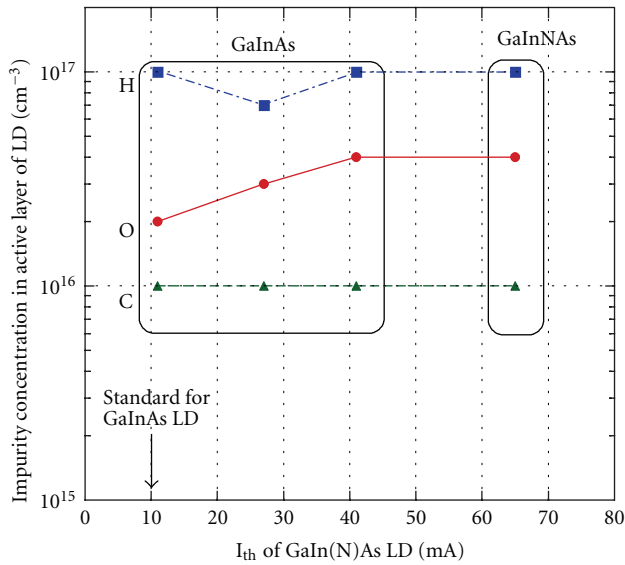


FIGURE 8: Relationship between the impurity concentrations and  $I_{th}$  of the GaIn(N)As LDs [30].

difficult to detect the Al signal at the GaInNAs quantum-well position in a sample with a whole layer structure due to a relatively high etching speed. Figure 9 shows an Al depth profile. Both sides correspond to the AlGaAs cladding layers. There was a distinct Al peak at the center of the GaInNAs/GaAs active layer (i.e., the position of the GaInNAs quantum well), even though Al was never supplied during GaInNAs growth. The Al concentration was as much as 0.1%. Coincidentally, this value agrees with that in OMVPE-grown GaInNAs [27]. According to Takeuchi et al. [27], Al generates three-dimensional growth and degrades the crystallinity of GaInNAs. Although the growth mechanism and the Al supply mechanism are different for OMVPE and MBE, it may be possible that GaInNAs is degraded by three-dimensional growth if 0.1% Al is incorporated. The Al incorporation in MBE may depend on the plasma condition of an N plasma cell and the inside structure of the growth chamber.

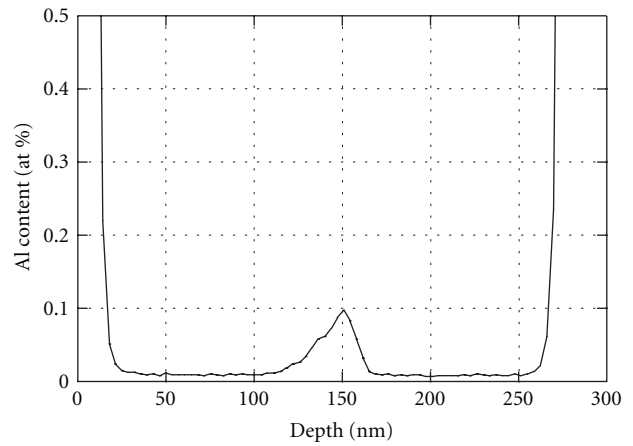
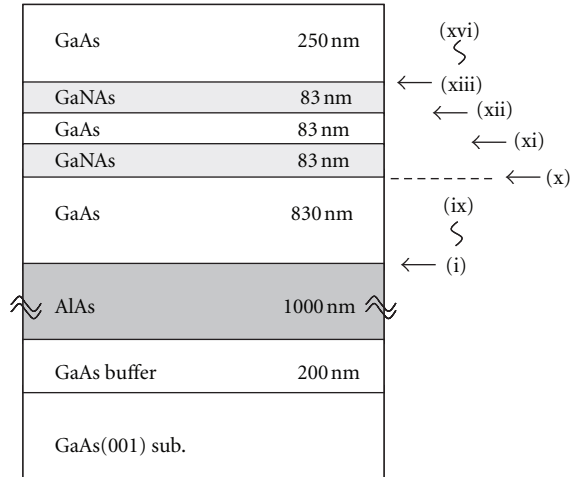


FIGURE 9: Al depth profile measured by SIMS [30].

**2.2. Investigation of Al Incorporation Mechanism.** Ishikawa et al. investigated the origin of the unintentional incorporation of Al during plasma-assisted MBE growth [32]. They grew samples having a GaNAs/GaAs/AlAs stacked structure at 450°C. Prior to growing the structure, a 200 nm GaAs buffer layer was grown at 580°C. They grew a 1 μm thick AlAs layer on the buffer to make the growth situation similar to that of the laser structure. The growth was carried out without interruption throughout the structure. After the growth of the AlAs layer, the shutter of the Al cell was closed and the shutter of Ga cell was opened simultaneously. Then, the Al source temperature was kept at the growth temperature of 1020°C until the end of full-structure growth. The growth of GaNAs with plasma-assisted MBE requires many operations. They grew the sample shown in Figure 10 with the procedure summarized in the same figure. They considered the layer grown with bright mode N plasma with its shutter opened as the GaNAs layer. There are 16 steps, labeled (i)–(xvi). They carried out the listed operations at the beginning of every step. They maintained the growth condition for 5 min, corresponding to the growth of 83 nm for each layer. However, step (i) was maintained for 10 min, growing 166 nm to prevent Al diffusion, as reported by



- (i) Grow GaAs
- (ii) Open variable leak valve
- (iii) Set N<sub>2</sub> flow rate at 0.12 sccm
- (iv) Open N shutter
- (v) Close N shutter
- (vi) Increase As BEP
- (vii) Decrease As BEP
- (viii) Turn on RF power, set at 300 W
- (ix) Set N<sub>2</sub> flow rate at 0.02 sccm
- (x) Open N shutter
- (xi) Close N shutter
- (xii) Open N shutter
- (xiii) Close N shutter
- (xiv) Turn off RF power
- (xv) Set N<sub>2</sub> flow at 0 sccm, close VLV
- (xvi) Close Ga shutter and finish the growth

FIGURE 10: Schematic of the sample structure with the list of growth procedures. Every step has its thickness of 83 nm except step (i) of 166 nm [32].

Sundgren et al. [29]. These thicknesses were chosen to resolve the effect of each operation on the concentrations of the investigated elements with SIMS measurement. The details of this procedure are as follows. Ishikawa et al. first (i) grew GaAs. During this procedure, the cell shutters of N and Al were closed and the N<sub>2</sub> gas flow rate was 0 sccm. They (ii) opened the variable leak valve (VLV), which was attached between the mass flow controller (MFC) and the plasma cell, and (iii) set the N<sub>2</sub> gas flow rate to 0.12 sccm to supply a sufficient amount of N<sub>2</sub> gas that would enable the succeeding plasma ignition. They (iv) opened and (v) closed the N shutter to examine these effects. To examine the effect of As flux, they increased and decreased its beam equivalent pressure (BEP) in steps (vi) and (vii), as shown in Figure 11. The As<sub>2</sub> BEP of  $3.5 \times 10^{-6}$  Torr in step (vii) is the standard

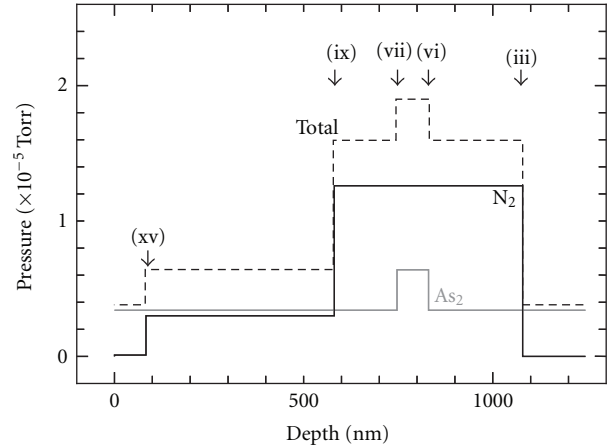


FIGURE 11: Partial pressures of N<sub>2</sub> and As<sub>2</sub> estimated from total background pressure [32].

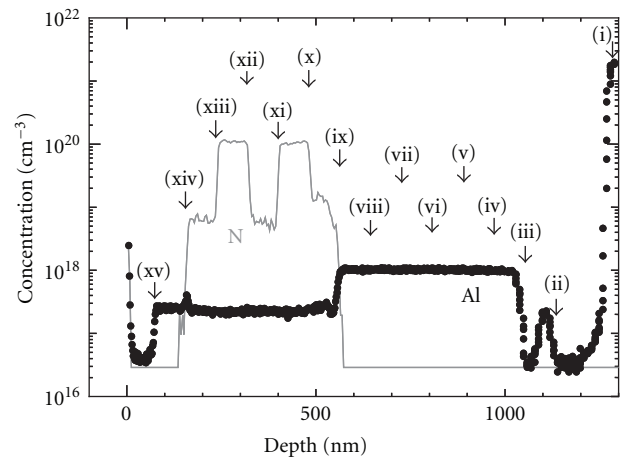


FIGURE 12: SIMS depth profile of N and Al for the sample shown in Figure 10 [32].

growth condition for GaAs at 1.0 ML/s in their MBE system. They (viii) turned on the RF power of the plasma cell and adjusted it to 300 W where N plasma ignites in dark mode. In step (ix), the N<sub>2</sub> flow rate was decreased to 0.02 sccm to make the plasma transfer to bright mode. In steps (x)–(xiii), they opened and closed the shutter of the N plasma cell and repeated this twice to accurately examine its effect. In step (xiv), the RF power was turned off and then the plasma was extinguished. In step (xv), the N<sub>2</sub> flow rate was set to zero and VLV was closed. The shutter of the Ga cell was closed to finish growth in step (xvi).

Figure 12 shows the SIMS depth profiles of N and Al for the sample. The N concentration is preferably controlled by the applied power, flow rate, resulting plasma mode transfer, and its shutter operation. Aluminum was incorporated in spite of the closed shutter of the Al cell. When the VLV was opened in step (ii), the Al profile showed a peak. The largest concentration of  $1.0 \times 10^{18} \text{ cm}^{-3}$  was observed between steps (iii) and (viii). The concentration decreased to  $2 \times 10^{17} \text{ cm}^{-3}$  in step (ix), maintaining that amount until step

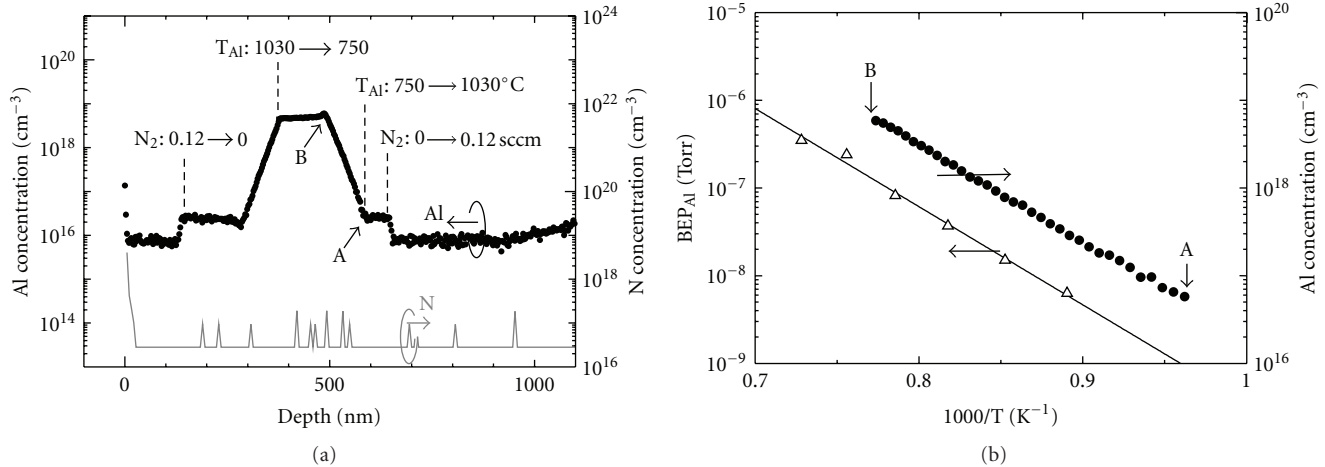


FIGURE 13: (a) SIMS depth profile of Al and N for the sample grown at various  $T_{Al}$  values as indicated.  $N_2$  gas flowed at the indicated points. (b) Plots of Al vapor pressure and concentration of incorporated Al as functions of reciprocal temperature. The solid line indicates a linear fit on the results [33].

(xv). The concentration then dropped to  $3 \times 10^{16} \text{ cm}^{-3}$ . The above results cannot be due to the failure of the shutter control since Al concentration was suppressed in steps (i) and (xv) where N was not introduced. These results cannot be related to the diffusion or segregation from the AlAs layer, as mentioned by Sundgren et al. [29] since the incorporation of Al was not detected in the GaAs layer in step (i) locating just above the AlAs layer. Consequently, the Al concentration solely depends on the  $N_2$  flow rate and the vapor pressures of  $N_2$ . The plasma power, mode, shutter conditions, and As flux that varied within the parameters had no impact. A peak observed in step (ii) probably resulted from the residual  $N_2$  gas remaining at the gas line between VLV and MFC. It was evacuated in about 1 min corresponding to the 16 nm GaAs growth, which agreed well with the peak widths. Since the variation in As BEP has no impact on the concentration of extrinsic Al, the phenomena observed are considered due to the specific characteristics of  $N_2$  under their conventional growth conditions.

Ishikawa et al. also investigated the correlation between the vapor pressures of N and Al to ascertain the origin of the incorporated Al [33]. They carried out an experiment similar to the one above at various Al vapor pressures during growth. Figure 13(a) shows the SIMS results for the sample. They used a lower growth rate of 0.3 ML/s to efficiently detect unintentional Al flux. The N plasma was not ignited throughout growth. Initially, the temperature of the Al cell ( $T_{Al}$ ) was set at the common idling temperature of  $750^\circ\text{C}$ , and  $N_2$  gas was not introduced. As indicated in the figure, they introduced the  $N_2$  gas at a flow rate of 0.12 sccm for a certain period. After that, they shut off the flow. Within this period, they increased and decreased  $T_{Al}$  to vary the vapor pressure of Al. At position A, indicated in the figure, they started to increase  $T_{Al}$  from  $750^\circ\text{C}$  to  $1030^\circ\text{C}$  at a ramp rate of  $20^\circ\text{C}/\text{min}$ . Subsequently,  $T_{Al}$  reached  $1030^\circ\text{C}$  at position B. As is clearly shown in Figure 13(a), they observed Al incorporation during the period the N gas was flowing

into the chamber. Moreover, the concentration depended on  $T_{Al}$ . In contrast, N was not incorporated into the sample. Figure 13(b) shows the vapor pressure and concentration of Al as functions of reciprocal temperature. Remarkably, the temperature dependences were completely identical. This result indicates that the unintentionally incorporated Al originating from the Al beam sublimated from the Al source. The Al remaining on the chamber wall, cell wall, or backside of the shutter is not likely the origin because of this temperature dependence. The Al incorporation is not followed by incorporation of N, that is, these species cannot bind to each other. The research team presumed that the introduction of  $N_2$  gas at a high vapor pressure would modulate Al beam dispersion, resulting in an inefficient shut off of the Al flux by the shutter. This phenomenon would be similar to the case of solid-source As and Sb at a high vapor pressure. These sources show unintentional incorporation even when the mechanical shutters are closed and with concentrations at a certain proportion of the initial sublimation [34, 35].

The above results suggest that the density of incorporated Al ( $n_{Al}$ ) has linear dependencies on the vapor pressures of  $N_2$  and Al. An analytical gas-phase-scattering model reproduced these dependencies, suggesting that a large amount of  $N_2$  gas causes the scattering of residual Al atoms with occasional collisions resulting in atoms directed toward the substrate [33]. Calculated  $n_{Al}$  agreed well with the experimental values within the errors of one order of magnitude, indicating the adequacy of the model.

**2.3. Solution.** As discussed above, the origin of the unintentional incorporation of Al, which generates three-dimensional growth and degrades the crystallinity of the GaInNAs active layer and LD performance, is the Al source in the MBE growth chamber. Adachi et al. made GaInNAs LDs with very low  $I_{th}$  by using a brand new Al-free MBE growth chamber [36]. They used GaInP in place of AlGaAs

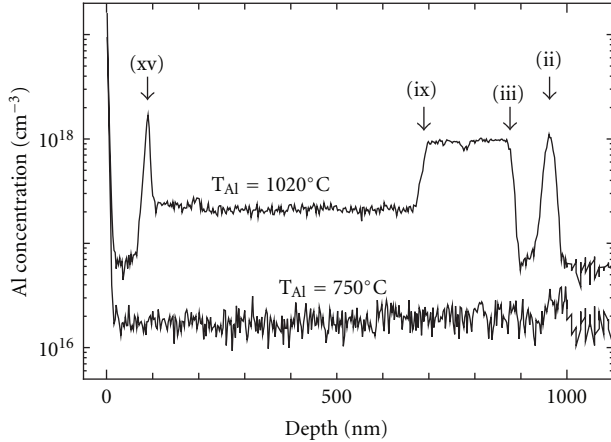


FIGURE 14: Depth profile of Al for the samples grown at the Al cell temperature ( $T_{Al}$ ) of 1020°C and 750°C [32]. Those were grown with the sequences (i)–(xvi) skipping the procedures between (iv) and (vii) shown in Figure 12. The representative numbers of the steps are mentioned in Figure 10.

as the cladding layer. Although they succeeded in making excellent edge-emitting LDs, they could not make VCSELs because GaInNAs should be grown over an AlAs/GaAs DBR. Bank et al. used an MBE system with dual growth chambers [37]. One chamber was used for growing GaInNAs, and the other was for growing AlGaAs. With this MBE system, they could make VCSELs [38]; however, their MBE system is very expensive.

Figure 13 shows that Al is hardly incorporated into the epi-layer even under high vapor pressures of  $N_2$  when  $T_{Al}$  is set at 750°C. Ishikawa et al. carried out a similar experiment to that shown in Figure 12 for two samples grown with different  $T_{Al}$  [32]. They prepared two samples grown with the same procedure of the sample shown in Figure 12, skipping steps (iv) and (vii). Figure 14 shows the Al concentration for those samples obtained by SIMS. The sample grown at  $T_{Al}$  of 1020°C exhibited a similar Al concentration profile to that in Figure 12. A peak observed at a depth around 100 nm, corresponding to step (xv), was due to the mechanical failure of the MFC. When they set the flow rate value to zero, the MFC occasionally showed spiky pressure increases, inducing the observed peak. In contrast, the sample grown at  $T_{Al}$  of 750°C showed no Al incorporation corresponding to the  $N_2$  gas flow rate throughout the structure. These results imply that the unintentionally incorporated Al originated from the Al beam sublimated from the Al source metal. It is difficult to determine the origin of the Al remaining on the chamber wall, cell wall, or backside of the shutter because of the dependence on cell temperature. Hence, at the common Al cell idling temperature, unintentional incorporation of Al can be efficiently suppressed even though the MBE chamber has an Al cell and epilayers containing Al have been grown inside.

The introduction of N may also enhance the concentration of other undesirable impurities such as C and O, possibly originating from the constituents of  $N_2$  gas or residuals in the

chamber. These impurities may be harmful to the epitaxial layers, resulting in poorer device performance. Ishikawa et al. carried out an experiment similar to that described in the previous section by focusing on impurities other than N and Al within the layer [33]. Figures 15(a) and 15(b) show SIMS results for samples grown at different  $T_{Al}$  of 1020 and 750°C, respectively. The concentrations of C, O, Al, and S are plotted in the figures against the  $N_2$  gas flow rates of 0 and 0.12 sccm, at which the  $N_2$  gas shows its partial pressures of 0 and  $1.3 \times 10^{-5}$  Torr, respectively. The growth rate was 1.0 ML/s. Sulfur stemming from epi-ready treatment was observed within the samples. The S concentration was  $1 \times 10^{15} \text{ cm}^{-3}$ , which does not depend on  $T_{Al}$  and  $N_2$  gas flow rate. In contrast, the concentrations of C, O, and Al varied with changes in the above parameters. At  $T_{Al}$  of 1020°C shown in Figure 15(a), the concentration of Al clearly increased following the introduction of  $N_2$  gas. Furthermore, C and O also showed similar behavior. In contrast, at  $T_{Al}$  of 750°C, as shown in Figure 15(b), the dependence on  $N_2$  gas flow rate was solely observed for O and was negligible for C and Al. Oxygen concentration showed a dependence on the  $N_2$  gas flow rate but was much smaller, over one order of magnitude, than that shown in Figure 15(a). It was as low as  $2 \times 10^{16} \text{ cm}^{-3}$  even with the  $N_2$  gas flow rate of 0.12 sccm. This result indicates that a heated Al cell and Al partial pressure can enhance O incorporation into the epitaxial layer. It should be noted that they have also measured the concentration of N on the layer, not shown in Figure 15, since it was below the detection limit. These may result from the getter effect of Al, which would be effective for O, which has a strong affinity to Al, but not with inert  $N_2$  gas.

The unintentional incorporation of Al and the related phenomena can result in deterioration of the epitaxial layer due to undesirable impurity incorporation and decreased diffusion length of atoms on the growing surface, which becomes pronounced at low temperatures. We should emphasize that the above phenomena are not dependent on the plasma working conditions possibly due to the dominant  $N_2$  constituent. Thus, they arise during the entire plasma-assisted nitride growth by MBE. Accordingly, nitrides should be grown under conditions that prevent the previously described unintentional incorporation of Al by suppressing the Al partial pressure or efficient shielding of  $N_2$  gas dispersion.

### 3. Summary

GaInNAs can be grown pseudomorphically on a GaAs substrate and is a light-emitting material with a bandgap energy that corresponds to near infrared. By combining GaInNAs with GaAs, an ideal band lineup for LD application is achieved. GaInNAs is also promising as a material for use in near-infrared VCSELs because a GaInNAs active layer can be grown on a highly reflective GaAs/AlAs DBR mirror over a GaAs substrate in a single stage of epitaxial growth. GaInNAs VCSELs are currently on the market.

GaInNAs can be grown by both OMVPE and MBE. However, LDs with a long lifetime are limited to MBE-grown devices. Therefore, from the viewpoint of industry

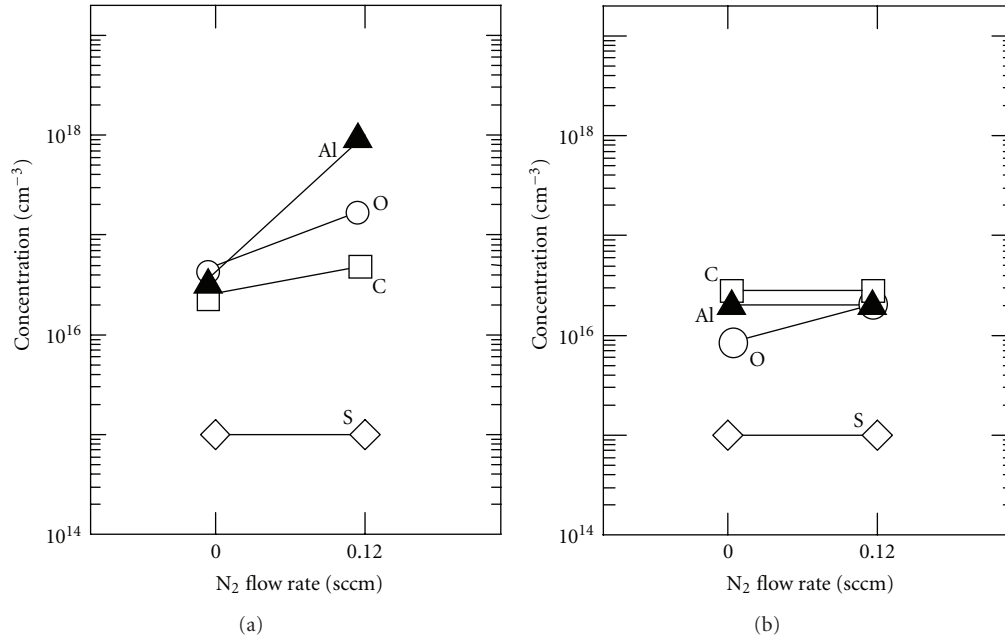


FIGURE 15: Concentrations of C, O, Al, and S obtained from SIMS measurement varying the N<sub>2</sub> gas flow rate for 0 and 0.12 sccm at different T<sub>Al</sub> of (a) 1020°C and (b) 750°C [33].

use, MBE growth is important for GaInNAs. During plasma-assisted MBE growth, Al is unintentionally incorporated into the epi-layer followed by the concomitant incorporation of O and C even though the shutter of the Al cell is closed. The origin of the unintentionally incorporated Al is the Al beam sublimated from the Al source but not Al remaining on the chamber wall, cell wall, or backside of the shutter. A gas-phase-scattering model can explain these phenomena, suggesting that a large amount of N<sub>2</sub> gas causes the scattering of Al beam sublimated from the Al source with occasional collisions resulting in the Al atoms being directed toward the substrate. Hence, the reduction of the sublimated Al beam during the growth period can suppress the incorporation of unintentional impurities, resulting in a highly pure epitaxial layer. Thus, we can reproduce the growth of high-quality GaInNAs simply by setting the temperature of the Al cell at the common idling temperature of 750°C, even though the MBE chamber has an Al cell and epilayers containing Al have been grown inside.

The above phenomena are not dependent on the plasma working conditions, possibly due to the dominant N<sub>2</sub> constituent. Thus, they arise during the entire plasma-assisted nitride growth by MBE. Accordingly, nitrides should be grown under conditions that prevent the above-described unintentional incorporation of Al by suppressing the Al partial pressure or efficient shielding of N<sub>2</sub> gas dispersion.

## References

- [1] M. Kondow, K. Uomi, A. Niwa, T. Kitatani, S. Watahiki, and Y. Yazawa, "A novel material of GaInNAs for long-wavelength-range laser diodes with excellent high-temperature performance," in *Proceedings of the International Conference on Solid State Devices and Materials*, Osaka, Japan, 1995.
- [2] M. Kondow, K. Uomi, A. Niwa, T. Kitatani, S. Watahiki, and Y. Yazawa, "GaInNAs: a novel material for long-wavelength-range laser diodes with excellent high-temperature performance," *Japanese Journal of Applied Physics 1*, vol. 35, no. 2, pp. 1273–1275, 1996.
- [3] J. N. Baillargeon, K. Y. Cheng, G. E. Hofler, P. J. Pearch, and C. Heigh, "Luminescence quenching and the formation of the GaP<sub>1-x</sub>N<sub>x</sub> alloy in GaP with increasing nitrogen content," *Applied Physics Letters*, vol. 60, article 2540, 3 pages, 1992.
- [4] O. Igarashi, "Heteroepitaxial growth of GaP<sub>1-x</sub>N<sub>x</sub> ( $x \lesssim 0.09$ ) on sapphire substrates," *Japanese Journal of Applied Physics*, vol. 31, article 3791, 1992.
- [5] S. Miyoshi, H. Yaguchi, K. Onabe, R. Ito, and Y. Shiraki, "Metalorganic vapor phase epitaxy of GaP<sub>1-x</sub>N<sub>x</sub> alloys on GaP," *Applied Physics Letters*, vol. 63, no. 25, pp. 3506–3508, 1993.
- [6] M. Sato and M. Weyers, "GaAsN alloys: growth and optical properties," in *Proceedings of the 19th International Symposium on GaAs and Related Compound Semiconductors*, vol. 129 of *Institute of Physics Conference*, pp. 555–560, Bristol and Philadelphia: Institute of Physics, Karuizawa, Japan, 1992.
- [7] M. Kondow, K. Uomi, K. Hosomi, and T. Mozume, "Gas-source molecular beam epitaxy of GaN<sub>x</sub>As<sub>1-x</sub> using a N radical as the N source," *Japanese Journal of Applied Physics 2*, vol. 33, no. 8, pp. L1056–L1058, 1994.
- [8] S. Sato, "Room temperature operation of InGaNAs/InGaP DH lasers grown by MOCVD," in *Proceedings of the 57th Autumn Meeting Japan Society of Applied Physics*, p. 951, Fukuoka, Japan, 1996.
- [9] M. Kondow, T. Kitatani, M. C. Larson, K. Nakahara, K. Uomi, and H. Inoue, "Gas-source MBE of GaInNAs for long-wavelength laser diodes," *Journal of Crystal Growth*, vol. 188, no. 1–4, pp. 255–259, 1998.
- [10] S. Sakai, Y. Ueta, and Y. Terauchi, "Band gap energy and band lineup of III-V alloy semiconductors incorporating nitrogen

- and boron," *Japanese Journal of Applied Physics 1*, vol. 32, no. 10, pp. 4413–4417, 1993.
- [11] J. C. Phillips, *Bonds and Bands in Semiconductors*, Academic Press, New York, NY, USA, 1973.
- [12] T. Kitatani, M. Kondow, T. Klkawa, Y. Yazawa, M. Okai, and K. Uomi, "Analysis of band offset in GaNAs/GaAs by x-ray photoelectron spectroscopy," *Japanese Journal of Applied Physics 1*, vol. 38, no. 9, pp. 5003–5006, 1999.
- [13] S. A. Ding, S. R. Barman, K. Horn et al., "Valence band discontinuity at a cubic GaN/GaAs heterojunction measured by synchrotron-radiation photoemission spectroscopy," *Applied Physics Letters*, vol. 70, no. 18, pp. 2407–2409, 1997.
- [14] S. Sakai and T. Abe, "Band lineup of nitride-alloy heterostructures," in *Proceedings of the 41st Spring Meeting of the Japan Society of Applied Physics*, p. 186, Tokyo, Japan, 1994.
- [15] M. Kondow, S. Fujisaki, S. Shirakata, T. Ikari, and T. Kitatani, "Electron effective mass of  $\text{Ga}_{0.7}\text{In}_{0.3}\text{N}_x\text{As}_{1-x}$ ," in *Proceedings of the 30th International Symposium on Compound Semiconductors*, MB 3.8, San Diego, Calif, USA, 2003.
- [16] C. Skierbiszewski, P. Perlin, P. Wisniewski et al., "Effect of nitrogen-induced modification of the conduction band structure on electron transport in GaAsN alloys," *Physica Status Solidi B*, vol. 216, no. 1, pp. 135–139, 1999.
- [17] Z. Pan, L. H. Li, Y. W. Lin, B. Q. Sun, D. S. Jiang, and W. K. Ge, "Conduction band offset and electron effective mass in GaInNAs/GaAs quantum-well structures with low nitrogen concentration," *Applied Physics Letters*, vol. 78, no. 15, pp. 2217–2219, 2001.
- [18] M. Hetterich, M. D. Dawson, A. Y. Egorov, D. Bernklau, and H. Riechert, "Electronic states and band alignment in GaInNAs/GaAs quantum-well structures with low nitrogen content," *Applied Physics Letters*, vol. 76, no. 8, pp. 1030–1032, 2000.
- [19] M. C. Larson, M. Kondow, T. Kitatani et al., "GaInNAs-GaAs long-wavelength vertical-cavity surface-emitting laser diodes," *IEEE Photonics Technology Letters*, vol. 10, no. 2, pp. 188–190, 1998.
- [20] M. Kondow, T. Kitatani, K. Nakahara, and T. Tanaka, "A 1.3- $\mu\text{m}$  GaInNAs laser diode with a lifetime of over 1000 hours," *Japanese Journal of Applied Physics 2*, vol. 38, no. 12, pp. L1355–L1356, 1999.
- [21] J. Jewell, L. Graham, M. Crom et al., "Commercial GaInNAs VCSELs grown by MBE," *Physica Status Solidi C*, vol. 5, no. 9, pp. 2951–2956, 2008.
- [22] I. Buyanova and W. Chen, *Physics and Applications of Dilute Nitrides*, Taylor & Francis, New York, NY, USA, 2004.
- [23] N. Tansu, J. Y. Yeh, and L. J. Mawst, "Low-threshold 1317-nm InGaAsN quantum-well lasers with GaAsN barriers," *Applied Physics Letters*, vol. 83, no. 13, pp. 2512–2514, 2003.
- [24] S. M. Wang, Y. Q. Wei, X. D. Wang, Q. X. Zhao, M. Sadeghi, and A. Larsson, "Very low threshold current density 1.3  $\mu\text{m}$  GaInNAs single-quantum well lasers grown by molecular beam epitaxy," *Journal of Crystal Growth*, vol. 278, no. 1–4, pp. 734–738, 2005.
- [25] R. Fehse, S. Jin, S. J. Sweeney et al., "Evidence for large monomolecular recombination contribution to threshold current in 1.3  $\mu\text{m}$  GaInNAs semiconductor lasers," *Electronics Letters*, vol. 37, no. 25, pp. 1518–1520, 2001.
- [26] S. Nakatsuka, M. Kondow, M. Aoki, M. Kudo, T. Kitatani, and S. Tsuji, "Amplified spontaneous emission measurement of GaInNAs laser wafers with and without rapid thermal annealing," *Japanese Journal of Applied Physics 2*, vol. 42, no. 8, pp. L1012–L1014, 2003.
- [27] T. Takeuchi, Y. L. Chang, M. Leary et al., "Al contamination in InGaAsN quantum wells grown by metalorganic chemical vapor deposition and 1.3  $\mu\text{m}$  InGaAsN vertical cavity surface emitting lasers," *Japanese Journal of Applied Physics 1*, vol. 43, no. 4, pp. 1260–1263, 2004.
- [28] T. Takahashi, M. Kaminishi, N. Jikutani, A. Itoh, and S. Sato, "Improvement of the optical property of 1 step MOCVD grown GaInNAs/GaAs MQW on AlGaAs cladding layer," in *Proceedings of the 64th Autumn Meeting of the Japan Society of Applied Physics*, 1p-K-18, Fukuoka, Japan, 2003.
- [29] P. Sundgren, C. Asplund, K. Baskar, and M. Hammar, "Morphological instability of GaInNAs quantum wells on Al-containing layers grown by metalorganic vapor-phase epitaxy," *Applied Physics Letters*, vol. 82, no. 15, pp. 2431–2433, 2003.
- [30] M. Kondow, M. Kudo, S. Tanaka, S. Fujisaki, and K. Nakahara, "Residual impurities in MBE-grown GaInNAs laser diodes," in *Proceedings of the 13th International Conference on Molecular Beam Epitaxy*, TuC2.5, Edinburgh, UK, 2004.
- [31] T. Kitatani, M. Kondow, and T. Tanaka, "Molecular beam epitaxy of GaInNAs by using solid source arsenic," *Journal of Crystal Growth*, vol. 227–228, pp. 521–526, 2001.
- [32] F. Ishikawa, S. D. Wu, M. Kato, M. Uchiyama, K. Higashi, and M. Kondow, "Unintentional aluminum incorporation related to the introduction of nitrogen gas during the plasma-assisted molecular beam epitaxy," *Journal of Crystal Growth*, vol. 311, no. 7, pp. 1646–1649, 2009.
- [33] F. Ishikawa, S. Wu, M. Kato, M. Uchiyama, K. Higashi, and M. Kondow, "Unintentional source incorporation in plasma-assisted molecular beam epitaxy," *Japanese Journal of Applied Physics*, vol. 48, no. 12, Article ID 125501, 2009.
- [34] J. Schmitz, J. Wagner, M. Maier, H. Obloh, P. Koidl, and J. D. Ralston, "Unintentional As incorporation in molecular beam epitaxially grown InAs/AlSb/GaSb heterostructures," *Journal of Electronic Materials*, vol. 23, no. 11, pp. 1203–1207, 1994.
- [35] C. E. C. Wood, T. M. Kerr, T. D. McLean et al., "State-of-the-art AlGaAs alloys by antimony doping," *Journal of Applied Physics*, vol. 60, no. 4, pp. 1300–1305, 1986.
- [36] K. Adachi, K. Nakahara, J. Kasai et al., "Low-threshold GaInNAs single-quantum-well lasers with emission wavelength over 1.3  $\mu\text{m}$ ," *Electronics Letters*, vol. 42, no. 23, pp. 1354–1355, 2006.
- [37] S. R. Bank, H. Bae, L. L. Goddard et al., "Recent progress on 1.55- $\mu\text{m}$  dilute-nitride lasers," *IEEE Journal of Quantum Electronics*, vol. 43, no. 9, pp. 773–785, 2007.
- [38] M. A. Wistey, S. R. Bank, H. B. Yuen, L. L. Goddard, and J. S. Harris, "GaInNAs(Sb) vertical-cavity surface-emitting lasers at 1.460  $\mu\text{m}$ ," *Journal of Vacuum Science and Technology B*, vol. 22, no. 3, pp. 1562–1564, 2004.

## Research Article

# Monitoring Composites under Bending Tests with Infrared Thermography

Carosena Meola,<sup>1</sup> Giovanni Maria Carlomagno,<sup>2</sup>  
Carmela Bonavolontà,<sup>3</sup> and Massimo Valentino<sup>3</sup>

<sup>1</sup>Department of Aerospace Engineering (DIAS), University of Naples Federico II, Via Claudio 21, 80125 Naples, Italy

<sup>2</sup>Department of Aerospace Engineering (DIAS), University of Naples Federico II, Piazzale Tecchio 80, 80125 Naples, Italy

<sup>3</sup>CNR-SPIN, Piazzale Tecchio 80, 80125 Naples, Italy

Correspondence should be addressed to Carosena Meola, carmeola@unina.it

Received 2 August 2012; Accepted 2 October 2012

Academic Editor: Antoni Rogalski

Copyright © 2012 Carosena Meola et al. This is an open access article distributed under the Creative Commons Attribution License, which permits unrestricted use, distribution, and reproduction in any medium, provided the original work is properly cited.

The attention of the present paper is focused on the use of an infrared imaging device to monitor the thermal response of composite materials under cyclic bending. Three types of composites are considered including an epoxy matrix reinforced with either carbon fibres (CFRP) or glass fibres (GFRP) and a hybrid composite involving glass fibres and aluminium layers (FRML). The specimen surface, under bending, displays temperature variations pursuing the load variations with cooling down under tension and warming up under compression; such temperature variations are in agreement with the bending moment. It has been observed that the amplitude of temperature variations over the specimen surface depends on the material characteristics. In particular, the presence of a defect inside the material affects the temperature distribution with deviation from the usual bending moment trend.

## 1. Introduction

Infrared thermography (IRT) has proved helpfulness in many industrial and research fields as stated by the proceedings of the four main international symposia [1–4]. Amongst its many applications, an infrared imaging device is helpful for thermoelastic stress analysis (TSA) purposes [5, 6] and to monitor the surface temperature change (thermoelastic effect) which is experienced by a body when subjected to stress variations under load [7].

The thermoelastic effect was first conceived by Lord Kelvin (Thomson) in 1978 [8]. Many years later, in 1956 [9], Biot performed a thermodynamic analysis and formulated the classical thermoelastic equation, which expresses the change in temperature ( $T$ ) of a solid in terms of the change in the sum of the principal stresses ( $\sigma$ ). The temperature variation, under reversible and adiabatic conditions (i.e., in the elastic regime and neglecting heat transfer within the

body and to the environment), for isotropic materials can be written as

$$\Delta T = -KT_a \Delta\sigma, \quad (1)$$

where  $T_a$  is the absolute body temperature,  $\Delta\sigma$  is the mean stress amplitude, and  $K$  is the material thermoelastic constant. Equation (1) relates the temperature local variations to the stress variations. In particular, under adiabatic conditions, positive dilatation (tension) entails cooling of the material and vice versa. In metals, the thermoelastic limit is generally assumed [10] as an indication for the yielding point. In orthotropic materials as fibre-reinforced polymers (FRP) (1) is modified as

$$\Delta T = -\frac{T_a}{\rho c_p} (\alpha_1 \Delta\sigma_1 + \alpha_2 \Delta\sigma_2) \quad (2)$$

with  $\alpha_1$  and  $\alpha_2$  being the thermal expansion coefficients along the principal material directions and  $\rho c_p$  the mean

volumetric heat capacity. For complex composite materials a direct relationship between the mean stress and TSA data is not possible [5]; however, in any case, the availability of the temperature map is important for materials characterization [11–16]. Thus, IRT represents a valuable mean for rapid determination of the fatigue limit (Risitano method) [11] and for damage evolution assessment.

It is worth nothing that within the fatigue concept IRT has been till now mainly used for TSA purposes associated with cyclic tension-compression tests [5, 6, 11–15]. Owing to bending tests, Luong [13] reports on the use of infrared thermography for detecting the onset of intrinsic dissipation, or damage indicator, owing to the thermo-mechanical coupling. The adopted procedure was to acquire a thermal image after a fixed number of cycles. In all these cases the analysis was driven towards the thermoplastic phase in which the temperature variation is significant and then easy to be measured [17]. A more difficult point is to deal with measurements of temperature variations experienced by the material during the elastic phase, that is, thermoelastic effects. Recently, Meola and Carlomagno tackled with such difficult endeavour; in particular, by choosing an appropriate image sampling rate, they succeeded in appraising the material temperature variations, which are due to both thermoelastic and thermoplastic effects, under low-energy impact [7, 18]. In particular, Meola and Carlomagno [18] supplied, through measurements of temperature rising and warm area extension, information about initiation and propagation of the impact damage in glass/epoxy materials.

As a next step in the analysis of thermoelastic effects, the thermal behaviour of composite materials under cyclic bending is addressed in this paper. Under cyclic bending the material undertakes tension and/or compression with cooling/warming effects involved. The main question, which arises, regards the possibility to acquire information on the material characteristics by simply monitoring the thermoelastic effects. Another question is if, which, and how material properties interfere with thermoelastic effects. And then, the attention of this work is focused on the use of an infrared imaging device for monitoring the thermal response of different types of composites during cyclic bending tests.

## 2. Experimental Analysis

The investigation is carried out in laboratory considering several different specimens made of different composite materials [17]. Specimens are subjected to bending tests with two different configurations, which are later described, and are also nondestructively inspected with lock-in thermography.

## 3. Materials

Several specimens are fabricated of three different types of composites owing to the composition (i.e., fibre and matrix).

- (i) GFRP includes E glass fibres embedded in a low viscosity epoxy matrix. More specifically, this type of specimen is obtained by hand layup of eight

epoxy adhesive prepregged unidirectional glass fibres and allowed to cure at ambient temperature. The stacking sequence is  $[0_2, 90_4]_s$  with an overall specimen thickness  $s = 2.9$  mm. Specimens are 30 mm wide and 134 mm long.

- (ii) GI specimens came from a type of FRML including 3 Al with 2 GFRP layers in between them; the overall thickness is  $s = 1.5$  mm. This material is fabricated following industrial standards with curing in autoclave. Specimens are 30 mm wide and 148 mm long. In particular, one specimen, called GI1, presents the outside surface covered with an aeronautical coating. In another one, called GI2, the external aluminium layer was removed (through milling) from the side viewed by the infrared camera. And thus, the surface viewed by the infrared camera is practically that of a GFRP with the difference that there is no epoxy resin finishing.
- (iii) CFRP is based on an epoxy-matrix (HFM 934) reinforced with T400 carbon fibres content of 55% by volume, fabricated by hand layup and autoclave curing. The stacking sequence is  $[(0/90), \pm 45]_s$ , with an overall specimen thickness  $s = 2.0$  mm. Specimens are 20 mm wide and 196 mm long.

### 3.1. Setup for Bending Tests

#### 3.1.1. Bending Tests Are Performed with Two Configurations

*Conf I.* The specimen is fixed at the extreme A and is in contact with a punch in point C as sketched in Figure 1. Bending arises under the action of the force  $F$  that is applied cyclically at the extreme B and is directed downside. The infrared camera is positioned to see the surface on the top.

*Conf II.* The specimen is fixed at the extreme A as in *Conf I* with the exception that the punch is removed and then the configuration is that of a cantilever beam. In this case, tests are performed with the force acting cyclically in the direction upside-rest, down-rest, and upside-downside (downside-upside). For each type of test both surfaces (top and bottom) are monitored with the infrared camera. In particular, the bottom surface is viewed with the aid of a mirror placed at  $45^\circ$  underneath the specimen.

For both configurations the load is applied manually with care paid to assure adiabatic conditions. The amplitude is set with the aid of fixed supports, while the bending frequency is calculated as number of cycles in a given time measured by a chronometer.

Two infrared cameras are used, which are the SC3000 and the SC6000 (Flir Systems) both equipped with a QWIP detector working in the  $8\text{--}9\ \mu\text{m}$  infrared band. The standard acquisition rate for the SC3000 is 60 Hz full frame  $320 \times 240$  pixels, but it can reach up 900 Hz with a reduced field of view of 16 lines. Conversely, the SC6000 offers a better thermal sensitivity and spatial resolution with  $640 \times 512$  pixels full frame and a windowing option linked to frequency frame rate and temperature range.

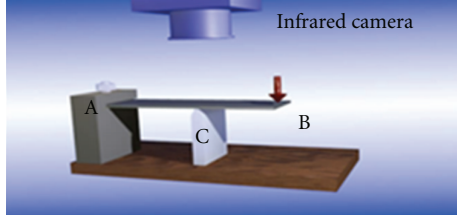
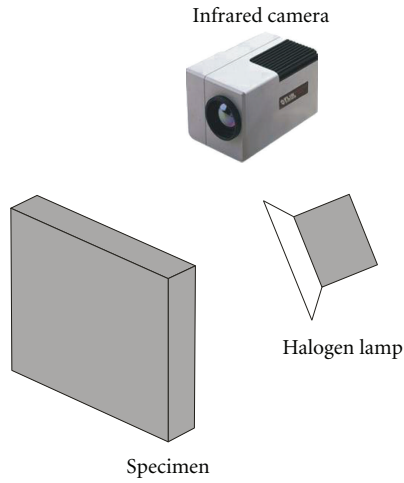

 FIGURE 1: Sketch of the *Conf I* test setup.


FIGURE 2: Setup for tests with lock-in thermography.

3.2. *Setup for Nondestructive Inspection.* Nondestructive tests are carried out with the SC3000 camera coupled with the Lock-in option and the IRLockIn software [19]. Thermal stimulation is performed with a halogen lamp; a sketch is shown in Figure 2; the heating frequency  $f$  is varied to inspect the material at different layers through the thickness according to the relationship:

$$\mu = \sqrt{\frac{\alpha}{\pi f}} \quad (3)$$

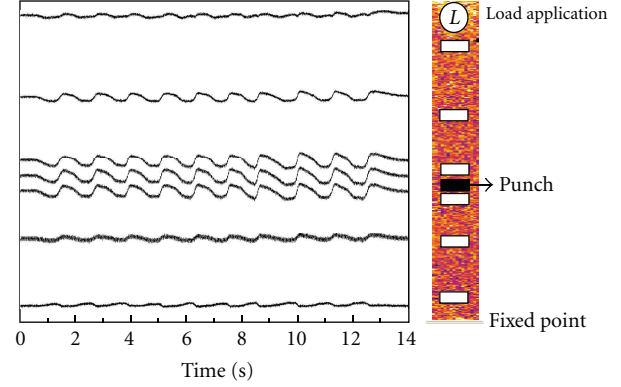
with  $\mu$  the thermal diffusion length,  $\alpha$  the thermal diffusivity, and  $f$  the heating frequency. Results are shown as phase images.

## 4. Bending Tests

Thermal images are taken in time sequence starting before loading application and ending after force removal to account for thermal phenomena with respect to the ambient temperature. The first image ( $t = 0$ ) of the sequence (i.e., the ambient temperature of the specimen surface before load) is subtracted to each subsequent image so as to have a map of temperature difference  $\Delta T$ :

$$\Delta T = T(i, j, t) - T(i, j, 0) \quad (4)$$

$i$  and  $j$  representing lines and columns of the surface temperature map. Therefore, a sequence of  $\Delta T$  images is created.


 FIGURE 3:  $\Delta T$  variation versus time in several areas located on the left and on the right of the punch under cyclic load for the G11 specimen.

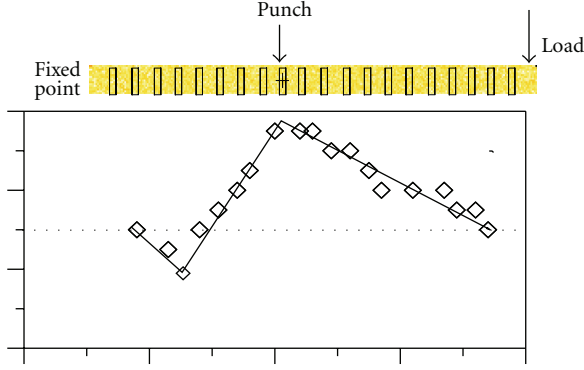
4.1. *Tests with Conf I.* First, tests are carried out by monitoring, with the SC3000 camera, the top surface of the specimen while subjected to three points bending, which means employing the *Conf I* arrangement (Figure 1). In this case, thermal images are acquired in time sequence at 900 Hz; in general, each test involves ten cycles and so sequences of over 20 k images are obtained.

As an example, in Figure 3 are shown  $\Delta T$  values against time at different positions over the G11 specimen under bending with *Conf I*. The specimen is undergoing a deflection of 10 mm at a frequency of about 0.85 Hz. In particular, each  $\Delta T$  value is obtained by averaging the values inside a given area, which may be located on the left and on the right with respect to the punch position. More specifically, the position of each area (white rectangle) over the thermal image is shown on the right side in Figure 3; this image appears rotated by 90° counterclockwise with respect to the test setup (Figure 1).  $\Delta T$  displays quasi-sinusoidal variations, which are perfectly coupled to the cyclic load.

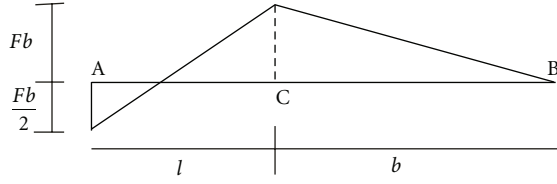
Next, the temperature amplitude variation strongly depends on the position of the area over the specimen surface that is, on the area relative position with respect to its distance from the punch; this is in good agreement with the bending moment diagram. This feature is shown in Figure 4. In more details, in Figure 4(a) the  $\Delta T$  variation moving left and right with respect to the punch position (*Conf I*) are reported. Such a distribution is similar for every specimen; of course, quantitative values depend on the specimen material (for this reason no scale is added). In Figure 4(b) the diagram of the bending moment is shown; this comes out from the theory of elasticity.

With reference to Figure 4(b), the maximum bending momentum  $M_{b_{\max}}$  is equal to the load (or force)  $F$  multiplied the distance  $b$ :

$$M_{b_{\max}} = Fb \quad (5)$$



(a) Temperature amplitude distribution over the specimen surface under load



(b) Bending moment diagram

FIGURE 4: Comparison between temperature amplitude distribution (a) and bending moment diagram (b).

while the deflection of point B  $D_F$  is linked to the load  $F$ , the distances  $b$  and  $l$ , the area moment of inertia of the cross-section  $I$ , the specimen thickness  $s$ , the Young modulus  $E$ , and the stress  $\sigma$  through the following relationship:

$$D_F = \frac{Fb^2}{EI} \left( \frac{b}{3} + \frac{l}{4} \right) = \frac{2\sigma b}{Es} \left( \frac{b}{3} + \frac{l}{4} \right). \quad (6)$$

Considering (1) it is possible to write the relationship:

$$D_F Es = k\sigma = k' \Delta T \quad (7)$$

and then

$$\Delta T \propto D_F Es. \quad (8)$$

Of course, as already specified, (1) generally applies for isotropic materials, while, for composites, it takes a more complex form (2) involving components along fibres direction. However, stress analysis is outside the aim of the present paper, which is mainly focused on the possibility to assess the material integrity through the analysis of thermoelastic effects.

The average maximum  $\Delta T$  values in the area over the punch (as indicated in Figure 4(a)) are compared in Figure 5 for the different types of specimens. As can be seen, the highest value is achieved for the Glare<sup>(R)</sup> specimen GL1, while the value displayed by the GL2 is slightly higher than the values obtained with both CFRP and GFRP. This because the  $\Delta T$  amplitude depends on the material's thermal conductivity. Of course, the thermal conductivity of a composite material depends on both the matrix and the reinforce as well the stacking sequence. Within the present

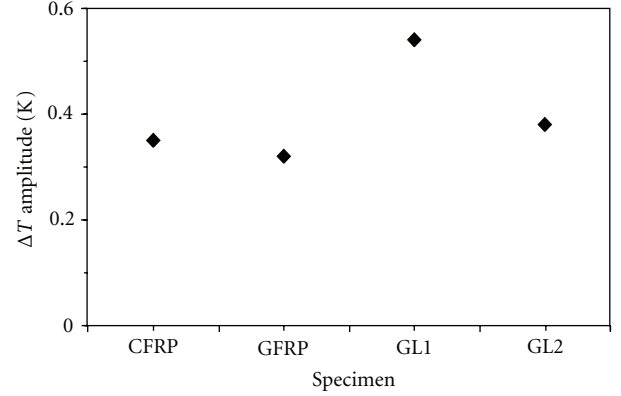


FIGURE 5: Maximum  $\Delta T$  amplitude versus specimen type.

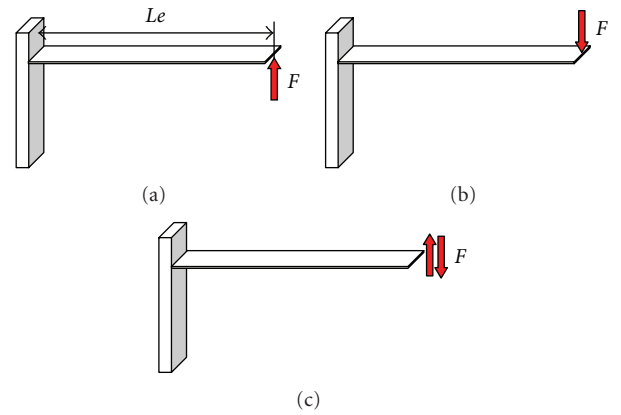


FIGURE 6: Sketch of the load application modes for tests with *Conf II*.

context, the main role is surely played by the outside layer, which is also affected by the presence of any coating. It has to be taken into account that the outside surface of any composite material is composed of a thin layer of epoxy resin, which, generally, acts as surface finishing, and that the thermal conductivity of the epoxy resin is lower than that of the carbon and the glass fibres. Thus, the distribution of  $\Delta T$  values in Figure 5 is justified.

4.2. *Tests with Conf II*. These tests are performed by applying the load  $F$  in different ways as schematically depicted in Figure 6:

- (i) from the bottom side directed upside (Figure 6(a)),
- (ii) from the top side directed downside (Figure 6(b)),
- (iii) for complete cycles upside-downside (Figure 6(c)) or downside-upside.

For each of the different load application modes, both of the specimen surfaces (top and bottom) are monitored with the SC6000 by acquiring sequences of images at 85 Hz during load application. The sequences of images are then transformed into sequences of  $\Delta T$  images according to (4).

For a general comparison between data obtained with the two test configurations, the thermal response of the

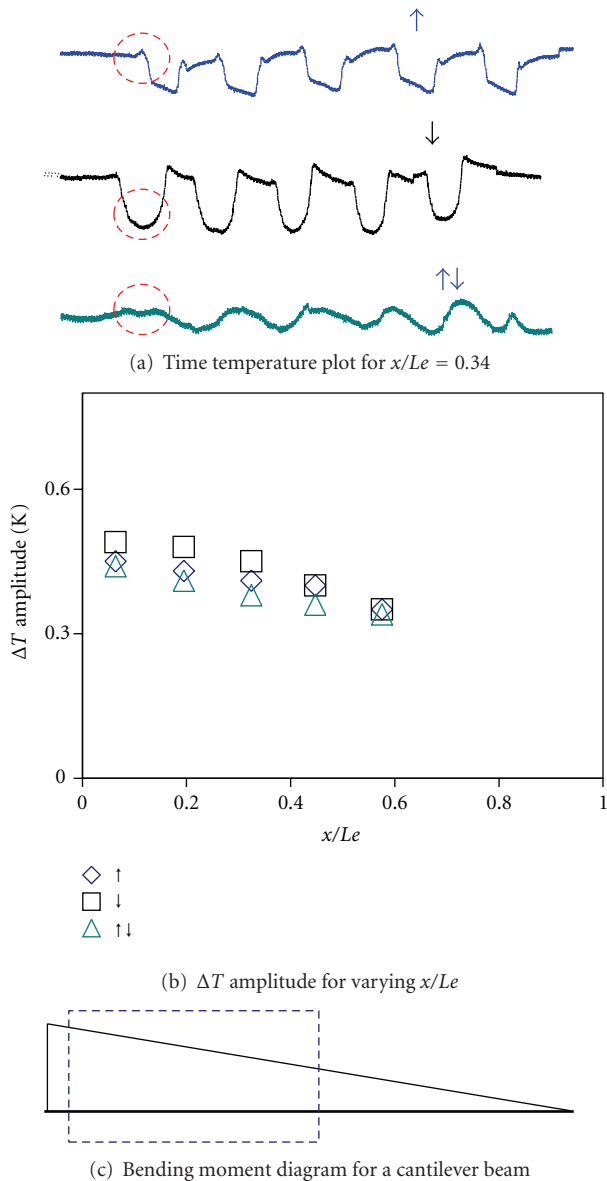


FIGURE 7: Behaviour of the GL1 specimen by varying the load direction.

GL1 specimen is analyzed and compared with the bending moment in Figure 7. First, the  $\Delta T$  value is extracted as average in a small area located at 34% from the fixture on the top surface and plotted for different load conditions in Figure 7(a);  $Le$  is the cantilever length (Figure 6(a)). Then,  $\Delta T$  values obtained at different distances  $x$  along the length  $Le$  are plotted in Figure 7(b), while the bending moment is shown in Figure 7(c). For a direct comparison between the  $\Delta T$  distribution and the bending moment, the area considered for thermal analysis is enveloped with the dashed rectangle.

Looking at Figure 7 two main considerations arise

- (1) As already observed for data obtained with *Conf I* (Figure 4), the distribution of the  $\Delta T$  amplitude is

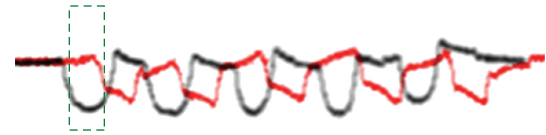


FIGURE 8: Variation of the temperature response for varying the load direction (red line upside as in Figure 6(a) and dark line downside as in Figure 6(b)).

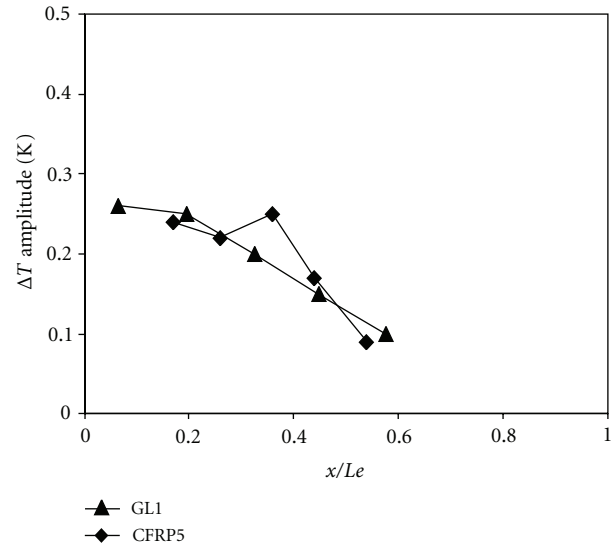


FIGURE 9:  $\Delta T$  distribution on the bottom surface (under tension) of GL1 and CFRP5 specimens with increasing  $x/Le$ .

again in good agreement with the bending moment diagram.

- (2) The temperature variation is in perfect concurrence with the load direction. In fact, following the red circle, the temperature increases, or decreases, depending on the surface being, respectively, under compression or under tension.

The latter aspect is better depicted in Figure 8 in which two  $\Delta T$  profiles taken in the same area (same  $x/Le$  ratio), which is one time in compression (red line) and the other one in tension (dark line), are compared. More specifically, it is possible to see (by looking inside the dashed rectangle) the prompt inversion (rise/decrease) in the temperature distribution by changing load direction. However, it is also possible to see the higher amplitude with also a more regular trend displayed during cooling down with respect to that occurring during the warming up phase.

To gain information about the material behaviour under bending, maximum  $\Delta T$  values, which were taken on the surface, being in tension, of two specimens GL1 and CFRP5, are plotted against the  $x/Le$  ratio in Figure 9.

As a general comment, for both specimens,  $\Delta T$  decreases with increasing the distance from the fixture; this is in agreement with the bending moment (Figure 7(c)). However, what catches eyes is the peak at about 37% of  $Le$  for the CFRP5 specimen. This may appear strange at first sight, but

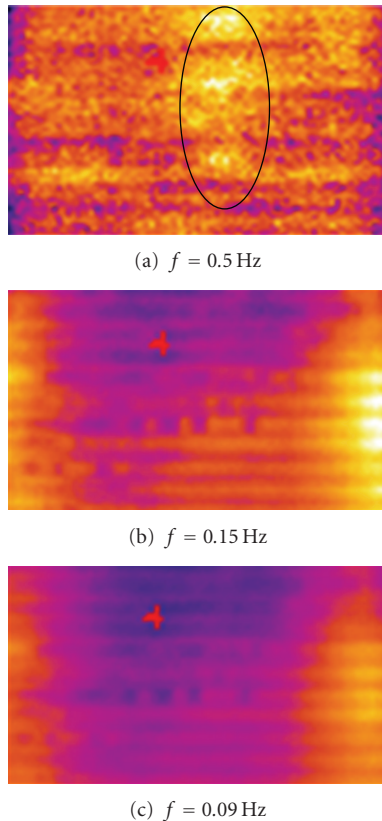


FIGURE 10: Phase images, taken at different heating frequency, for the specimen CFRP5.

it is easily explicable looking at the phase images, shown in Figure 10, which were obtained through nondestructive inspection with lock-in thermography (Figure 2). In fact, it is clear that the peak is caused by the anomaly (encircled in Figure 10(a)), which is present at low depth the viewed from one side of the specimen. Such anomaly tends to disappear going more in depth by decreasing the heating frequency  $f$  to 0.15 Hz (Figure 10(b)) and to 0.09 Hz (Figure 10(c)). There are some variations of the phase angle on the right edge (Figures 10(b) and 10(c)), but they have no effects on the  $\Delta T$  distribution in Figure 9 since they are located in the part in which the specimen is clamped during bending tests and so not enclosed in the  $\Delta T$  distribution. It is worth noting that, in Figure 10, the specimen appears rotated by  $180^\circ$  with respect to the position it had during bending tests (Figures 6–9); practically, in Figure 10,  $x/Le$  increases moving from right to left.

To better investigate the influence the buried anomaly has on the specimen thermoelastic behaviour under bending load, the  $\Delta T$  distributions on both top and bottom surfaces, being one under compression and the other one under tension, are compared in Figure 11. It is possible to see that the anomaly, which is present on the bottom side, affects the temperature amplitude distribution. In fact, on the top side, the  $\Delta T$  distribution attains higher values towards the fixture decreasing with increasing  $Le$  in good compliance with the bending moment (Figure 7(c)). Instead the  $\Delta T$

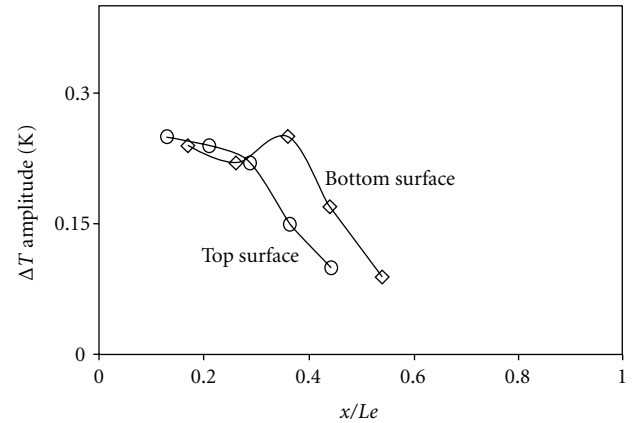


FIGURE 11: Comparison between  $\Delta T$  distribution on top (under compression) and bottom (under tension) surfaces of the specimen CFRP5.

amplitude distribution on the bottom side presents the already mentioned peak at 37% of  $Le$  which corresponds to the position of the anomaly (Figure 10(a)). This means that the presence of a defect does not allow the material to freely expand/contract under tension/compression, but increases the local material resistance to the deformation. This feature manifests itself through a subsequent local thermal signature. Therefore, monitoring the thermal response of the material to a bending force may supply two types of information:

- (i) material mechanical characterization through the link between the temperature variation and the stress amplitude (1) or (2),
- (ii) detection of buried defects.

## 5. Conclusions

The thermal response to cyclic bending of different types of specimens was analyzed with infrared thermography. Two different bending configurations were considered, with the specimen either hanged as a cantilever beam, or with a punch as central support. For both configurations, the load was manually applied with care paid to assure adiabatic conditions. As a main finding, for all test conditions and for all the specimens, the temperature variations follow the bending moment trend. Deviation from such a trend was observed which, in our opinion, is due to the presence of anomalies in the specimen material. This was ascertained through nondestructive evaluation of specimens with lock-in thermography.

The added value of this work resides in the possibility to gain, in a fast and easy way, through the use of a simple hand-handled mechanism and an infrared imaging device, information on the material thermal characteristics. This feature may be very important for the nondestructive evaluation of composite materials considering the even broad production of such materials and the need for their fast and reliable characterization.

It has to be, however, pointed out that the present study is only a preliminary research and new tests are under way, which include a wider variety of specimens and power-driven load application with change of parameters such as bending amplitude and frequency.

## References

- [1] Proceedings of the Annual SPIE Thermosense Conferences, Bellingham, Wash, USA, 1978.
- [2] Proceedings of the Advanced Infrared Technology & Applications (AITA), 1991.
- [3] Proceedings of the Biennial Quantitative Infrared Thermography (QIRT) Conferences, 1992.
- [4] Proceedings of the InfraMation, 2000.
- [5] J. M. Dulieu-Barton, T. R. Emery, S. Quinn, and P. R. Cunningham, "A temperature correction methodology for quantitative thermoelastic stress analysis and damage assessment," *Measurement Science and Technology*, vol. 17, no. 6, pp. 1627–1637, 2006.
- [6] U. Galietti, D. Modugno, and L. Spagnolo, "A novel signal processing method for TSA applications," *Measurement Science and Technology*, vol. 16, no. 11, pp. 2251–2260, 2005.
- [7] C. Meola and G. M. Carlomagno, "Infrared thermography of impact-driven thermal effects," *Applied Physics A*, vol. 96, no. 3, pp. 759–762, 2009.
- [8] W. Thomson, "On the thermoelastic, thermomagnetic and pyroelectric properties of matters," *Philosophical Magazine*, vol. 5, pp. 4–27, 1978.
- [9] M. A. Biot, "Thermoelasticity and irreversible thermodynamics," *Journal of Applied Physics*, vol. 27, no. 3, pp. 240–253, 1956.
- [10] M. G. Beghi, C. E. Bottani, and G. Caglioti, "Irreversible thermodynamics of metals under stress," *Res Mechanica*, vol. 19, no. 4, pp. 365–379, 1986.
- [11] G. La Rosa and A. Risitano, "Thermographic methodology for rapid determination of the fatigue limit of materials and mechanical components," *International Journal of Fatigue*, vol. 22, no. 1, pp. 65–73, 2000.
- [12] G. Fargione, A. Geraci, G. La Rosa, and A. Risitano, "Rapid determination of the fatigue curve by the thermographic method," *International Journal of Fatigue*, vol. 24, no. 1, pp. 11–19, 2002.
- [13] M. P. Luong, "Fatigue limit evaluation of metals using an infrared thermographic technique," *Mechanics of Materials*, vol. 28, no. 1–4, pp. 155–163, 1998.
- [14] P. R. Cunningham, "Thermoelastic characterisation of damage around a circular hole in a GRP component," *Key Engineering Materials*, vol. 204–205, pp. 453–463, 2001.
- [15] R. J. H. Paynter and A. G. Dutton, "The use of a second harmonic correlation to detect damage in composite structures using thermoelastic stress measurements," *Strain*, vol. 39, no. 2, pp. 73–78, 2003.
- [16] Ö. S. Şahin, M. Selek, and Ş. Kahramanlı, "Investigation of bending fatigue of composite plates by using infrared thermography," *Advanced Materials Research*, vol. 268–270, pp. 406–411, 2011.
- [17] C. Bonavolontà, M. Valentino, C. Meola, and G. M. Carlomagno, "NDT of polymer nanocomposite for structural applications using electromagnetic techniques," *International Journal of Applied Electromagnetics and Mechanics*, vol. 39, no. 1–4, pp. 363–368, 2012.
- [18] C. Meola and G. M. Carlomagno, "Impact damage in GFRP: new insights with infrared thermography," *Composites A*, vol. 41, no. 12, pp. 1839–1847, 2010.
- [19] C. Meola and G. M. Carlomagno, "Infrared thermography in non-destructive inspection: theory and practice," in *Recent Advances in Non Destructive Inspection*, C. Meola, Ed., pp. 89–123, Nova Science, New York, NY, USA, 2010.

## Research Article

# Chemical Warfare Agents Analyzer Based on Low Cost, Room Temperature, and Infrared Microbolometer Smart Sensors

**Carlo Corsi, Andrea Dundee, Paolo Laurenzi, Nicola Liberatore, Domenico Luciani, Sandro Mengali, Angelo Mercuri, Andrea Pifferi, Mirko Simeoni, Gaetano Tosone, Roberto Viola, and Donatella Zintu**

*Centro Ricerche Elettro Ottiche, SS.17 Località Boschetto, 67100 L'Aquila, Italy*

Correspondence should be addressed to Sandro Mengali, sandro.mengali@consorziocreo.it

Received 2 August 2012; Revised 26 September 2012; Accepted 26 September 2012

Academic Editor: Antoni Rogalski

Copyright © 2012 Carlo Corsi et al. This is an open access article distributed under the Creative Commons Attribution License, which permits unrestricted use, distribution, and reproduction in any medium, provided the original work is properly cited.

Advanced IR emitters and sensors are under development for high detection probability, low false alarm rate, and identification capability of toxic gases. One of the most reliable techniques to identify the gas species is absorption spectroscopy, especially in the medium infrared spectral range, where most of existing toxic compounds exhibit their strongest rotovibrational absorption bands. Following the results obtained from simulations and analysis of expected absorption spectra, a compact nondispersive infrared multispectral system has been designed and developed for security applications. It utilizes a few square millimeters thermal source, a novel design multipass cell, and a smart architecture microbolometric sensor array coupled to a linear variable spectral filter to perform toxic gases detection and identification. This is done by means of differential absorption spectroscopic measurements in the spectral range of the midinfrared. Experimental tests for sensitivity and selectivity have been done with various chemical agents (CAs) gases and a multiplicity of vapour organic compounds (VOCs). Detection capability down to ppm has been demonstrated.

## 1. Introduction

One of the most reliable techniques to identify the gas species is absorption spectroscopy in the medium infrared spectral range, where most of existing toxic compounds exhibit their strongest rotovibrational absorption bands [1, 2].

The present work will describe a compact point sensor for providing early warning in the presence of CAs in the air. Battlefields and urban areas at risk of terroristic attack were the foreseen application scenarios. Wide chemical range and effective identification of targets and rejection of other vapours were given as the key performance objectives.

The sensor is based on Active Multispectral Infrared Absorption Spectroscopy in the gas phase and uses 38 spectral channels to represent molecular fingerprints across the LongWave IR spectrum (LWIR).

The heart of the sensor is an advanced detector device that integrates microbolometers, optical filter arrays, and front-end electronics on silicon chip.

## 2. Sensor System

The sensor system essentially consists of an IR thermal source, a multipass optical cell, and an array of detectors and filters, plus electronics and software for signal read-out, processing and analysis. Figure 1 shows a scheme of the sensor system. A description of the early design of the sensor system has been reported in [3].

The IR radiation emitted by the source is first modulated by a mechanical oscillator (to achieve improved S/N by means of lock-in detection), then passed through the cell, (where it is attenuated by gas molecules at their IR resonant wavelengths), and, finally, focused onto the detector array (Figure 2). As the optical cell is in open air, the composition of the air in the sensor is the same as in the space around the sensor.

The thermal source is a commercial device made by a set of high emissivity thick-film filaments that can be heated up to around 1000 K. Source modulation is provided by a taut band oscillator. Its working frequency (7 Hz) was selected to

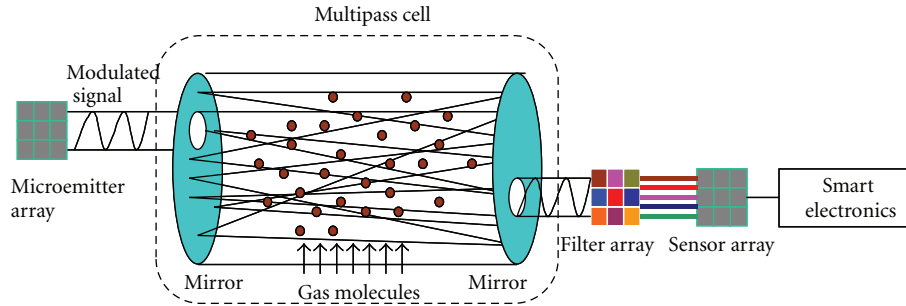


FIGURE 1: Scheme of the sensor system.

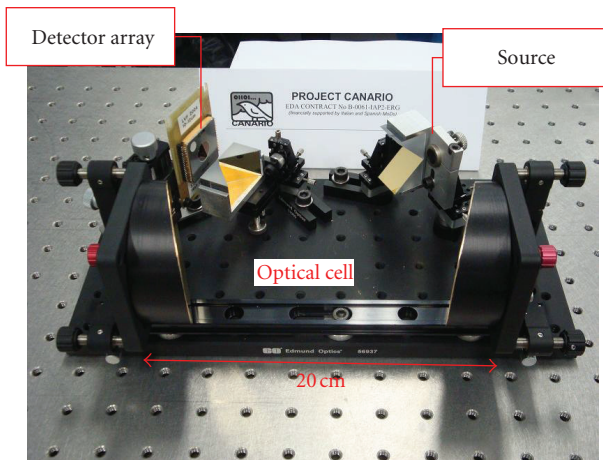


FIGURE 2: Optical cell.

match with the response time of the microbolometers. The optical cell [4] has been specifically designed to achieve high throughput efficiency with large entrance and exit apertures (to match the size of the hybrid detector array and the thermal source), long optical path, and compact volume.

In the technological demonstrator, a total of 38 microbolometers were arranged to fit in an area equal to the image of the source on the focal plane. Each pixel was closely coupled to a specific spectral filter and defines a specific spectral channel. All the spectral channels work in parallel to acquire an IR absorption spectrum.

The resolving power and the identification capacity of the system depend on the total number, position, and bandwidth, of the spectral channels. The final choice of the channels was made with the help of multivariate statistical analysis, by taking into account the spectral fingerprints of some 400 compounds [5], of which 20 were CAs, while the others were toxic industrial compounds (TICs) and VOCs of different nature and use. In its final configuration, the system spans the IR spectrum from 7.5 to 14 microns with an almost uniform spectral resolution of about 0.18 micron/channel. This is sufficient to resolve the absorption bands of most CAs, but some problems may arise with blood agents such as HCN, which have only one narrow ( $\sim 0.08 \mu\text{m}$ ) absorption peak at the edge of the sensor spectral window ( $\sim 14 \mu\text{m}$ ).

Simulations have shown identification failures when the system is tested with 10s ppm of HCN.

For each spectral channel, absorption due to IR active vapours was calculated by comparing the signal to an average made over a set of previous acquisitions, used as background or reference. The background is a moving average that is continuously updated to account for drifts in the environmental conditions and in the air composition. As such, the system recognizes only spectral features that “pop up” in the timeframe of a few acquisitions (i.e., fast events as those due to accidents or attacks with CAs) and cannot be easily messed up by the presence of persistent gases.

### 3. Detector Array

Each microbolometer consists of an active layer of vanadium oxide (with its contacts) grown on a silicon nitride micro-bridge suspended over a silicon die (Figure 3(a)). Detectors are made with large area and specifically designed to optimize S/N rather than spatial resolution or response time (as would be the case for an imaging array).

The detectivity ( $D^*$ ) of the microbolometers (Figure 3(b)), measured on a test bench, is higher than  $1 \times 10^8 \text{ cm} \sqrt{\text{Hz}}/\text{W}$  at a modulation frequency of 7 Hz and in the whole spectral range 7–14  $\mu\text{m}$ . As such, it is at the state of the art for this type of detectors. With an active area ( $A$ ) in excess of  $1 \text{ mm}^2$ , the noise equivalent power of the detector ( $\text{NEP} = \sqrt{A}/D^*$ ) is calculated better than  $1 \times 10^{-9} \text{ W}/\sqrt{\text{Hz}}$ . Since the system is designed to deliver to the detector an average in band power of several  $\mu\text{W}$ , we could expect a signal-to-noise ratio (S/N) better than  $10^4$  for an integration time of 10 s. However, the measured S/N of the sensor system was never found better than  $10^3$ , so demonstrating that detectors do not represent the bottleneck in sensitivity, and room exists to improve optical coupling efficiency and electronic noise.

Microbolometers were fabricated as linear arrays and closely coupled to linear variable (LV) interferential filters grown on independent substrate. The LV filters cover a major part of the LWIR spectrum, from 7.5 to 14 micron.

The same linear array was implemented into a hybrid device, which also includes four PbSe detectors, monolithically integrated with their corresponding interference filters, and working in the MWIR spectral range [6].

A printed circuit board (PCB) was designed and implemented for signal readout, lock-in amplification, and A/D conversion of 38 electronic channels.

The integrated sensor (Figure 4) unit comprises room temperature arrays of microbolometers, filters, and, optionally, integrated electronics on silicon chips.

#### 4. Technological Demonstrator

A technological demonstrator (Figure 5) has been constructed, consisting of a compact ( $35 \times 25 \times 15 \text{ cm}^3$ ) sensor head, externally connected to a laptop computer and to software specifically developed for data analysis system control.

A dedicated human machine interface (HMI) has been developed to control the acquisition and data processing of the sensor.

Experimental spectra are acquired and displayed at a rate of 1 Hz. Pattern recognition routines compare the measured spectrum to the already mentioned database of 400 compounds. In case of matching, the name of the compound is displayed on the computer screen together with its estimated concentration and reference spectrum (Figure 6). If the compound is a chemical agent (a “target”), the system delivers an alarm signal, while if it is not, the system just delivers a warning signal for the presence of an “interferent.”

#### 5. Experimental Tests and Results

Experimental tests were carried out with the sensor inside a glass box  $600 \times 400 \times 300 \text{ mm}$  and under a vapour tight steel lid (Figure 7). During the tests, the box was kept under an extraction hood as an additional safety measure.

The box featured heating elements and thermal control, to speed up vaporization and prevent recondensation of low volatile liquids. Use of fans favored air circulation and uniform distribution of the vapours in the air volume. Chemicals were injected as liquids through a silicone septum by means of a microsyringe. Other silicone ports were used to extract air samples from the box in the course of the test and analyze air composition by commercial GC Mass Spectrometer.

A short list of some representative compounds was selected to perform an acceptance test (AT). This list is reported in Table 1. The tests were performed in the facilities of CETLI (Centro Tecnico Logistico Interforze) and no false negative or false positive were observed, while all the chemicals (both targets and interferents) were correctly detected and identified. Response time was in the order of a few seconds (anyhow depending on vaporization dynamics rather than on intrinsic response time of the sensor). Limit of detection (LoD) and limit of identification (LoI) depend on absorption coefficients (different for different chemicals) and on correlation thresholds (adjustable parameters). Values found for DMMP were  $\text{LoD} \approx 900 \text{ ppb}$ ;  $\text{LoI} \approx 7 \text{ ppm}$ .

The system performance, during the tests with the substances in Table 1, is summarized in Table 2.

TABLE 1: List of compounds that have been used for the sensor validation.

Substance name	Class
Chloropicrin	Target (pulmonary agent)
Dimethyl methyl phosphonate (DMMP)	Target (precursor and simulant of nerve agent Sarin)
1,4-Thioxane	Interferent (VOC, product of the degradation of S-mustard)
Triethyl-amine	Interferent (VOC, chemical analog of N-mustard)
Isopropyl alcohol	Interferent (VOC)
Ethanol	Interferent (VOC)
Trichloroethylene	Interferent (TIC)
Carbon tetrachloride	Interferent (TIC)

TABLE 2: System performance.

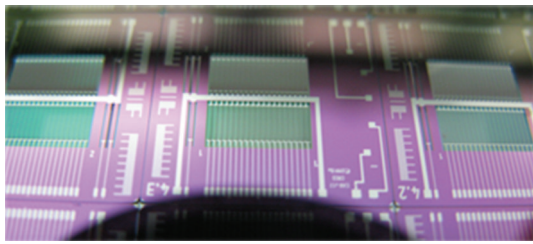
Chemical detection range	All the 8 chemicals detected during AT. During AT, DMMP was found at $\text{LoD} < 900 \text{ ppb}$ and $\text{LoI} < 7 \text{ ppm}$ .
Sensitivity	LoD and LoI depend on absorption coefficients and on correlation parameters settings. Typical values are few ppm. Very strong ability to recognize targets and interferents.
Selectivity	All the 8 chemicals were correctly identified during AT, by comparing the experimental spectra to the full DB of 400 chemicals.
Response time	Few seconds to detect the gas.
False negative rate	No false negative during AT.
False positive rate	No false positive during AT.
Size and power needs	Size $\approx 30 \times 20 \times 15 \text{ cm}$ ; weight $\approx 7 \text{ Kg}$ ; power $< 15 \text{ W}$ (sensor head).

#### 6. Discussion

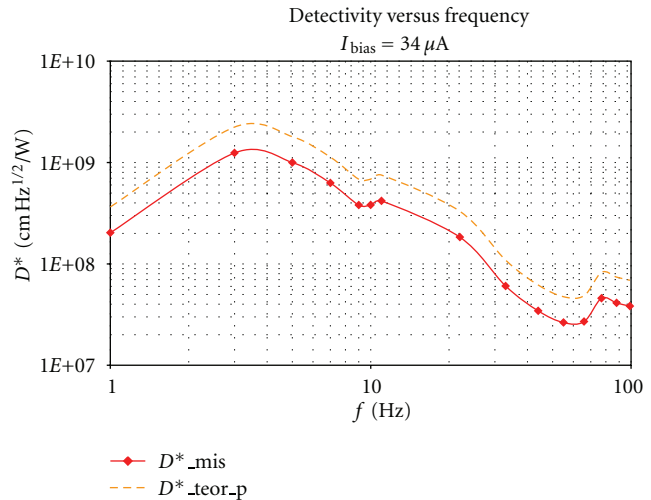
The tests made with DMMP can be used to estimate with good accuracy the performance of the system against Sarin and other nerve agents of the G and V classes. Since the strength ( $\alpha$ ) and position ( $\lambda_{\text{max}}$ ) of the absorption peaks are so close for DMMP ( $\alpha_{\text{DMMP}} = 2.7 \cdot 10^{-3} \text{ ppm}^{-1} \text{ m}^{-1}$  at the wavelength  $\lambda = 9.52 \mu\text{m}$  [7]) and Sarin ( $\alpha_{\text{Sarin}} = 3.0 \cdot 10^{-3} \text{ ppm}^{-1} \text{ m}^{-1}$  at the wavelength  $\lambda = 9.88 \mu\text{m}$  [8]), the LoD for Sarin can be calculated as

$$\text{LoD}_{\text{Sarin}} = \text{LoD}_{\text{DMMP}} \cdot \frac{\alpha_{\text{Sarin}}}{\alpha_{\text{DMMP}}} \approx 816 \text{ ppb}. \quad (1)$$

Limits of detection in the 1 ppm range can be expected also for the other G and V agents, since they all have absorption peaks in the range 9–11 micron and absorption strengths in the range  $(1 \div 5) \cdot 10^{-3} \text{ ppm}^{-1} \text{ m}^{-1}$ . Similar considerations lead to estimate LoDs under 10 ppms for mustards as well. With this sensitivity, our sensor cannot be classified as a trace



(a)



(b)

FIGURE 3: Application-designed VOx microbolometer arrays on SiN microbridges (a) and their detectivity (b).

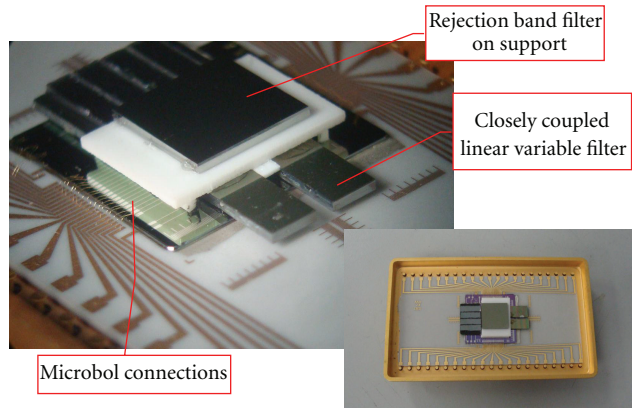


FIGURE 4: Integrated detector array.

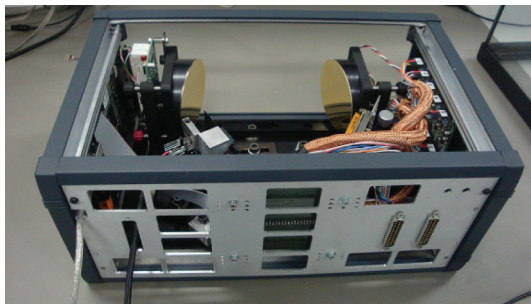


FIGURE 5: Technological demonstrator.

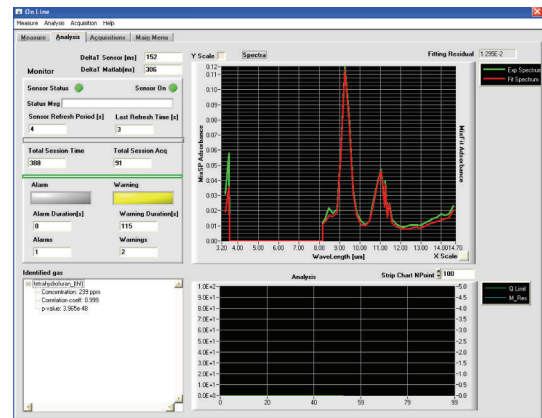


FIGURE 6: Results visualization.

sensor suitable to detect CA agents at their minimum toxic or even lethal doses. However, its sensitivity is appropriate for early warning applications in real scenarios. In fact, in the course of a terroristic attack, the quantities of toxic agents released in the air would vastly exceed their lethal dose and could reach or even exceed their saturation concentration at the local temperature. Saturation concentration values of

Table 3 suggest that the sensor would deliver a prompt alarm in the presence of almost any CA, with the possible one

TABLE 3: Saturation concentrations for some of the most common CAs.

Substance name	Tabun, GA (nerve agent)	Sarin, GB (nerve agent)	VX (nerve agent)	Sulfur mustard, H (blister agent)	Nitrogen mustard, HN-1 (blister agent)	Lewisite (blister agent)	Diphosgene (pulmonary agent)
Saturation concentration in the gas phase at 25°C (ppm)	92	3289	1	92	329	461	13553



FIGURE 7: Experimental setup for the sensor validation.

exception of VX, that has a saturation concentration too low and too close to the LoD of the system.

## 7. Conclusions

A new design of advanced point sensor has been developed and validated, based on nondispersive Infrared (NDIR) absorption spectroscopy, capable of providing early warning in the presence of chemical agents or other toxic compounds in the air, and suitable for operation on battlefields or in urban areas at risk of terroristic attack.

Key assets of the sensor are its wide chemical range and strong selectivity. Results of repeated tests made over a wealth of chemical agents, solvents, perfumes, and other VOC, show that the sensor goes beyond the simple distinction between targets and interferents, as it is capable of correctly identifying chemicals selected from a list of 400 potential candidates.

With limits of detection and identification in the range from one to a few ppm, this sensor cannot be classified as a trace sensor according to nowadays standards. However, its sensitivity is appropriate for early warning in real scenarios, where the quantities of toxic agents released in the course of an attack would reach or even exceed the saturation concentration, which is generally higher than the lethal dose.

## Acknowledgments

This work has been supported by the European Defence Agency (EDA) under the framework of the CANARIO (CWA Analyzer based on low cost dual band IR microsystems)

Project. CANARIO Project has been carried out in cooperation with Spanish Partners coordinated by ITM-CIDA Technological Institute.

## References

- [1] Y. Sun and K. Y. Ong, *Detection Technologies for Chemical Warfare Agents and Toxic Vapors*, CRC Press, 2005.
- [2] M. E. Webber, M. Pushkarsky, and C. K. N. Patel, "Optical detection of chemical warfare agents and toxic industrial chemicals: simulation," *Journal of Applied Physics*, vol. 97, no. 11, Article ID 113101, pp. 1–11, 2005.
- [3] C. Corsi, N. Liberatore, S. Mengali, A. Mercuri, R. Viola, and D. Zintu, "Advanced applications to security of IR smart microbolometers," in *Proceedings of the International Society for Optical Engineering*, vol. 6739 of *Proceedings of SPIE*.
- [4] R. Viola, "High-luminosity multipass cell for infrared imaging spectroscopy," *Applied Optics*, vol. 45, no. 12, pp. 2805–2809, 2006.
- [5] S. W. Sharpe, T. J. Johnson, R. L. Sams, P. M. Chu, G. C. Rhoderick, and P. A. Johnson, "Gas-phase databases for quantitative infrared spectroscopy," *Applied Spectroscopy*, vol. 58, no. 12, pp. 1452–1461, 2004.
- [6] C. Sierra, S. Mengali, M. C. Torquemada et al., "Multicolor microbolometer and VPD PbSe hybrid focal plane sensors for analytical applications," in *Proceedings of the 5th International Symposium on Optronics in Defence and Security (OPTRO '12)*, 2012.
- [7] A. Mukherjee, I. Dunayevskiy, M. Prasanna et al., "Sub-parts-per-billion level detection of dimethyl methyl phosphonate (DMMP) by quantum cascade laser photoacoustic spectroscopy," *Applied Optics*, vol. 47, no. 10, pp. 1543–1548, 2008.
- [8] S. W. Sharpe, T. J. Johnson, P. M. Chu, J. Kleimeyer, and B. Rowland, "Quantitative, infrared spectra of vapor phase chemical agents," in *Proceedings of the Chemical and Biological Sensing IV*, vol. 5085 of *Proceedings of SPIE*, August 2003.